EXPERIMENTAL STUDY OF PHOTO-ELECTRON DIFFRACTION FROM TWO-CENTER MOLECULES BY MEANS OF THE COLTRIMS TECHNIQUE

by

TIMUR OSIPOV

B.S., University of Nevada, Reno, 1998

A DISSERTATION

Submitted in partial fulfillment of the

requirements for the degree

DOCTOR OF PHILOSOPHY

Department of Physics
College of Arts and Sciences

KANSAS STATE UNIVERSITY
Manhattan, Kansas

2003

Approved by:

Major Professor

C. Lewis Cocke

COPYRIGHT

EXPERIMENTAL STUDY OF PHOTO-ELECTRON DIFFRACTION FROM TWO-CENTER MOLECULES BY MEANS OF THE COLTRIMS TECHNIQUE

TIMUR OSIPOV

2003

Copyright by Timur Osipov, 2003

COPYRIGHT

EXPERIMENTAL STUDY OF PHOTO-ELECTRON DIFFRACTION FROM TWO-CENTER MOLECULES BY MEANS OF THE COLTRIMS TECHNIQUE

TIMUR OSIPOV

2003

ABSTRACT

The molecular k-shell photoionization process launches an outgoing electron wave originating at the innermost point of the corresponding molecular potential. This wave can be used as a deep probe of this potential by analyzing the scattering from it. Gas targets consisting of molecules of acetylene (C_2H_2) and ethylene (C_2H_4) were subjected to x-ray radiation at energies slightly above the carbon k-shell electron ionization potential. This photoionization process, followed by Auger decay, leads to the Coulomb explosion of the resulting molecular ion ($C_2H_2^{++}$ or $C_2H_4^{++}$). By using the cold-target-recoil-ion-momentum-spectroscopy (COLTRIMS) technique with a multi-hit-detection capability the recoils of the reaction were measured in coincidence with the photo-electron. The measured positions and the times-of-flight were converted into the momenta of the particles on an event-by-event basis. The momenta of the positively charged recoils defined the orientation of the molecule before the break up occurred and was used, with the electron momentum, to create the photo-electron angular distribution in the body-fixed frame of the molecule. One particular characteristic of the cross sections studied in this work is the debated presence of an f-wave shape resonance that occurs at photon energies of a few eV above the carbon 1s electron ionization potential. The ability to measure photo-electron angular distributions in the body-fixed frame provided information about this resonance not available earlier.

Another novel technique presented in this thesis is a way of timing molecular rearrangements on a 100fs time scale. The strongly peaked photoelectron emission patterns were used to "start a clock" which was used to measure the subsequent chemical rearrangement. The photoelectron distribution was used to indicate the alignment of the target molecular axis at the time of photoionization, and the associated final momentum distribution of the heavy fragments was used to deduce information about the time scale and pathways for the fragmentation.

Table of Contents

Table of Contents i

List of Figures iii

List of Tables viii

Acknowledgements ix

1 Introduction 1

2 Experimental Specifics 4

2.1 Details of the Observed Reactions 4

2.2 Experimental Setup 7

2.3 Data Analysis Details 24

2.3.1 Row Signals. Multi-hit Reconstruction 24

2.3.2 Calibration 28

2.3.3 PIPICO Spectrum, Recoil Momentum 39

2.3.4 Electron Momentum 46

2.3.5 Extraction of Electron Angular Distributions in a Body Fixed Frame 47

3 F-wave Shape Resonance Analysis 59

3.1 Previous studies, Experiment and Theory 62

3.2 Hydrocarbons 65

3.3 Results 81

3.3.1 Total Cross Section of the Reaction 81

3.3.2 Spherical Harmonics Fits. Extraction of Transition Amplitudes . . . 83

4 Electrons as a Clock **129**
4.1 Acetylene/Vinylidene issue 130

5 Summary **150**

A ALS Beam Lines Specifications **153**

B Extraction of the Jet Parameters From the Experimental Data **154**

C Delay Line Detectors **163**

D Electron Momentum Reconstruction in the Magnetic Field **173**

E Exact Wiggles Spectrum Curve Calculation **180**

F The PIPICO Spectrum Fitting **183**

G Fitting Photo-Electron Angular Distribution **192**

H Plotting the Experimental Angular Distributions **203**

I Acetylene/Vinylidene Momentum Picture Interpretation **211**

J Calculation Of C–C bond rotation in the Isomerization Process **215**

References **221**

LIST OF FIGURES

2.1 Lawrence Berkeley National Lab 8
2.2 ALS Beamlines Diagram 9
2.3 Apparatus Photo 11
2.4 Apparatus Schematics 12
2.5 Spectrometer 14
2.6 Electron Trajectories in COLTRIMS Spectrometer 15
2.7 Detector Image 16
2.8 Electronics Setup 17
2.9 Photon Flux Monitoring in the Energy-Scanning Mode 18
2.10 Signal Diagram 20
2.11 Kmax Data Acquisition Software 22
2.12 PAW Screen Shot 23
2.13 Position Signals 25
2.14 Reconstruction Algorithm Results 27
2.15 Electrons in the Spectrometer EM Field 29
2.16 Wiggles and Fish Spectra 31
2.17 Mono-energetic Electrons Wiggles Spectrum and Its Fit 34
2.18 Detector Image from the Calibration Mask. 38
2.19 Ethylene Breakup Channels Labelling 40
2.20 Ethylene Breakup Channels Detailed Labelling 41
2.21 Recoil Momentum Component Calibration 42

2.22 Experimental Spatial Resolution Definition 44
2.23 Electron Momentum and Kinetic Energy Release 48
2.24 Electron Momentum Calibration 49
2.25 Quick Electron Angular Distribution at 302eV Photon Energy 51
2.26 $f(\theta, 0, \theta')$ Angular Distribution for 295eV Circular Light 54
2.27 $f(\theta, 0, \theta')$ Angular Distribution for 302eV Circular Light 55
2.28 $f(\theta, \phi, 0)$ Angular Distribution for 295eV Circular Light 56
2.29 $f(\theta, \phi, 0)$ Angular Distribution for 302eV Circular Light 57

3.1 Calculated F-wave Shape Resonance in Hydrocarbons 61
3.2 CO K-shell Photo-Ionization Diagram 63
3.3 Fragmentation of N_2 After K-shell Photoionization 66
3.4 Comparison of Experimental and Theoretical Partial CO Cross Sections . . . 67
3.5 Dipole Matrix Elements $d_{l\sigma}$ for CO C K-edge Photoionization 68
3.6 Comparison of Experimental and Theoretical Partial N_2 Cross Sections . . . 69
3.7 CO angular Distribution of 10.4 eV Carbon K-photoelectrons 70
3.8 Angular distribution of 9.8 eV K-photoelectrons from N_2 71
3.9 C_2H_2 PIPICO 72
3.10 C_2H_4 PIPICO 73
3.11 C_2H_6 PIPICO 74
3.12 Hydrocarbons Reaction Steps, Energetics and Dynamics 76
3.13 C_2H_2 Momentum 77
3.14 C_2H_4 Momentum 78
3.15 C_2H_6 Momentum 79
3.16 C_2H_4 Breakup Branching Ratios 80
3.17 Total Cross Section versus the Photon Energy 82
3.18 Electron Energy as a Function of the Photon Energy 84
3.19 Gated Electron Momentum and Kinetic Energy Release 85
3.20 Electron Angular Distribution at 293eV Photon Energy 87
3.21 Electron Angular Distribution at 295eV Photon Energy 88
3.22 Electron Angular Distribution at 298eV Photon Energy 89

3.23 Electron Angular Distribution at 302eV Photon Energy 90
3.24 Electron Angular Distribution at 306eV Photon Energy 91
3.25 Electron Angular Distribution at 309eV Photon Energy 92
3.26 Electron Angular Distribution at 312eV Photon Energy 93
3.27 Electron Angular Distribution at 315eV Photon Energy 94
3.28 Electron Angular Distribution at 318eV Photon Energy 95
3.29 Electron Angular Distribution at 320eV Photon Energy 96
3.30 Electron Angular Distribution Fit at 293eV Photon Energy (section 1) . . . 99
3.31 Electron Angular Distribution Fit at 293eV Photon Energy (section 2) . . . 100
3.32 Electron Angular Distribution Fit at 293eV Photon Energy (section 3) . . . 101
3.33 Electron Angular Distribution Fit at 302eV Photon Energy (section 1) . . . 102
3.34 Electron Angular Distribution Fit at 302eV Photon Energy (section 2) . . . 103
3.35 Electron Angular Distribution Fit at 302eV Photon Energy (section 3) . . . 104
3.36 Electron Angular Distribution Fit at 315eV Photon Energy (section 1) . . . 105
3.37 Electron Angular Distribution Fit at 315eV Photon Energy (section 2) . . . 106
3.38 Electron Angular Distribution Fit at 315eV Photon Energy (section 3) . . . 107
3.39 $f(\theta, 0, \theta')$ Angular Distribution Fit for 295eV Circular Light 109
3.40 $f(\theta, \phi, 0)$ Angular Distribution Fit for 295eV Circular Light 110
3.41 $f(\theta, 0, \theta')$ Angular Distribution Fit for 302eV Circular Light 111
3.42 $f(\theta, \phi, 0)$ Angular Distribution Fit for 302eV Circular Light 112
3.43 Ratio of the σ Cross Section to the π Cross Section 113
3.44 Absolute Values of the σ and π Cross Sections 114
3.45 Comparison of the σ and π Cross Sections With Theory 115
3.46 C_2H_4 Calculated Angular Distributions for 293eV Photon Energy (part 1) . 116
3.47 C_2H_4 Calculated Angular Distributions for 293eV Photon Energy (part 2) . 117
3.48 C_2H_4 Calculated Angular Distributions for 293eV Photon Energy (part 3) . 118
3.49 C_2H_4 Calculated Angular Distributions for 302eV Photon Energy (part 1) . 119
3.50 C_2H_4 Calculated Angular Distributions for 302eV Photon Energy (part 2) . 120
3.51 C_2H_4 Calculated Angular Distributions for 302eV Photon Energy (part 3) . 121
3.52 C_2H_4 Calculated Angular Distributions for 318eV Photon Energy (part 1) . 122
3.53 C_2H_4 Calculated Angular Distributions for 318eV Photon Energy (part 2) . 123

3.54 C_2H_4 Calculated Angular Distributions for 318eV Photon Energy (part 3) . 124
3.55 f-wave Amplitude 125
3.56 Comparison of f-wave Amplitudes from Different Fits 126
3.57 f-wave Phase 127
3.58 Amplitudes of the Partial Waves 128
3.59 Partial Waves Phase Shift Differences 128

4.1 PIPICO Spectrum of the Acetylene/Vinylidene Breakup Channels 131
4.2 Labeled PIPICO Spectrum of the Acetylene/Vinylidene Breakup Channels . 132
4.3 C_2H_2 Proton + Proton PIPICO Coincidence 133
4.4 C_2H_2 Distribution of the Angle Between the Proton Momentum Vectors . . . 135
4.5 Polar Plot of the Angle Between the Proton Momentum Vectors 136
4.6 Momentum and Kinetic Energy Release of Acetylene and Vinylidene 137
4.7 Photo-Electron Angular Distributions Comparison 138
4.8 χ^2 Distribution for Vinylidene Fitting 141
4.9 Fitting Results For Different Rotation Angles 142
4.10 Steps of the Isomerization Process 145
4.11 Ethylene Molecule Rotation Simulation $h\nu$=302eV 147
4.12 Event Sequence For Acetylene and Vinylidene Breakup Channels 148

B.1 Hot Gas Stripe on the Recoil Detector 156
B.2 PIPICO Gate for the C_2H_2 Deprotonation Reaction 157
B.3 Deprotonation Reaction Position Spectra 158
B.4 Deprotonation Reaction Position Spectra with Marked Centers 160
B.5 Y Component of the Center-of-Mass Velocity Distribution 161

C.1 Schematics of the RoentDek Delay Line Detector 164
C.2 Ideal RoentDek Delay Line Detector Resolution 166
C.3 RoentDek Delay Line Detectors 167
C.4 Hex Delay Line Anodes 171
C.5 Pulse Pair Resolution 172

F.1 C_2H_6 PIPICO with Analytical Curves 188

H.1 $f_l(\theta, \theta')$ for the 302eV X-rays on the C_2H_4 Molecule. 204

I.1 Y vs X Momentum Plot of the C_2H_2 Target Symmetric Breakup 212

LIST OF TABLES

3.1 Branching Ratio for Different Target Gases 75

A.1 Beamline 9.3.2 153
A.2 Beamline 4.0.2 153

G.1 C_2H_4 Fitting Results #1 202
G.2 C_2H_4 Fitting Results #2 202

J.1 Angle of the C–C Bond in Trans Bend Geometry of Acetylene Dication . . . 216
J.2 Angle of the C–C Bond in the Vinylidene Dication 220

Acknowledgements

Having completed the work on my dissertation, I would like to express my gratitude to all the people who contributed and helped me during my research. First I would like to thank my advisor Prof. Lew Cocke. This work would never have been completed without his support, insightful ideas, advice and participation. In fact, without him this project would never have been started. I am grateful for his clear, straightforward, and direct style of expressing his opinion, whether it is a compliment on the work well done or a criticism which would stimulate a greater effort to meet his higher expectations.

I wish to thank the director of the J. R. MacDonald Laboratory, Prof. Patrick Richard, for his support and encouragement in my research. The detailed discussions of different theoretical concepts of the data analysis with Prof. Larry Weaver were absolutely essential for the completion of this work. I want to thank all of my Ph.D. committee members, which also includes the chairperson, Prof. Kenneth Carpenter, and Prof. Robert Burckel, for taking the time for a detailed study of my thesis and for insightful suggestions, and corrections.

I am thankful to great teachers Profs. Itzik Ben-Itzhak, Amit Chakrabarti, Nathan Folland, Chii-Dong Lin, and Uwe Thumm from whom I had a chance to learn during my course work.

I would like to express my appreciation to the machine-shop personnel and the JRM lab staff — Bob Gearing, Dave Hill, Scott Chainey, Ron Jackson, Mike Wells, Al Rankin, and Charles Fehrenbach. My thanks go to Dr. Kevin Carnes and Vince Needham for their help with the computer issues and JRM lab experimental setups. I am also grateful for our greater physics department family — Peggy Matthews, Deanna Selby, Jane Peterson, and

Treva Singleton are only a few of its members. I am particularly thankful to Dea Richard for the help with my thesis.

The experimental part of my research, completed at the Advanced Light Source, Lawrence Berkeley National Laboratory, would not be possible without a great friend and colleague, Mike Prior. I am grateful for his participation in all aspects of my Ph.D. work. I thank Harald Bräuning for being my first guide in the world of experimental atomic physics. My thanks go to Reinhard Dörner for teaching me a great deal about the diverse aspects of our experimental setup and analysis techniques, for making my experimental work so much fun. I also thank him for great conceptual insights about the physics involved in my research. I thank all members of the Frankfurt COLTRIMS experimental group. Among those, Thorsten Weber, Matthias Weckenbrock, Lutz Foucar, Ottmar Jagutzki, Lothar Schmidt, Jasmin Titze, Markus Schöffler, Achim Czasch, Andre Staudte, Horst Schmidt-Böcking are just a few.

I appreciate the interest of theorists Mauro Stener and Robert Lucchese in my research, their calculations are very important for my dissertation. I also thank them for the permission to present their results in my thesis.

I wish to thank my fellow students — Ali Alnaser, Steven Voss, Manolis Benis, Chakra Mahrajan, Mikhail Zamkov, Erge Edgü-Fry, Ingrid Reiser and Allen Landers — for their interest and detailed discussions of my results.

I am grateful to my family — my parents, my brother Maxim, my wife Oksana Tkachuk and my dear daughter Nadia — for their moral support and encouragement during my studies.

At this point I would like to acknowledge the financial support of the Chemical Sciences, Geosciences and Biosciences Division, Office of Basic Energy Sciences, Office of Science U. S. Department of Energy.

Here you go, Mom!

Chapter 1

Introduction

Quantum mechanical solutions for the energy levels and wave-functions of the hydrogen atom can be found in analytical form. The situation with the He atom (a two-electron system) is a little more complicated — its solution already requires certain approximations and models. The atomic systems corresponding to other elements of the periodic table and representing many-electron systems are usually described quantitatively by the results of long numerical calculations based on simplified models. When the subject of research is a molecular system, the complexity of the problem increases even more. The many degrees of freedom in molecules and their couplings make it absolutely impossible to describe such a system exactly, and even qualitative numerical description is not a simple task in this case. Experiments allowing for comprehensive study of molecular structure are very valuable. Without these even the available *ab initio* calculation techniques cannot be properly validated.

Photoionization of K-shell electrons is one of the simplest experimental techniques that provides a means for the investigation of the corresponding potential of the system. When

applied to molecules, the resulting dissociation allows for the determination of the molecular orientation at the time of the photoelectron emission, which is then used to obtain the angular distribution of these photoelectrons in the frame of the molecule. This body-fixed-frame angular distribution in turn can provide very detailed information about the corresponding molecular potential. The specific interference characteristics of these angular distributions reveal features of the scattering of the photoelectrons in the potential of the molecular ion left behind and can be used to probe the structure of this potential. This thesis deals with the k-shell electron photoionization of hydrocarbon molecules (C_2H_2, C_2H_4, C_2H_6).

The experimental setup and the detailed analysis are thoroughly covered in the chapter 2.

One of the major components of the experimental detection system used here is the COLTRIMS[1] multihit/multiparticle spectrometer. The associated 4π solid angle momentum imaging technique has been first introduced (by the collaboration of atomic physicists from Kansas State and Frankfurt Universities) about a decade ago and has since been used very successfully in numerous experiments. The word COLTRIMS today is associated more often with the particular type of spectrometer rather than with the whole experimental technique. Over the years it has been modified and improved to allow for the performance of more sophisticated and complete measurements. Today COLTRIMS is used for measurements of reaction product parameters of x-rays on gas jet systems, ion beams and lasers on the optically cooled targets. The use of COLTRIMS in crossed-beam (ion/ion, ion/laser, etc.) experiments show that the cold target is not a necessary requirement for the application of

[1] COLd Target Recoil Ion Momentum Spectroscopy.

the technique — experimental systems consisting of almost every combination of the above "targets" and "projectiles" have been successfully studied by means of the corresponding momentum-imaging approach.

Chapter 3 of this thesis reviews some previous similar experimental and theoretical studies of molecular structure in the case of CO and N_2 k-shell photoionization. The second part of that chapter is devoted to the major results of the analysis of the hydrocarbon molecules.

A novel approach to the exploration of molecular ion dissociation pathways and their time durations are covered in the chapter 4. The case studied here is the isomerization of the dication of acetylene to vinylidene.

A set of appendices offers derivations and details for concepts of the present analysis that require extra attention.

Chapter 2

Experimental Specifics

2.1 Details of the Observed Reactions

The experiment covered in this thesis studies the following atomic reactions. A two-center molecule is subjected to x-ray radiation at a frequency that corresponds to a photon energy of 1 to 30eV above the k-shell ionization threshold of one of the molecular centers. The following k-shell photoionization is a fast process: a 1eV photoelectron leaves the molecule[1] on a time scale of 10^{-16}sec. The motion of the nuclei during this time is negligible. Thus the photoelectron is prompt, and its angular distribution with respect to the axis of the target molecule is determined before the breakup occurs. About 10fs after the ionization the molecular ion Auger decays and a second electron is ejected with an energy close to the 1s electron ionization potential. Lacking two outer shell electrons, the molecule is then likely to break up and undergo a Coulomb explosion as shown in the following schematics:

[1]The size of the molecules studied in the experiment can be characterized by the inter-nuclear distance of the atomic constituents and is on the order of a few a.u. of distance.

$$
\begin{aligned}
CO + h\nu(\sim 300eV) &\longrightarrow CO^{+} + e^{-}(\sim 10eV) \\
&\qquad\qquad \hookrightarrow CO^{2+} + e^{-}(\sim 290eV) \\
&\qquad\qquad\qquad \hookrightarrow C^{+} + O^{+} \\
C_2H_2 + h\nu(\sim 300eV) &\longrightarrow C_2H_2^{+} + e^{-}(\sim 10eV) \\
&\qquad\qquad \hookrightarrow C_2H_2^{2+} + e^{-}(\sim 290eV) \\
&\qquad\qquad\qquad \hookrightarrow CH^{+} + CH^{+} \\
C_2H_4 + h\nu(\sim 300eV) &\longrightarrow C_2H_4^{+} + e^{-}(\sim 10eV) \\
&\qquad\qquad \hookrightarrow C_2H_4^{2+} + e^{-}(\sim 290eV) \\
&\qquad\qquad\qquad \hookrightarrow CH_2^{+} + CH_2^{+} \\
C_2H_6 + h\nu(\sim 300eV) &\longrightarrow C_2H_6^{+} + e^{-}(\sim 10eV) \\
&\qquad\qquad \hookrightarrow C_2H_6^{2+} + e^{-}(\sim 290eV) \\
&\qquad\qquad\qquad \hookrightarrow CH_3^{+} + CH_3^{+}
\end{aligned}
$$

The molecular break up lasts on the order of 100fsec (to reach 10 times the initial internuclear distance[2].). It can be shown that the explosion of the two ions m_1, q_1 and m_2, q_2 can be reduced to the problem of the motion of a single particle of mass $\mu = \frac{m_1 m_2}{m_1+m_2}$ in the central force potential given by $V(r) = -\frac{k}{r} = \frac{q_1 q_2}{4\pi\varepsilon_0}\frac{1}{r}$, with l equal to the angular momentum value of the original two-ion system. The resulting trajectory equations, which describe the motion in the spherical potential (see, for example, equations (3-35), (3-36) of [1]), are

$$
d\theta = \frac{l dr}{mr^2\sqrt{2/m\left(E - V(r) - \frac{l^2}{2mr^2}\right)}} \Rightarrow \Delta\theta = \int_{r_0}^{\infty} \frac{dr}{r^2\sqrt{\frac{2mE}{l^2} - \frac{2mV}{l^2} - \frac{1}{r^2}}},
$$

[2]The general form of equation for time calculation is similar to the one for $\Delta\theta$ and is given by $t = \int_{r_0}^{r} dr/\sqrt{2/m\,(E - V - l^2/(2mr^2))}$

where $\vec{r}$ is the vector separation of the two fragments, described by r and θ.

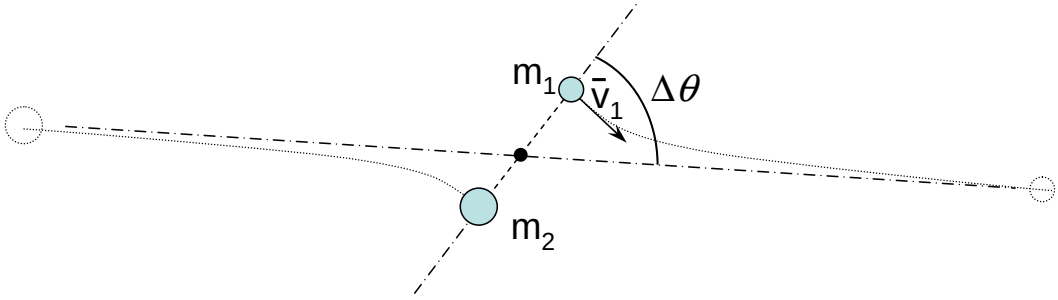

The energy of the particle in the field $V(r)$ is given by $E = \frac{l^2}{2\mu r_0^2} - \frac{k}{r_0}$, where r_0 is the initial internuclear distance. Integration of the equation for $\Delta\theta$ yields

$$\Delta\theta = \mathbf{arccos}\left(\frac{\frac{l^2}{\mu k r} - 1}{\sqrt{1 + \frac{2l^2}{\mu k^2}\left(\frac{l^2}{2\mu r_0^2} - \frac{k}{r_0}\right)}}\right)\Bigg|_{\infty}^{r_0} \tag{2.1}$$

The angular momentum of the system about its center of mass is given by

$$l = l_{ae} \leqslant \frac{1}{2} r_0 p_{ae}$$

where p_{ae} and l_{ae} are the momentum and the angular momentum, respetively, imparted to the system by the Auger decay. After substituting typical values for all the parameters ($q_1 = q_2 = 1$ a.u, $r_0 \approx 2.4$ a.u., $m_1 = m_2 \approx 13 \cdot 1836$ a.u.[3], $p_{ae} \approx 5$ a.u. $\Rightarrow \mu \approx 6.5 \cdot 1836$ a.u., $k \approx -1$ a.u., $l \lesssim 6$ a.u.) the result of equation (2.1) gives an upper bound on the experimental value of $\Delta\theta$ equal to **0.05 rad** or **2.8**°. This small value of the angle justifies the use of the Axial Recoil Approximation which assumes that the molecule does not rotate during the Coulomb explosion and the direction of the measured relative recoil momentum is along the molecular orientation just before the break up.

[3]Higher values of the ion charge, internuclear distance or mass would correspond to even smaller rotation angle $\Delta\theta$.

In the case of hydrocarbons, the probability of breaking into a hydrogen atom (or proton) and the residual molecule is quite high, especially as the number of hydrogen atoms goes up. Another probable channel is a three- (or more) body break up. These channels do not in general provide information about the initial orientation of the molecule and thus are not useful for this work. The useful symmetric or nearly symmetric breakup channels can be clearly separated by means of the PIPICO spectra as discussed in section 2.3.3. The time-of-flight (TOF) and the 2d position of both recoil ions and the photoelectron are measured in coincidence with respect to the time of the x-ray pulse. This information is then used to calculate the initial momenta of all three particles which are than utilized in the further analysis (see section 2.3).

2.2 Experimental Setup

The experiment was conducted at the Advanced Light Source (ALS) facility (fig. 2.2) of Berkeley National Laboratory (fig. 2.1). 1.9GeV electrons circling in a storage ring 62m in diameter are converted into synchrotron radiation which is the source of x-rays for the experiment. The ALS can produce x-rays in two modes of operation. In the "multibunch mode" the storage ring is filled with 270–320 electron bunches with about 2ns separation time. For most experiments the x-rays produced in this mode can be considered a constant DC light. Twice a year ALS works in the "double-bunch" mode. In this case the storage ring is injected with only 2 electron bunches. This way the x-rays come as short pulses with a period of 328ns. Such a pulsed source of x-rays is essential for our experiment since

it provides a "master clock" pulse followed by an empty drift time necessary for the time-of-flight measurements. Part of the data was collected on beamline 9.3.2, but the main contribution was done on beamline 4.0.2 due to the factor-of-100-higher photon flux and better control of the light polarization (see appendix A for the beamline specifications).

Figure 2.1: The Lawrence Berkeley National Lab.

The photoionization reaction takes place inside a chamber (See Fig. 2.4) with a background pressure of 3x10^{-8}Torr. The chamber is designed to house the COLTRIMS spectrometer (see [2–4] for a similar setup) and has a two-stage supersonic gas jet attached to it. (See Fig. 2.3) The two stages of the jet are differentially pumped to minimize the background pressure by preventing the warm gas from drifting up to the chamber. Then the target gas undergoes a cooling expansion though a 60 micron nozzle and is also geometrically cooled by the .3mm diameter skimmer located 8mm above. A 1mm aperture is located about 40mm above the nozzle; it separates the chamber from the second pumping stage. By the time the vertical jet reaches the interaction region it has a transverse diameter of 2mm.

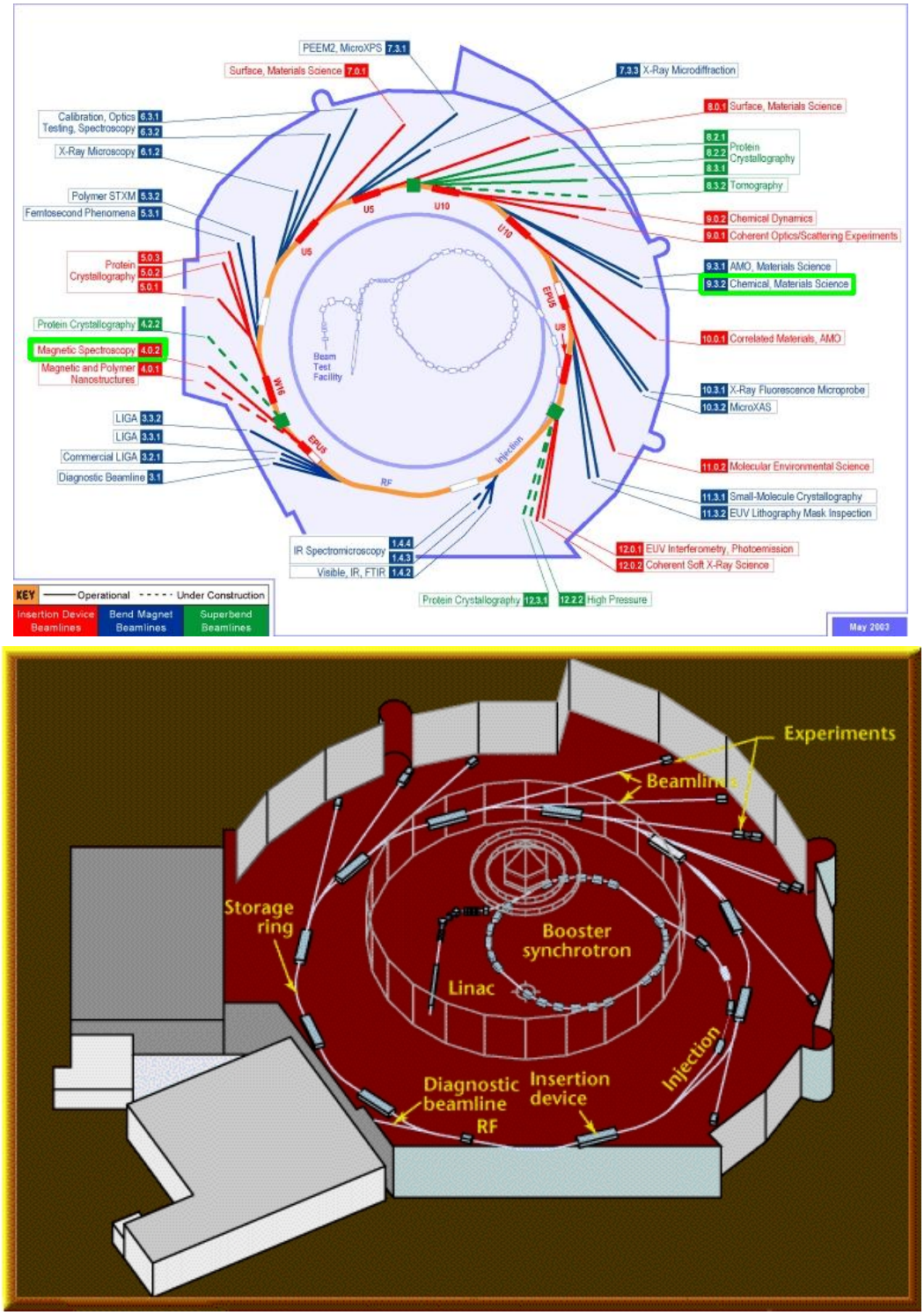

Figure 2.2: ALS Beamlines Diagram. The beam lines where the data collection was done for the current experiment are marked by light green rectangles.

The final target gas temperature is $\sim$.5K in the transverse direction, and <100K spread[4] in the longitudinal direction around the common jet velocity of $\sim$3x10^{-4}a.u. The target density in the interaction region is $\sim 10^{10}$cm^{-3}. A specially designed jet dump is located just above the spectrometer. It serves the purpose of catching the gas jet and preventing it from spreading in the chamber and thus increasing the background pressure (See Fig. 2.4). Both chamber and the jet were built in Germany and brought from Frankfurt to Berkeley for the double-bunch mode experiments.

The COLTRIMS spectrometer located inside the chamber is a standard parallel-plate spectrometer with two electric field regions separated by an 80% transmittance grid to minimize the electrostatic lens effects (see Fig. 2.5). The first region is for acceleration and usually has a 10-15V/cm electric field. The field of this region provides the initial separation and acceleration for the positive (molecular fragments) and the negative ions (electrons). This acceleration field together with the 5cm flight distance ensures that the molecular fragments with typical energies of around 6eV each do not spread further than 2/3 of the detector size (5cm in diameter) in the transverse direction. This way enough of the high energy tail of the recoil distribution is still registered over the whole 4π solid angle. The second region is used for a field-free drift and is located on the electron side of the spectrometer. It has a length twice that of the acceleration path for the electrons for time focusing. The spectrometer is

[4]This spread is likely to be $\ll$100K — the accuracy of the procedure for determining this spread as described in appendix B is limited to this value due to the contribution of other factors. The width of the peak in figure B.5 can be due to the competing factors of the finite target region size and Auger electron kick. The similar width of the center-of-mass velocity along the spectrometer direction (not shown here) supports this last point. For example, if the size of the X-ray beam were around 0.7mm in diameter instead of the assumed .1mm (fig. 2.22), it would compensate completely for the extracted velocity distribution.

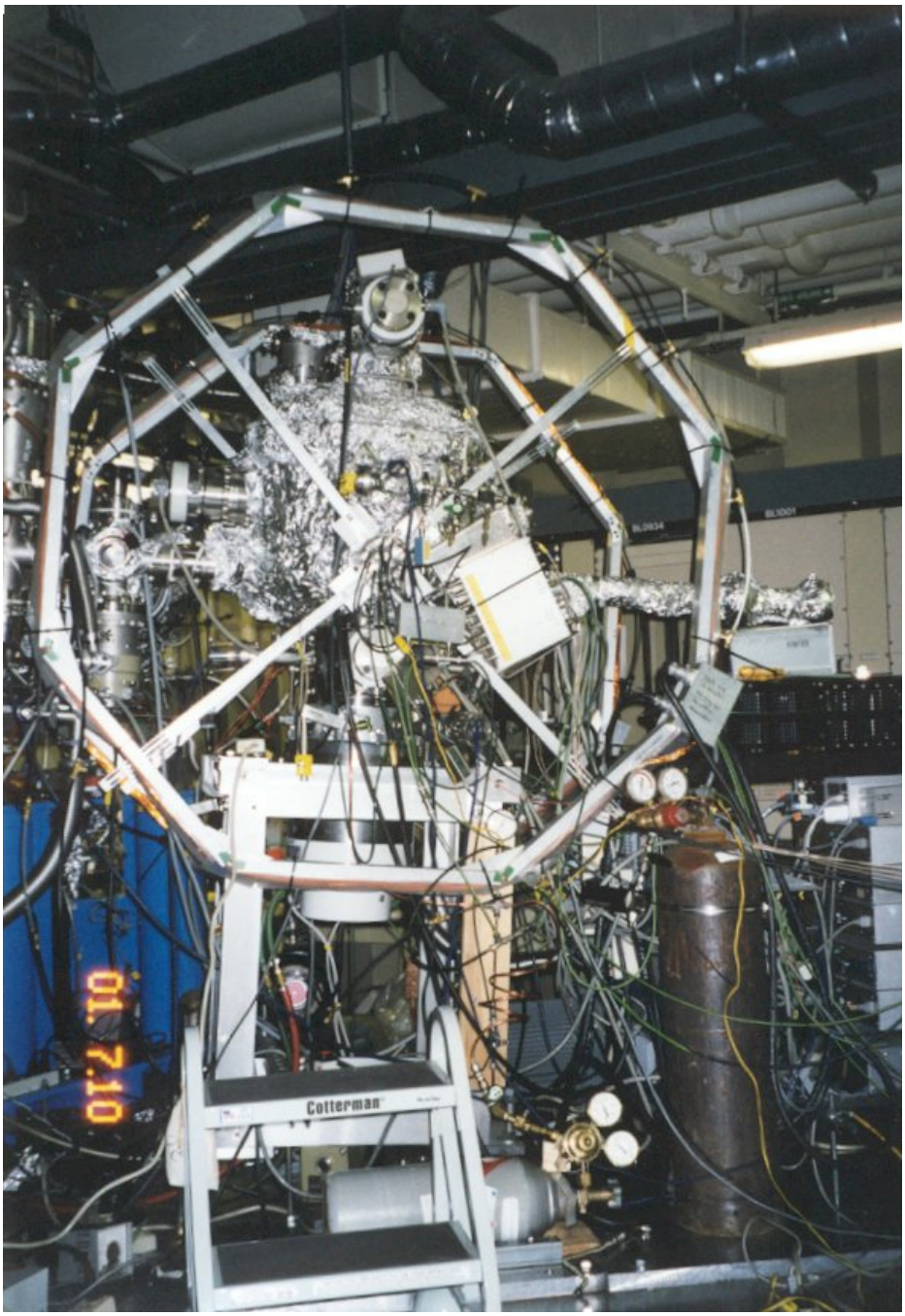

Figure 2.3: A photograph of the apparatus.

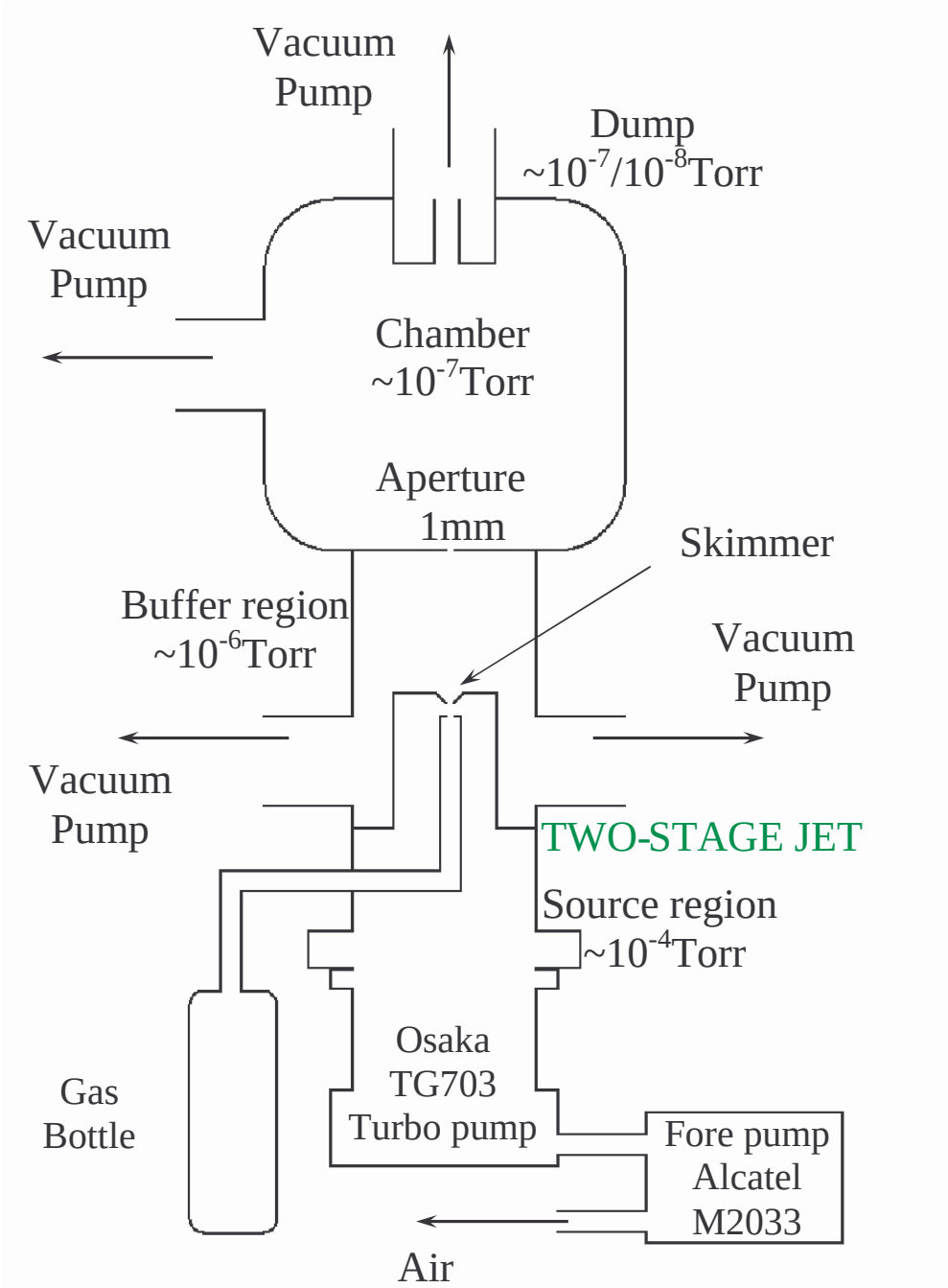

Figure 2.4: Apparatus schematics.

positioned such that its extraction direction is perpendicular to both the direction of light and the gas jet, as shown by Figure 2.5. An electric field of 10-15V/cm is sufficient to obtain a reasonable resolution for the electron longitudinal momentum. However, it is not strong enough to keep all electrons inside the 80mm diameter spectrometer tube. To make sure that 4π solid angle for the electrons is registered, a set of magnetic field coils is assembled around the chamber in the Helmholtz geometry. The magnetic field vector parallel to the electric field of the spectrometer assures that electrons with high initial transverse momentum follow spiral-like trajectories towards the detector instead of escaping (see Fig. 2.6). A magnetic field of about 11Gs keeps all the electrons below 30eV initial transverse energy inside the spectrometer, while having no significant effect on the heavy recoil motion. A position-sensitive detector registers the time-of-flight and 2d position of the electron impact. Together with the value of the magnetic field, this information is enough to reconstruct the complete trajectory of the electrons and thus calculate the complete 3d initial momentum for such electrons (see section 2.3 and Appendix D).

The position-sensitive detectors (PSD) used in this experiment are RoentDek 80mm delay-line detectors (see fig. 2.7 for a typical detector image). Appendix C covers the details on handling the signals from delay-line anode. This state-of-the-art PSD system is equally capable of detecting 2d position and time-of-flight of heavy recoil ions, electrons and even neutral atoms and molecules if they have enough energy to set off an electron avalanche on impact with the channel plates. The delay-line position resolution with the proper electronics can be less than .1mm, and its multi-hit capability with a pulse pair resolution of less than

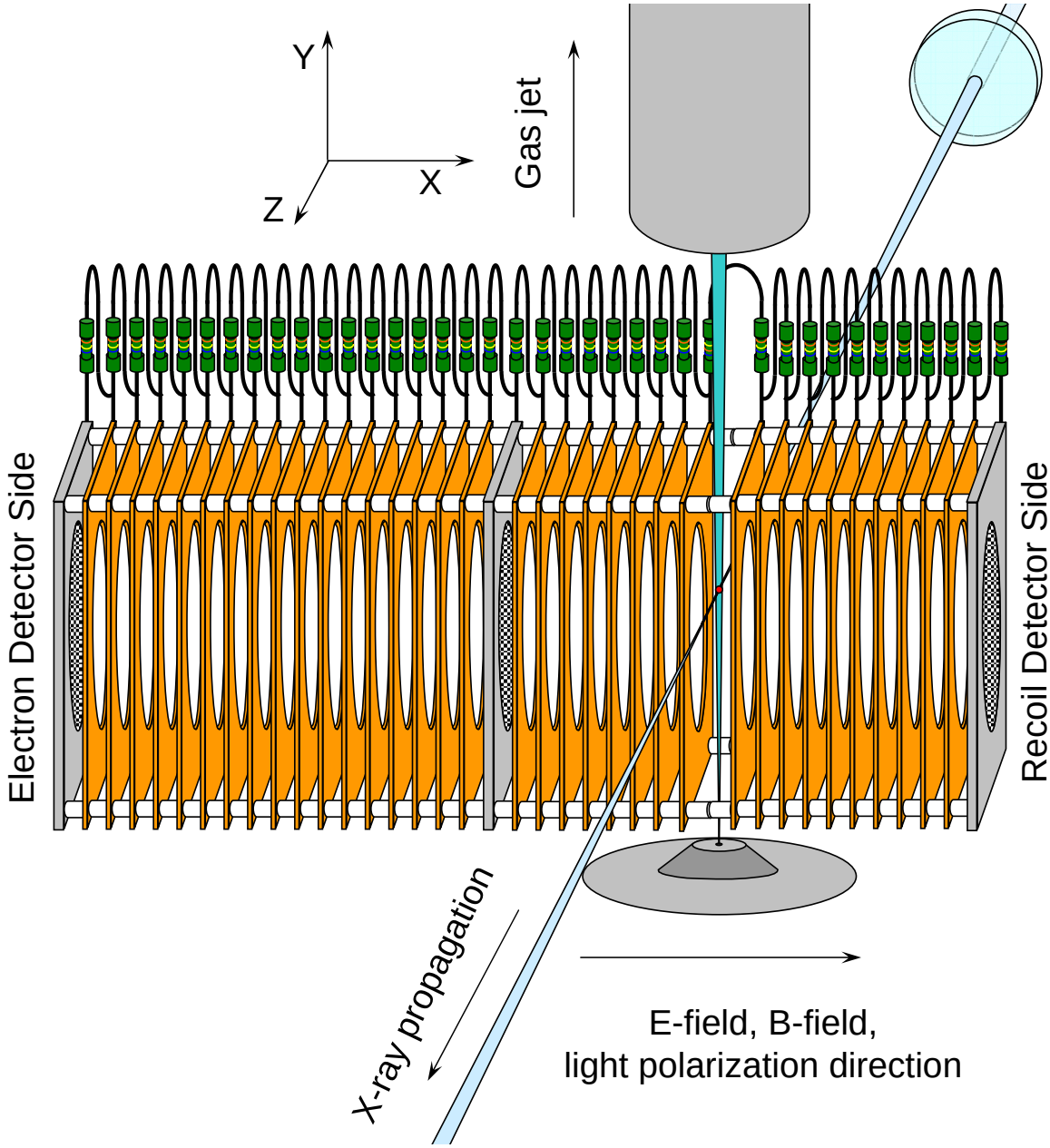

Figure 2.5: Experimental spectrometer setup.

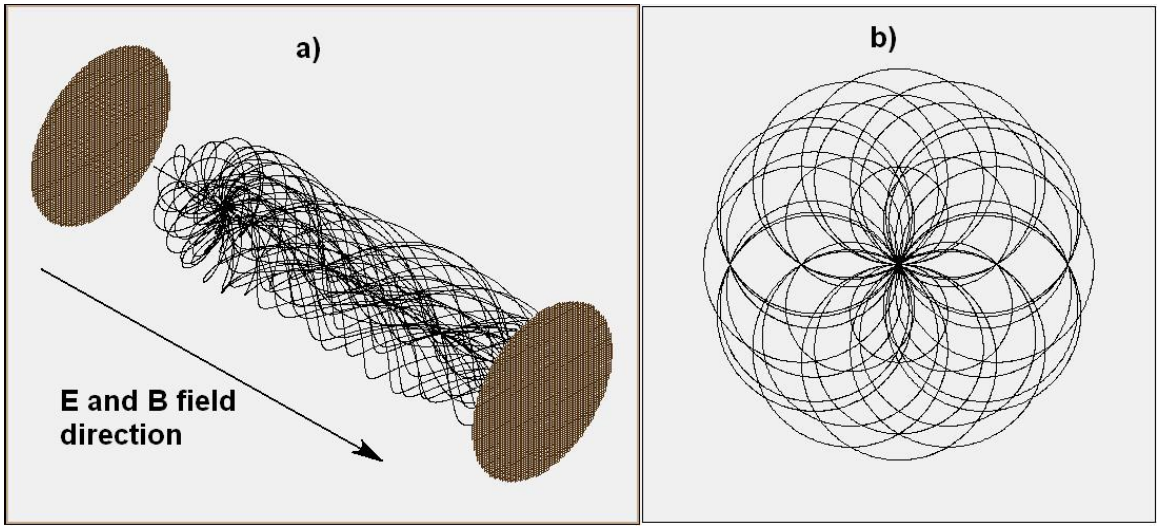

Figure 2.6: Electron Trajectories in the Magnetic and Electric field of the COLTRIMS Spectrometer. 3d view of the whole spectrometer(**a**), projection on the detector plane (**b**). All trajectories pass through the central axis of the spectrometer; i.e., every electron crosses the axis of the spectrometer every time it makes an integer number of turns. The time it takes for the electron to make a full turn is independent of the electron momentum and is defined by the magnetic field strength.

10ns is essential for the described types of the COLTRIMS experiments. The spectrometer has two of these detectors mounted on it, one on each end, for registering positive recoil ions and electrons.

To successfully digitize all the multi-hit signals coming from the delay-line PSDs the proper electronics setup is in order (see Fig. 2.8 for details). The multiple coincidence nature of the experiment requires a quite sophisticated electronics setup to avoid collecting too much useless data. Figure 2.10 shows the signal diagrams for most of the raw signals as well as the specially gated signals that contribute to the final strobe signal of the triple coincidence event. Most parts of the diagram are self explanatory. The two bottom blocks of the figure deal with the collection of the "master clock" signals. These signals are generated

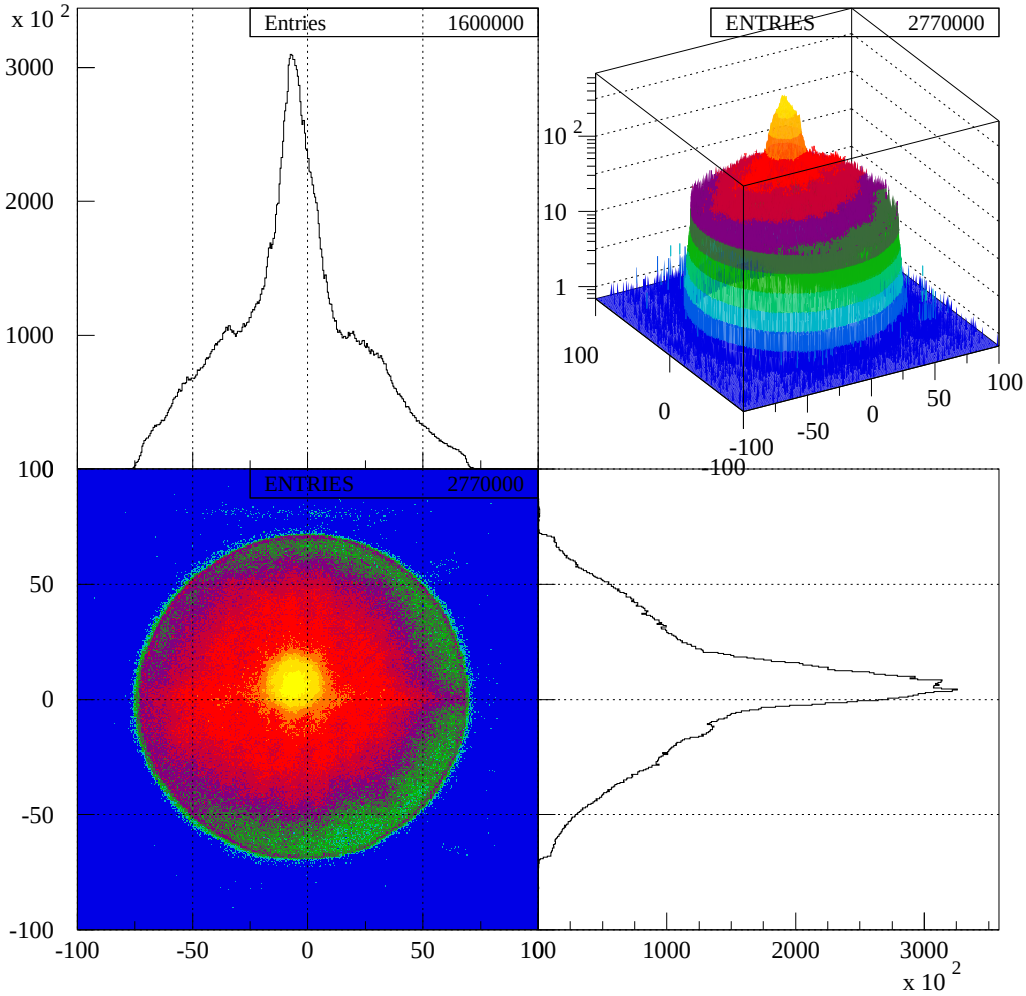

Figure 2.7: Detector Image Obtained with Delay Line Anode.

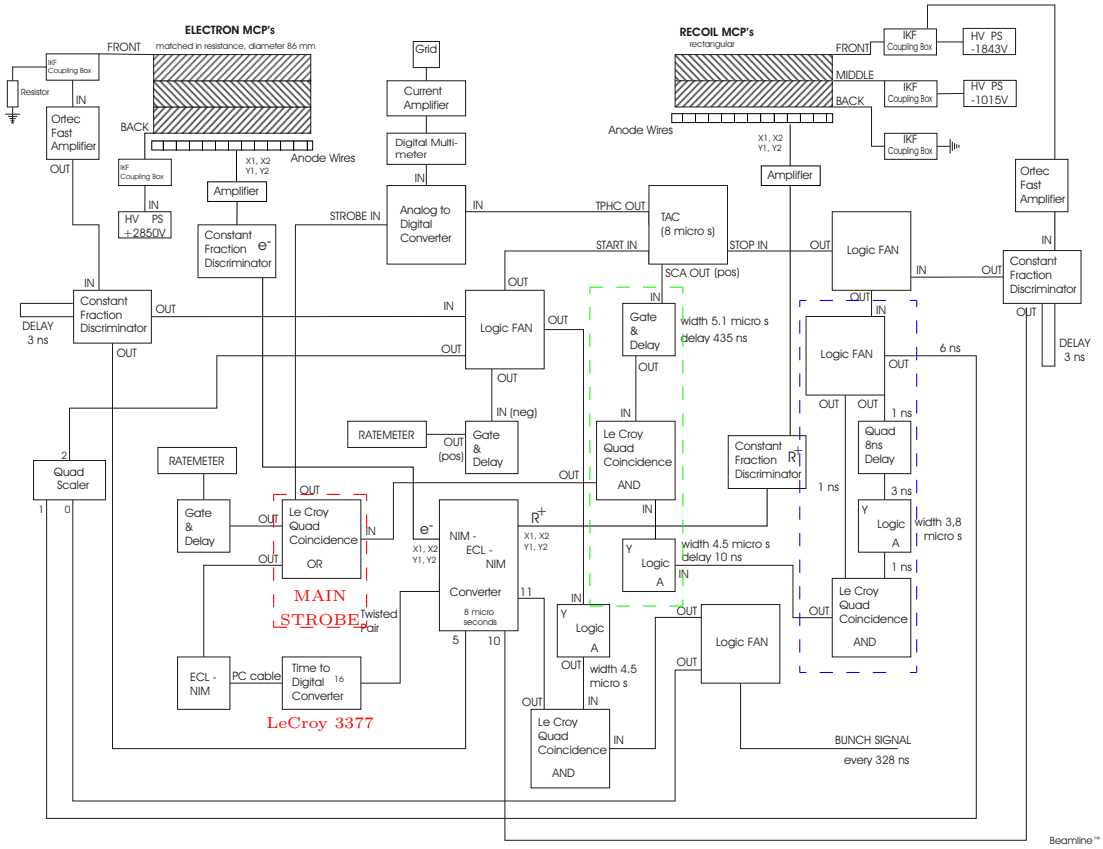

Figure 2.8: **Electronics Setup.** This schematic depicts the part of the experiment with the triple coincidence. The blue rectangle surrounds the main logic of the recoil-recoil coincidence; green — electron-recoil coincidence. The resulting signal is properly stretched and delayed (red rectangle) to serve as the main strobe for ADC and TDC. The Multi-hit LeCroy 3377 TDC collects all the signals from the detectors. The ADC is mostly used for measuring electron and recoil time-of-flight with better resolution. A Quad Scaler keeps track of elapsed time and count rates when in the energy-scanning mode (see also fig. 2.9).

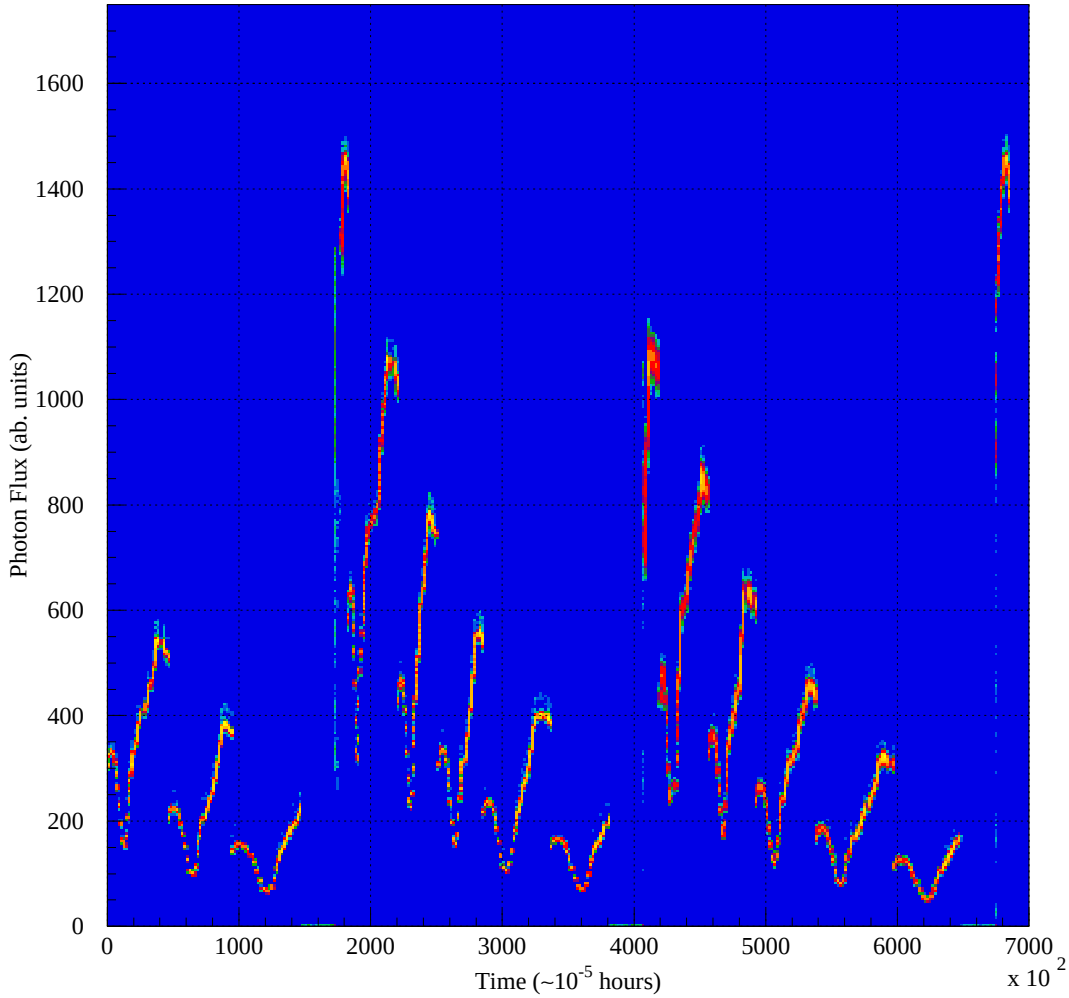

Figure 2.9: Photon Flux Monitoring in the Energy-Scanning Mode. One channel of the counter (Quad Scaler) has a constant frequency input to keep track of the current time; one of the ADC channels has I_{zero} input — value proportional to the photon flux in the interaction region. The long period ($\sim$2.5 hours) exponential decays correspond to the synchrotron ring refill times; short period ($\sim$ half an hour) oscillations correspond to a single (experimental) energy sweep 290–320eV. The structure within a single sweep is due to the beamline internal optics photoabsorption cross-section energy dependence.

every 328ns. The average time of the event is defined by the time-of-flight of heavy recoils and is on the order of several microseconds. During this time about 10 to 20 master clock signals can be registered. Writing all of them in the data file would be a waste of the memory, so a special coincidence is set up to only register the master clock signal when the rest of the event is valid. Ideally a single master-clock pulse per event would provide the time reference for the rest of the signals. It does not matter whether this signal comes before or after the event, since the master clock has a fixed period. In this gating scheme, however, the first master clock signal can be partially corrupted (see line 19 of fig. 2.10); thus it is important to register 2 (or even 3) of these pulses per event, keeping in mind that the first one should not be used in the final analysis.

Two other components of the electronics setup are particularly important. The LeCroy 3377 TDC is a 32-channel Multi-Hit Time-to-Digital-Converter capable of registering up to 16 hits per channel. It has 0.5ns timing resolution, 10ns pulse-pair resolution, 8ns to 32μs time range per event. This TDC can buffer large blocks of data before transferring it to the computer, thus minimizing the event-by-event transfer time overhead. This feature is only useful, however, if the TDC is the only CAMAC-crate module being read. Since other modules need to be read for every event, a List Processor (HYTEC LP1341) is used for the data buffering purposes (not shown on the schematic). This is a single-slot auxiliary CAMAC-crate controller. It can read data from other modules with the high frequency of the CAMAC-crate clock, thus allowing a readout rate of about 10,000 parameters per second with no dead time. The list Processor has 128K x 24bit words of data memory and

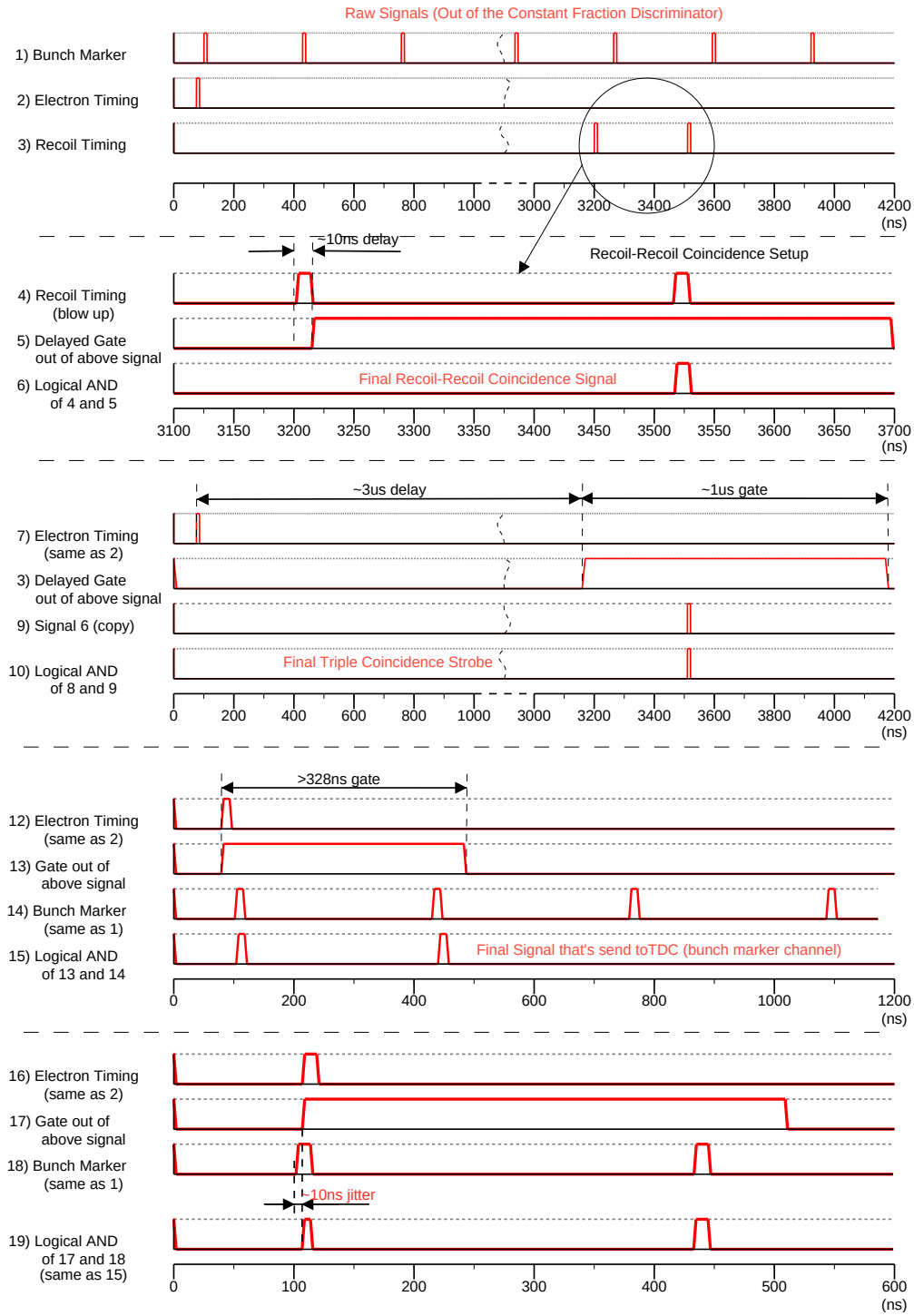

Figure 2.10: Signal Diagram for the Coincidence Setup.

8K x 16bit words Instruction Store. It is capable of running simple programs consisting of module-querying commands, read-out commands, conditional and unconditional jumps, etc. When the memory buffer of the List Processor is filled with data, it transfers all of it to the computer in one block. This transfer operation takes only a fraction of a second.

This typical COLTRIMS setup including the detectors and the listed electronic modules form the detection system with the following performance characteristics and limitations. Every ion of moderate energy (heavy ions of up to 10eV and electrons of up to 40eV) born inside the spectrometer has about a 10-20% chance (due to the detector's channel plate efficiency) of being registered and providing its 2d position and time-of-flight information. The time of flight can be up to 32μs with a one-half-nanosecond resolution. The x and y positions on the detector are measured with a resolution of about quarter of a mm. The position and the time-of-flight resolution as well as its range are defined by the Lecroy 3377 Multihit TDC. Since it has about 10ns dead time after each hit it also introduces a pulse-pair resolution equal to this dead time. That is, if two ions hit the same detector within ten nanoseconds only one hit will be registered and the position information of that hit might be questionable. If, however, the hits are separated by more than 10ns in time, the 3377 TDC can successfully collect up to 16 of them per event, per detector. Other resolution-limiting factors, dictated by the physics of the experiment, and the ways to deal with them will be discussed in the section 2.3.

Kmax software (see fig. 2.11) by Sparrow Corporation for the Power Mac was the data acquisition system used for computer/CAMAC-crate communication, data collection and

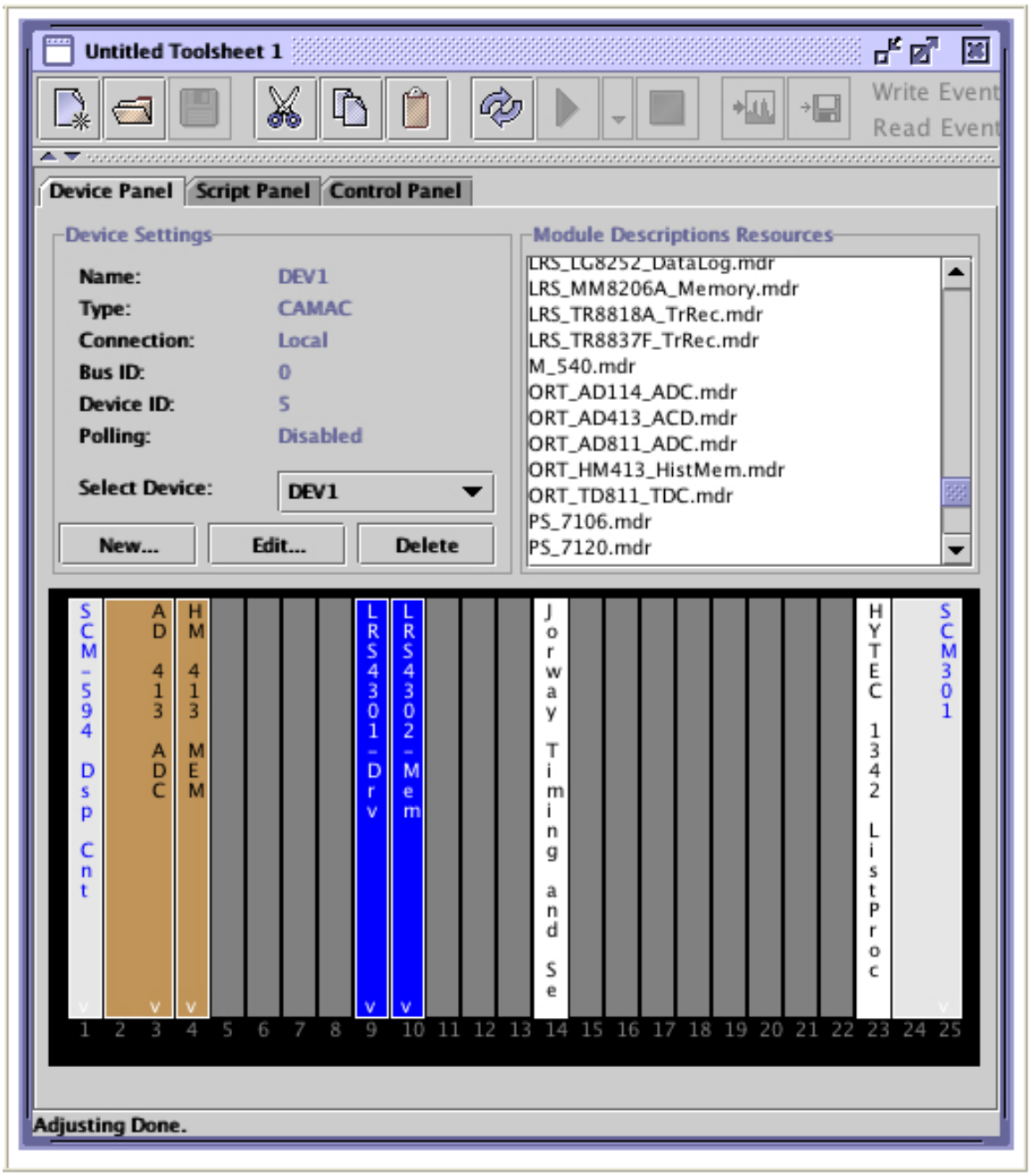

Figure 2.11: Kmax Data Acquisition Software.

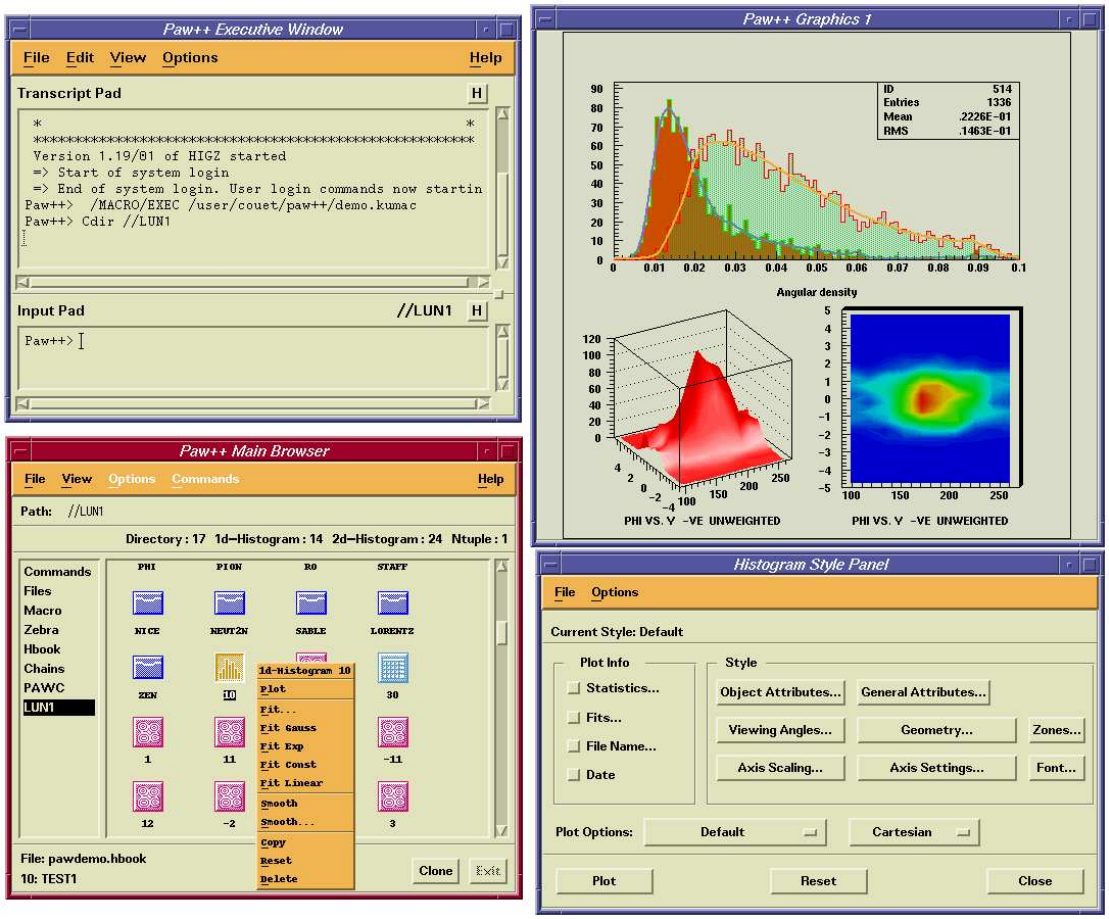

Figure 2.12: Physics Analysis Workshop.

online data analysis. This software, in combination with the List Processor, allowed for a data collection rate of up to 20Mbyte per minute. More details and examples on List Processor operation and Kmax software can be found in [5]. Offline data analysis was done by means of the FORTRAN/C/C++ programs. Final result representation[5] was performed in the Physics Analysis Workshop (PAW) software by CERN (see Figure 2.12).

2.3 Data Analysis Details

This section presents the detailed[6], step by step, overview of the COLTRIMS analysis process used for the investigation of the k-shell photoionization of ethylene molecules (see section 3.2 for the choice of gas here).

2.3.1 Row Signals. Multi-hit Reconstruction

Every analysis starts with the sorting of the raw signals collected. In this particular setup there are eleven timing signals[7] collected by the Multi-Hit TDC, sometimes up to three Analog-to-Digital Converter(ADC) channels and up to three SCALAR channels are also read for energy scanning and photon flux normalization[8]. Most of the data in a regular mode of operation is, however, supplied by the eleven TDC channels: five per detector, plus the master clock signal, also called "bunch marker" since it is synchronized with electron

[5]Most of the macros, used for generation of the of final figures of data plots, histograms, fitting results and movies, can be found in subfolders of the folder "pawfiles/macros" on the attached CD.

[6]Analyzed data files related to this section can be found in the folder "pawfiles/ethylene" of the attached CD. The FORTRAN code used for sorting routines in the presented analysis can be found in folder "programs".

[7]More precisely, it is eleven channels of the TDC; number of signals collected per event can be much higher due to the possibility of multi-hit.

[8]ADC also often used in conjunction with Time-to-Analog Converter(TAC) to get higher resolution for timing signals when the one-half-nanosecond TDC resolution becomes too low.

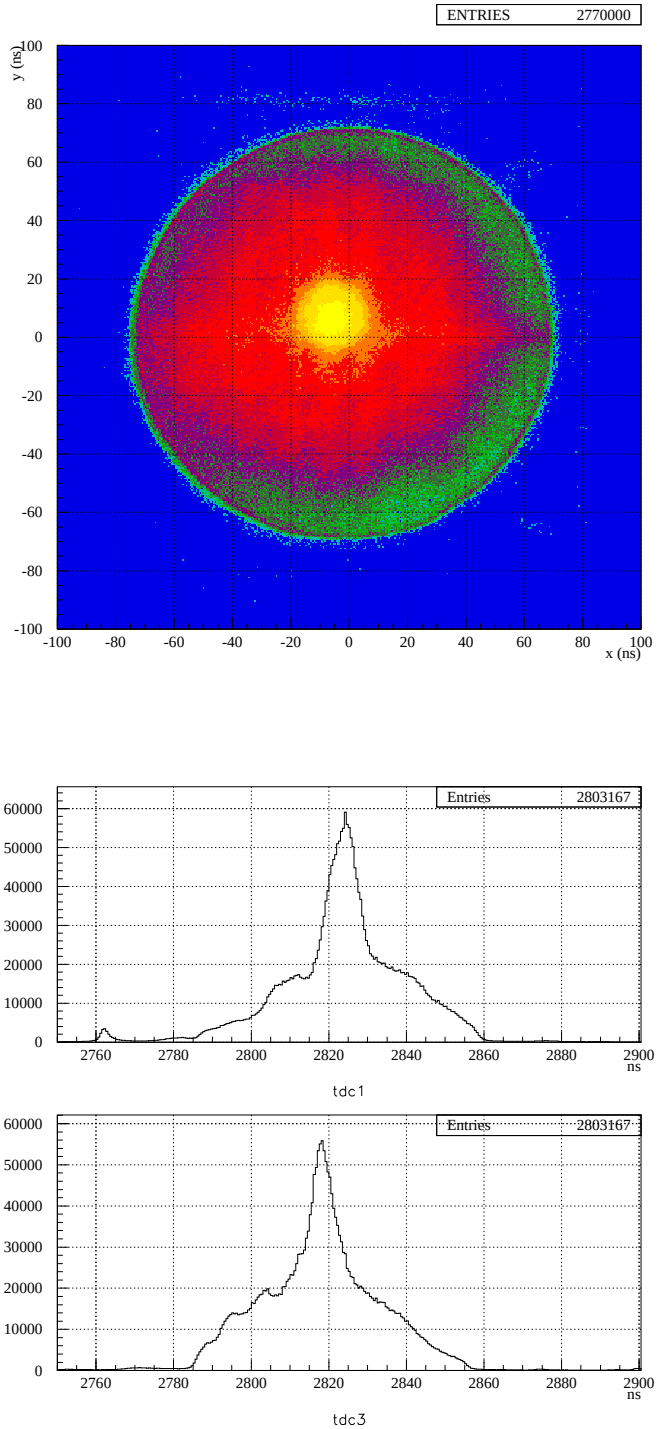

Figure 2.13: Raw Position Signals ("left" and "right") on the bottom, appropriate 2d image at the top.

bunches in the storage ring. Four out of five detector signals come from the delay-line anode and provide the position information (two per dimension — left/right and top/bottom — see Appendix C for conversion equations and special cases) and one time-of-flight signal from the Multi-Channel-Plate (MCP signal). Figure 2.13 shows the pair of raw position signals (left/right) and the corresponding 2d image (top/bottom signals are not shown). The multi-hit capability of the detectors is mainly used on the recoil side of the spectrometer since the detection of both recoils is essential for the kinematically complete experiment. Only the photo-electron needs to be registered on the other detector, but the Auger electrons might also strike the detector thus causing multiple pulses on the electron side of the spectrometer. A real experiment always has background random hits as well as noise in the electronics, all of which also contribute to the number of multi-hit events registered. Every time there are two or more ions hitting the same detector close in time there is a chance that their position signals get mixed up (see Appendix C for examples and reconstruction details). A sophisticated algorithm is used to reconstruct the entangled multi-hit events and to associate the time-of-flight signal with its appropriate position signals. It also helps to recover hits with an incomplete set of signals and to sort out the electronic noises. While this algorithm shows its full power when reconstructing multi-hit events (see fig. 2.14), the single-hit detection does benefit from it, too. The redundant position information is also used in the reconstruction process to enhance the quality of the data[9].

[9]The FORTRAN code for the reconstruction routine can be found in the folder "programs" of the attached CD.

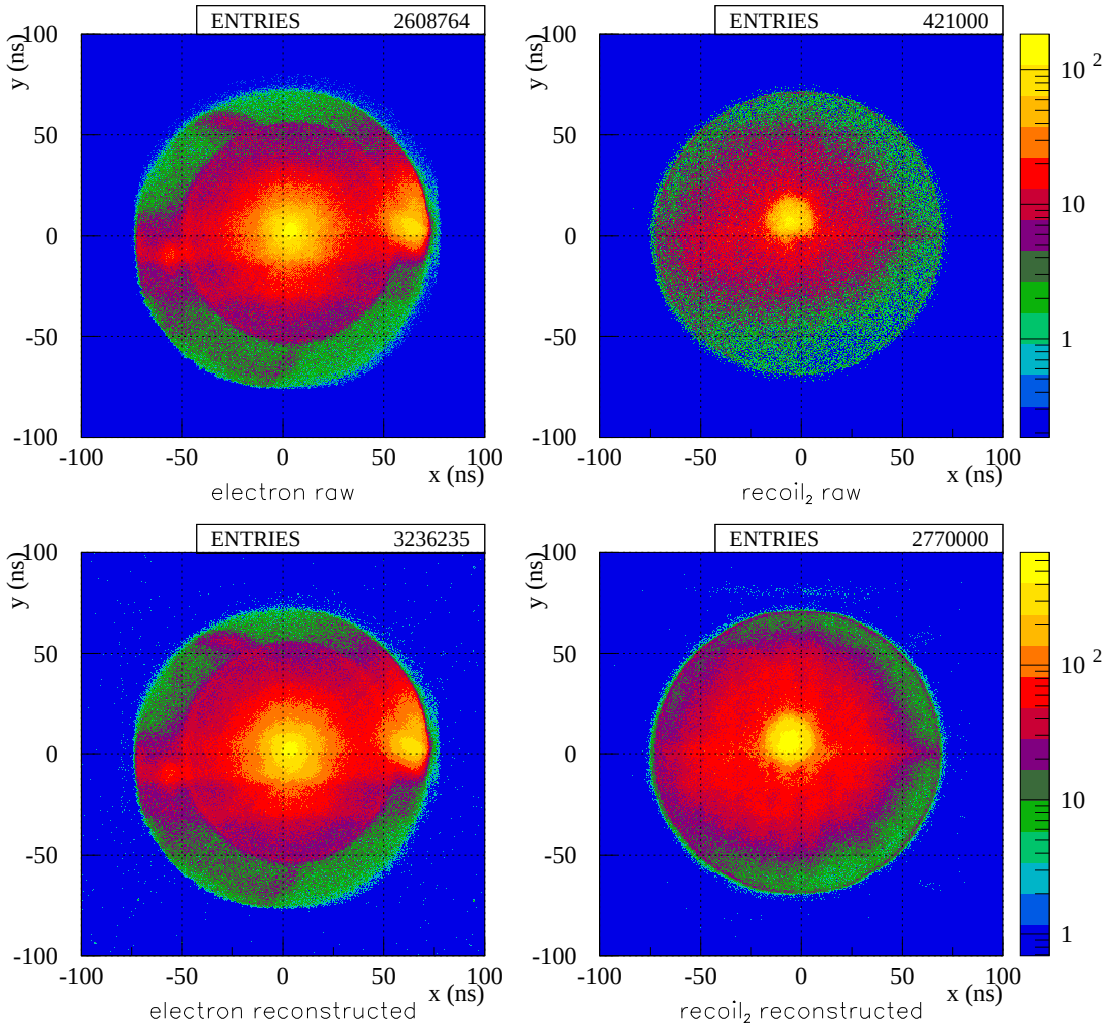

Figure 2.14: **Reconstruction Algorithm Results.** The top two pictures are the electron and recoil detector images without reconstruction. Two valid hits are required on the recoil side, while only one hit is required on the electron side independently. At the bottom are the same images but after reconstruction. Depending on the experimental setup the statistics of the result can be increased up to five times for the multi hit data after reconstruction.

2.3.2 Calibration

One of the advantages of the COLTRIMS data analysis is that it is practically self calibrating. This means that most of the constants, factors and parameters defined by the experimental setup can be extracted from the data itself. The list of parameters that are essential for the momenta calculations includes all the spectrometer distances, absolute time-zero[10], magnetic and electric field strength, and time-to-position conversion factors for each dimension of each position-sensitive detector.

The spectrometer geometry is always precisely measured during its assembly and thus well known before the beginning of the experiment. In the experiment, however, the number of measured parameters is usually higher than the number of unknowns which are needed. Thus even the spectrometer distances can be deduced from the data .

The absolute time-zero and the magnetic field strength are usually calibrated together by the same procedure that uses the unique characteristics of the electron motion in the uniform magnetic field. Figure 2.15 shows the motion of 40eV electrons in a weak electric field (10V/cm) and magnetic field of 15Gs. The initial momentum vector for these electrons is distributed on a circle in the plane defined by the electric field direction and the vertical line through the interaction region. Three different views are shown to make it easier to visualize

[10]For precise time-of-flight measurements one needs the start signal and the stop signal. Omitting the electronics setup details, the start signal is obtained from the bunch-marker signal that is synchronized with the X-ray pulses. "Synchronized" in this case means that it has the same frequency but not necessarily the same position in time as the photo-ionization reaction that takes place inside the chamber. There is usually a constant time shift between the two delays, defined by the specific parameters of the beam-line and the wire length in the electronics. This constant time shift will be referred to as the *absolute time-zero*. In the experiment it can be as long as hundreds of nanoseconds.

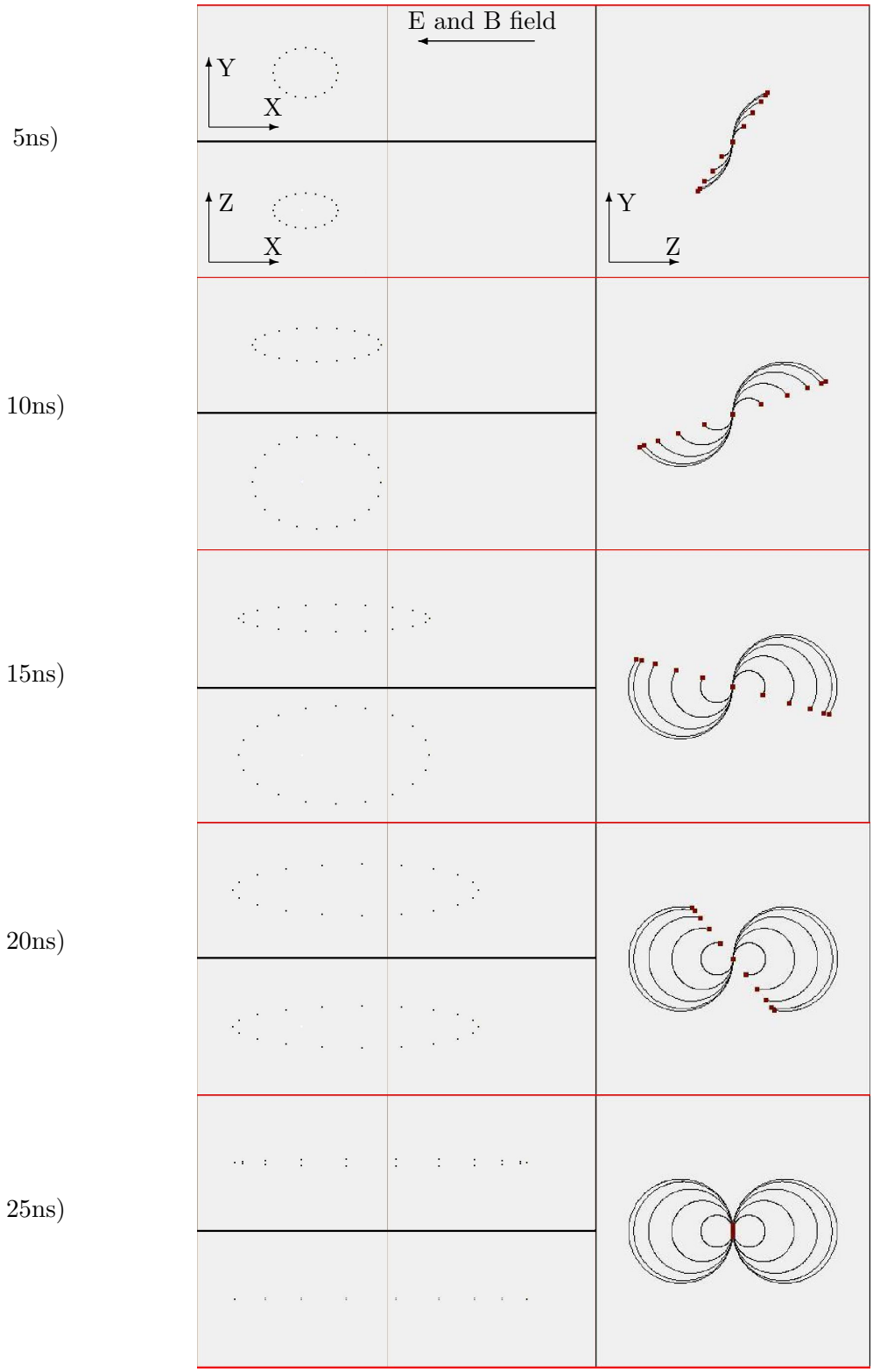

Figure 2.15: Electrons in the Spectrometer EM Field.

the spiral trajectories of these electrons. In a real experiment, of course, one usually deals with one electron at a time, but this picture gives a better idea how the statistics accumulate after a long collection time. From the side-view projections of the spirals, one can see that, independent of the initial momentum, all the electrons come back to the center of the detector at the same time. This also follows from the calculations in Appendix D. If electron momentum were randomly distributed on the whole sphere instead of just on the plane circle used in fig. 2.15, the motion could be illustrated in the following way. Electrons would cover a sphere in space that with time would stretch along the spectrometer field direction, at the same time the sphere[11] would rotate around this axis, and it would contract down to the line at every time mark equal to an integer number of cyclotron periods. This ellipsoid may stretch long enough so that during the time it takes to completely cross the detector plane it contracts several times. That is, all the electrons that happen to have time-of-flight equal to an integer number of cyclotron periods will hit the detector at the same (x_0,y_0) position they started from. Ideally this position is the center of the detector; in reality there are a couple of reasons why it might be a little shifted, and it will be discussed later in this section.

If one plots the distance of the electron hit position from the center of the detector versus its time-of-flight, one obtains a spectrum that is referred to as a "wiggles" spectrum (see top of the fig. 2.16). The wiggles spectrum nodes — points in time when all electrons hit the center — are located exactly one cyclotron period from each other. It is also clear that the absolute time zero position should coincide with one of the nodes. Usually this

[11] It would look more like an ellipsoid of rotation at that point.

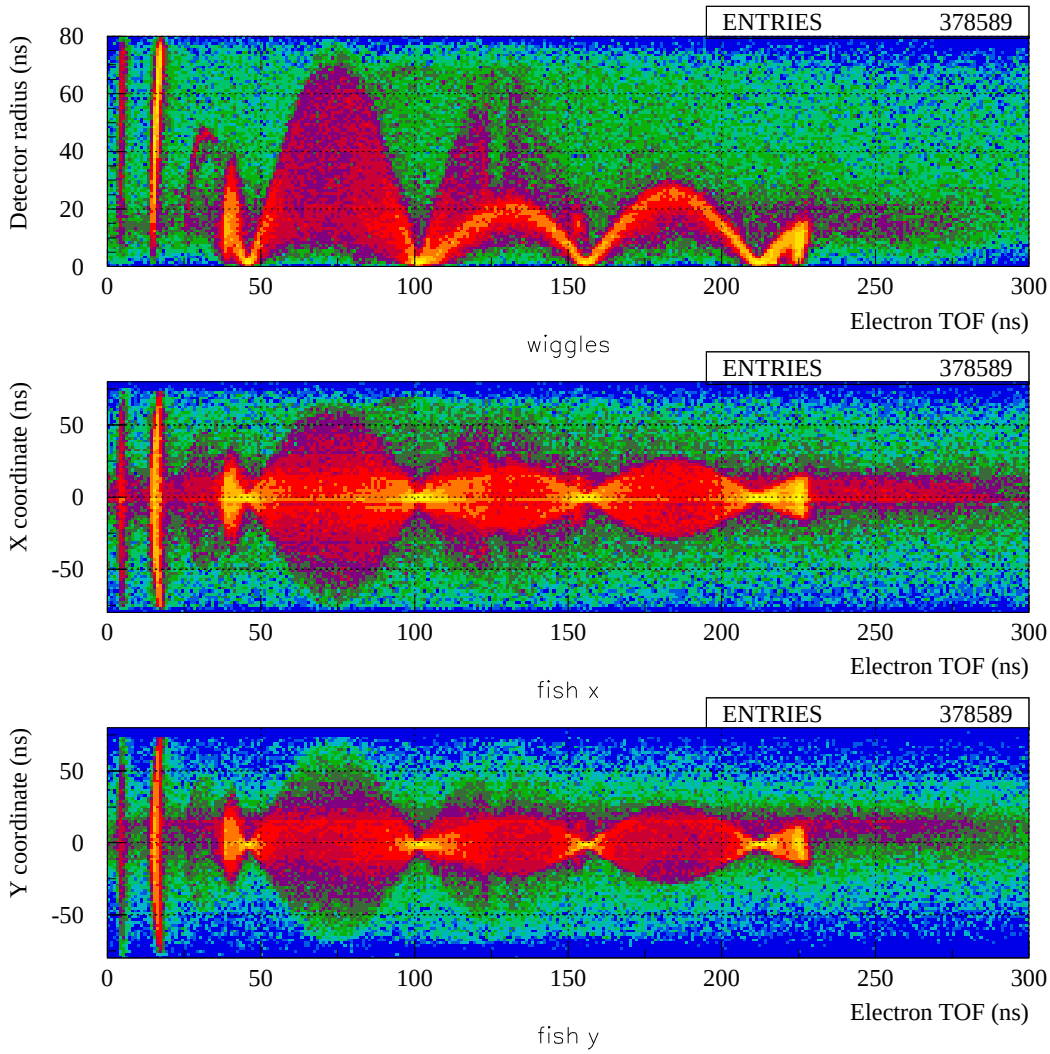

Figure 2.16: Wiggles(top) and Fish Spectra.

position needs to be extrapolated from the positions of other nodes since no electrons have zero time-of-flight and thus that part of the spectrum has no counts in it. To accomplish this extrapolation and define the cyclotron period with appropriate precision it is a good practice to fill the spectrum in such a way that it covers four or more nodes. Since the node position in time does not depend on either the electron momentum or the electric field of the spectrometer, both of these values can be changed in order to shift the electron distribution around and cover the higher number of nodes. This is how the spectra on the figure 2.16 are generated. In the experiment the momentum (or energy) of the photo-electrons is changed by changing the X-ray photon energy.

It is important to remember that calibrating the position of too many nodes might also lead to some erroneous results. The whole electron time of flight distribution should not exceed the time between the two bunch marker signals (328ns). After that it becomes impossible to associate electrons with the proper bunch marker signal. The time-of-flight spectrum in this case starts folding on itself. The first impression is that it is only inappropriate for the main data collection process but is OK for the calibration. This is a wrong idea! In general the time between the bunches is not equal to the integer number of cyclotron periods. The time folding will create a set of false nodes. The position of these nodes will not be in agreement with the integer number of periods rule, and mixed with the good ones it will create a very messy wiggles spectrum. Use of these nodes in the calculations will completely scramble the results.

Once this wiggles calibration process is over, the electric field of the spectrometer as well

as the photon energy are kept constant and the wiggles spectrum looks more like the one on fig. 2.17. This is the case when the photo-electrons created in the reaction are mono-energetic. If the photo-electrons cover the whole range of energies up to some maximum value either because of the specific reaction or because of the scanning of the photon energy, the spectrum on fig. 2.17 would look completely filled everywhere under the bright curve. The bottom part of figure 2.17 shows the same wiggle spectrum but with the analytical curve on top of it (see Appendix E for the derivation of the exact equation of this curve). By fitting the spectrum with this known analytical form one can also extract the absolute time-zero, cyclotron period, electric field strength and the electron energy. Unfortunately this function has the nice analytical form only for the simplest spectrometer with a single acceleration region. As the spectrometer design becomes more complicated this fitting technique becomes unusable.

Figure 2.16 has two more spectra that were also found to be very useful in the calibration procedure. As was mentioned above the position (x_0,y_0), where all the electrons hit the detector if their time-of-flight coincides with the node, is not always (0,0). This usually happens if the spectrometer is not perfectly centered in the chamber, or if the magnetic field is not totally parallel with the electric field. If the (x_0,y_0) values used in the software are a little off from the real position, the nodes in the wiggles spectrum will not reach all the way down to the time axis of the picture and will not look their sharpest. This introduces the additional error in the extrapolation procedure[12]. The so-called "fish" spectra allow for

[12]The accurate values of (x_0,y_0) are also needed for the electron momentum calculations.

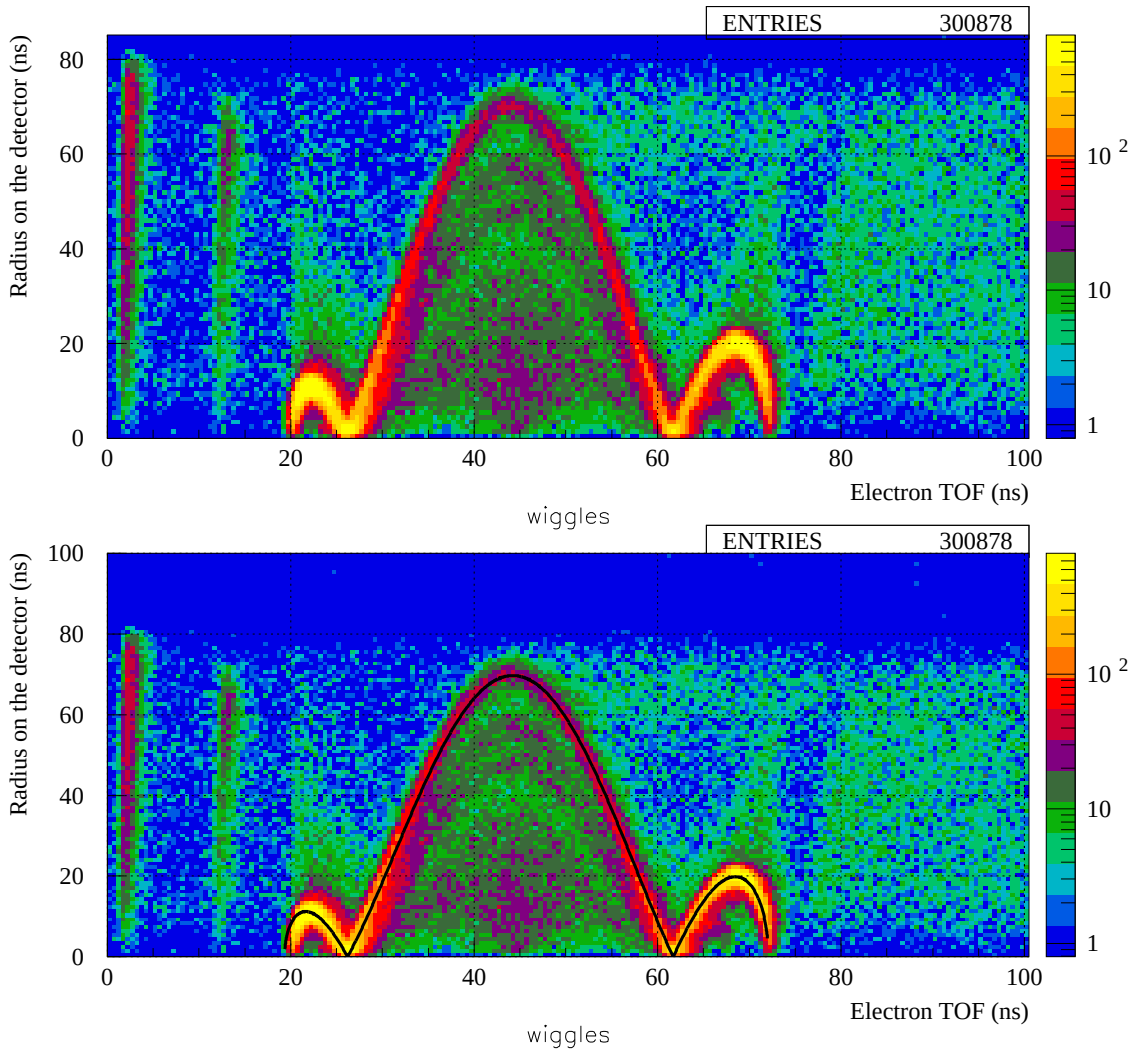

Figure 2.17: Mono-energetic Electrons Wiggles Spectrum and Its Fit (CO molecule, $h\nu$=302eV, E=15V/cm, B=11Gs)

the accurate cyclotron period and absolute time-zero calculation without the use of initial position. However, one can extract the precise values for (x_0,y_0) from the same fish spectra for use in further calculations. The idea behind the fish spectra is that each detector coordinate of the electron hit by itself can be described by the oscillating equation. So if the x position (relative to any common point) of the hit is plotted versus the time-of-flight, the obtained spectrum will also have nodes but now these nodes will not be at the bottom of the picture but on the line $x = x_0$ since that is the only x position which is visited by all electrons at some time. The same can be done with the y direction.

Sometimes, due to the fact that the electric field is not parallel with the magnetic field, the (x_0,y_0) position of one node might be different form the (x_0,y_0) of another node. That is because all electrons have the same drift velocity ($\bar{E} \times \bar{B}$) and due to the different time-of-flight the drifted distance will also be different. One solution to that situation is to have (x_0,y_0) values given not just as constants but as functions of time-of-flight. In this case a word of caution is in order. When collecting data for both wiggles and fish spectra the electric field of the spectrometer should be kept constant and equal to the value at which the main measurement will take place. This means that the only parameter that can be changed is the photon energy. The reason for this is that if the electric field is changed the drift velocity will become different and the time dependence of the (x_0,y_0) position won't stay the same either.

It is a good practice to conduct the main measurement at an electric field high enough so that the whole electron time-of-flight distribution is located completely inside the space

between two nodes. It is intuitively clear and also follows from the derivations in Appendix D that the error in the electron momentum calculation goes to infinity when this electron is in the node.

The question of the direction of the magnetic field should also be properly addressed. Neither of the spectra mentioned above have any information about the direction of the field. Even though the cyclotron period might be calculated very precisely, the wrong sign in the momentum calculation equations will completely destroy all the electron angular distribution information. There are at least two ways to determine the correct direction of the magnetic field besides the first principles approach, which usually still end up being hardly better than 50% accurate. The most traditional way to calibrate the magnetic field direction is to run the single ionization of He. The correct choice of the field will produce a $-45°$ line in the spectra of each electron momentum component plotted versus the proper He^+ momentum component due to momentum conservation. Otherwise the transverse momentum (in the plane of the detector) of the photo-electron will be completely scrambled and the proper plot will look like a shapeless blob. Another way to choose the right direction of the field is to run the experiment covered in this chapter with a target gas like CO or N_2, for which the photo-electron angular distribution is well known and has some sharp features.

Another important parameter that needs to be determined with high precision is the extraction field strength of the spectrometer. While the magnetic field is only important for electrons, the electric field strength comes into the momentum calculations of all ions. Of course, one way to measure the electric field is to keep very good track of the values

of all the resistors in the spectrometer circuit, monitor all the voltages applied, and have precise knowledge of the spectrometer distances. All of this is always carefully taken care of but the calculation of the electric field is still only accurate down to 1V/cm. A more precise measurement of the electric field can be done by fitting the sharp peaks of the recoil time-of-flight spectrum. If the experiment involves the recoil-recoil coincidence, fitting the different stripes in the PIPICO spectrum gives even better results and does not require sharp peaks. Appendix F presents the derivation of the analytical relationship — time-of-flight of the second recoil as a function of the time-of-flight of the first recoil, with recoil masses, charges, flight distance and electric field as parameters. Fitting the unique curvature and the position of each stripe provide very high precision for the values of these parameters[13]. The basic idea behind these equations is momentum conservation between the recoils and the classical linear acceleration motion. On the other hand this function can be used to perfectly identify the features of the PIPICO spectrum (see fig. 2.20 for example) and set the clear gates to separate specific breakup channels.

Finally, the detector position calibration is done by the use of a mask (see fig. 2.18) with well known features. The detector calibration is usually done once per detector not per experiment — the conversion factors are only defined by the size of the detector and the length of the delay-line wire; they do not change from one experiment to another. Since all the measured distances are eventually converted into the momentum or energy of the particle, the detector calibration can be done by using the reversed process. First particles

[13]The parameters that actually get fitted are the flight distance and the electric field. The recoil masses and charges take only integer values.

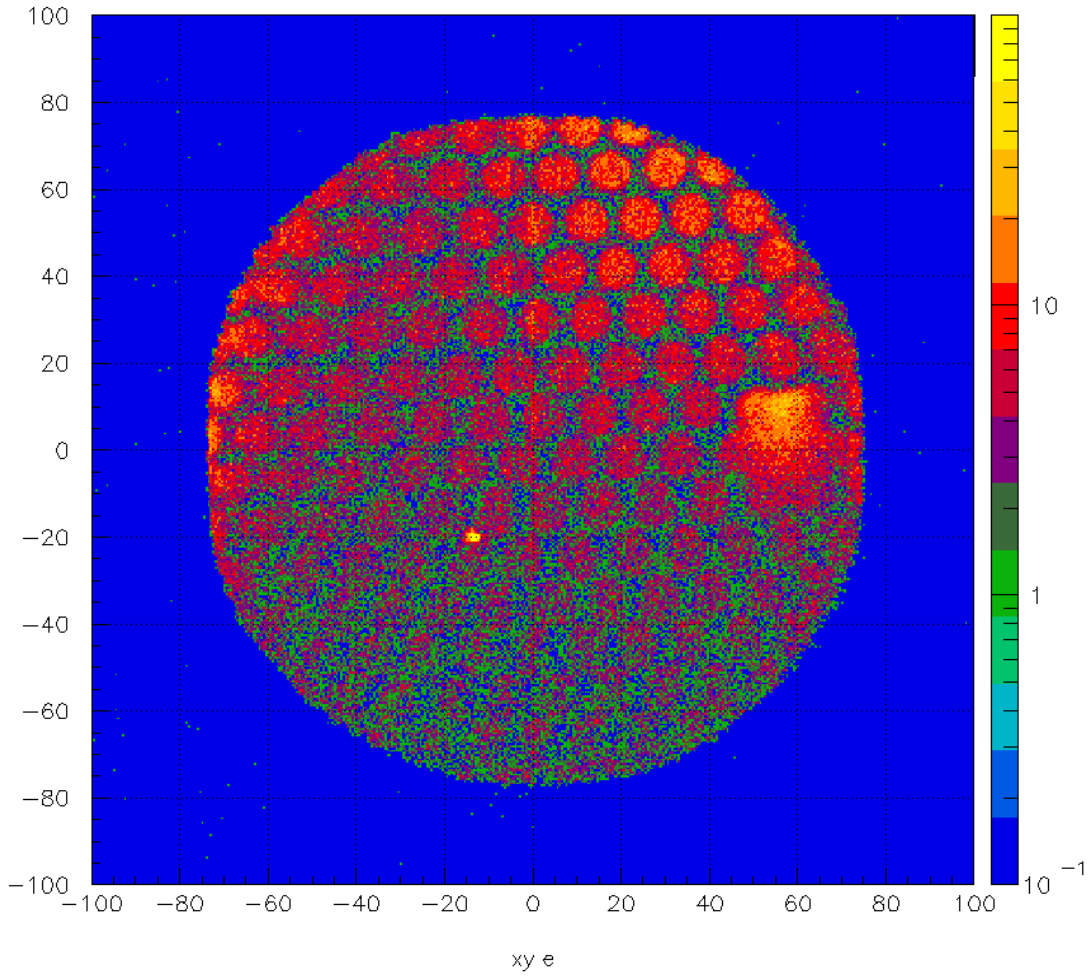

Figure 2.18: Detector Image from the Calibration Mask.

of known energy are registered (photo-electrons at the fixed X-ray energy for example), and then the conversion factors are adjusted so that the calculated energy yields the correct value.

2.3.3 PIPICO Spectrum, Recoil Momentum

Before the actual momentum calculation begins, the breakup channel of interest needs to be isolated. This is done by setting gates on the PhotoIon-PhotoIon-Coincidence (PIPICO) spectrum. Figures 2.19 and 2.20 show PIPICO spectra for an ethylene target with the final breakup channels labeled. The symmetric breakup that yields CH_2^+ and CH_2^+ ions is the only one that provides the information about the molecular orientation and constitutes a kinematically complete experiment. The proper gate is generated by calculating the second recoil time-of-flight (TOF) by using the function from Appendix F with the same masses taken to be 14 a.m.u. and same charges equal to 1 a.u. The calculated TOF value of the second recoil is compared to the measured one, and the event is thrown away if the difference is more than 50 ns. Setting a simple gate that limits the TOF of the first recoil also helps to clear the final momentum picture. When doing so one must check that this gate does not cut the PIPICO spectrum stripes too early, otherwise this will eliminate events with the molecular breakup direction in the plane of the detector. The formulae for the recoil

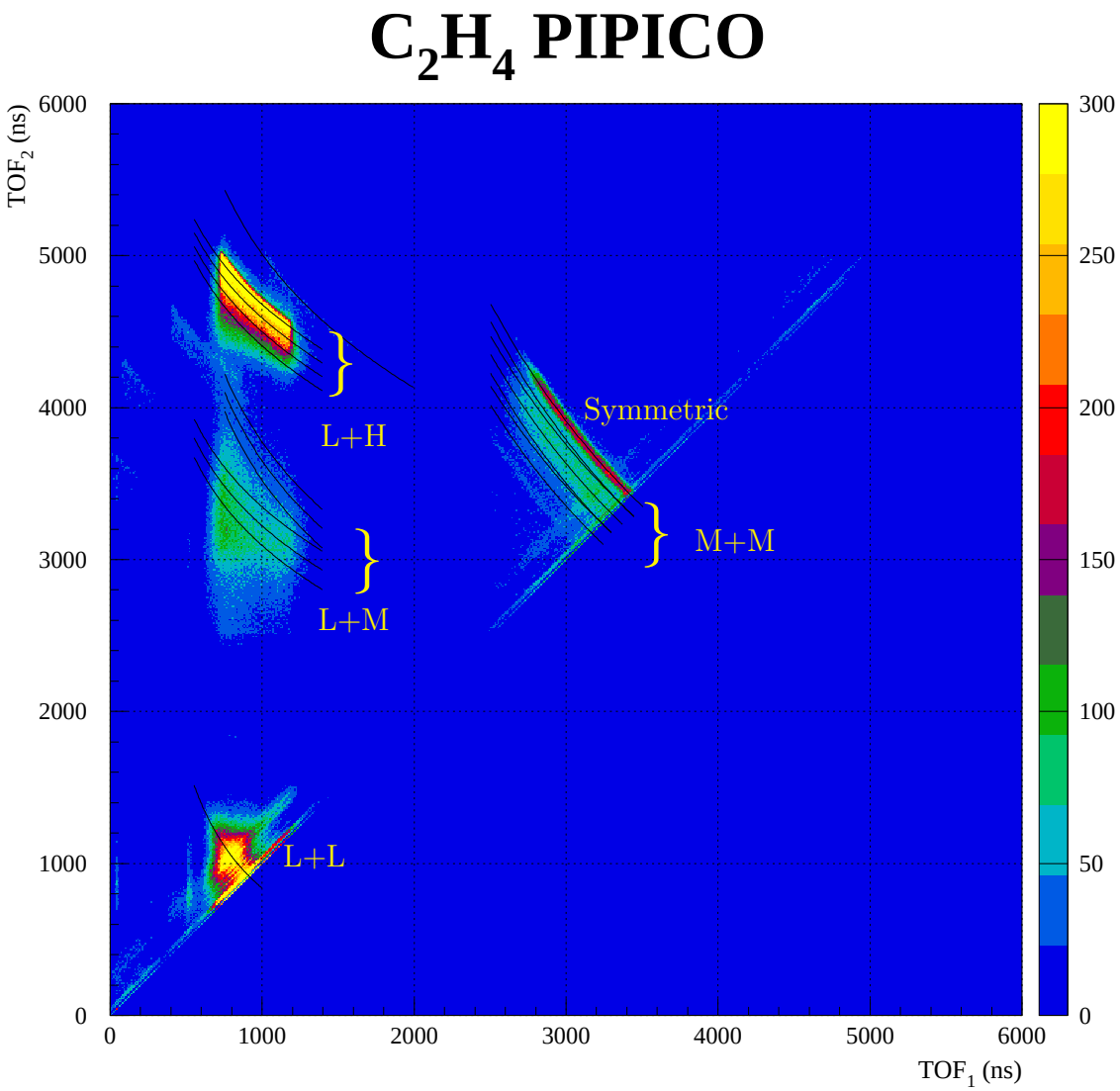

Figure 2.19: Ethylene Breakup Channels Labelling ($h\nu$=302eV).
L - light mass ions; **M** - medium mass ions; **H** - heavy mass ions.

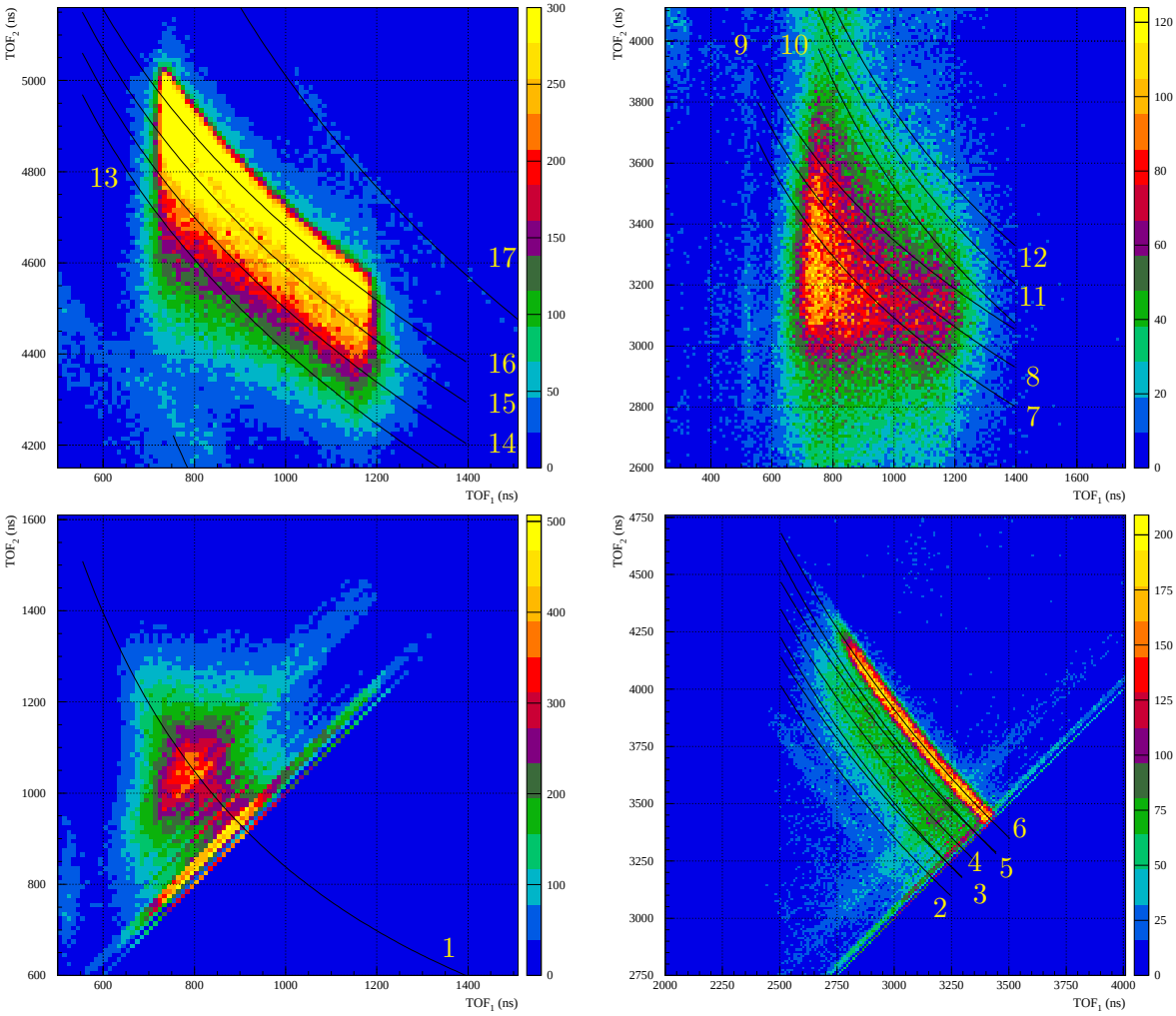

Figure 2.20: Ethylene Breakup Channels Detailed Labelling ($h\nu$=302eV).
1) p+p; **2)** C^++C^+; **3)** CH^++C^+; **4)** CH^++CH^+; **5)** CH_2^++CH^+; **6)** CH_2^++CH_2^+; **7)** p+C^+; **8)** p+CH^+; **9)** p+CH_2^+; **10)** H_2^++C^+; **11)** H_2^++CH^+; **12)** H_2^++CH_2^+; **13)** p+C_2^+; **14)** p+C_2H^+; **15)** p+$C_2H_2^+$; **16)** p+$C_2H_3^+$; **17)** H_2^++$C_2H_2^+$.

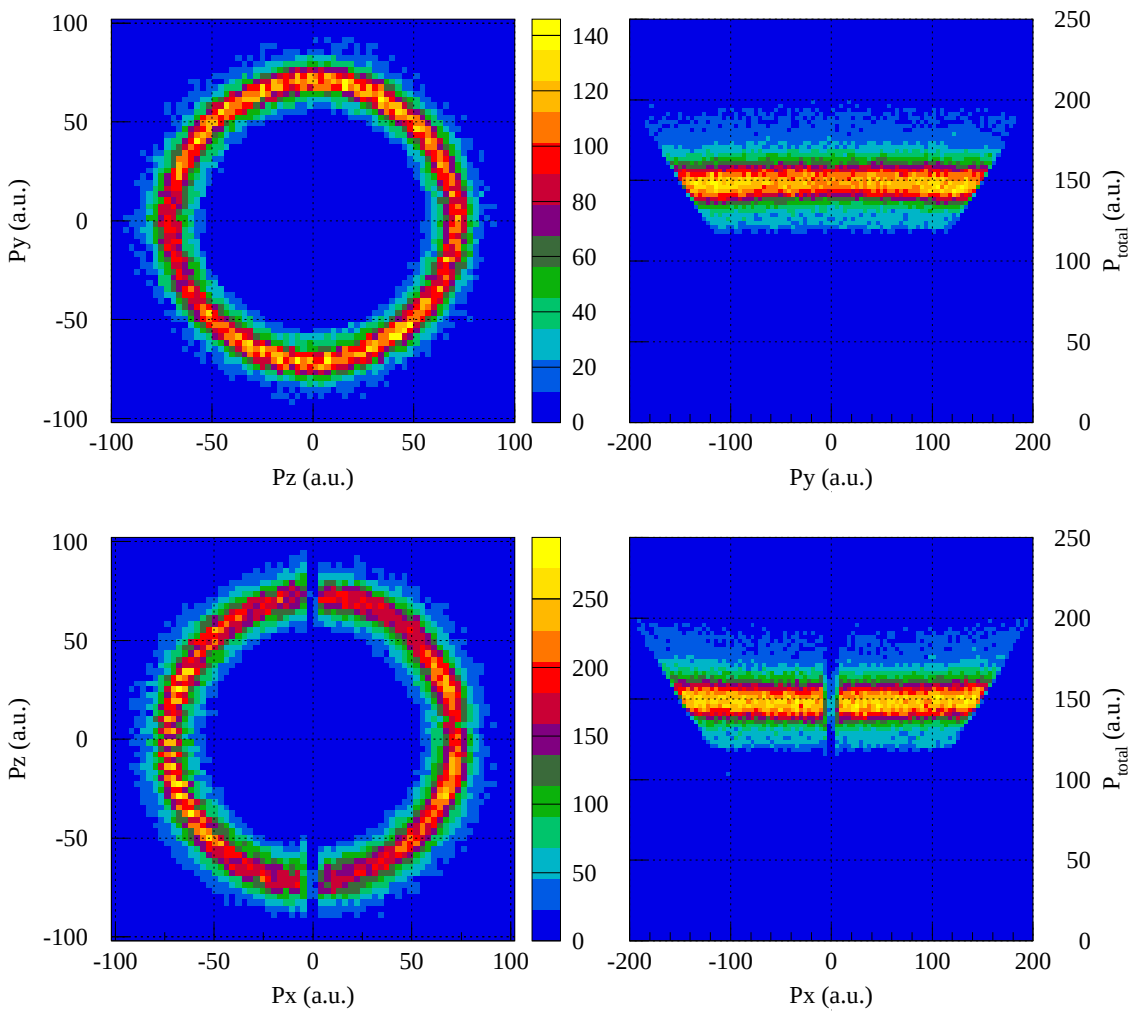

Figure 2.21: Recoil Momentum Component Calibration in Case of Ethylene.

momentum in the laboratory frame are given by[14]:

$$\begin{cases} P_{xi\,\mathrm{lab}} = Sm_i/t_i - Eq_i t_i^2/2 & S \text{ is a recoil flight distance} \\ P_{yi\,\mathrm{lab}} = m_i(\triangle y_i/t_i - V_j) & E \text{ is the spectrometer electric field} \\ P_{zi\,\mathrm{lab}} = m_i \triangle x_i/t_i & V_j \text{ is the jet velocity} \end{cases} \tag{2.2}$$

Here the index i stands for the recoil number. These equations do not make good use of momentum conservation and are not the best for the calculation of the relative recoil momentum. They are however a good starting point for obtaining some rough results and calibrating the relative scaling factors for different dimensions. These are the exact equations that created figure 3.13 and brought the acetylene/vinylidene breakup features to proper attention. The relative component scaling factors can best be found by separately plotting the total momentum versus each single momentum component and making sure that it creates a straight line (see fig. 2.21). Even this simple approach should provide well rounded momentum spheres. When all of these parameters are optimized, a more elaborate equation can be used to calculate the relative momentum with higher accuracy. The calculation of the recoil momentum in the center-of-mass frame involves two parameters for each momentum component. These are S and $V_{cm\,x}$ for the X component, y_0 and $V_{cm\,y}$ for the Y component, and x_0 and $V_{cm\,z}$ for the Z component. The momentum components in the center-of-mass frame are given by

$$\begin{cases} P_{x\,i} = \frac{Sm_i}{t_i} - \frac{Eq_i t_i}{2} - m_i V_{cm\,x} \\ P_{y\,i} = m_i \left(\frac{y_i - y_0}{t_i} - V_{cm\,y} \right) \\ P_{z\,i} = m_i \left(\frac{x_i - x_0}{t_i} - V_{cm\,z} \right) \end{cases} \tag{2.3}$$

[14]The use of the $\triangle x_i$ in the calculation of the Z component of the momentum can be confusing. Traditionally the direction of the x-ray beam is denoted as z direction which coincides with the x coordinate of the detector position.

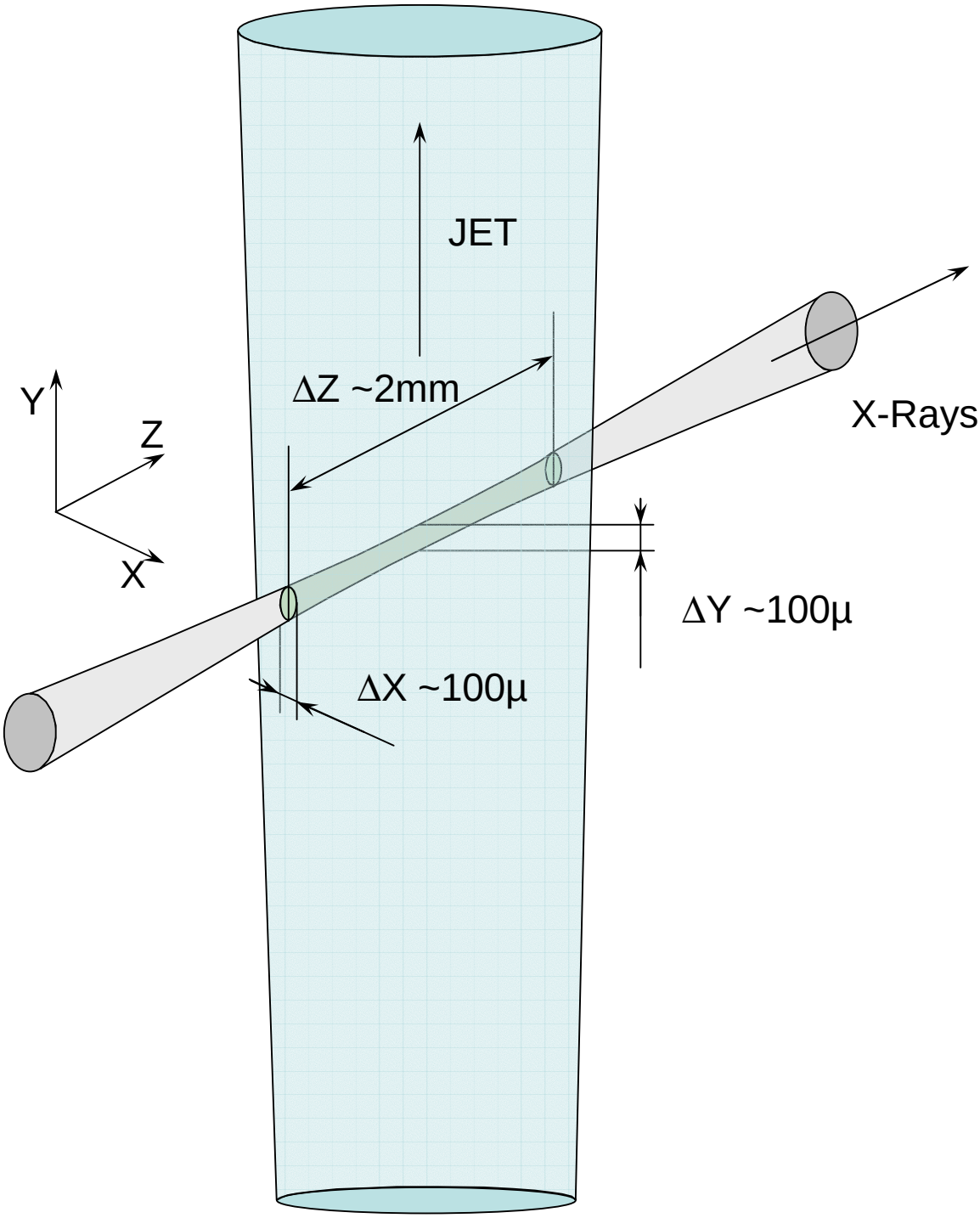

Figure 2.22: Experimental Spatial Resolution Definition.

Both S (x_0 or y_0) and $\bar{V}_{cm}$ can be considered unknown (within the error bar) and, ideally, need to be canceled out of these equations if high precision in the momentum calculation is to be achieved. Center-of-mass system momentum conservation $\bar{P}_2 = -\bar{P}_1$ allows canceling one of the above parameters. In practice one has to decide which parameter introduces the higher error bars for each momentum component and get rid of it. In this experiment the gas jet is very cold in the Z direction (x-ray propagation) and thus it makes sense to assume that the center-of-mass velocity along this axis is zero. On the other hand the initial position resolution is very poor for this direction due to the large target size (see fig. 2.22). Thus, the best result for the Z component of the recoil momentum is obtained by canceling out the initial position (x_0) dependence:

$$P_z = P_{z1} = -P_{z2} = m_1(x_1 - x_0)/t_1 = -m_2(x_2 - x_0)/t_2 \Rightarrow \boldsymbol{P_z = m_1 m_2 \frac{x_1 - x_2}{t_2 m_1 + t_1 m_2}} \quad (2.4)$$

On the other hand, the target size along the Y direction is quite small (see fig. 2.22) but the velocity of the center-of-mass distribution has a wide spread[15]. For this direction the calculation of the center-of-mass momentum involves cancellation of $V_{cm\,y}$ (which for this direction $\approx V_j$ — jet velocity):

$$P_y = P_{y1} = -P_{y2} = m_1(\triangle y_1/t_1 - V_{cm\,y}) = -m_2(\triangle y_2/t_2 - V_{cm\,y}) \Rightarrow$$

$$\boldsymbol{P_y = \frac{m_1 m_2}{m_1 + m_2}\left(\frac{\triangle y_1}{t_1} - \frac{\triangle y_2}{t_2}\right)} \quad (2.5)$$

Here, when using $\triangle y_1 = y_1 - y_0$ and $\triangle y_2 = y_2 - y_0$, it has been assumed that the y_0 position was accurately determined by one of the techniques described in Appendix B.

[15] As discussed in the section 2.2 and Appendix B the temperature of the target gas is about two orders of magnitude higher along the direction of the jet compared to both perpendicular directions.

The $V_{cm\,x}$ can be canceled out of the expression for the P_x in a similar way:

$$P_x = P_{x1} = -P_{x2} = \frac{Sm_1}{t_1} - \frac{Eq_1t_1}{2} - m_1V_{cm\,x} = -\frac{Sm_2}{t_2} + \frac{Eq_2t_2}{2} + m_2V_{cm\,x} \Rightarrow$$

$$\boldsymbol{P_x = \frac{m_1m_2}{m_1+m_2}\left(S\frac{t_2-t_1}{t_1t_2} + \frac{E}{2}\left(\frac{q_2t_2}{m_2} - \frac{q_1t_1}{m_1}\right)\right)} \tag{2.6}$$

The X-momentum-component calculation accuracy is defined mostly by the time-of-flight measurement and can be improved only a little by employing the two acceleration region calculations discussed in Appendix F.

For both, X and Y directions, the appropriate expressions for the V_{cm} can be used to estimate the gas temperature:

$$\begin{cases} V_{cm\,x} = \frac{1}{m_1+m_2}\left(S\left(\frac{m_1}{t_1} + \frac{m_2}{t_2}\right) - \frac{E}{2}\left(q_1t_1 + q_2t_2\right)\right) \\ V_{cm\,y} = \frac{1}{m_1+m_2}\left(\frac{m_1\triangle y_1}{t_1} + \frac{m_2\triangle y_2}{t_2}\right) \end{cases} \tag{2.7}$$

2.3.4 Electron Momentum

The electron momentum calculation would be completely similar to that for the recoils if it were not for the magnetic field. The time of flight component of the momentum can be obtained by means of the top formula from 2.2 or by the formula for the two acceleration region spectrometer (see Appendix F) if the drift or retardation region is used. In the case of a more complicated spectrometer design a simple lookup table can be constructed to avoid the long and tedious analytical derivations. The transverse momentum of each electron is calculated according to equations[16] D.3 or D.4. Figure 2.23 shows the typical electron momenta and the Kinetic Energy Release (KER) spectra. Just as it was done for the recoils

[16]If the magnetic field is not used the calculation of the electron transverse momentum is trivial, it is obtained by means of the two bottom equations of 2.2.

the aspect ratios and the center of the electron momentum sphere are accurately adjusted by means of the spectra shown in figure 2.24. When a symmetric electron momentum sphere is obtained the absolute momentum (energy) scale should be properly calibrated. To do this the spectrum of the electron kinetic energy plotted versus the photon energy can be used. This spectrum is either obtained from the analysis of the energy scanning part of the experiment(fig. 3.18), or by plotting the results of different photon energy points on the same picture. The C 1s main line electrons should show up as a stripe that has an exact 45° angle if both axes have the same units[17]. If this angle is different from 45° the common factor of the proper value should be introduced for all three electron momentum components.

2.3.5 Extraction of Electron Angular Distributions in a Body Fixed Frame

Linear Polarization Case

This section describes the production of the photo-electron angular distribution as a function of two variables — the angle between the electron and the molecule and the angle between the molecule and the polarization direction. In the axial recoil approximation the orientation of the molecule at the time of the Coulomb explosion is defined by the recoil momentum direction. In the lab frame the polarization direction is constant and the measured orientation of the molecule can have any direction with respect to it. The reconstruction of the molecular orientation on an event-by-event basis allows one to select

[17]The absolute scale of the photon energy on beam lines 4.0.2 and 9.3.2 for different gratings can sometimes be accurate only down to ∼1eV. However the $\triangle E_{photon}$ can be controlled with 10meV steps.

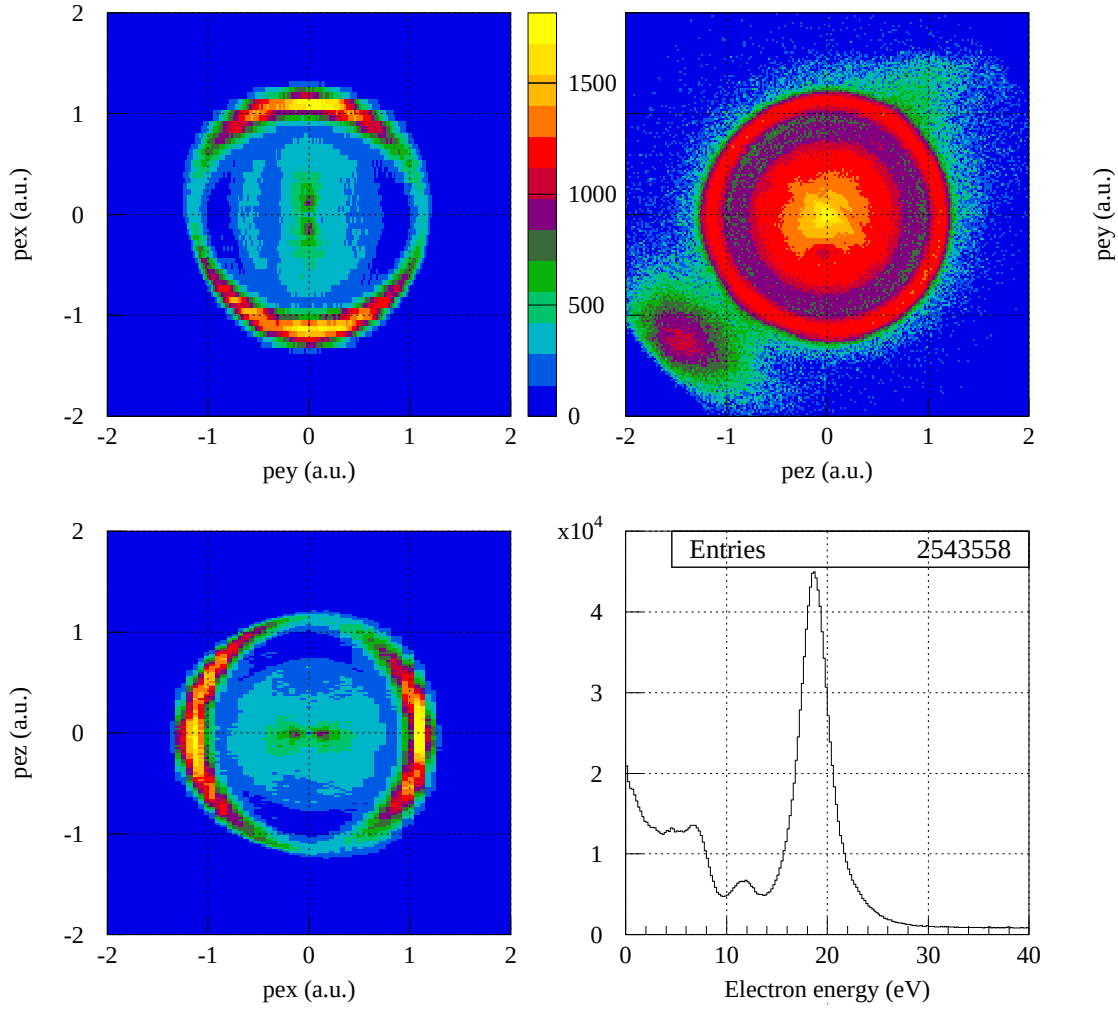

Figure 2.23: Electron Momentum and Kinetic Energy Release from C_2H_4 at 309eV photon energy.

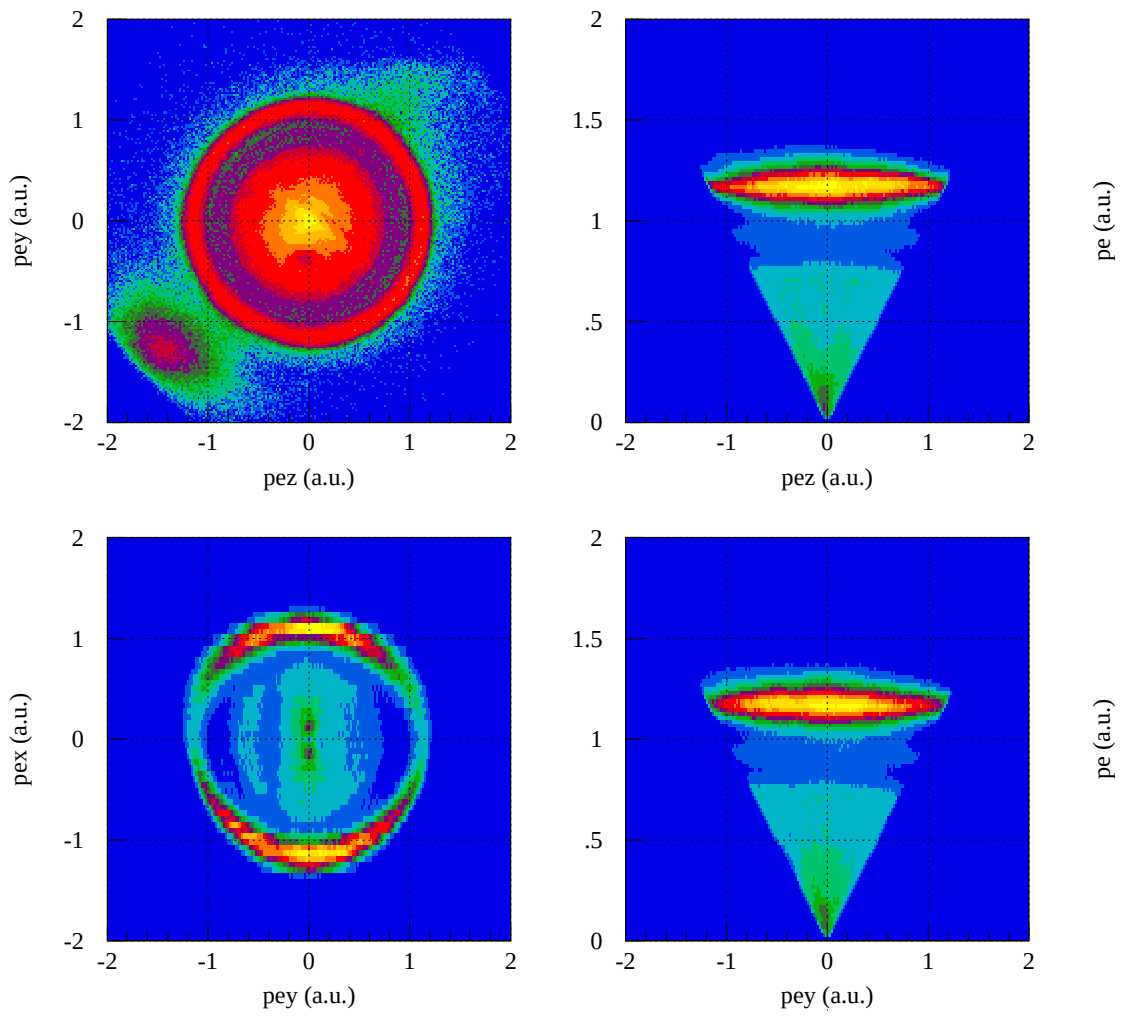

Figure 2.24: Electron Momentum Sphere Calibration.

the coordinate system (in general unique for each event) that is associated with the molecule — the new Z axis is aligned with the C–C (C–O or N–N in case of CO or N_2) bond and the new X axis is chosen so that the polarization vector is in the XZ plane. Now the angular distribution of the photoelectrons with respect to the molecule can be plotted as a function of the polarization direction.

The body-fixed-frame coordinate system in this case are defined as shown in the following schematic where $\bar{P}_e$ is the photo-electron momentum. This means that, in general, the photoelectron angular distribution is a function of θ, ϕ and θ' — $f_l(\theta, \phi, \theta')$. In this thesis these angular distributions are presented in the plane defined by $\phi = 0$; that way the distribution is a function of two variables and can be presented in a form of the "movie" where each frame corresponds to a different value of θ'.

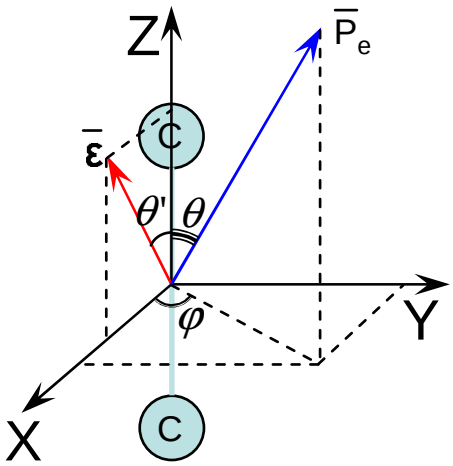

The simplest way to generate these polar plots is to confine both molecules and electrons to have momentum in the XZ laboratory plane (see fig. 2.5). The result of this procedure is shown in figure 2.25. The use of the XZ plane gate can lower tremendously the statistics of the polar plots but it also has a couple of advantages. First, it allows for the investigation of non-dipole effects in the electron angular distributions since in this case the distinction can be made between electrons flying along the positive Z direction or along the light propagation direction and electrons flying against it. The other reason for the use of the XZ plane

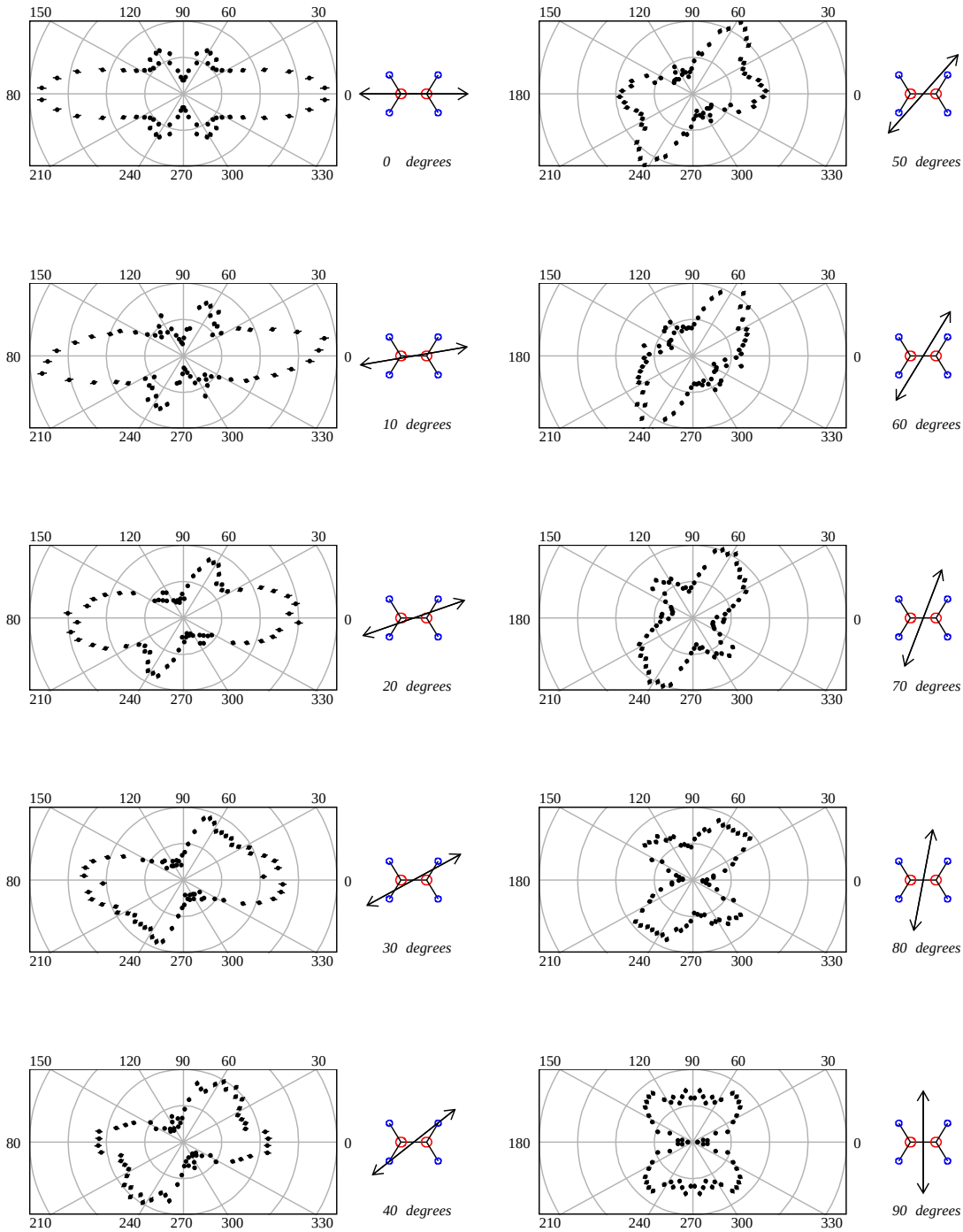

Figure 2.25: Electron Angular Distribution "Movie" at 302eV Photon Energy. Black arrow shows the direction of the polarization.

confinement is to eliminate the effect of ellipticity in the light polarization — beamline 9.3.2 was found to have that problem.

If neither of the above two aspects is of any concern then more sophisticated techniques of data sorting can be used to increase the statistics of the plots. One can similarly use the XY plane for the analysis. Certain data reflections can be used based on the symmetry of the system. Also if it is established that the angular distribution obeys a certain generalized analytical form then a special technique of projecting all different angles of molecules and electrons into one plane (see Appendix H for details) can be very powerful in terms of increasing statistics.

The following diagram illustrates the second point — the use of the symmetry of the system.

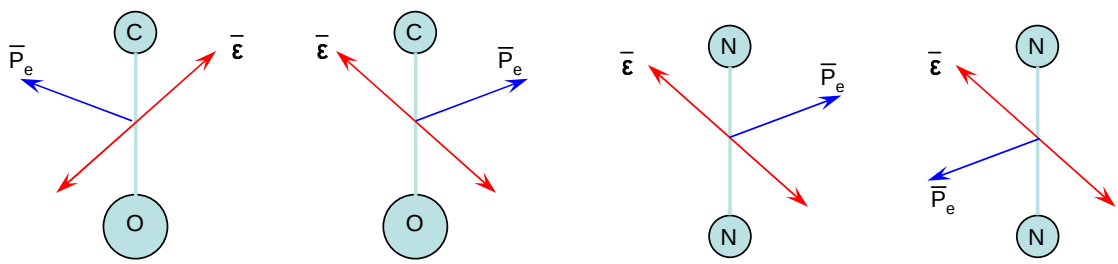

The first two configurations can be considered identical for any linear molecule — this corresponds to the symmetry of the data with respect to the direction of the Y axis of the body-fixed-frame. The other two configurations are also equivalent to the first one if the molecule is homo-nuclear like O_2 and N_2, or linear and symmetric like C_2H_2. In the further analysis of this experiment the molecule of ethylene (C_2H_4) will be assumed to have all the above symmetries as if it were truly a linear molecule. This approximation simplifies

the analysis and is still expected to give reliable results. The resulting polar plots shown in chapter 3 were symmetrized according to the above diagram and the ϕ angle projection (Appendix H) was used to increase the statistics.

Circular Polarization Case .

Data for two photon energies were collected using circularly polarized light. The light polarization in this case is given by the XY plane of the laboratory frame instead of just the X axis as was the case for the linearly polarized light (see fig. 2.5). Such data do carry more information about the molecular structure than the linear polarization case, and it is recommended that similar experiments be conducted with circularly polarized light as well.

The body-fixed-frame for this case is assigned in the following way: the Z axis again is defined by the direction of the C–C bond. The X axis is chosen in such a way that the polarization plane passes through it and thus has an angle θ' with respect to the XZ plane. The Y axis is then assigned to make up the proper right handed coordinate system. The θ and ϕ angles describe the photoelectron momentum direction in this coordinate system.

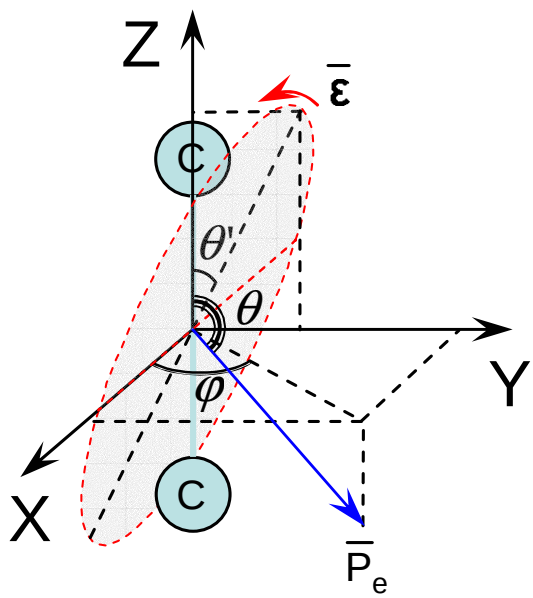

If the ϕ angle is set to 90° then angles θ and θ' will be measured in the same plane,

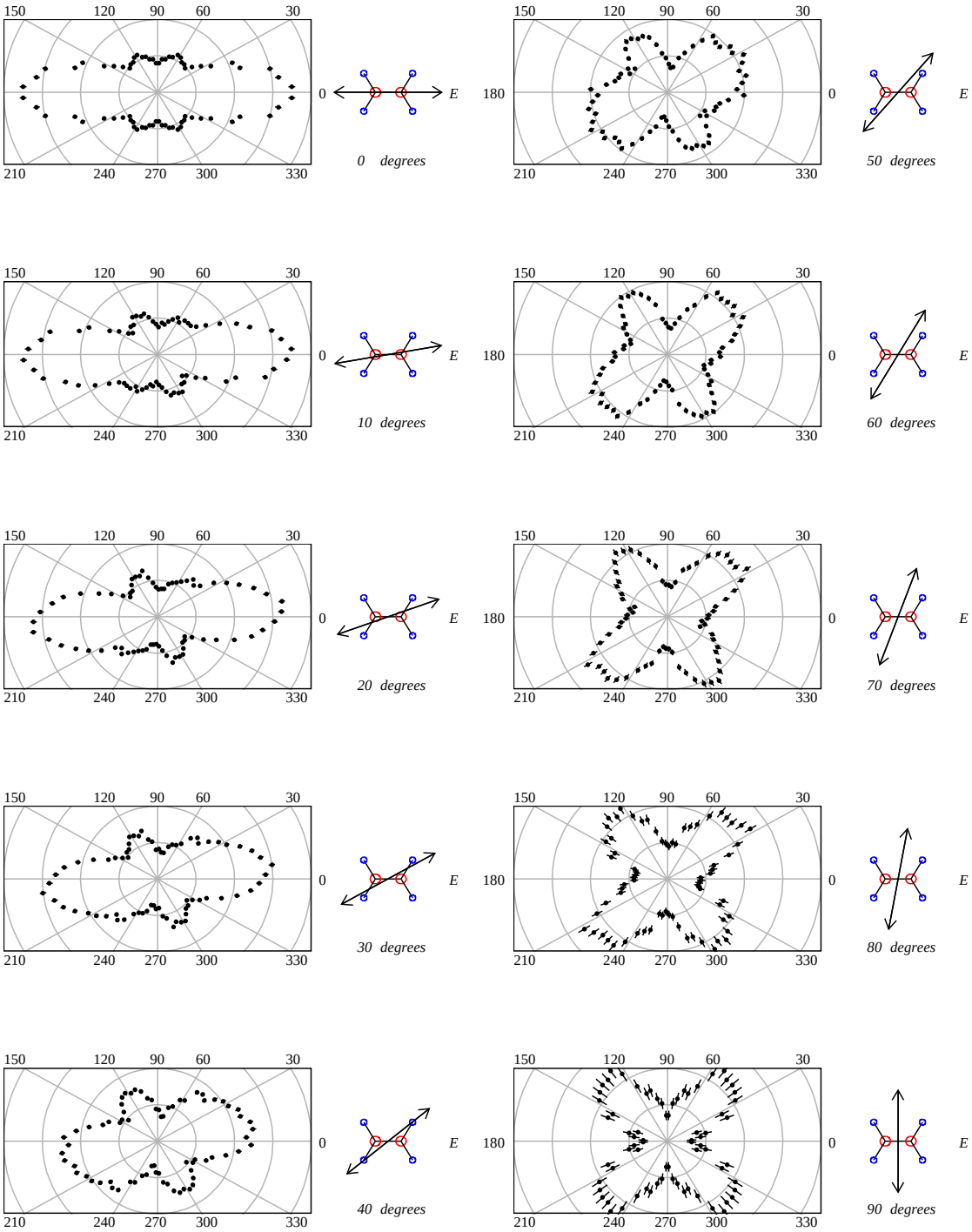

Figure 2.26: Electron Angular Distribution "Movie" from the Circularly Polarized light of 295eV.

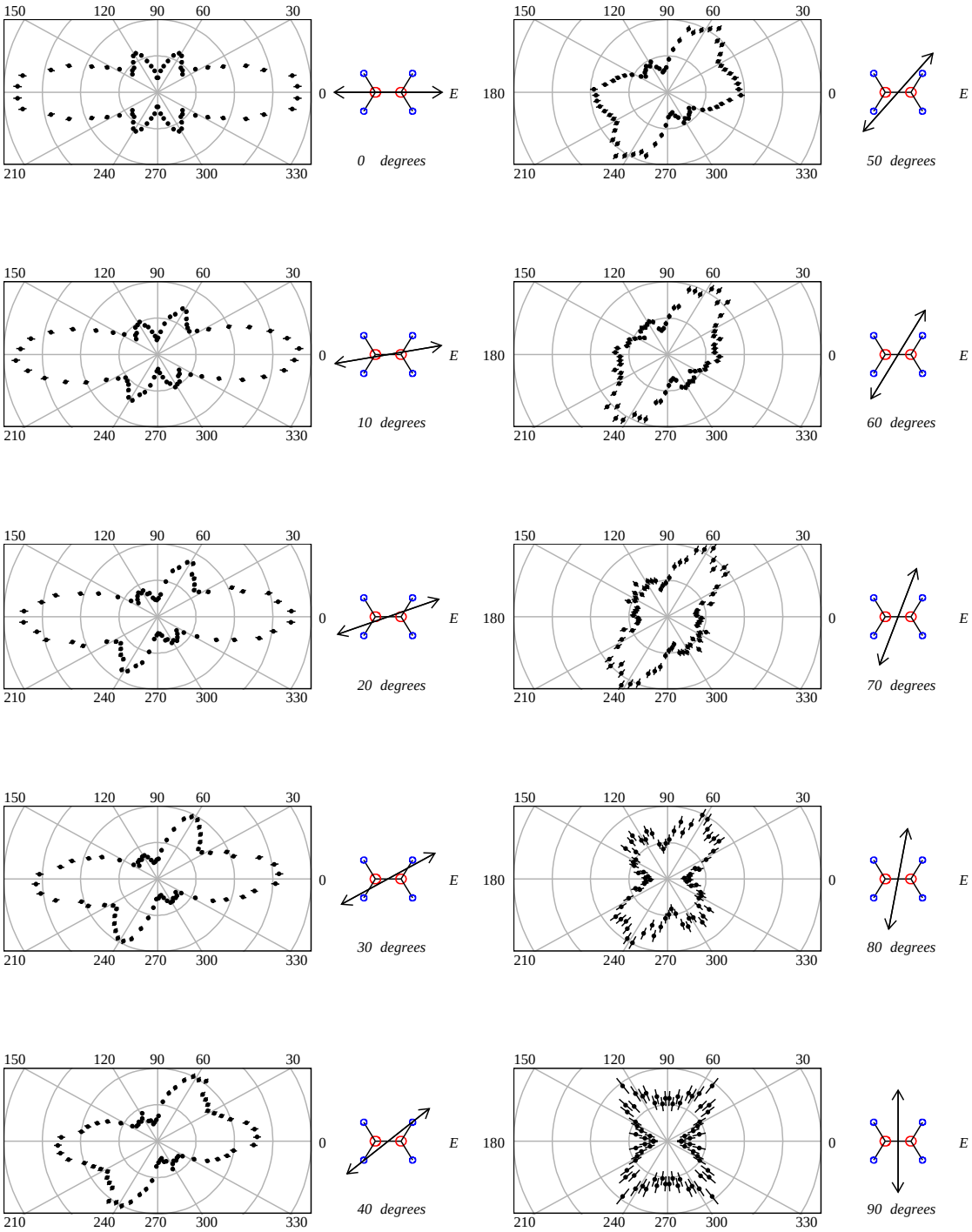

Figure 2.27: Electron Angular Distribution "Movie" from the Circularly Polarized light of 302eV.

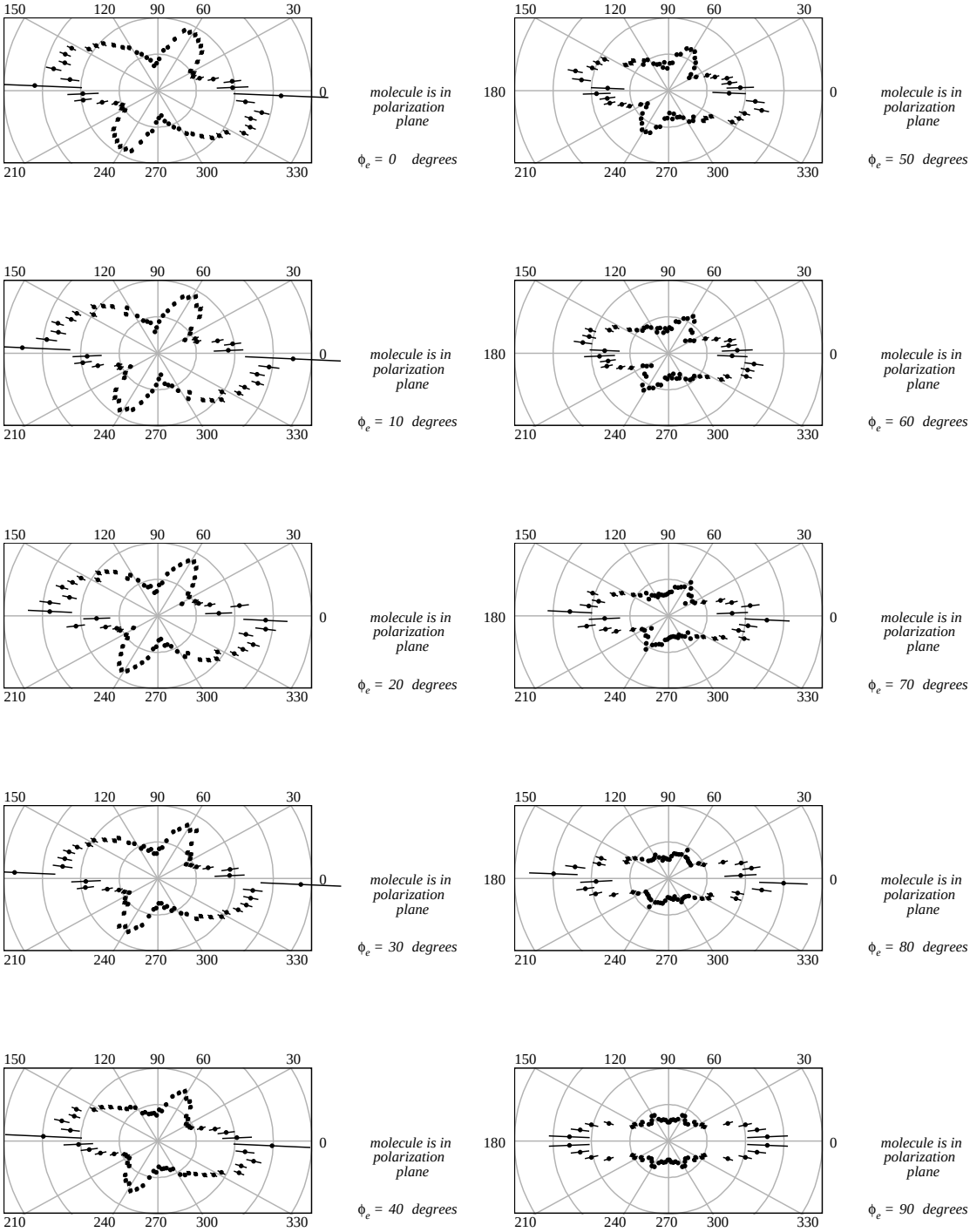

Figure 2.28: Electron Angular Distribution "Movie" from the Circularly Polarized light of 295eV.

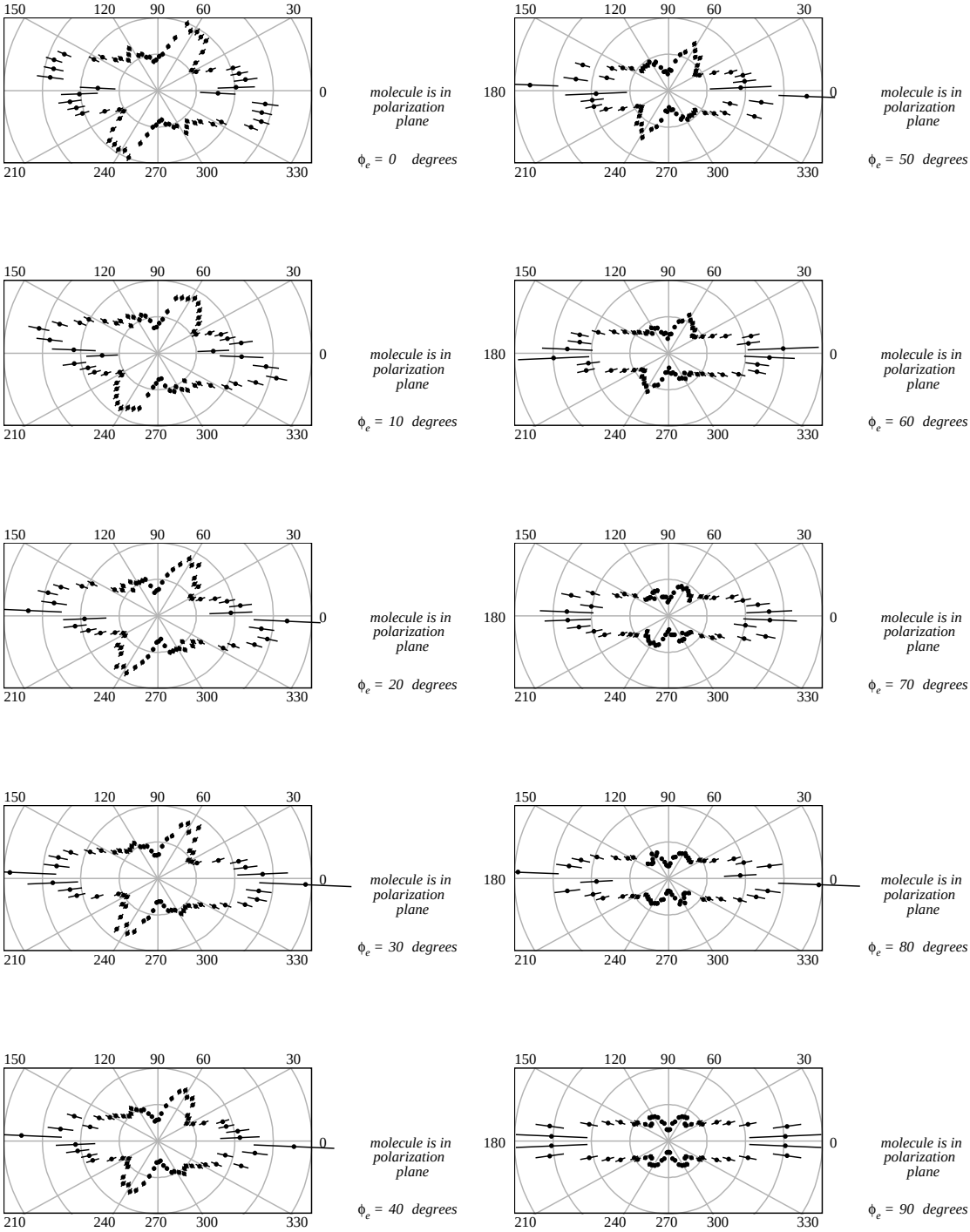

Figure 2.29: Electron Angular Distribution "Movie" from the Circularly Polarized light of 302eV for fixed θ'.

which in turn is always perpendicular to the polarization plane. The photoelectron angular distribution $f_c(\theta, \phi = 90°, \theta')$ created in such a way must be identical to $f_l(\theta, \phi = 0°, \theta')$ obtained for the linear polarization case. In the laboratory frame this corresponds, for example, to confining recoils and electrons to the XZ plane, it should result in the same distribution for both polarizations. In the case of circular polarization however the plane does not have to be just XZ — it can be any plane perpendicular to the plane of the polarization. By summing over those planes with the proper solid angle normalization one can obtain much higher statistics than with linear light for a particular case of the electron angular distribution when the molecule is parallel to the polarization vector. In the case of linear polarization this orientation of the molecule has the smallest solid angle thus producing the angular distribution with the highest error bars. The results for the distributions $f_c(\theta, \phi = 90°, \theta')$ are shown in figures 2.26 and 2.27.

The other aspect of the circular polarization data is that, when the electron azimuthal angle ϕ is allowed to change, the angular distribution provides information independent of other planes. This is not the case for the linear polarization. Figures 2.28 and 2.29 show the angular distribution obtained from the circular polarized light by fixing θ' to be zero and changing ϕ — $f_c(\theta, \phi, \theta' = 0°)$.

Chapter 3

F-wave Shape Resonance Analysis

Molecules of ethane (C_2H_6), ethylene (C_2H_4) and acetylene (C_2H_2) have been attracting the interest of scientific minds for many years. These smallest hydrocarbons are among the most basic blocks of the surrounding organic world and can be considered a "foundation of the field of organic chemistry". A knowledge and understanding of the chemical and atomic reactions involving these molecules, their parameters and features, geometrical structures, chemical activities and physical properties are essential when trying to comprehend, predict and even control the behavior of larger systems such as DNA molecules, for example.

The intent of this work was to address the differential photoionization cross sections of C_2H_6, C_2H_4 and C_2H_2 molecules in the X-ray energy region a few electron-volts above the carbon 1s electron ionization potential. The broad peaking structures in the continuum region of the corresponding X-ray absorption spectra of these molecules have been the focus of many studies in the past. A widely accepted interpretation (see Dehmer *et al.* [6]) is that these resonances originate from the temporary trapping of the photo-electron by a centrifugal barrier of the molecular potential in a quasibound state. The contribution of the particular

partial wave with the $l = 3$ in the final state of this electron becomes especially strong hence the name — f-wave resonance, although in fact the resonance is not limited to this particular wave alone. The presence of these so called σ^* shape resonances has been successfully shown for many diatomic molecules such as N_2, O_2 and CO. The study of this phenomenon in hydrocarbons was believed to provide additional information about the shape and position of these resonances as a function of the C-C bond length. Figure 3.1 shows calculated cross sections from the work presented by Haack *et al.* in [7]. *ab initio* calculations, reported in that work, seem to agree well with angular dependent experimental results of X-ray absorption of chemisorbed and physisorbed (on the Cu(100) surface) hydrocarbons performed by the same group [7].

There have been other studies of the hydrocarbons, however, that questioned the existence of the described-above shape resonances in the photoionization of C_2H_6, C_2H_4 and C_2H_2 molecules (See Kempgens *et al.* [8] for example). The photoelectron angular and energy resolution of these experiments allowed for the separation of the satellite electrons from the total cross section which in turn led to spectra for the main line with no apparent peak structure in them.

In this experiment the analysis was taken one step further . The use of the COLTRIMS technique provided the necessary means for obtaining photoelectron angular distributions in the molecular frame and thus extracting information about the particular contribution of the spherical harmonic with $l = 3$ as a function of the photon energy.

Before the analysis and the results of the current work are presented, certain background

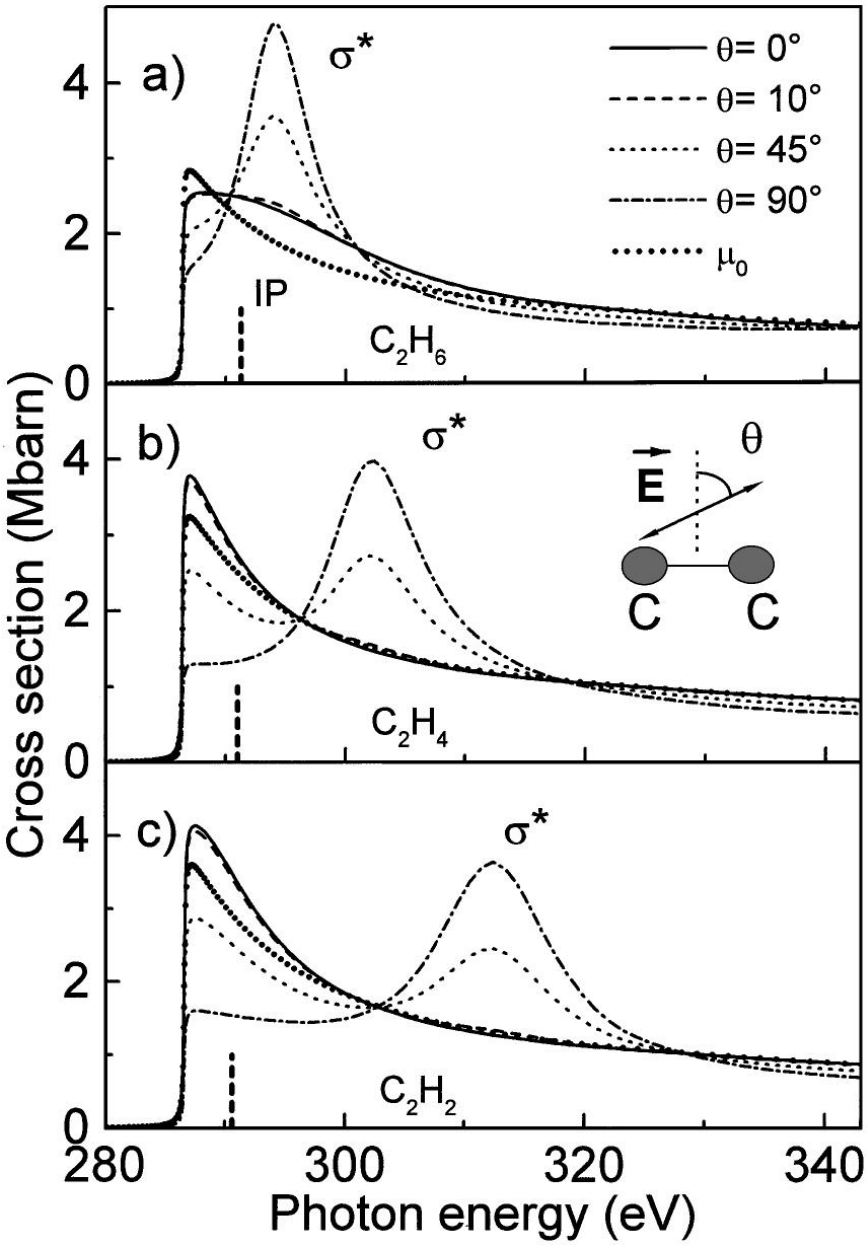

Figure 3.1: (Adapted from [7].) Calculated C 1s NEXAFS spectra of C_2H_6 (a), C_2H_4 (b), and C_2H_2 (c) for different orientations of the **E** vector of the photon beam with respect to the intramolecular C-C bond. $\theta = 0°$ corresponds to a perpendicular orientation, u $\theta = 90°$ to a parallel one [see inset of (b)]. Additionally to the angular dependence, the energy position of the σ^* shape resonance is changing depending on the C-C bond length of the hydrocarbon molecule. The atomic background $\mu_0(E)$ is indicated by the bold-dotted line. The vertical dashed lines represent the calculated ionization potential (IP).

about the experiment involving similar techniques would be in order.

3.1 Previous studies, Experiment and Theory

Photoionization is the simplest process which allows a detailed analysis of the molecular potentials. The theoretical details of the core electron photoionization are described to a great extent by Dehmer and Dill in [6; 9] in the simplest case of homonuclear and heteronuclear diatomic molecules. The K-shell photoabsorption spectra (for the photon energies about 10eV above the corresponding ionization potential) exhibit broad σ^* shape resonances, and therefore differ strongly from monotonically decreasing atomic K-shell spectra. Dehmer and Dill in [9] show that although the molecular K-shells remain essentially atomic-like, the p-wave photoelectrons are scattered by the anisotropic molecular field into states with other angular momenta, in particular, with $l = 3$. Their calculations for the N_2 molecule demonstrated that the spatial extent of the molecular field of the two atoms enables the $l = 3$ component of the σ continuum wave function to penetrate the centrifugal barrier into the molecular core region. This rapid penetration leads to the appearance of a broad σ^* shape resonance in the cross section. The calculations of [9] give only a qualitative description of the f-wave resonance. Unfortunately, experimental studies on photoionization of gas phase molecules were, until recently, limited to measurements of total, partial and differential photoionization cross sections ([8; 10–12] for example). Measured values correspond to averaging over all possible orientations of the molecular axis in space. The amount of

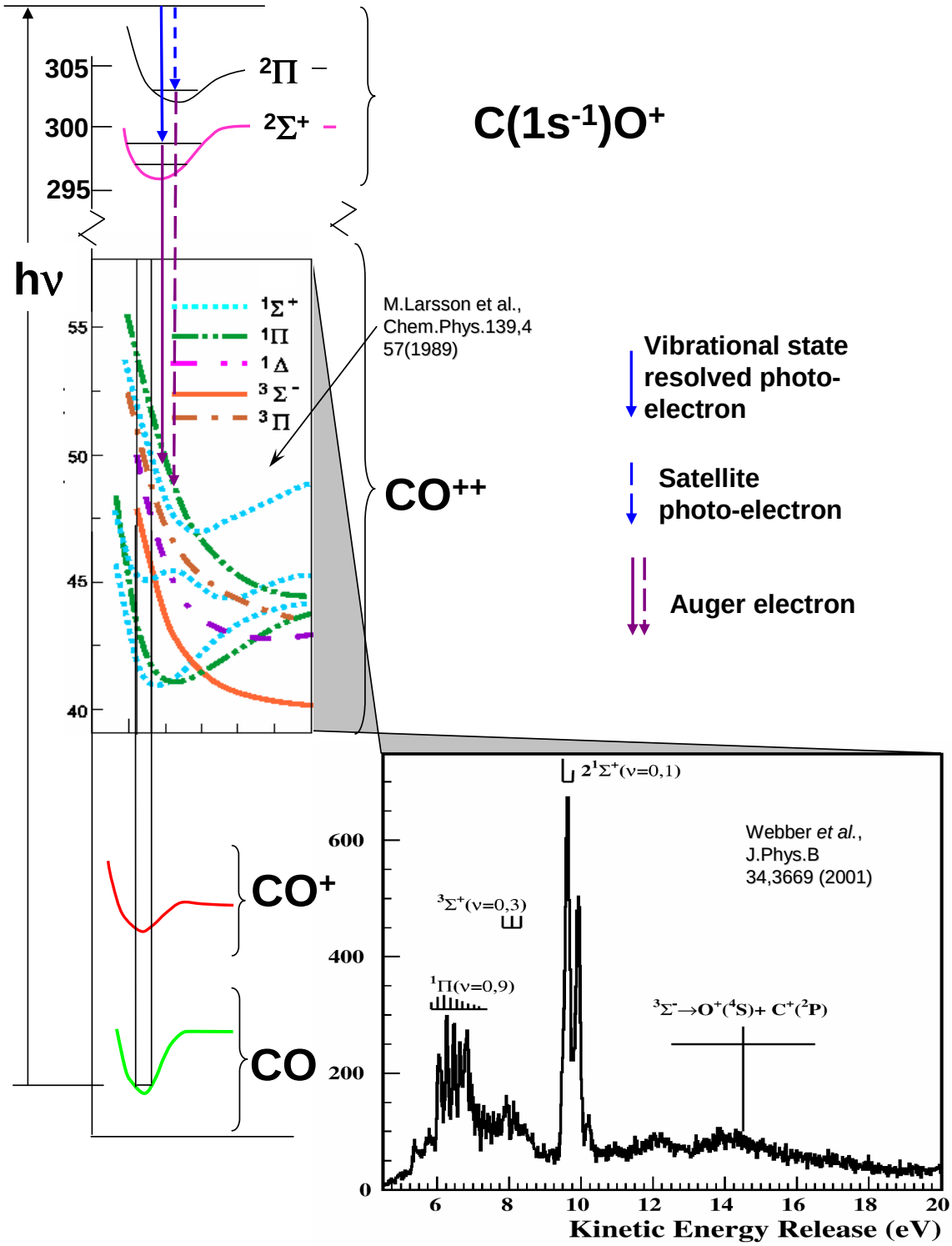

Figure 3.2: CO K-shell photo-ionization (306.4eV photon) potential diagram and the corresponding kinetic energy release spectrum.

information extracted from these measurements was too small compared with the information used in theoretical calculations of the photoionization process. Only very recently has it become possible to determine the molecular orientation (by detecting photoelectrons in coincidence with a fragment ion produced in dissociative photoionization) when investigating the photoionization process with gas phase molecules and to obtain the most detailed angular distributions of photoelectrons (ADP) with respect to the fixed direction of the molecular axis. The angle-resolved photoelectron-photoion coincidence technique (AR-PEPICO) employed in [13; 14] uses several rotatable detectors to obtain the ADP for different angles of molecular break up direction. The other approach is the COLTRIMS multi-hit detection setup used in [3; 4] and in this work. It allows the performance of the kinematically complete experiment by measuring the 4π solid angle for both — photoelectrons and all molecular ion recoils — in coincidence.

The reaction steps involved in the investigation of the K-shell photoionization by both of the above techniques are shown schematically in figure 3.2 for the case of CO molecule. The high resolution Kinetic Energy Release (KER) is labeled according to the corresponding potential curves of the molecular dissociation. The N_2 molecule is an example of a homonuclear system that has been studied ([3; 14]) by the same techniques (see fig. 3.3 for the energetics picture).

Along with the experimental results [13; 15] also offer the step-by-step theoretical considerations of the K-shell photoionization analysis. Routinely, the calculation of the partial cross sections is the first step of this theoretical analysis (fig. 3.4). The following in depth

study of the CO ADP's in a body-fixed frame allowed for the comparison of extracted transition dipole elements both from theory and experiment — see fig. 3.5. Results of the similar analysis performed by Motoki *et al.* in [14] for the $2\sigma_g \rightarrow \sigma_u$ shape resonance of N_2 are shown in fig. 3.6.

Having a lot more different aspects of the experimental data at their disposal, Weber *et al.* in [3] go even further in the analysis process trying to find a link between the photoelectron angular distribution features and the molecular decay dynamics. This analysis reveals some long-lived states in the dissociation channels of CO, which cause the washing out of the corresponding ADP's (fig. 3.7), while the N_2 molecular ion seems to dissociate promptly, independent of the final kinetic energy release (see fig. 3.8).

3.2 Hydrocarbons

One of the intriguing aspects about the f-wave resonances was their dependence on the C–C bond length discussed by Haack *et al.* in [7]. The sequence of gases C_2H_2, C_2H_4, and C_2H_6 would be the perfect system in which to study this effect. However the first priority of this work was to answer an even more general question convincingly — the question of whether or not the σ^* shape resonance in the hydrocarbon is present in the first place. Acetylene was considered the first choice for this test. This decision was also influenced by the results obtained by Haack (see fig. 3.1) — the structure of the calculated σ^* shape resonance seemed to have the best shape and position in terms of the experimental detection process. Initially the molecule of acetylene (C_2H_2) was considered to be the simplest since

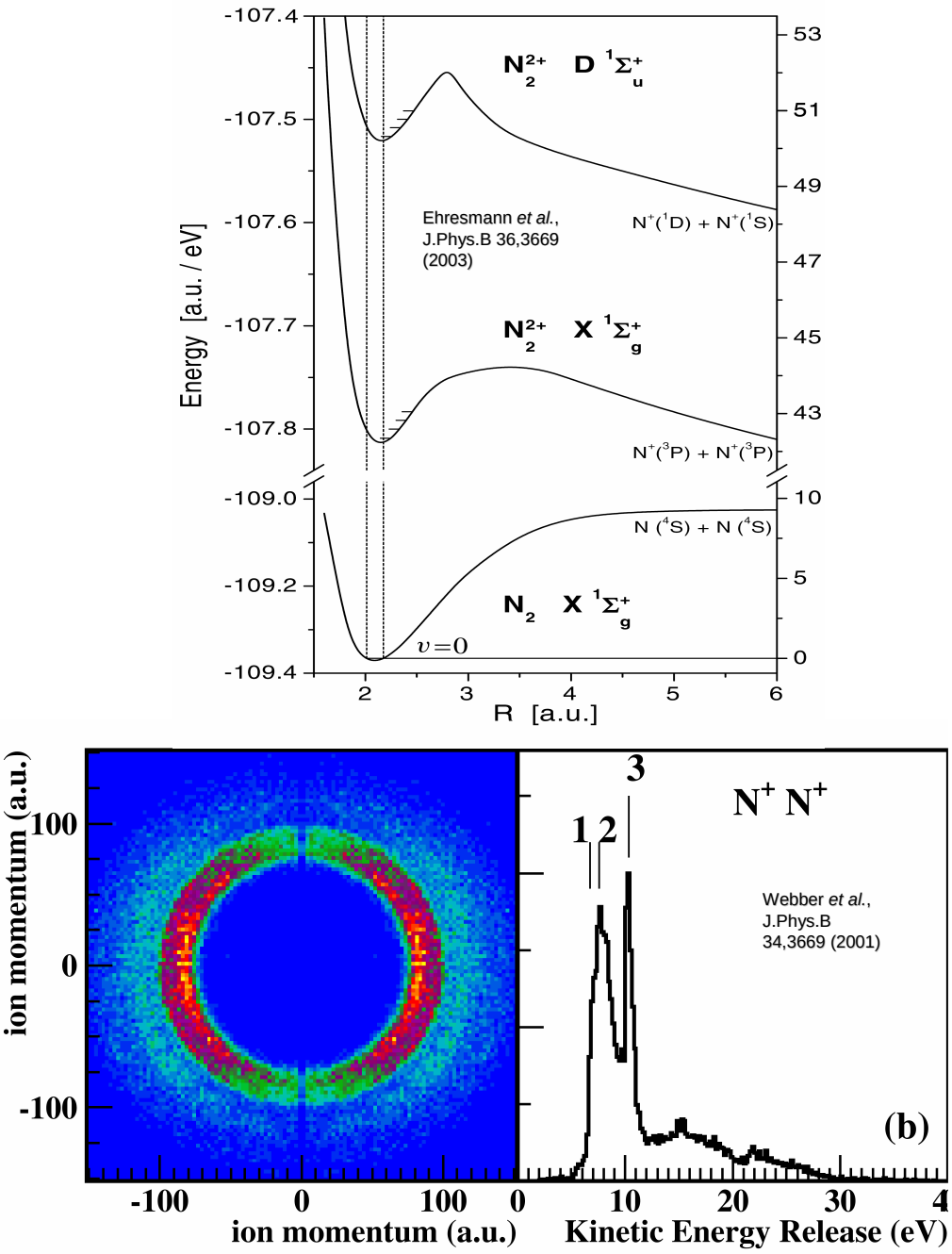

Figure 3.3: Top — adiabatic potential energy curves for the X $^1\Sigma_g^+$ ground state of the N_2 molecule and the X $^1\Sigma_g^+$ and D $^1\Sigma_u^+$ states of the N_2^{2+} ion (adapted from [16]);
Bottom — fragmentation of N2 after K-shell photoionization by 419.3 eV photons. (a) Momentum distribution of the N^+ ions from the N^++N^+ decay channel. The polarization is horizontal, the data are integrated over an angle of 25° out of the plane of the figure. (b) Kinetic energy release (i.e. sum of both fragment energies) for the N^++N^+ decay channel. Line 1: $A^1\Pi_u \rightarrow N^+(^3P)+N^+(^3P)$, line 2: $D^3\Pi_g \rightarrow N^+(^3P)+N^+(^3P)$, line 3: $D^1\Sigma_u^+ \rightarrow N^+(^3P)+N^+(^1D)$ (adapted from [3]).

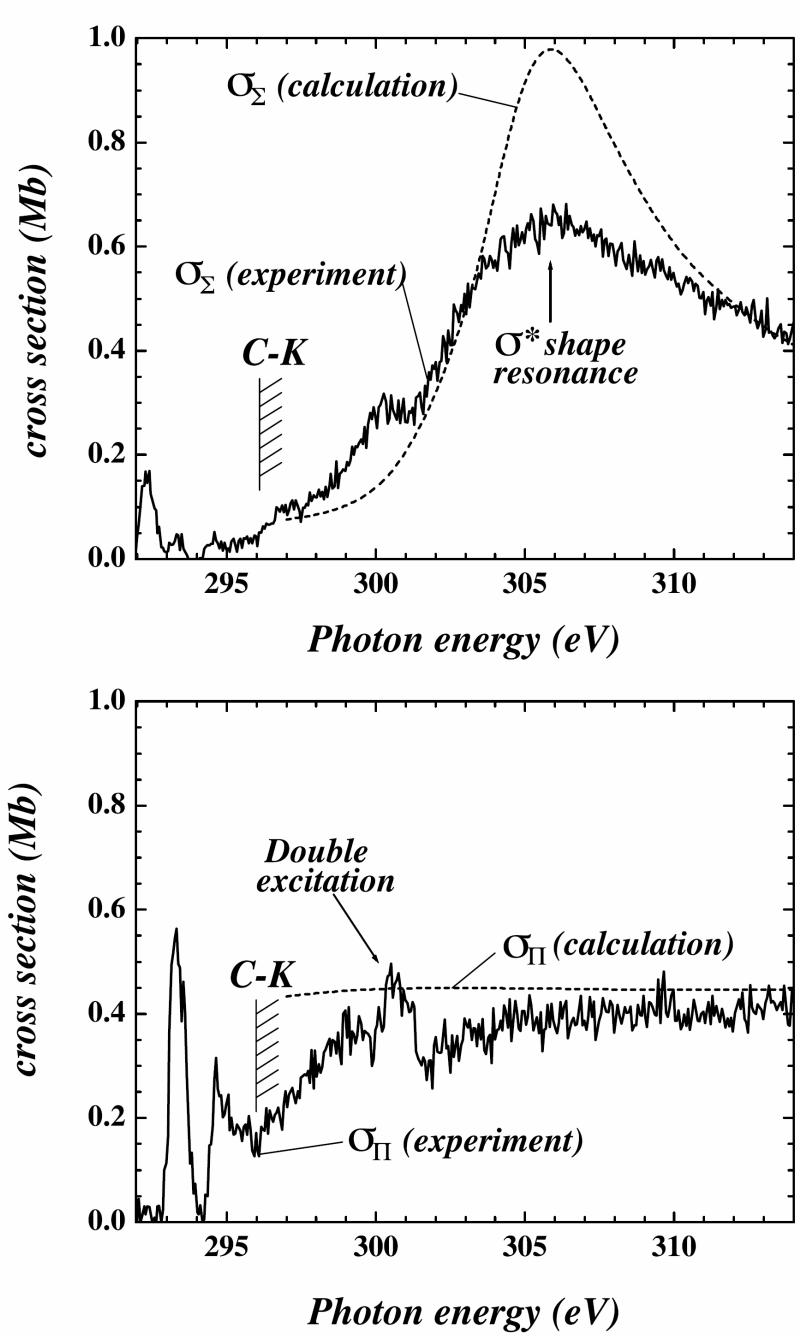

Figure 3.4: Comparison of the experimental partial cross Sections for (a) the C $1s\sigma \rightarrow \sigma$ and (b) $1s\sigma \rightarrow \pi$ cross sections measured by Shigemase *et al.* Phys.Rev.A 47, 1824(1993) with the theoretical results of Cherepkov *et al.* J.Phys.B 33,4213(2000) obtained in the RCHF approximation. The experimental cross section for the $1s\sigma \rightarrow \pi$ transition has been normalized to the theoretical one at a photon energy of 314 eV.

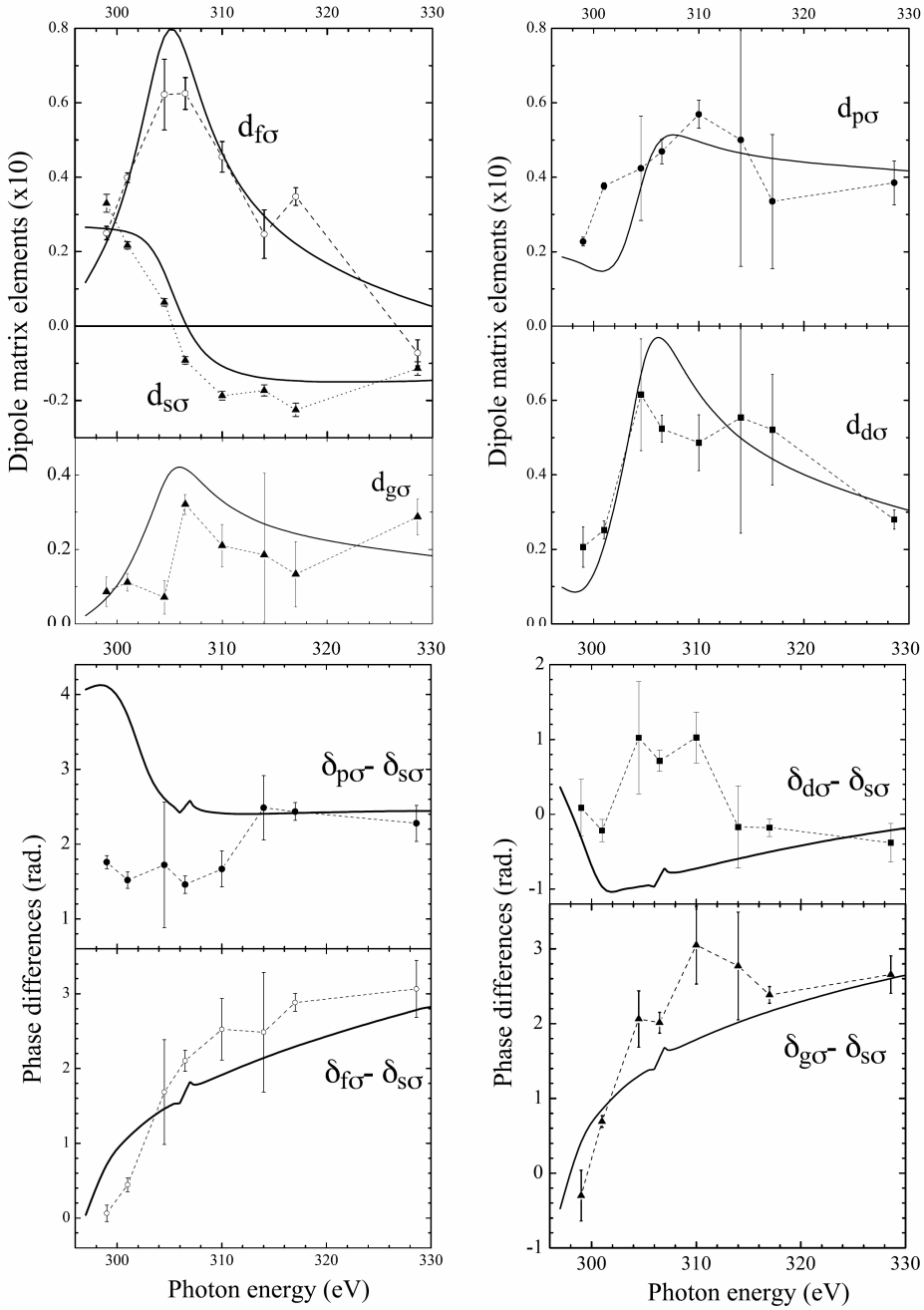

Figure 3.5: CO C K-edge Photoionization Dipole matrix elements $d_{l\sigma}$ (top)(in atomic units, multiplied by 10) and phase shift differences (bottom) for the C $1s\sigma \rightarrow \varepsilon l\sigma$ transitions with $0 \leqslant l \leqslant 4$ extracted from the experimental data (points with error bars connected by straight lines) and calculated in the RCHF approximation by Cherepkov *et al.* J.Phys.B 33,4213(2000).

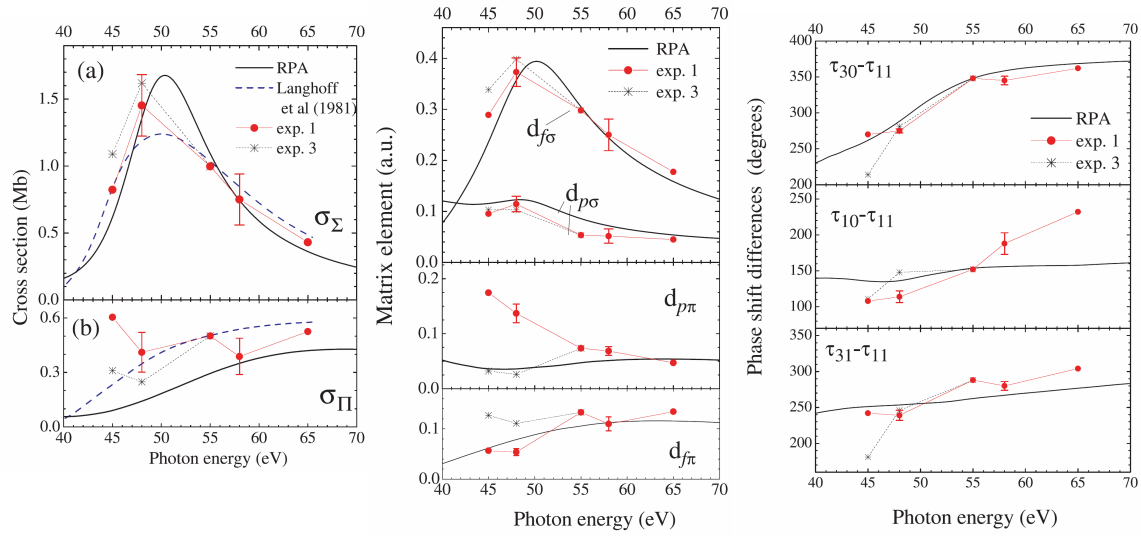

Figure 3.6: Comparison of the experimental and theoretical results by Motoki *et al.* in J.Phys.B 35,3801(2002) for N_2 partial cross sections (left), dipole matrix elements (middle) and phase shift differences(right).

it had the smallest number of hydrogen atoms and is linear.

The first glance at the PhotoIon-PhotoIon-Coincidence spectra (see figures 3.9, 3.10, 3.11) from this experiment also showed that acetylene was more advantageous in this respect. It was clear that after the photoionization the molecule of acetylene had the highest percentage of symmetric breakup (breakup of the C-C bond) of the three gases (see table3.1). This can be explained by the number of hydrogen atoms in each molecule. Since this breakup channel was essential for determining the molecular orientation (especially in the case of ethylene and ethane) the target gas that provides the highest statistics would be the most favorable.

The energy diagram with the involved process is shown in figure 3.12). One interesting difference from CO and N_2 molecules was in the resulting kinetic energy release spectra: The energy for the hydrocarbon recoils exhibited a nearly single-peak distribution. This

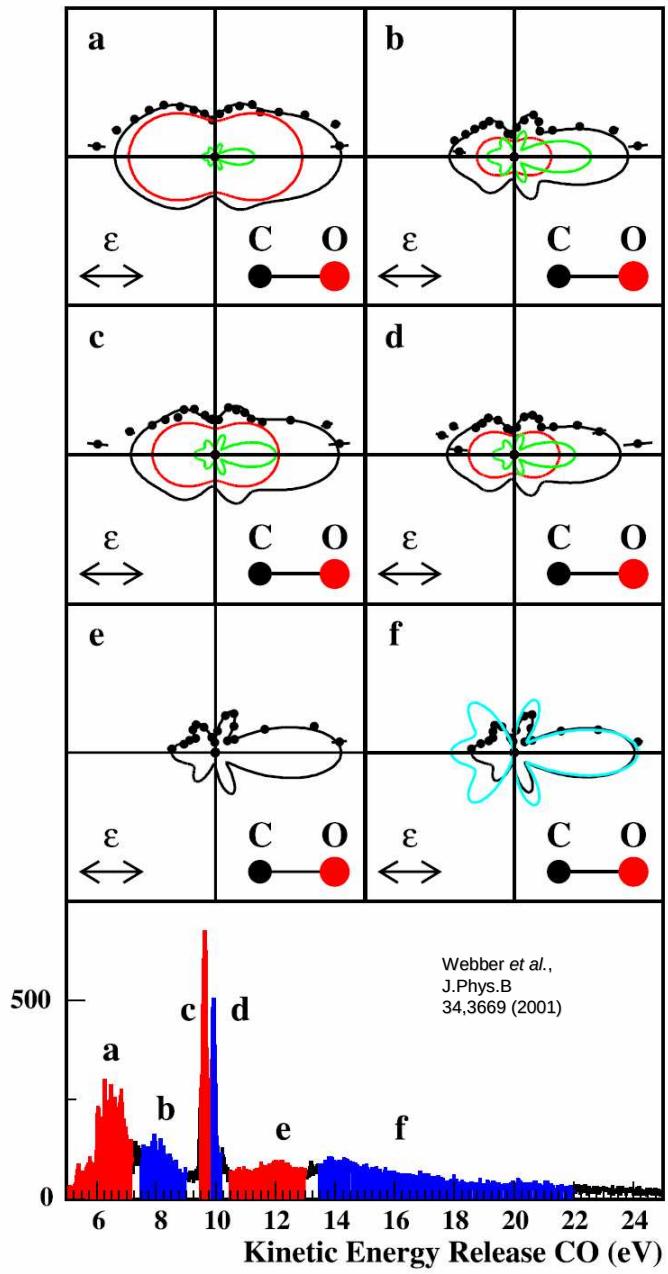

Figure 3.7: CO angular distribution of 10.4 eV carbon K-photoelectrons ($E_\nu = 306.4$ eV). The polarization of the linear polarized light is horizontal, the C^+ and O^+ fragments are detected parallel to the polarization (O^+ to the right). The electron and the fragments are emitted within $\pm 20°$ of the plane of the figure. Each panel is arbitrarily scaled. The data shown in panels (a)-(f) are electrons coincident with regions of kinetic energy release as indicated in the lower panel. The full black curve in panel (f) shows a fit with $l = 0,\ldots,8$. The blue (grey) curve in (f) shows the theoretical prediction scaled to the maximum of the distribution (adapted from [3]).

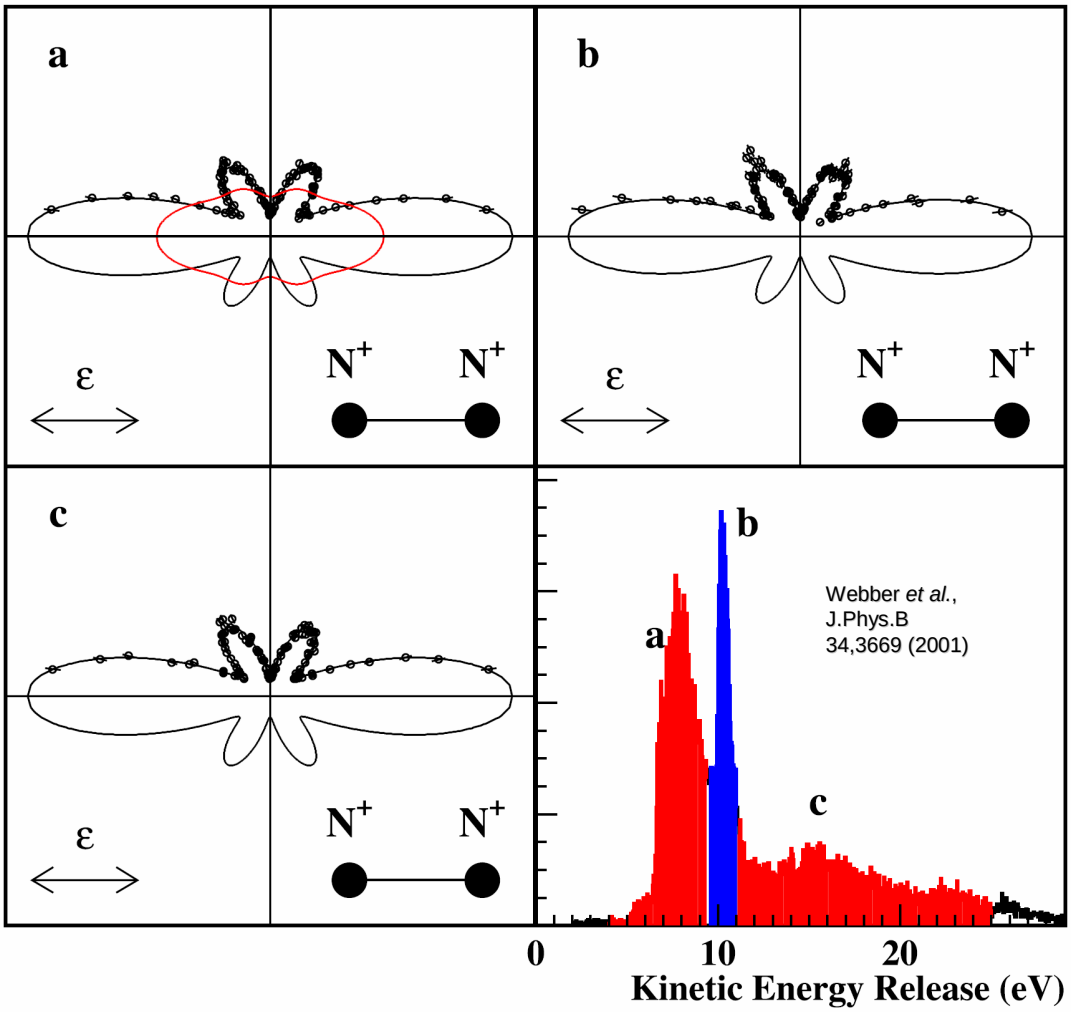

Figure 3.8: Angular distribution of 9.8 eV K-photoelectrons from N_2. The polarization of the linear polarized light is horizontal, the N^+ N^+ fragments are detected parallel to the polarization. The electron and the fragments are emitted within 20° of the plane of the figure. Each panel is arbitrarily scaled. The data shown in panels (a)(c) are electrons coincident with regions of kinetic energy release as indicated in panel (d). The full curve is a fit of the sum of Legendre polynomials (l = 0, 2, 4, 6, 8). The red curve in panel (a) shows the expected distribution for random rotation of the molecular axis (adapted from [3]).

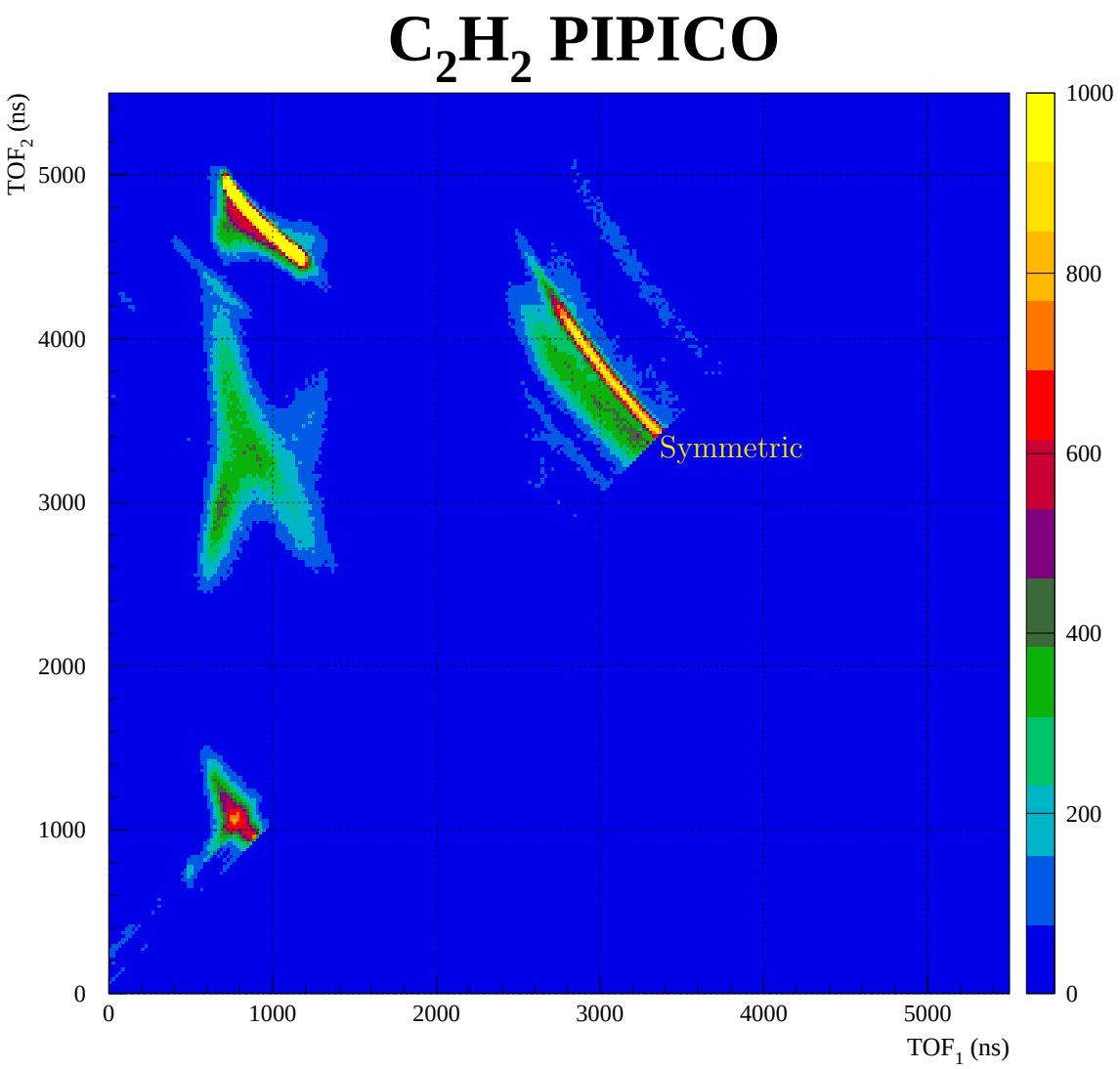

Figure 3.9: C_2H_2 PIPICO.

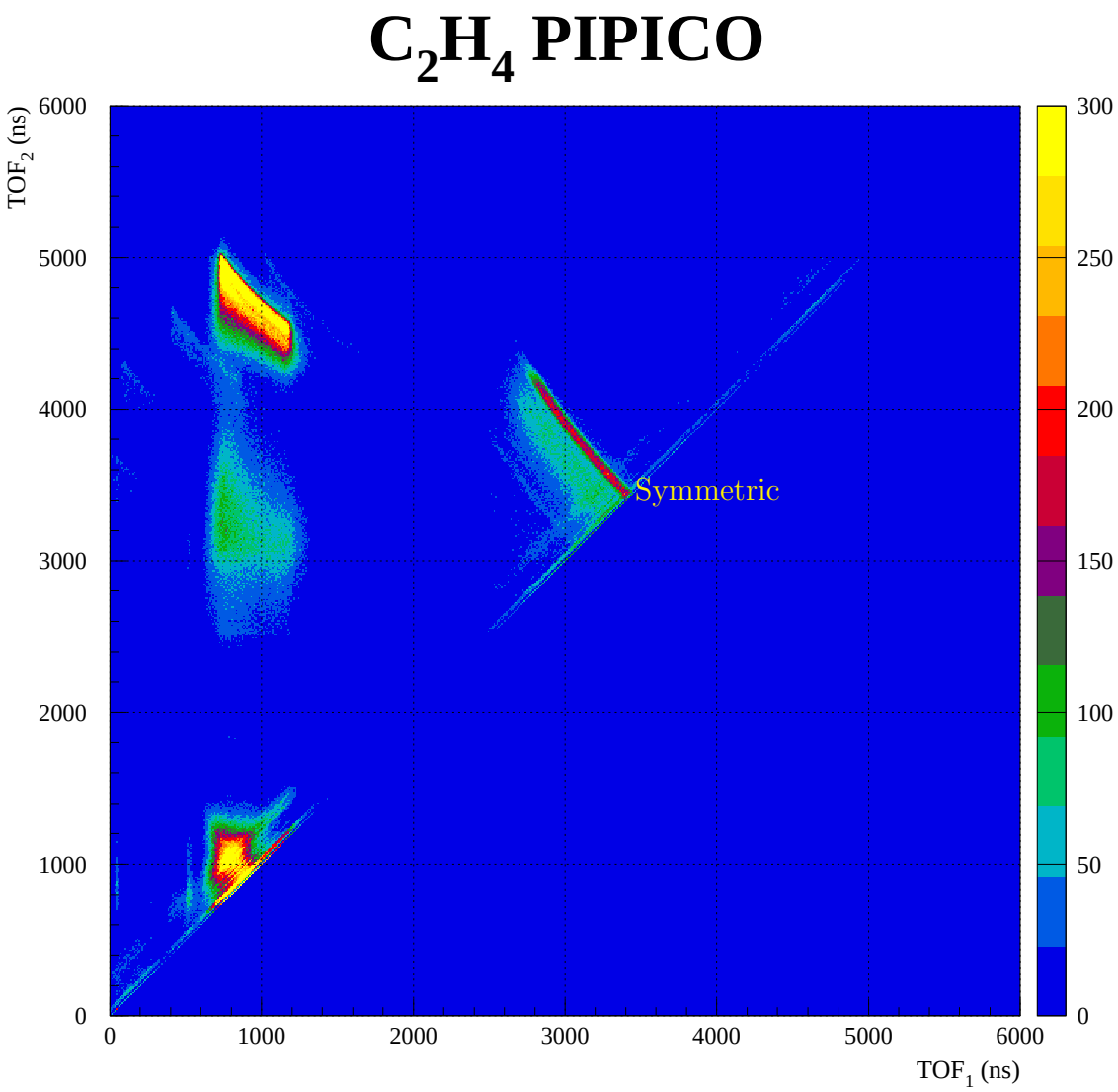

Figure 3.10: C_2H_4 PIPICO.

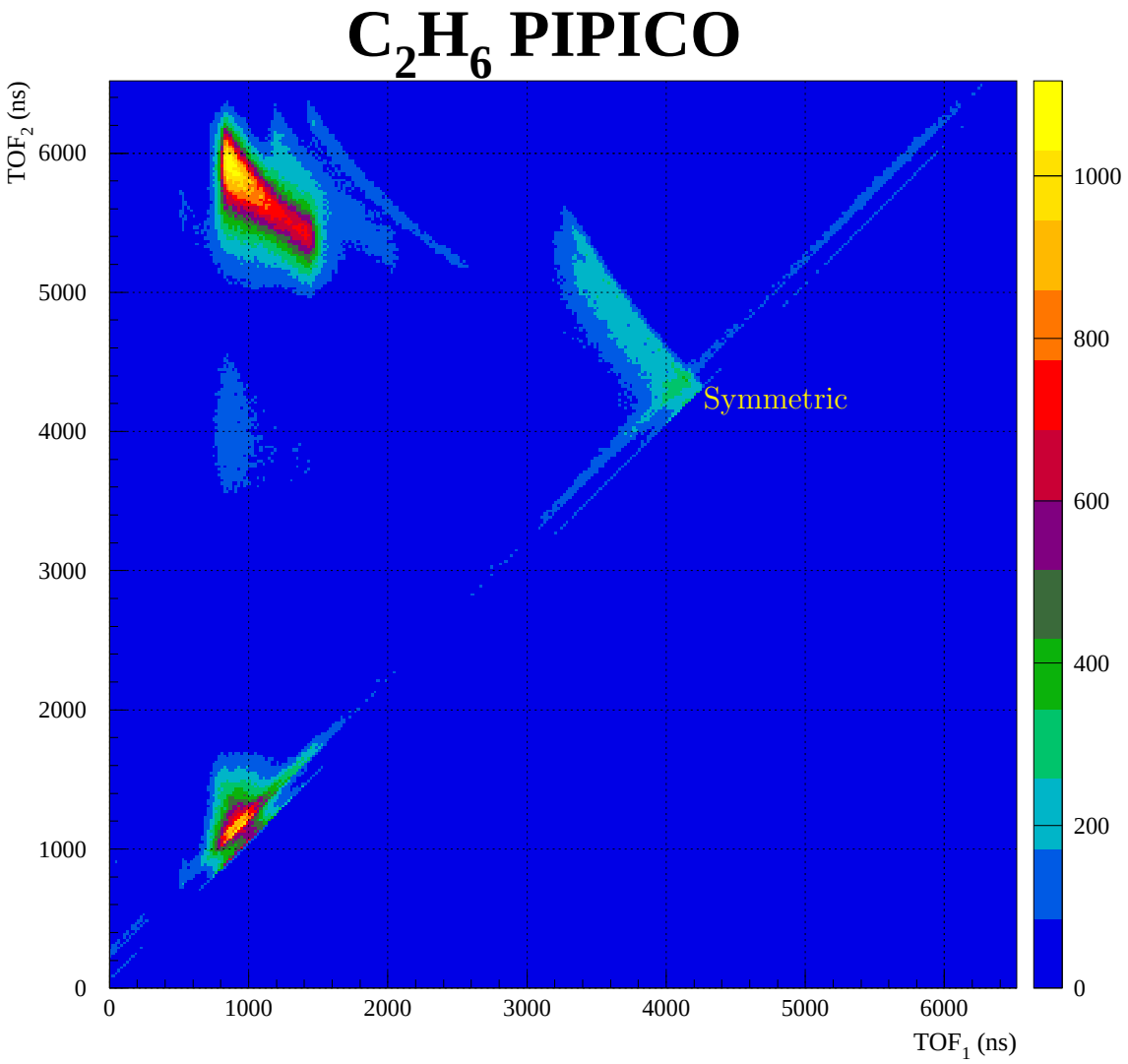

Figure 3.11: C_2H_6 PIPICO.

Table 3.1: **Branching Ratio for Different Target Gases.** The four rows of the table correspond to four main islands seen on the PIPICO spectra — four possible (with total mass constrain) combinations of pairs of **H**(heavy), **M**(medium) and **L**(light) singly charged positive ions. Heavy ions are those that contain two carbon atoms; Medium ions — contain only one carbon; Light ions — contain no carbon, ex. H^+, H_2^+, H_3^+; **S** stands for symmetric breakup, as in $(CH)^+$+$(CH)^+$, $(CH_2)^+$+$(CH_2)^+$, $(CH_3)^+$+$(CH_3)^+$, and it's the subset of **M + M**.

Branching	C_2H_2	C_2H_4	C_2H_6
L + H	19%	33%	51%
L + M	25%	21%	12%
L + L	13%	19%	16%
M + M (S)	42%(12%)	25%(7%)	19%(4%)

is believed to be primarily due to the fact that hydrocarbons have fewer potential curves contributing to a final symmetric molecular dissociation process[1].

More detailed momentum analysis of recoils from the different gases, however, revealed unexpected features associated with the acetylene symmetric breakup channel. While the spectra of the momentum spheres for ethylene and ethane (fig. 3.14 and fig. 3.15) looked perfectly round, which agreed with the almost mono-energetic breakup, the acetylene case (fig. 3.13) showed a strange structure along the time-of-flight direction (x-direction) that also made the Kinetic Energy Release (KER) spectrum less sharp. Later these features were explained by the presence of mass 12 a.m.u and 14 a.m.u ions due to the breakup of acetylene's isomer vinylidene see Appendix I. This isomerization reaction by itself gave rise to another interesting research topic and will be covered later in chapter 4. Due to the difficulty of clean separation of acetylene and vinylidene it was decided to continue the

[1]Very detailed analysis of the potential curves and Auger electron spectra for the ethylene dication dissociation is given in [17; 18]. The final energy levels (for the infinite separation of recoils) are not presented in the result, however. Due to this the kinetic energy release corresponding to the decays along these potential curves cannot be clearly determined.

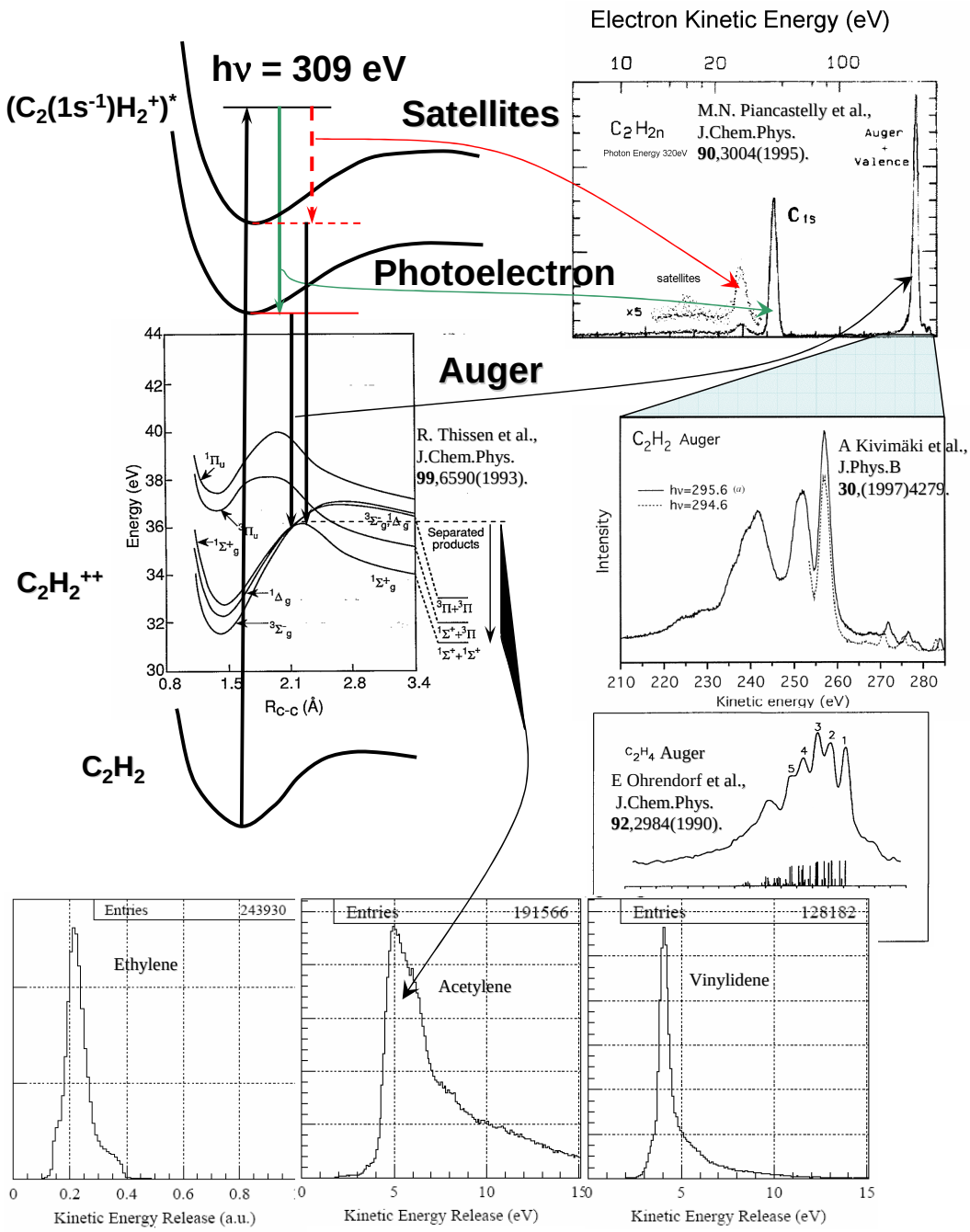

Figure 3.12: Hydrocarbons K-shell Photoionization, Reaction Steps, Energetics And Dynamics.

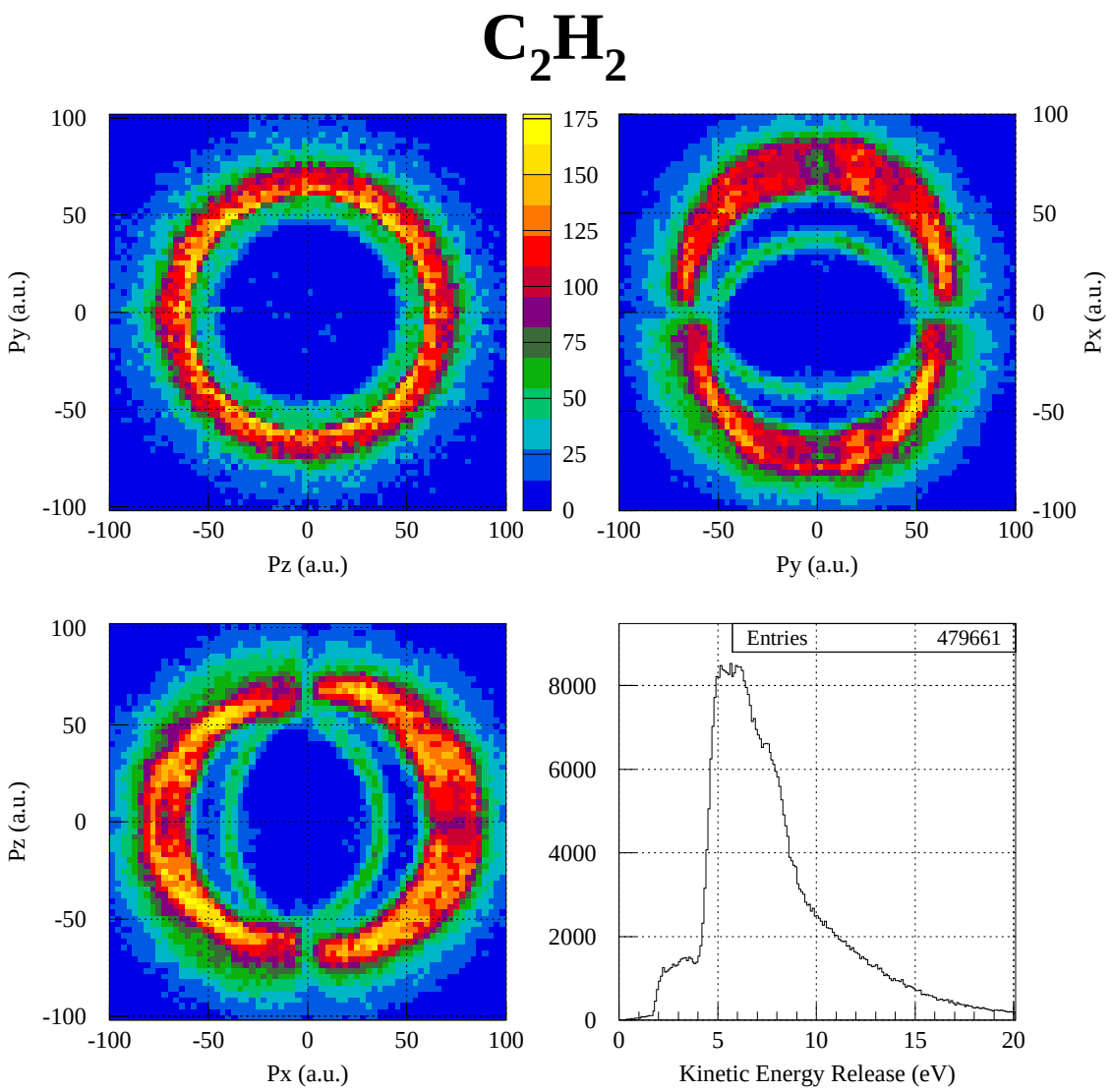

Figure 3.13: C_2H_2 momentum.

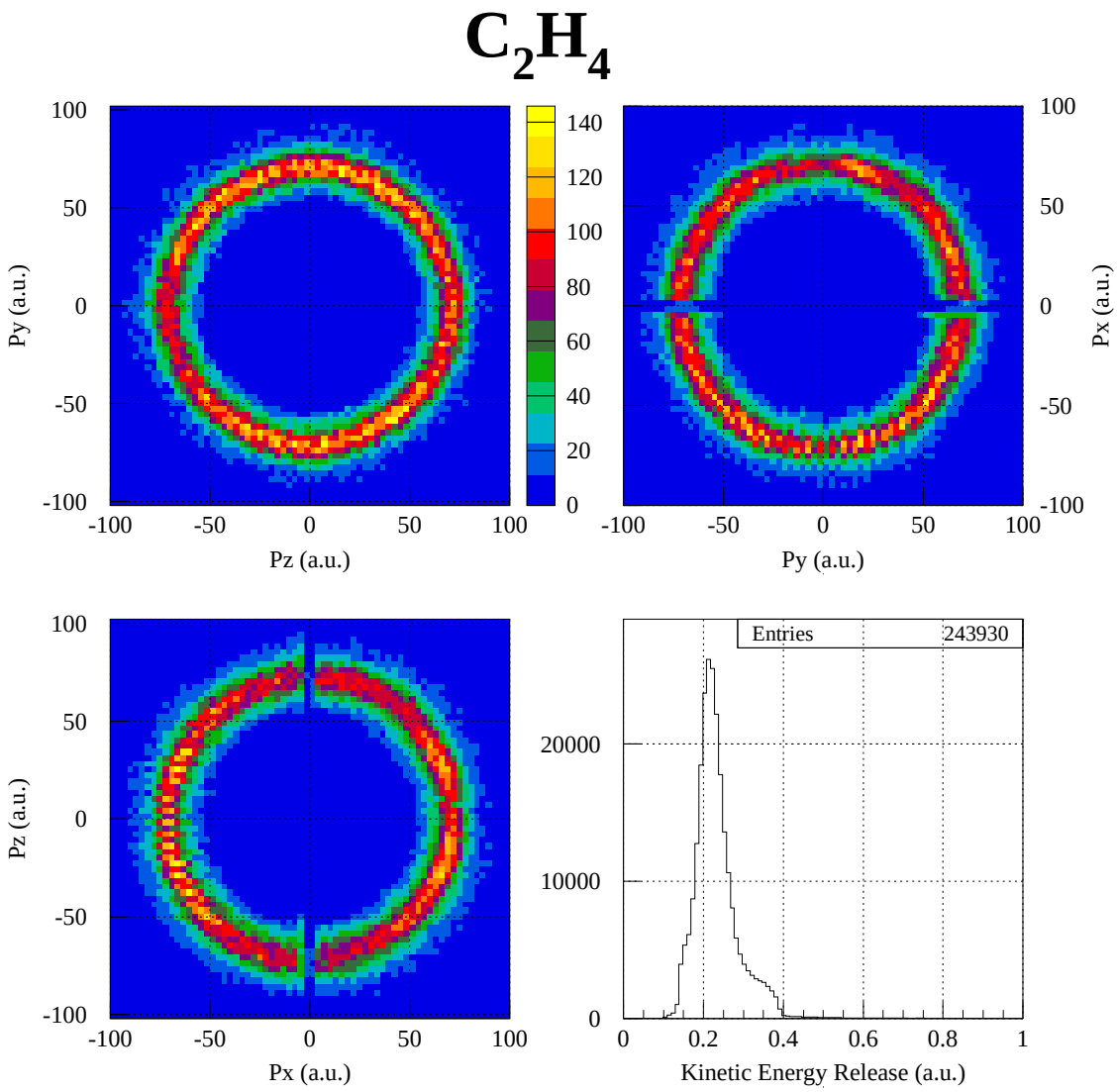

Figure 3.14: C_2H_4 momentum.

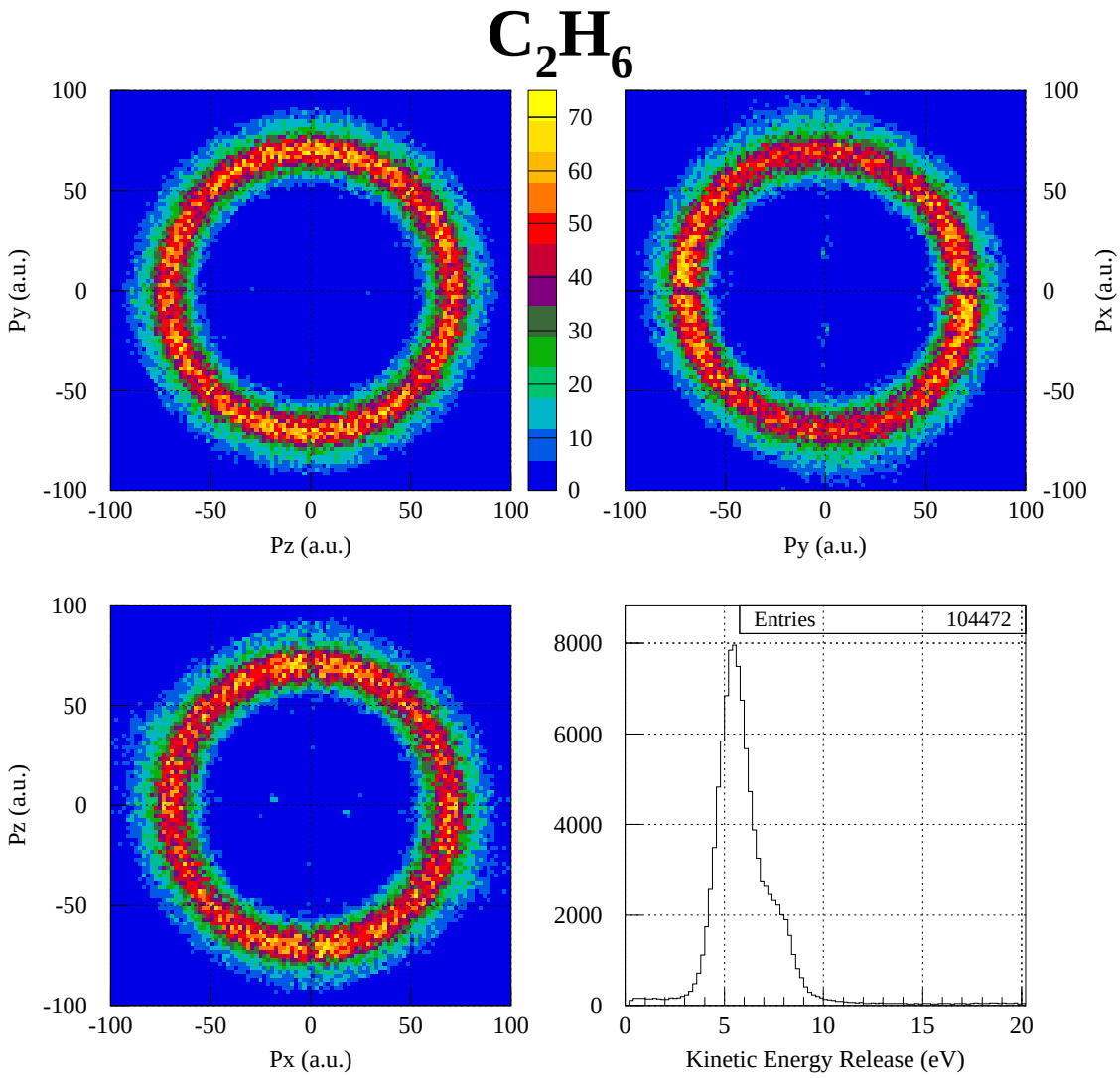

Figure 3.15: C_2H_6 momentum.

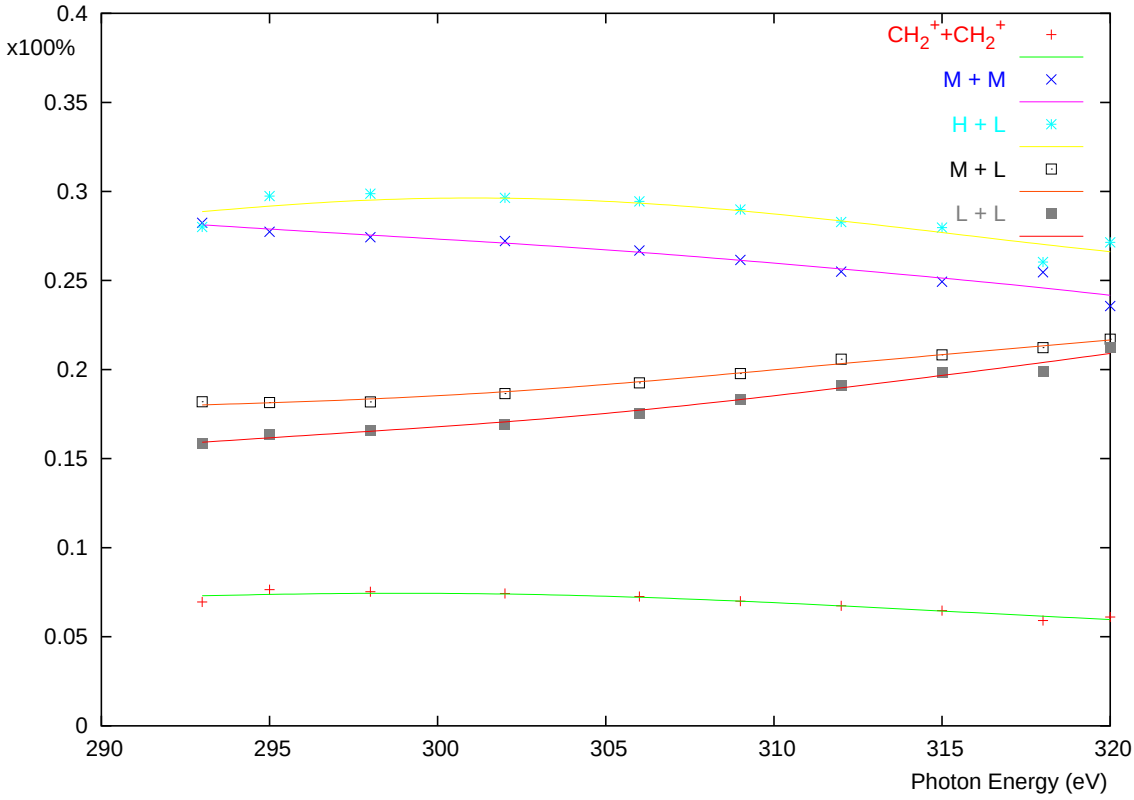

Figure 3.16: C_2H_4 Breakup Channels Fractions as a function of The Photon Energy.

further f-wave resonance analysis by studying the reaction with the molecules of ethylene (C_2H_4) fig. 3.14. It was determined from the experimental data that the branching ratio of different breakup channels registered for ethylene (fig. 2.19) was not changing much over the range of photon energies covered in the experiment (see fig. 3.16). In particular, the symmetric breakup fraction stayed nearly constant.

3.3 Results

It was initially believed that the very detailed data[2] on the photo-electron angular distributions in the body-fixed molecular frame obtained in the present experiment would be more than enough to uniquely characterize the ethylene molecular potential by extracting the dipole matrix element with very high precision. The final results of the detailed data analysis, presented in this section, show that the experimental data by itself, even as detailed as was obtained in this experiment, is not enough to uniquely extract the transition matrix elements[3]. It can, however, be a very powerful test for the theoretical models when comparing the intermediate results, which can be determined quite uniquely. One such parameter in the present analysis (see fig. 3.56) is the absolute value of the matrix element d_{30}, that is the contribution of the f partial wave into the transition amplitude. In spite of the ambiguity of the present analysis of the transition elements, the behavior of d_{30} is determined with a high degree of confidence and clearly shows resonant behavior in the vicinity of 300eV photon energy, in good qualitative agreement with theoretical results of [7].

3.3.1 Total Cross Section of the Reaction

The measurement of the absolute cross sections in this experiment is complicated mainly due to the lack of precise information about the target density. The gas jet assembly would have to be calibrated for every particular gas target to allow such measurements with the

[2]Analyzed data files related to this section can be found in the folder "pawfiles/ethylene" of the attached CD.

[3]This analysis can in most cases provide a finite number of sets of dipole matrix elements, one of which can be chosen by comparing with theory — see [15] for example.

proper accuracy. The relative cross sections however can be measured by means of monitoring the photon flux as a function of time (see fig. 2.9). By scanning the photoionization process over the range of energies in this matter and normalizing it to the number of photons, obtained by the integration of the photon flux over time, the cross sections were found to be in good agreement with previous results obtained by several experimental groups(see fig. 3.17). These previous experiments were able to measure electron energies and even angular distributions but only in the laboratory frame.

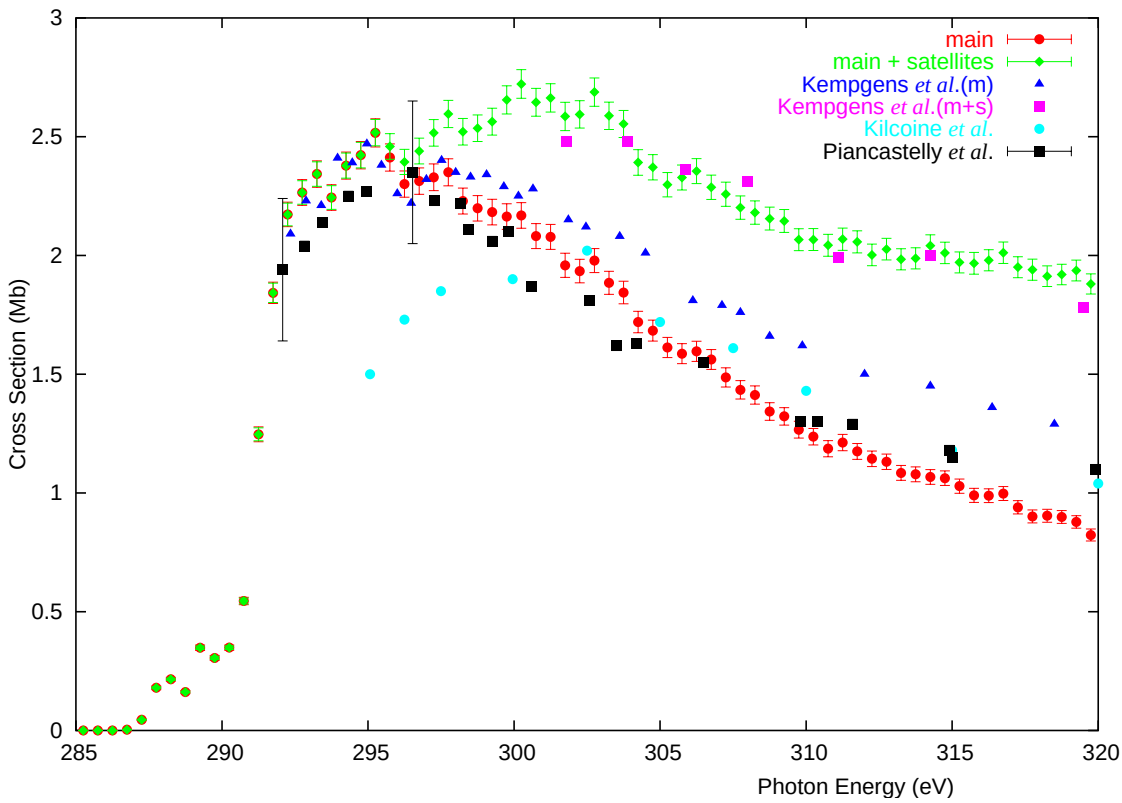

Figure 3.17: Total Cross Section versus The Photon Energy. Results from this work (green and red) compared to the results from [8; 11; 12].

Since the total cross section was the only source of information about the σ^* resonance in the older experiment their results had to rely on the presence of the clear peak structure

in the cross-section spectrum.

Kempgens *et al.* in [8] raised the question about the nature of the peak that was earlier attributed to the resonance. For the ethylene k-shell photoionization the peak was observed around 302eV photon energy. In his experiment Kempgens was able to measure the energy of the slow electrons[4] and to separate those events that were due to satellites. That was when the energy of the photoelectron was less than the photon energy minus the k-shell ionization potential. The molecular ion in this case was left in the higher excited state (above the C($1s^{-1}$)). When these electrons were excluded the cross section lost any peak structure (see fig. 3.17).

The issue of the satellite electrons was properly dealt with in the present analysis as shown in figure 3.18. All the final results of this work are obtained from the cross sections that have main line electrons properly singled out as shown in fig. 3.19 (versus the fig. 2.23).

3.3.2 Spherical Harmonics Fits. Extraction of Transition Amplitudes

Figures[5] 3.20 – 3.29 show the resulting polar plots of the angular distributions in the case of ethylene molecules for a set of different photon energies (see section 2.3.5 and appendix G for the plotting procedure details). In these figures the angle ϕ of the electron is chosen to be zero. From this point on the angles θ and ϕ will denote the longitudinal and azimuthal angles of the electron momentum in this body-fixed-frame, and θ' will be the angle between

[4]Same result was obtained earlier by M.N.Piancastelli *et al.* in [11].

[5]The movies of the angular distributions for several photon energies can also be found in the folder "thesis/movies" of the attached CD.

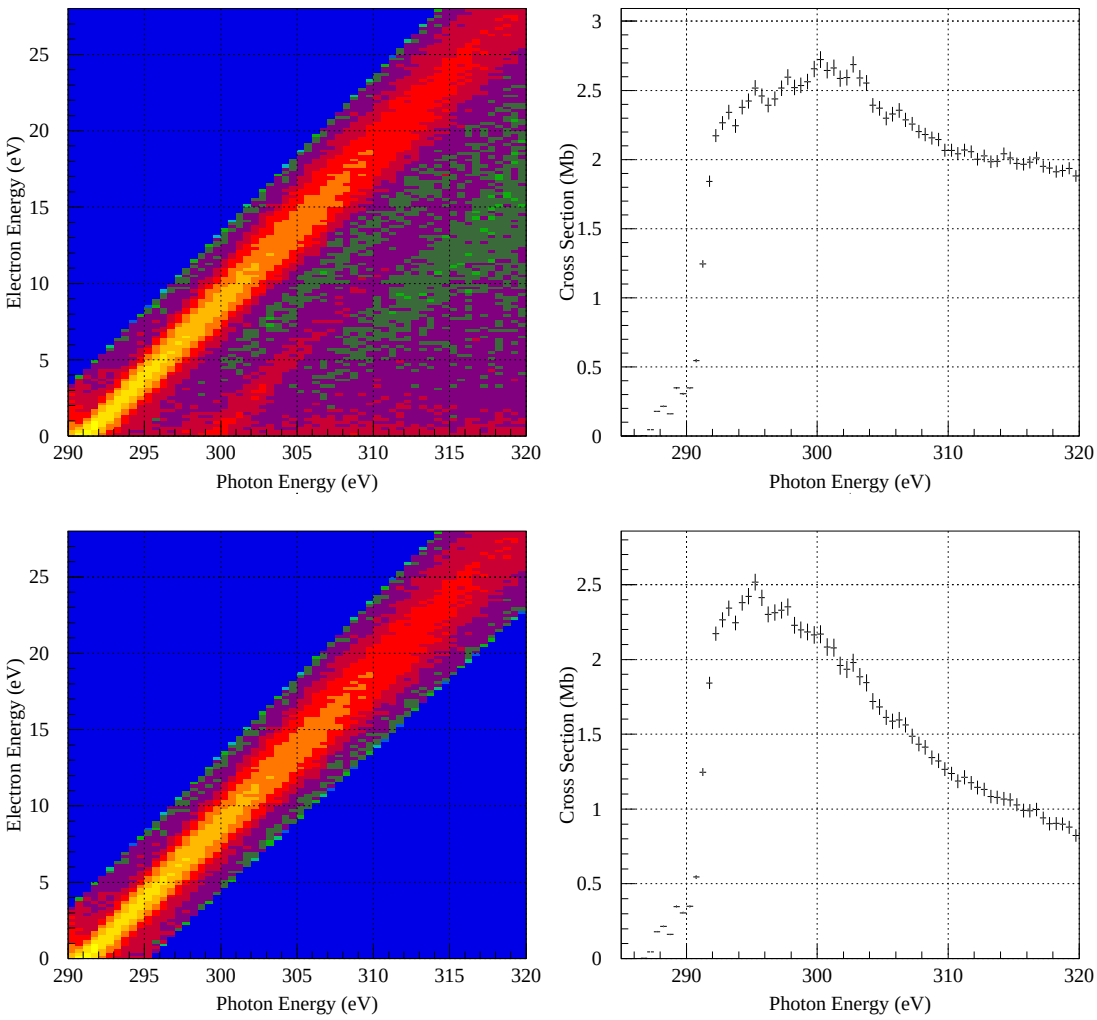

Figure 3.18: Electron energy as a function of the photon energy and the corresponding cross sections for the carbon 1s main line plus satellites (top) and just the main line (bottom) .

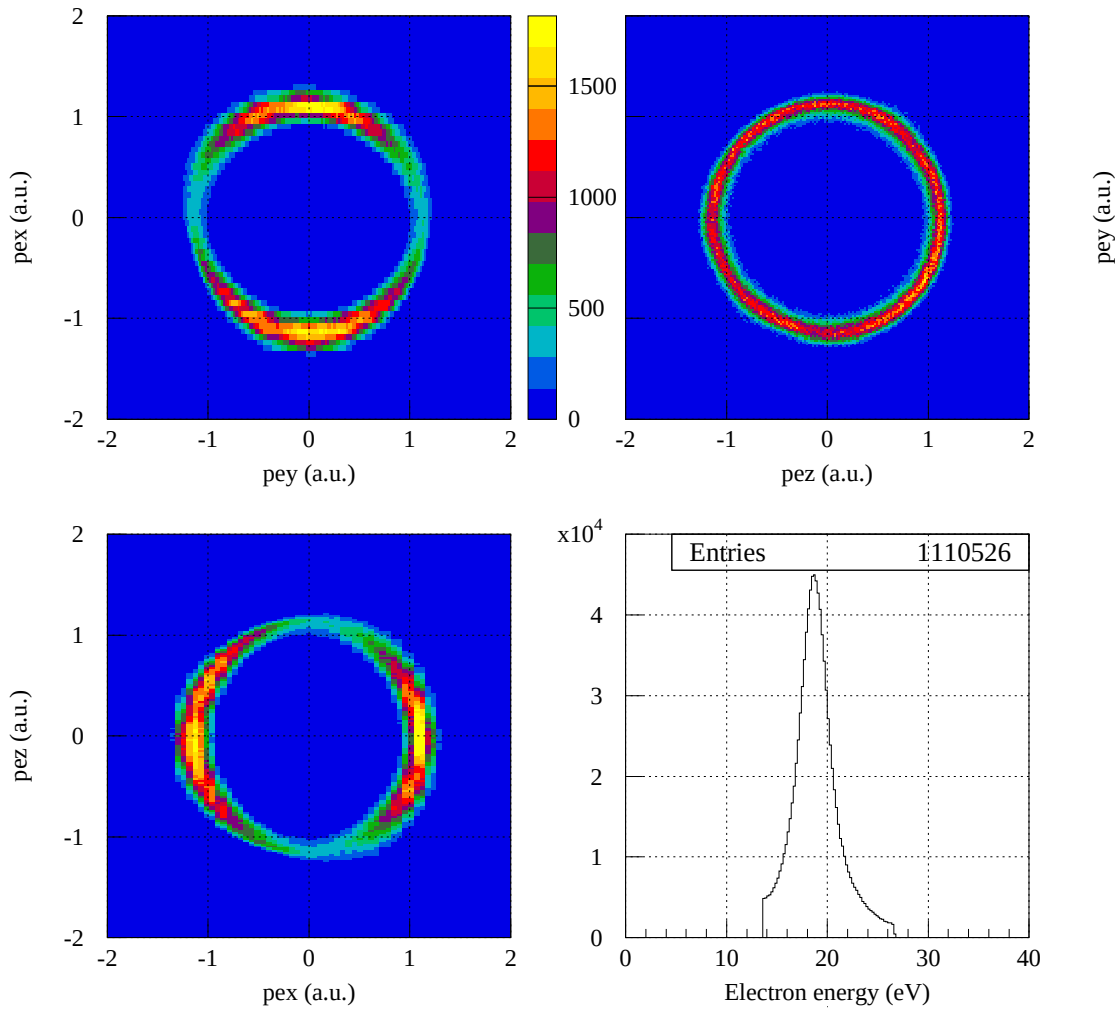

Figure 3.19: Gated Electron Momentum and Kinetic Energy Release from C_2H_4 at 309eV photon energy.

the X-ray polarization and the molecular orientation.

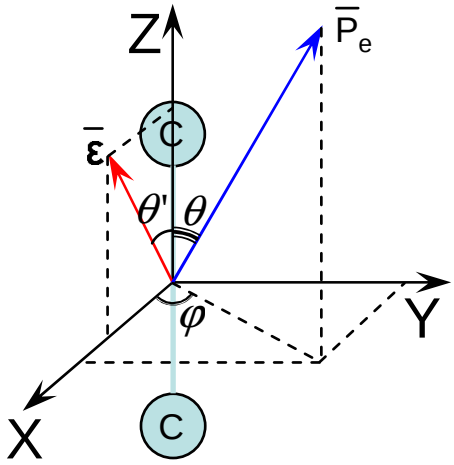

In the attempt to extract more detailed information about the molecular potentials of the ethylene molecule the above angular distributions were fitted with the following functions:

$$f_{\text{linear}}(\theta,\phi,\theta') =$$
$$= \left|\sum_{\text{even } l} A_l \cdot Y_{l0}(\theta,\phi)\cdot\cos\theta' + \sum_{\text{even } l} B_l \cdot \frac{Y_{l-1}(\theta,\phi) - Y_{l1}(\theta,\phi)}{\sqrt{2}}\cdot\sin\theta'\right|^2 +$$
$$+ \left|\sum_{\text{odd } l} A_l \cdot Y_{l0}(\theta,\phi)\cdot\cos\theta' + \sum_{\text{odd } l} B_l \cdot \frac{Y_{l-1}(\theta,\phi) - Y_{l1}(\theta,\phi)}{\sqrt{2}}\cdot\sin\theta'\right|^2$$

$$f_{\text{circular}}(\theta,\phi,\theta') =$$
$$= \frac{1}{2}\left|\sum_{\text{even } l} A_l \cdot Y_{l0}(\theta,\phi)\cdot\cos\theta' + \right.$$
$$\left. + i\sum_{\text{even } l} B_l \cdot \left(\frac{Y_{l-1}(\theta,\phi) + Y_{l1}(\theta,\phi)}{\sqrt{2}}\cdot\sin\theta' \pm \frac{Y_{l-1}(\theta,\phi) - Y_{l1}(\theta,\phi)}{\sqrt{2}}\right)\right|^2 +$$
$$+ \frac{1}{2}\left|\sum_{\text{odd } l} A_l \cdot Y_{l0}(\theta,\phi)\cdot\cos\theta' + \right.$$
$$\left. + i\sum_{\text{odd } l} B_l \cdot \left(\frac{Y_{l-1}(\theta,\phi) + Y_{l1}(\theta,\phi)}{\sqrt{2}}\cdot\sin\theta' \pm \frac{Y_{l-1}(\theta,\phi) - Y_{l1}(\theta,\phi)}{\sqrt{2}}\right)\right|^2$$

The $\pm$ sign in the second formula stands for right and left circular polarization. These

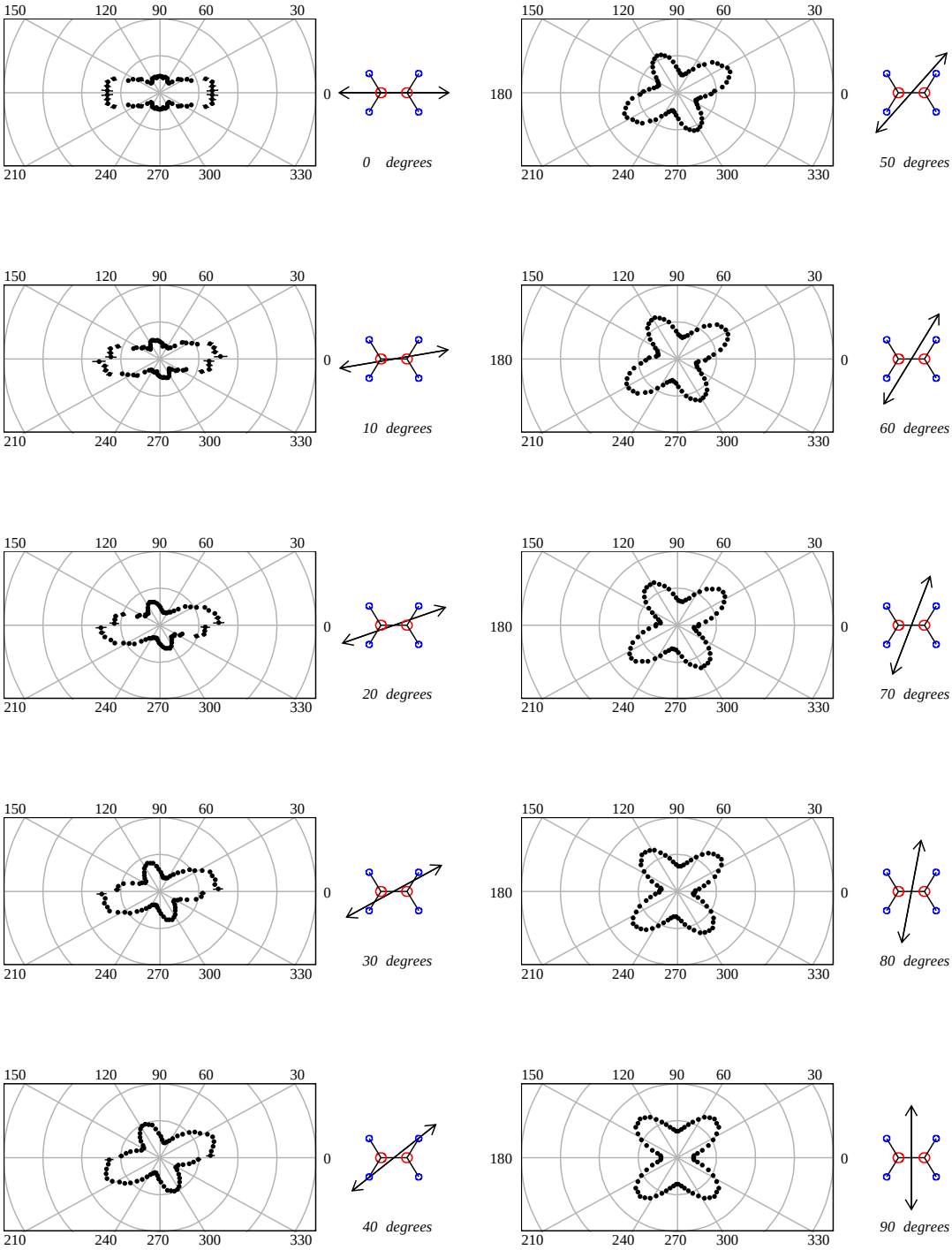

Figure 3.20: Electron Angular Distribution "Movie" at 293eV Photon Energy. Black arrow shows the direction of the polarization.

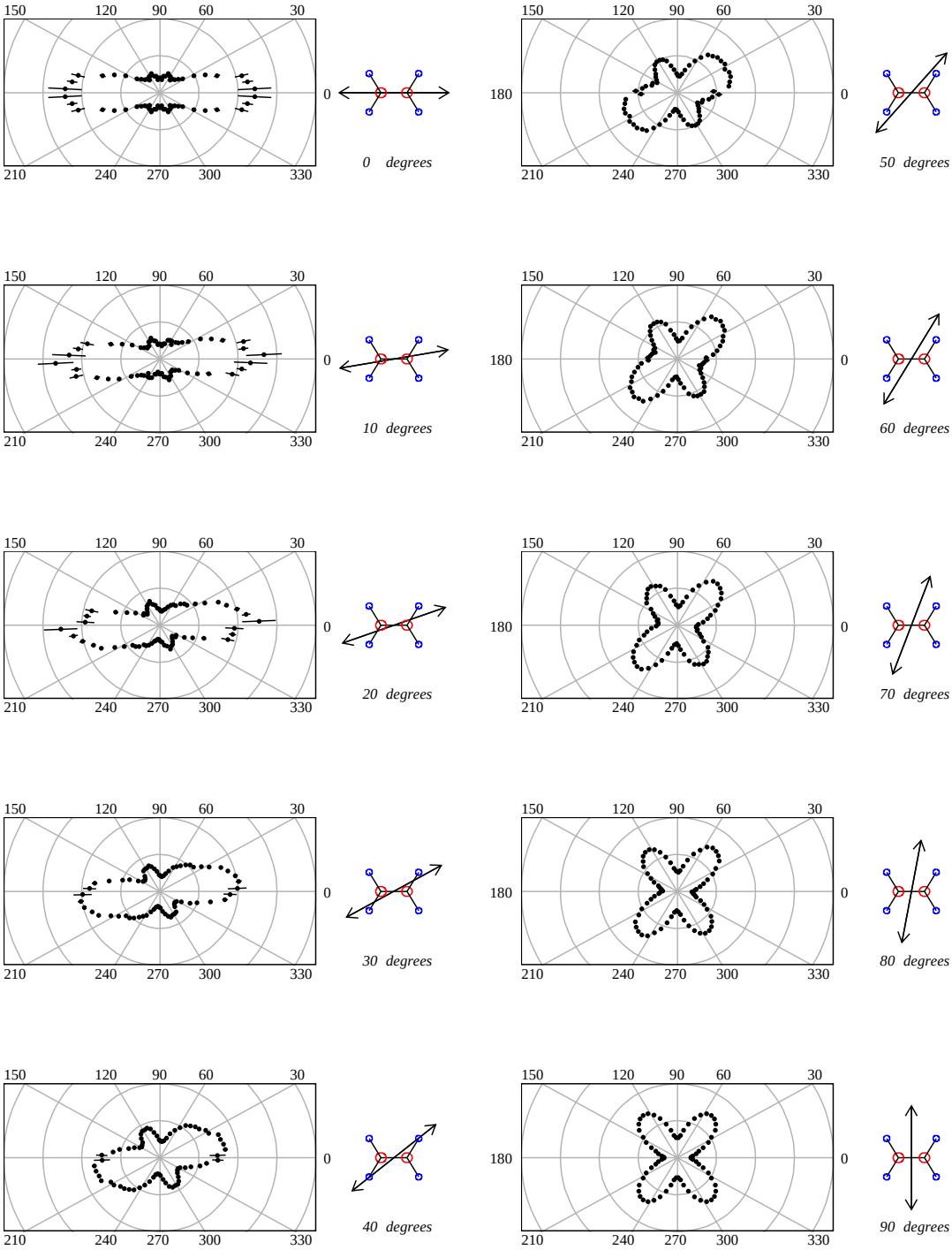

Figure 3.21: Electron Angular Distribution "Movie" at 295eV Photon Energy. Black arrow shows the direction of the polarization.

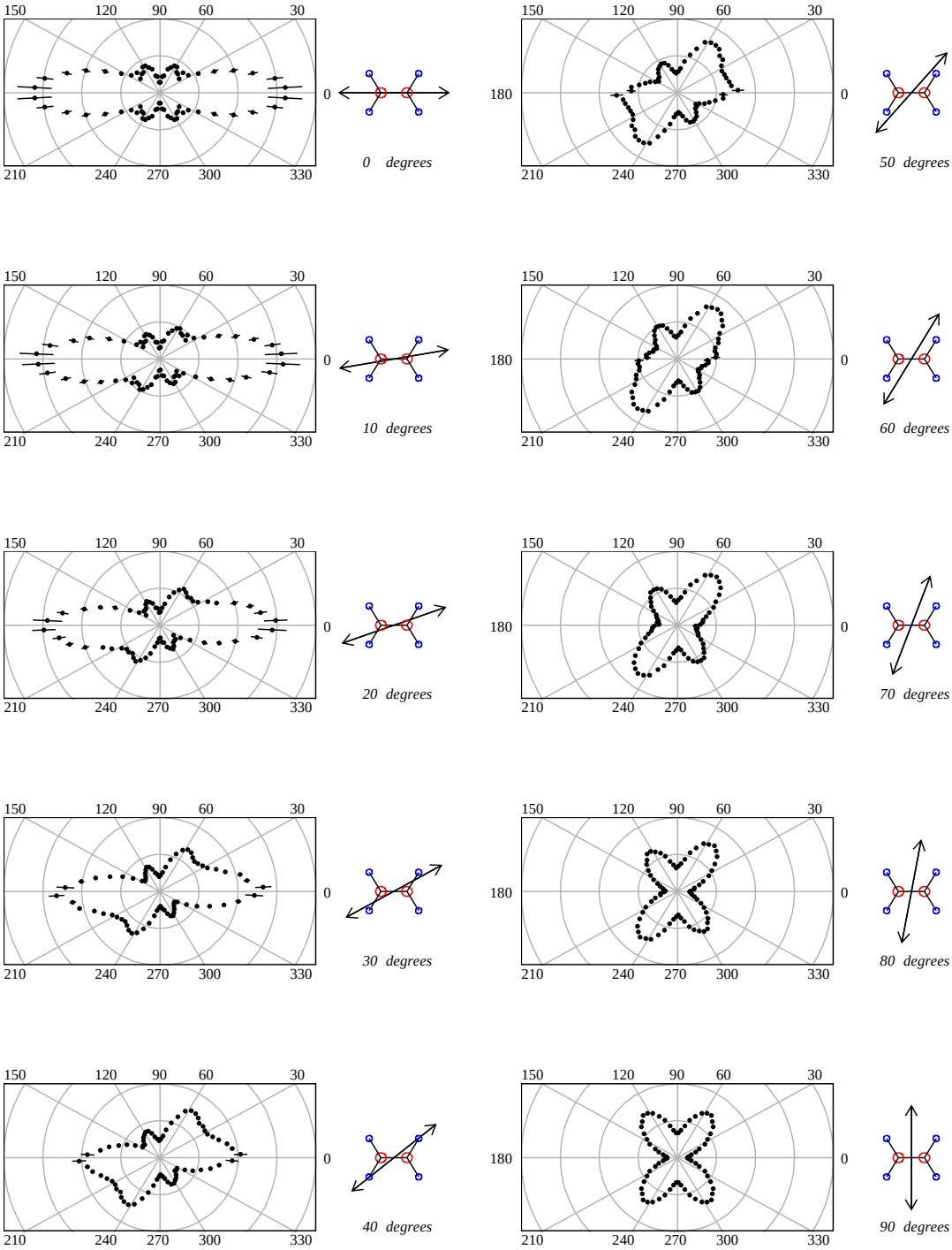

Figure 3.22: Electron Angular Distribution "Movie" at 298eV Photon Energy. Black arrow shows the direction of the polarization.

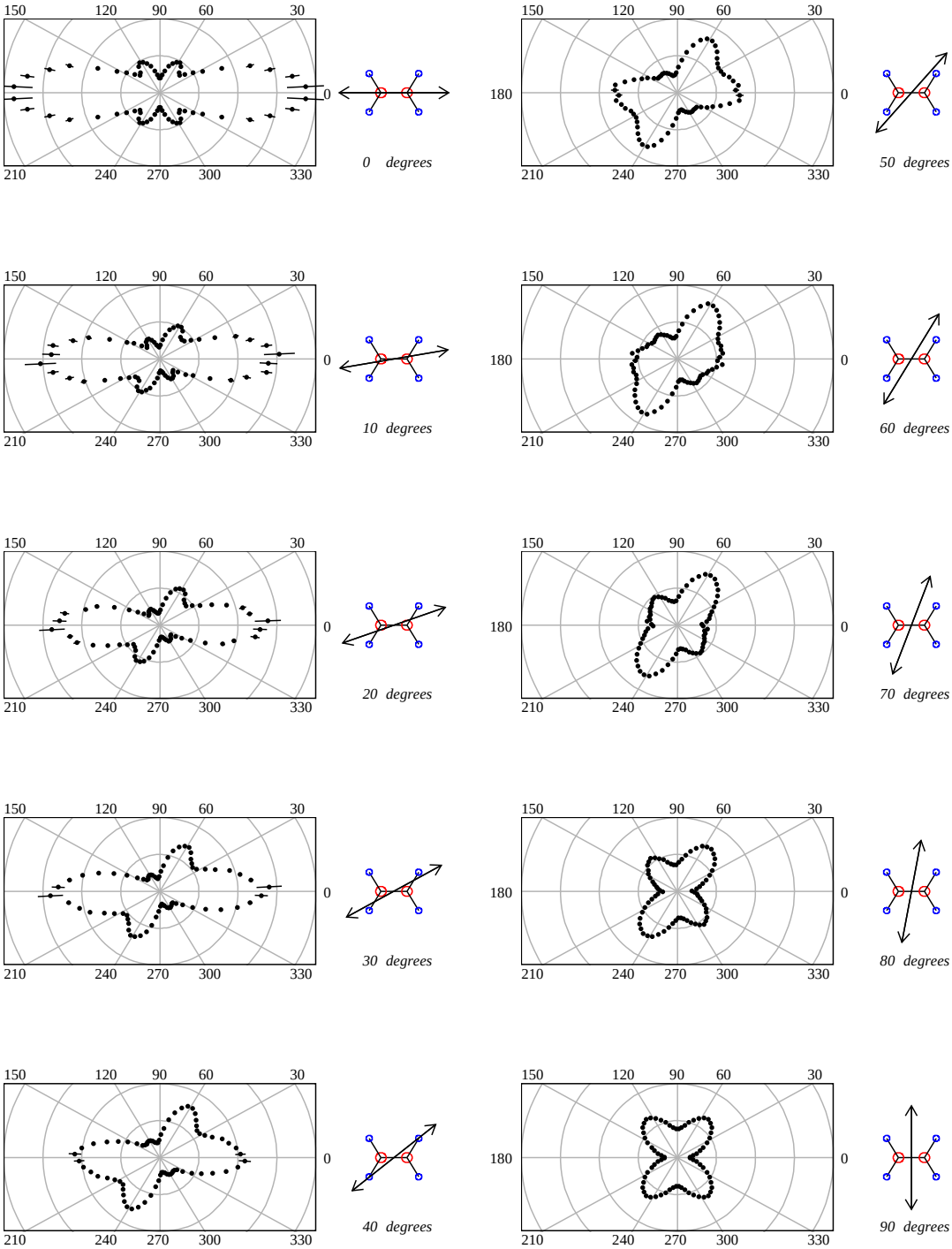

Figure 3.23: Electron Angular Distribution "Movie" at 302eV Photon Energy. Black arrow shows the direction of the polarization.

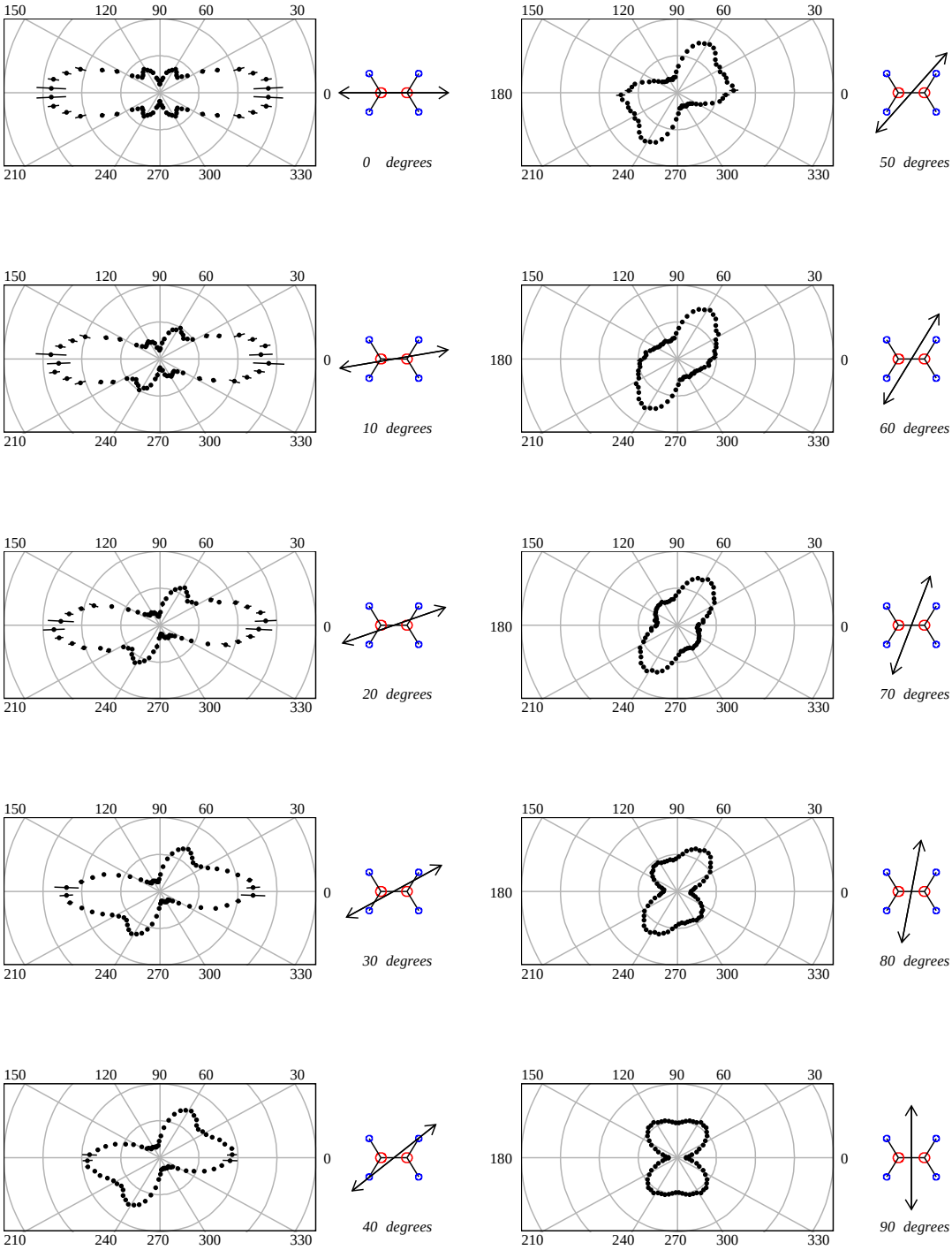

Figure 3.24: Electron Angular Distribution "Movie" at 306eV Photon Energy. Black arrow shows the direction of the polarization.

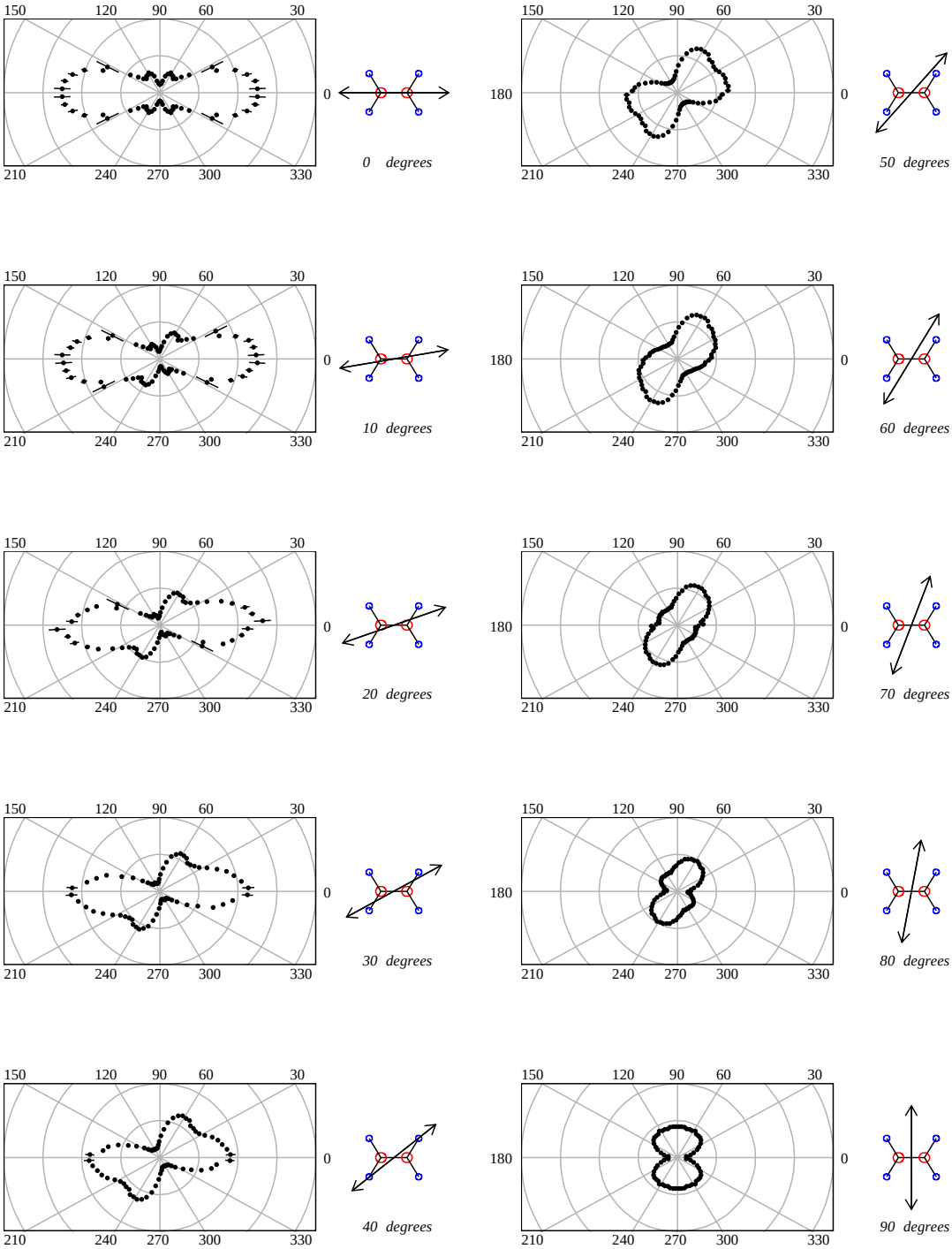

Figure 3.25: Electron Angular Distribution "Movie" at 309eV Photon Energy. Black arrow shows the direction of the polarization.

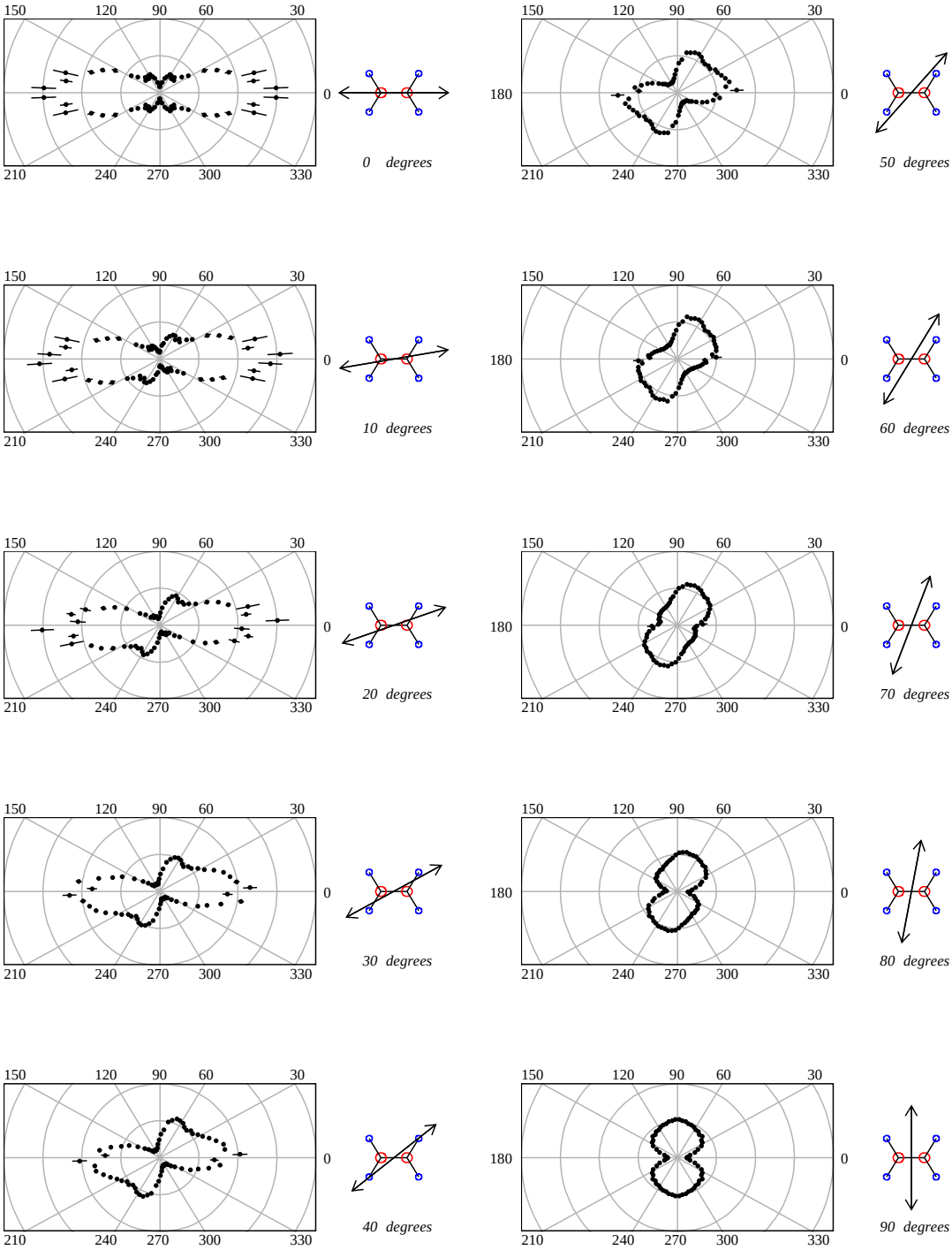

Figure 3.26: Electron Angular Distribution "Movie" at 312eV Photon Energy. Black arrow shows the direction of the polarization.

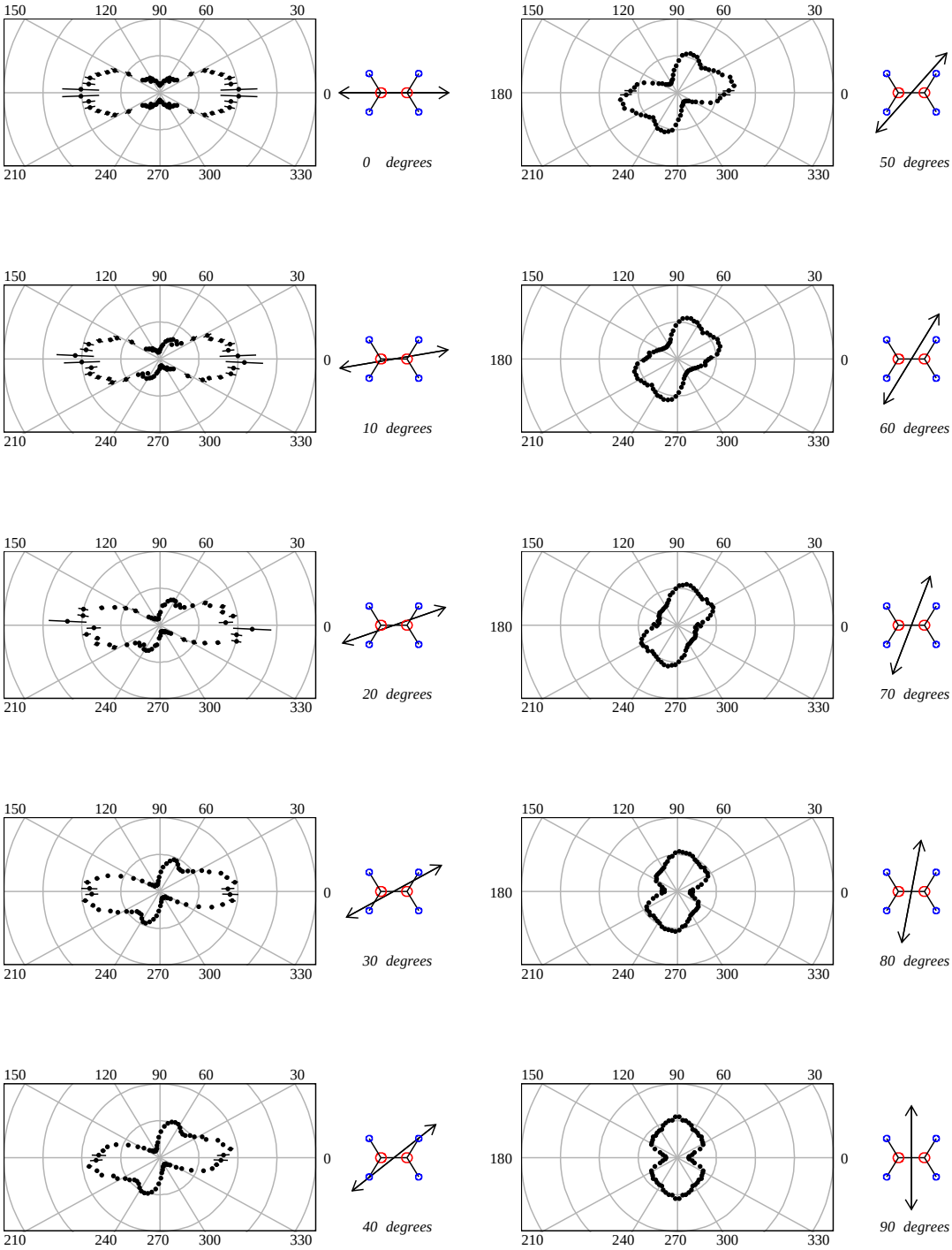

Figure 3.27: Electron Angular Distribution "Movie" at 315eV Photon Energy. Black arrow shows the direction of the polarization.

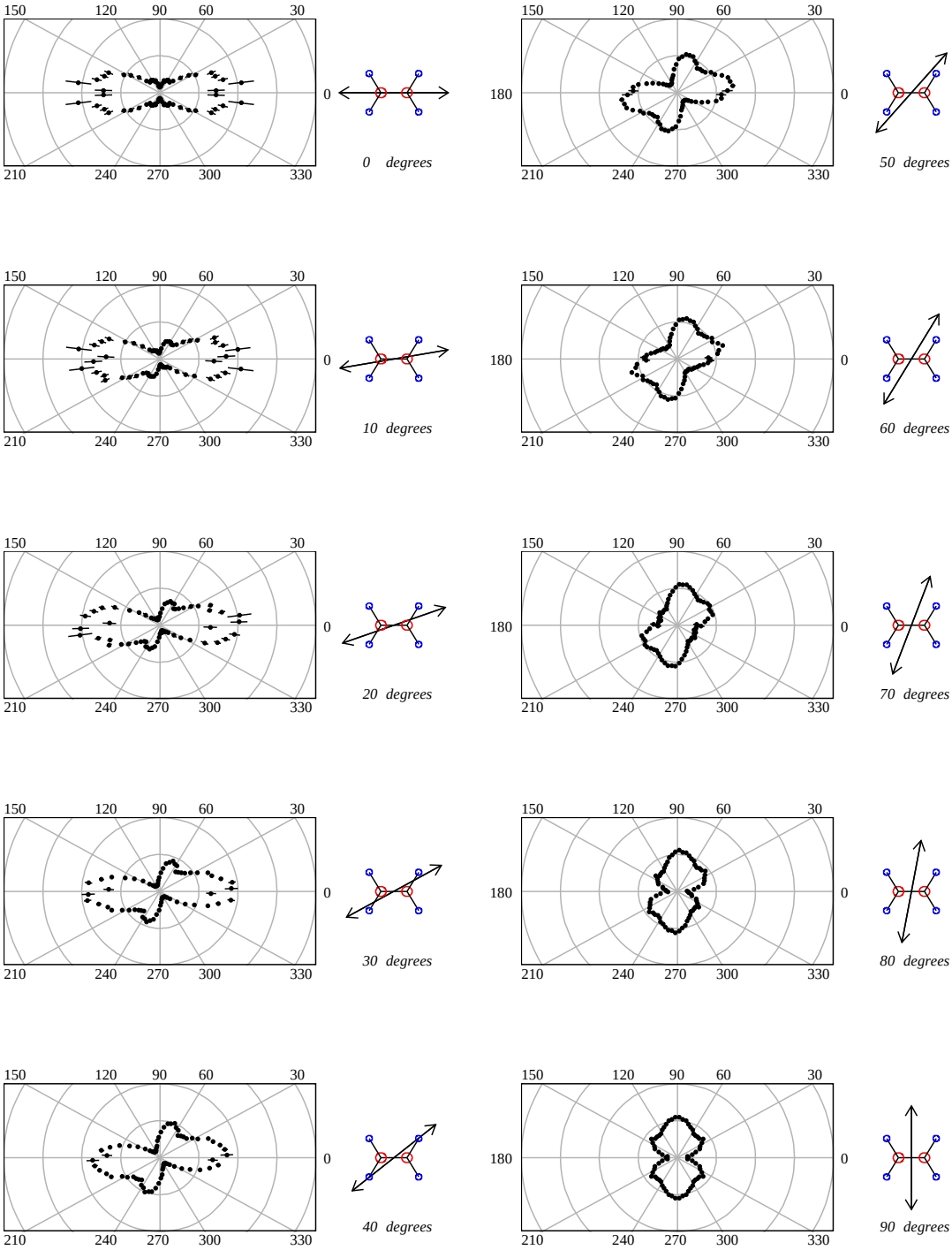

Figure 3.28: Electron Angular Distribution "Movie" at 318eV Photon Energy. Black arrow shows the direction of the polarization.

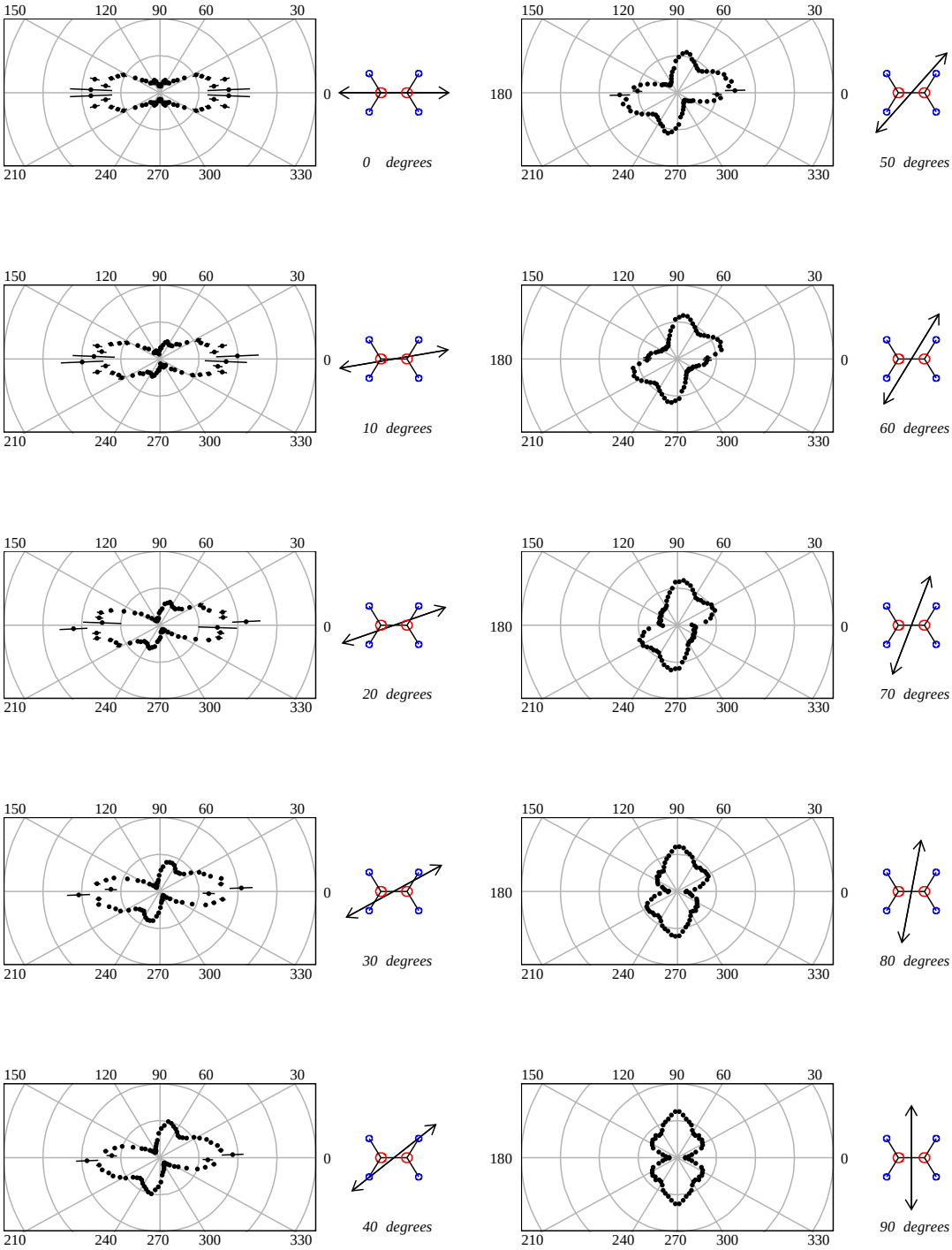

Figure 3.29: Electron Angular Distribution "Movie" at 320eV Photon Energy. Black arrow shows the direction of the polarization.

formulae use the same notation for θ and ϕ as defined above, and θ' in the case of the circular polarization is the angle between the polarization plane and the molecule(Z axis in a body-fixed frame). The separation of the even and odd l's is due to the *gerade* and *ungerade* wave functions on the symmetric two center molecule. The A_l's and B_l's are the complex amplitudes that need to be determined. They do not depend on the x-ray polarization and are defined only by the photon energy and the potential of the molecule. Taking into account that the only values present for the quantum number m are $0, \pm 1$ these formulae can be rewritten as:

$$\begin{aligned} & f_{\text{linear}}(\theta, \phi, \theta') = \\ & = \left| \sum_{\text{even } l} A_l \cdot Y_{l0}(\theta) \cdot \cos\theta' + \sum_{\text{even } l} B_l \cdot \frac{Y_l(\theta)}{\sqrt{2}} \cdot \cos\phi \sin\theta' \right|^2 + \\ & + \left| \sum_{\text{odd } l} A_l \cdot Y_{l0}(\theta) \cdot \cos\theta' + \sum_{\text{odd } l} B_l \cdot \frac{Y_l(\theta)}{\sqrt{2}} \cdot \cos\phi \sin\theta' \right|^2 \end{aligned} \tag{3.1}$$

$$\begin{aligned} & f_{\text{circular}}(\theta, \phi, \theta') = \\ & = \frac{1}{2} \left| \sum_{\text{even } l} A_l \cdot Y_{l0}(\theta) \cdot \cos\theta' + \sum_{\text{even } l} B_l \cdot \frac{Y_l(\theta)}{\sqrt{2}} (\sin\phi \sin\theta' \pm i \cos\phi) \right|^2 + \\ & + \frac{1}{2} \left| \sum_{\text{odd } l} A_l \cdot Y_{l0}(\theta) \cdot \cos\theta' + \sum_{\text{odd } l} B_l \cdot \frac{Y_l(\theta)}{\sqrt{2}} (\sin\phi \sin\theta' \pm i \cos\phi) \right|^2 \end{aligned} \tag{3.2}$$

where $Y_l(\theta)$ is defined as $Y_l(\theta) = Y_{l-1}(\theta, 0) - Y_{l1}(\theta, 0) = 2 \cdot Y_{l-1}(\theta, 0)$.

The simple dependence on the angle ϕ permits the use of the special data sorting technique described in Appendix G. In the case of linear polarization this technique allows for the elimination of the dependence on ϕ and thus sorting all electron angles into a two dimensional plot $f(\theta, 0, \theta')$ which is the set of polar plots presented in figures 3.20 – 3.29.

The final fitting forms have been truncated at $l_{max} = 3$. Figures 3.30–3.38 show the results of the fitting for three photon energies. The $l_{max} = 3$ truncation is evidently good enough for high-quality fit. As mentioned above the true complex amplitudes should be the same for linear and circular polarizations. Since the circular polarization provides certain extra information about these amplitudes, the fitting procedure was performed on both sets of data where available simultaneously to force the resulting amplitudes be the same (see fig. 3.39–3.42). Unfortunately it has been determined that this fitting procedure does not produce the unique results for the complex amplitudes (see appendix G or [15]). For the different starting points the fitting would return different sets of amplitudes with the same (down to several digits) value of the χ^2. This is mainly due to the fact that the fitting function has the squares of the *gerade* and *ungerade* contributions which makes them not entirely independent. This does not mean that the fitting results are absolutely unusable. Some characteristics are the same for all sets of results. Since the χ^2 is the same, the integral value of the distribution at fixed θ' is identical down to 5th digit. The uniqueness of the values for the fitting function $f(\theta, \theta')$ provides a reliable measurement of the ratio of σ cross section to π cross section as a function of the photon energy as shown in figure 3.43. This ratio has a definite peak around 305eV which is so far in good agreement with the theoretical calculations of Haack*et al.* in [7].

Another important parameter that is determined uniquely is the absolute value of the A_3 complex amplitude. It defines the contribution of the f-wave which allows for the further investigation of the shape resonance. Details of the fitting procedure along with several sets

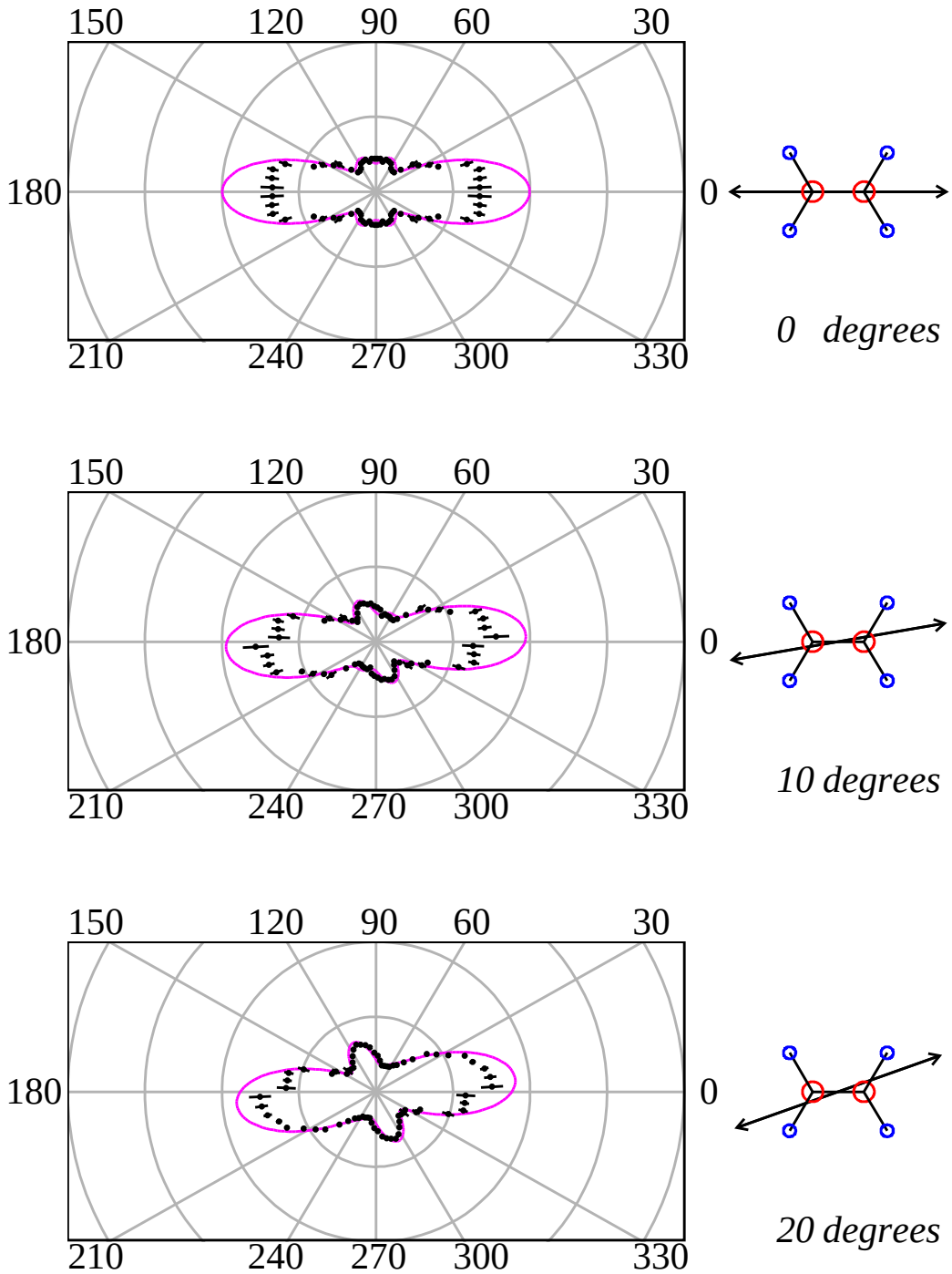

Figure 3.30: Electron Angular Distribution fit at 293eV Photon Energy (section 1). Black arrow shows the direction of the polarization.

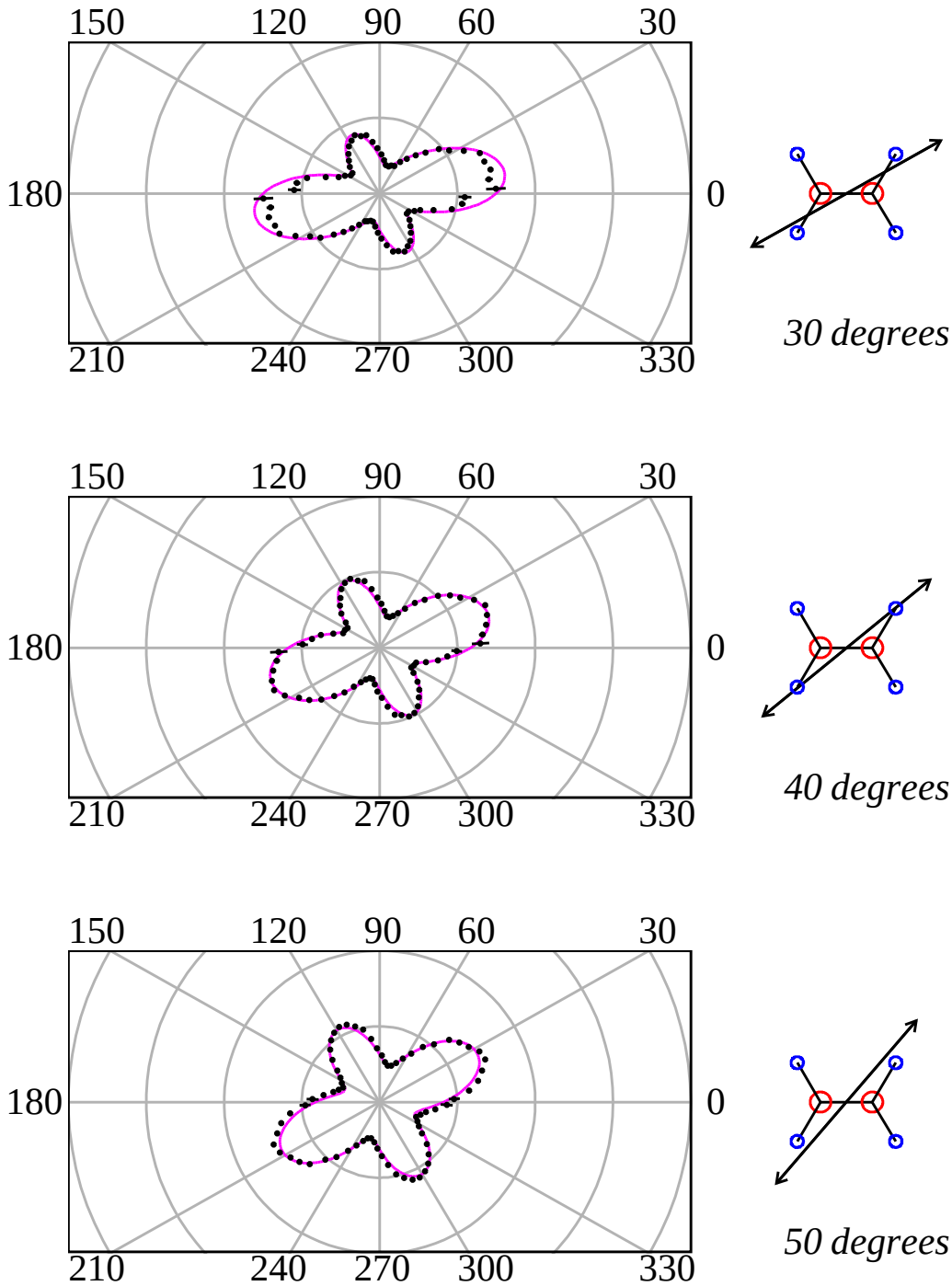

Figure 3.31: Electron Angular Distribution fit at 293eV Photon Energy (section 2). Black arrow shows the direction of the polarization.

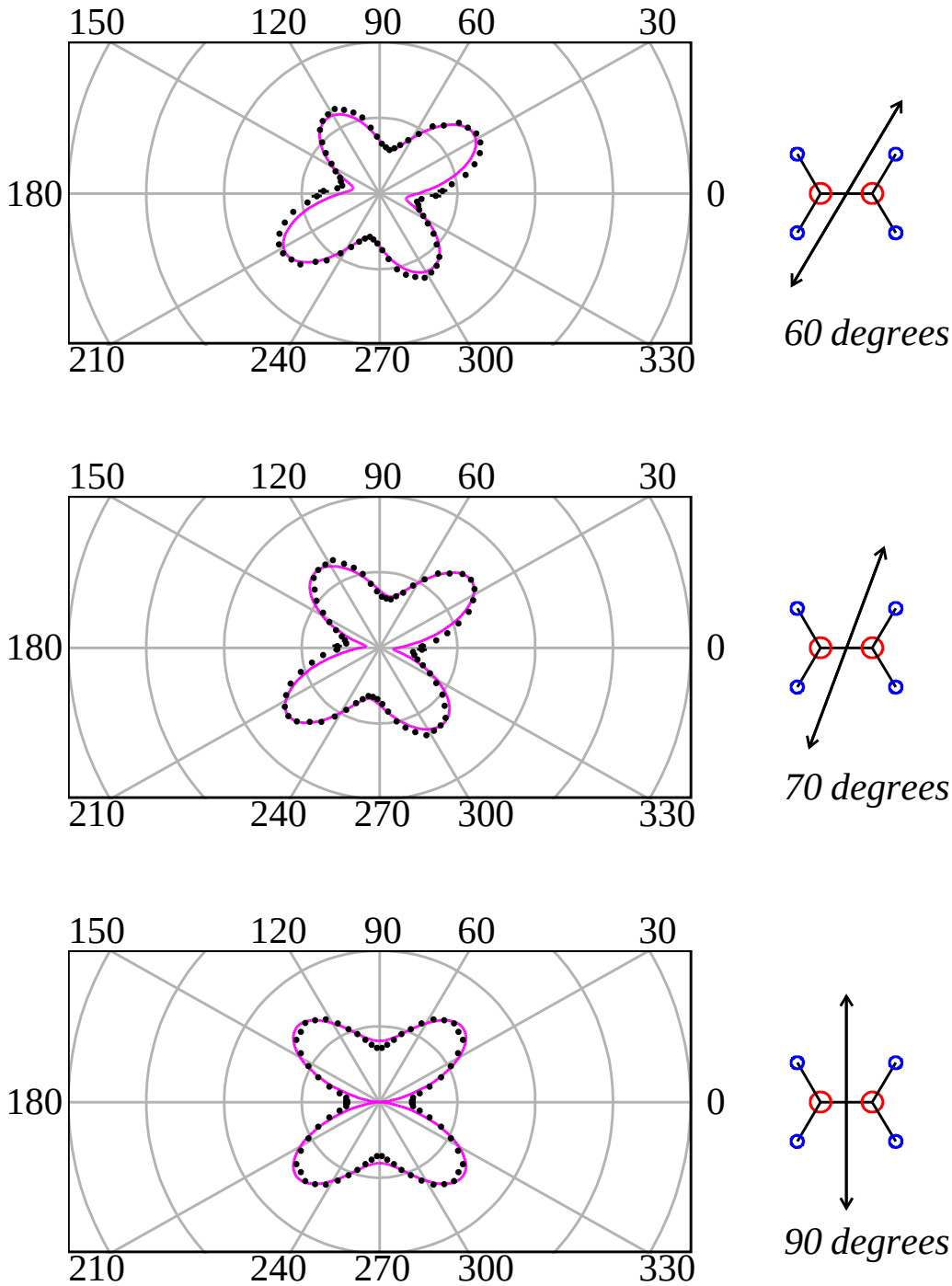

Figure 3.32: Electron Angular Distribution fit at 293eV Photon Energy (section 3). Black arrow shows the direction of the polarization.

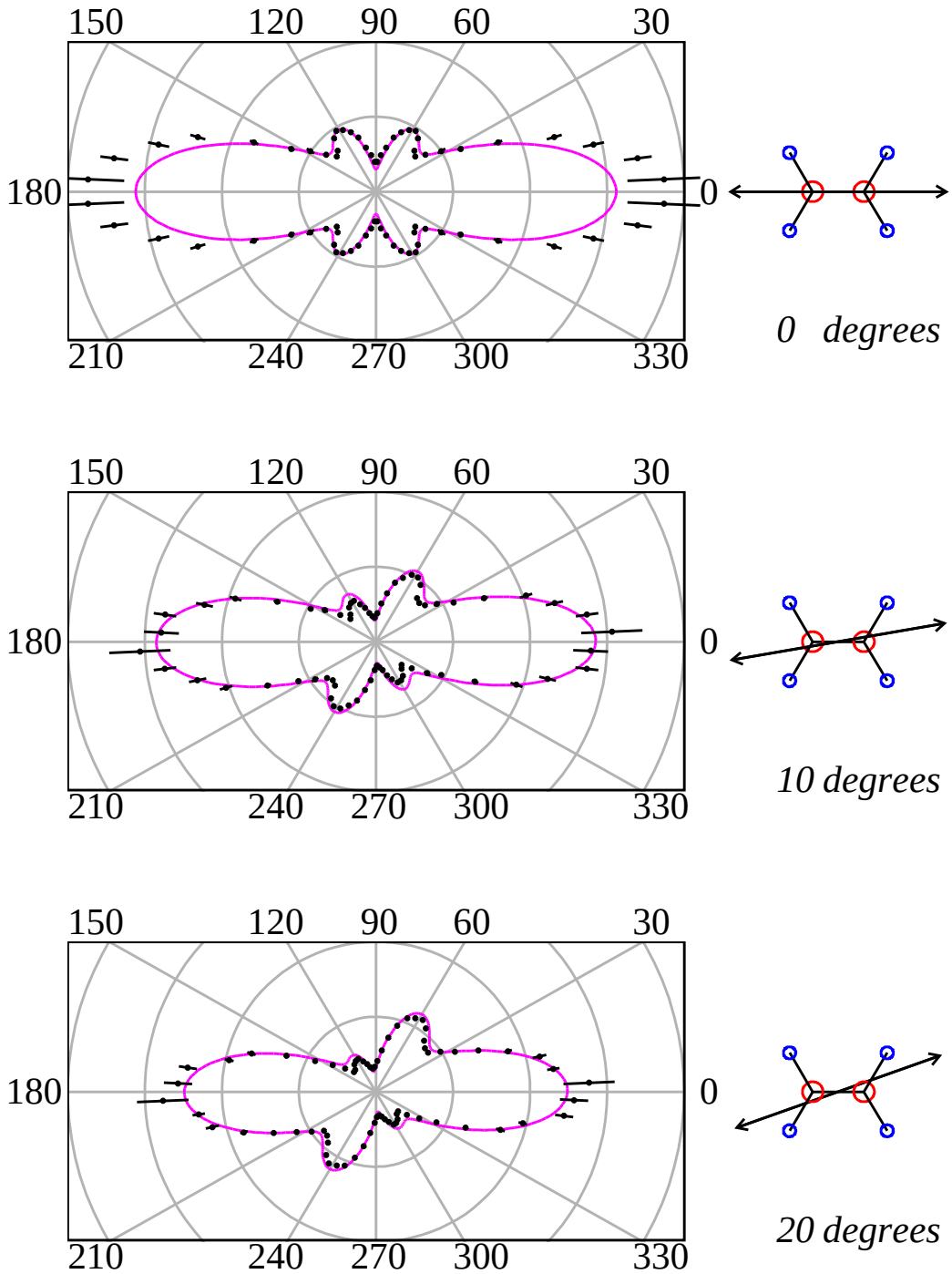

Figure 3.33: Electron Angular Distribution fit at 302eV Photon Energy (section 1). Black arrow shows the direction of the polarization.

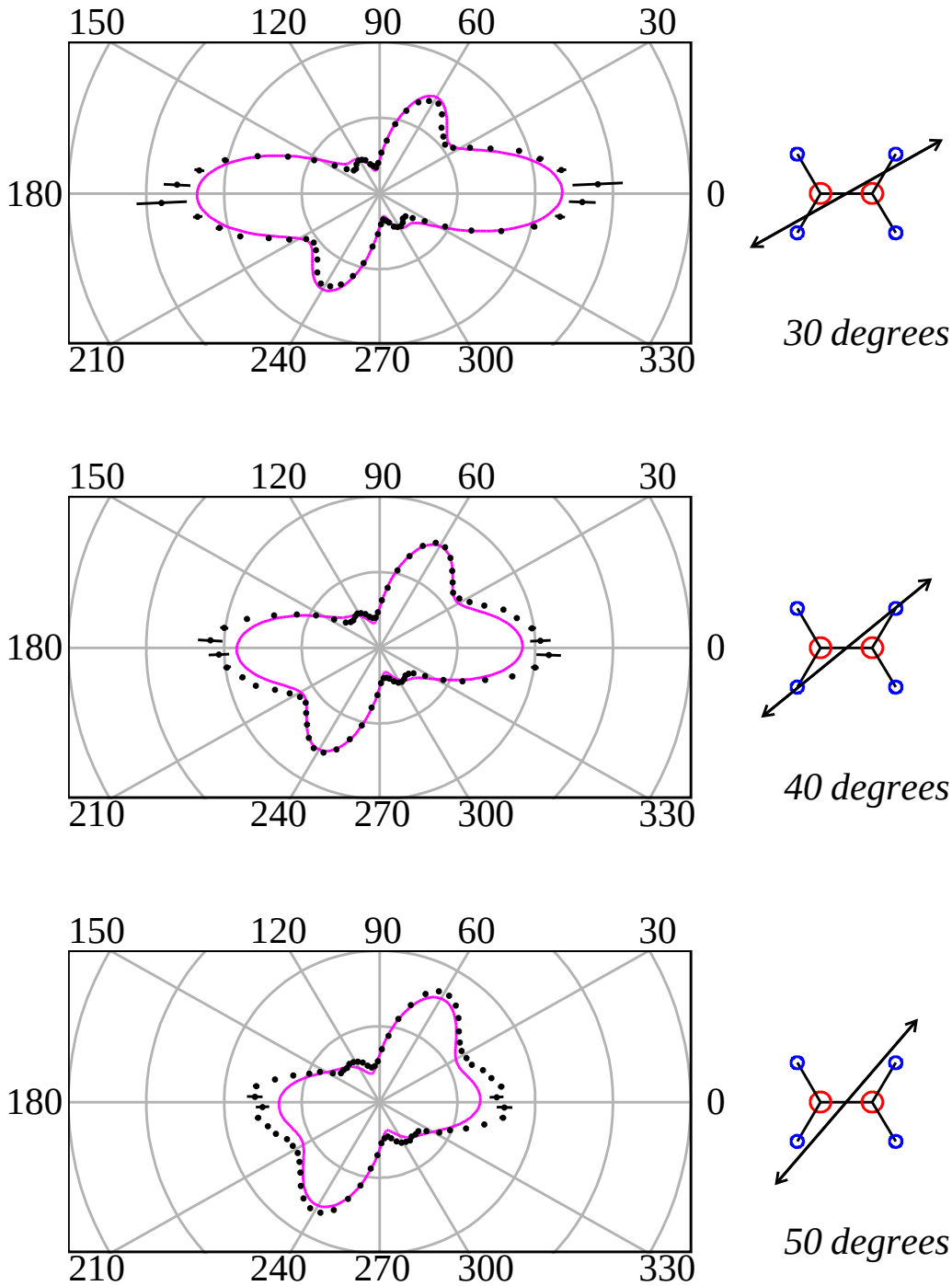

Figure 3.34: Electron Angular Distribution fit at 302eV Photon Energy (section 2). Black arrow shows the direction of the polarization.

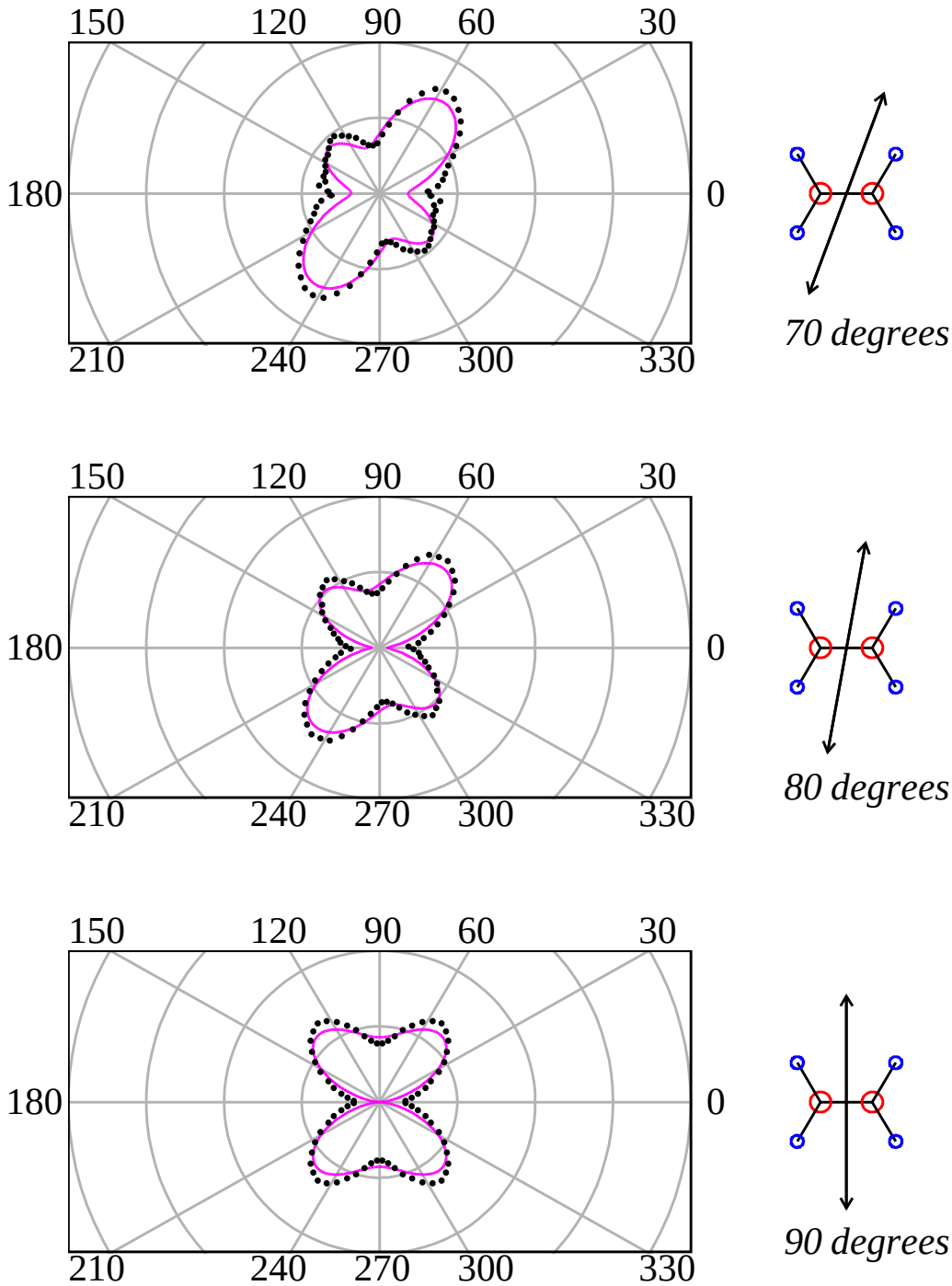

Figure 3.35: Electron Angular Distribution fit at 302eV Photon Energy (section 3). Black arrow shows the direction of the polarization.

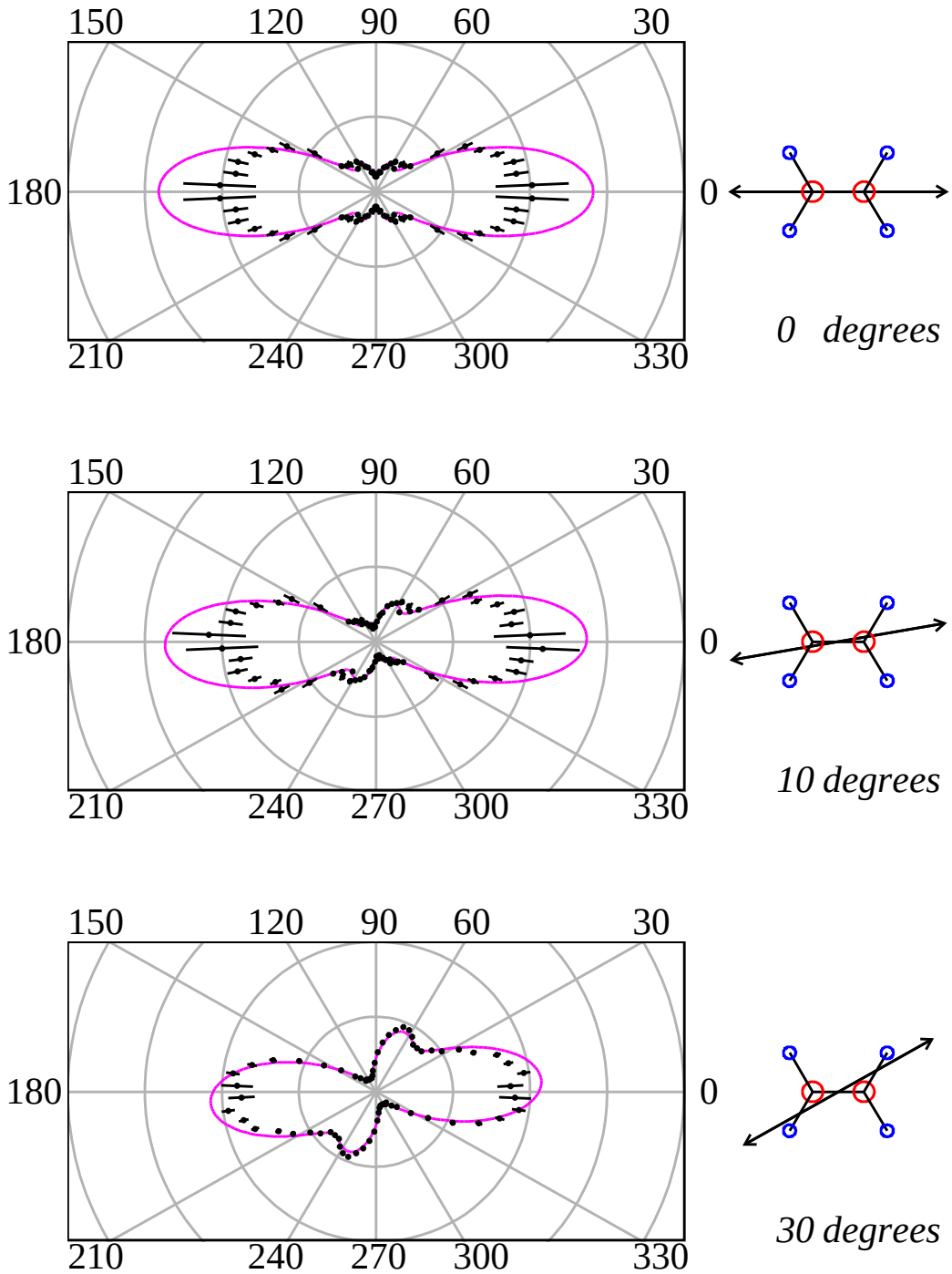

Figure 3.36: Electron Angular Distribution fit at 315eV Photon Energy (section 1). Black arrow shows the direction of the polarization.

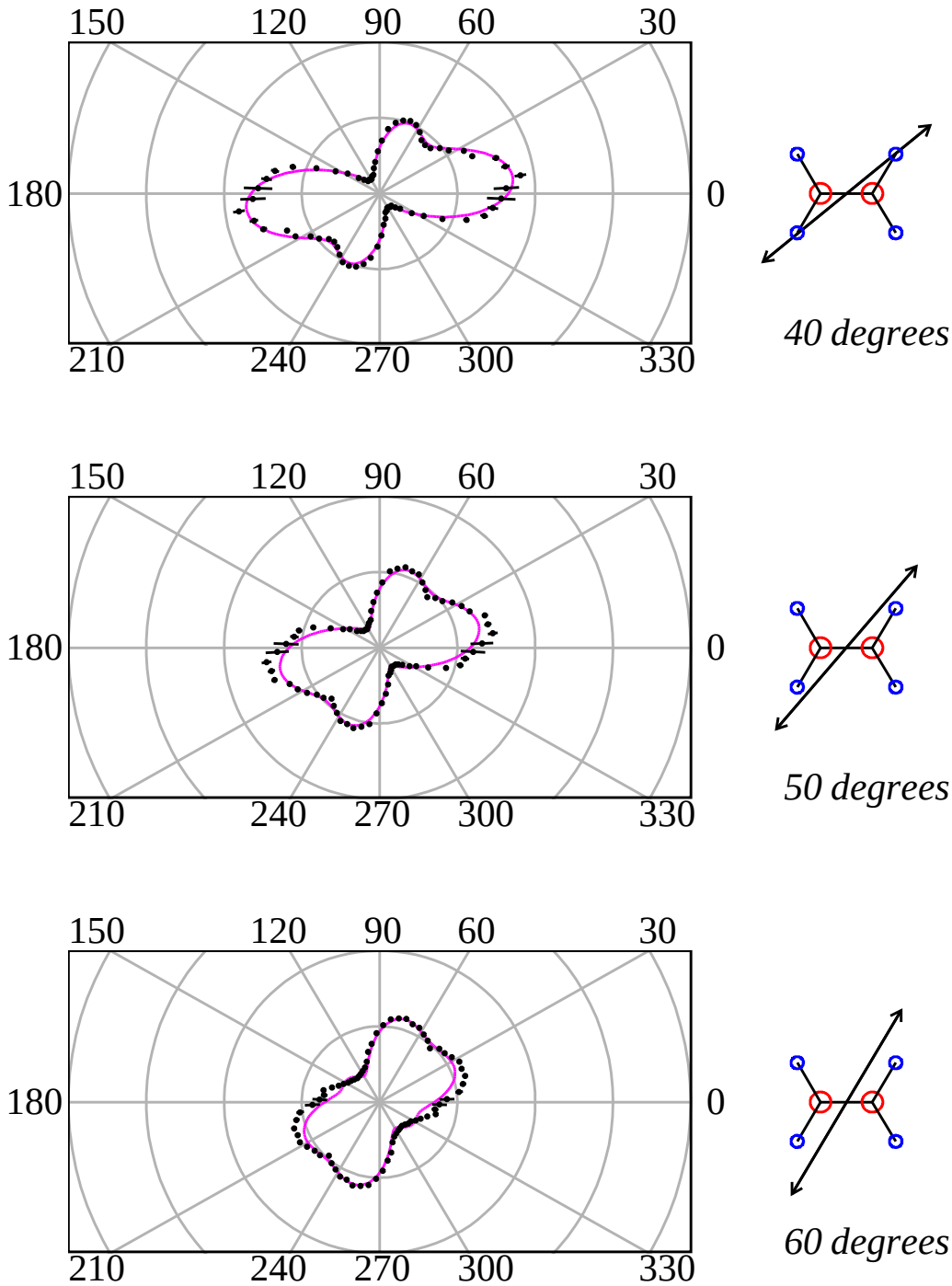

Figure 3.37: Electron Angular Distribution fit at 315eV Photon Energy (section 2). Black arrow shows the direction of the polarization.

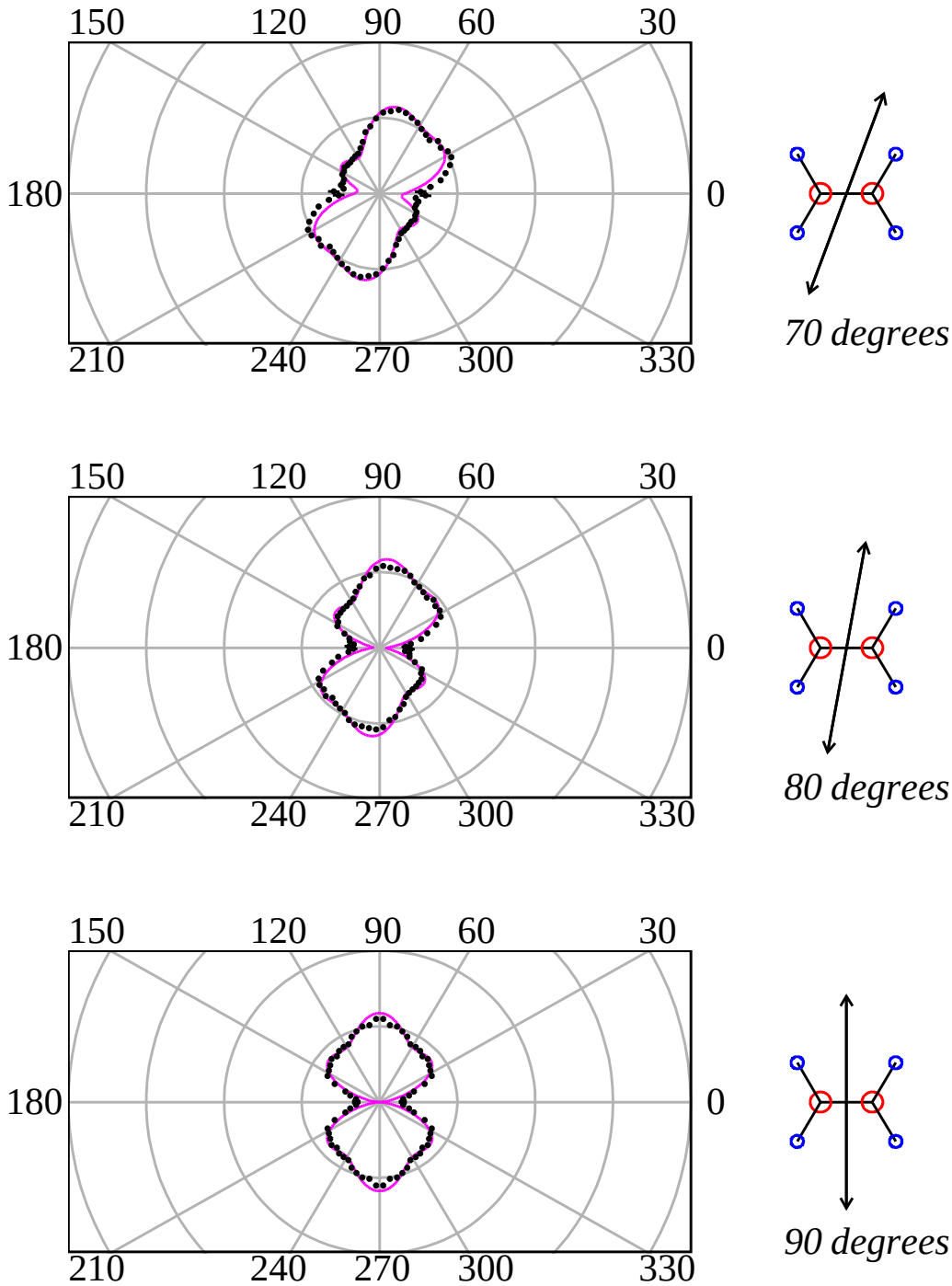

Figure 3.38: Electron Angular Distribution fit at 315eV Photon Energy (section 3). Black arrow shows the direction of the polarization.

of resulting amplitudes can also be found in Appendix G.

The absolute cross-section data can be used together with σ_σ over σ_π information to get absolute values for the σ and π contributions.

$$\begin{cases} f(h\nu) = \sigma + \pi \\ g(h\nu) = \sigma/\pi \end{cases} \Rightarrow \begin{cases} \sigma = \frac{f(h\nu)g(h\nu)}{1+g(h\nu)} \\ \pi = \frac{g(h\nu)}{1+g(h\nu)} \end{cases}$$

The results of this conversion are presented in the figure 3.44 that indicates a definite peak in the σ cross section. Figure 3.45 also shows the theoretically calculated cross sections for comparison.

These calculations were performed by Dr. Mauro Stener[6]. The agreement of the σ cross sections is almost perfect and the π cross sections qualitatively very similar but seem to have a constant shift. The theoretical calculations also include the photoelectron angular distributions. Figures 3.46 – 3.54 present the results on top of the experimental data for three different photon energies around the expected position of the f-wave resonance.

The total cross sections were used for normalizing the absolute value of the amplitudes, see fig. 3.55. Figure 3.56 shows the comparison of the f-wave amplitude obtained from different fitting conditions — it is clear that the amplitude does not vary much from fit to fit. The very well pronounced peak around the 300eV photon energy definitely supports the σ^* C–C resonance idea in ethylene.

Intuitively, another sign of the resonance might be a phase shift of π across the resonance for the f-wave amplitude. The information about the absolute phase of the amplitude cannot be extracted from the fit. The only way to observe this shift is to measure the phase with

[6]Dipartimento di Scienze Chimiche, Universita' di Trieste, Italy., Private communications(2002–2003)

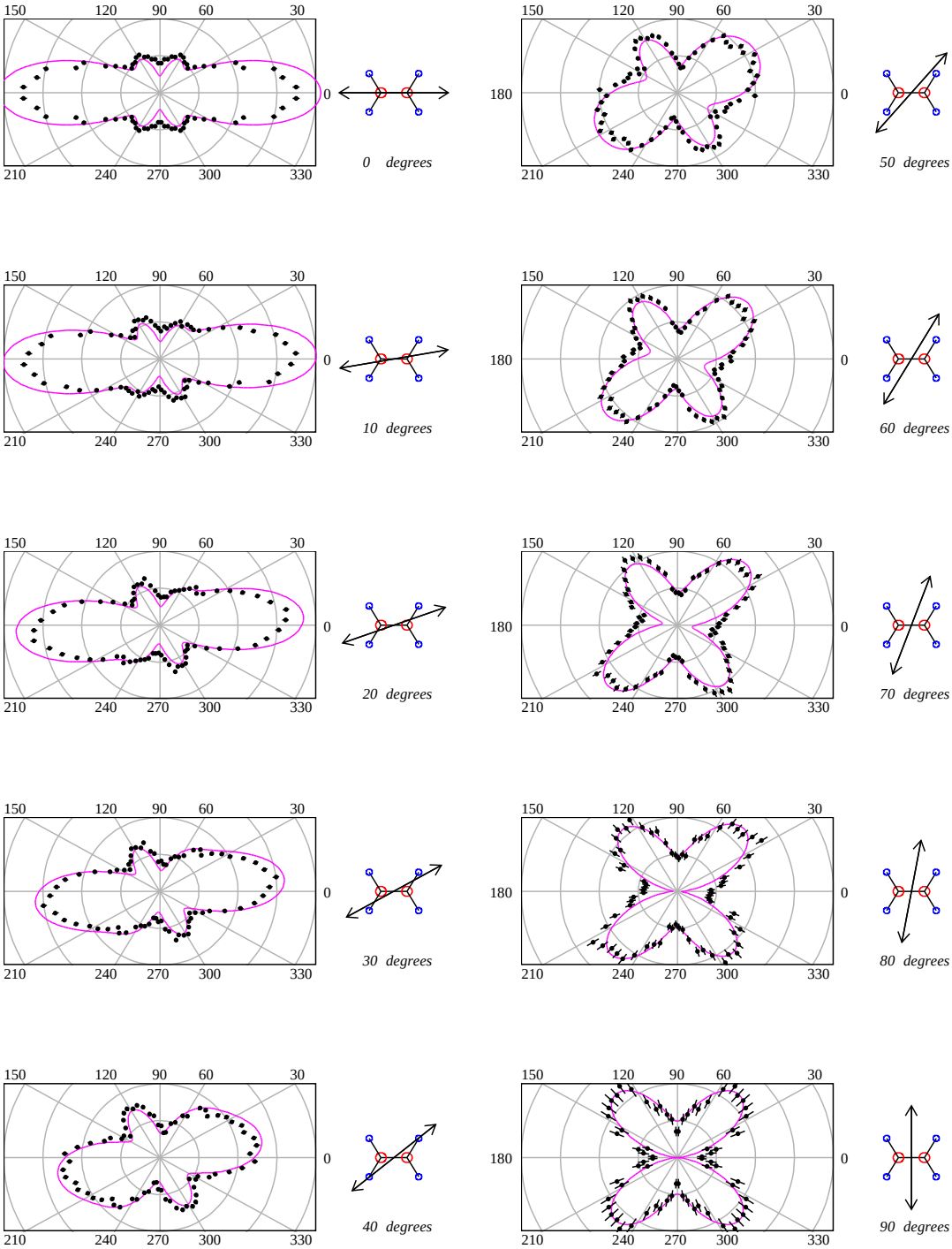

Figure 3.39: $f(\theta, 0, \theta')$ Angular Distribution Fit for 295eV Circular Light. Black arrow shows the direction of the polarization.

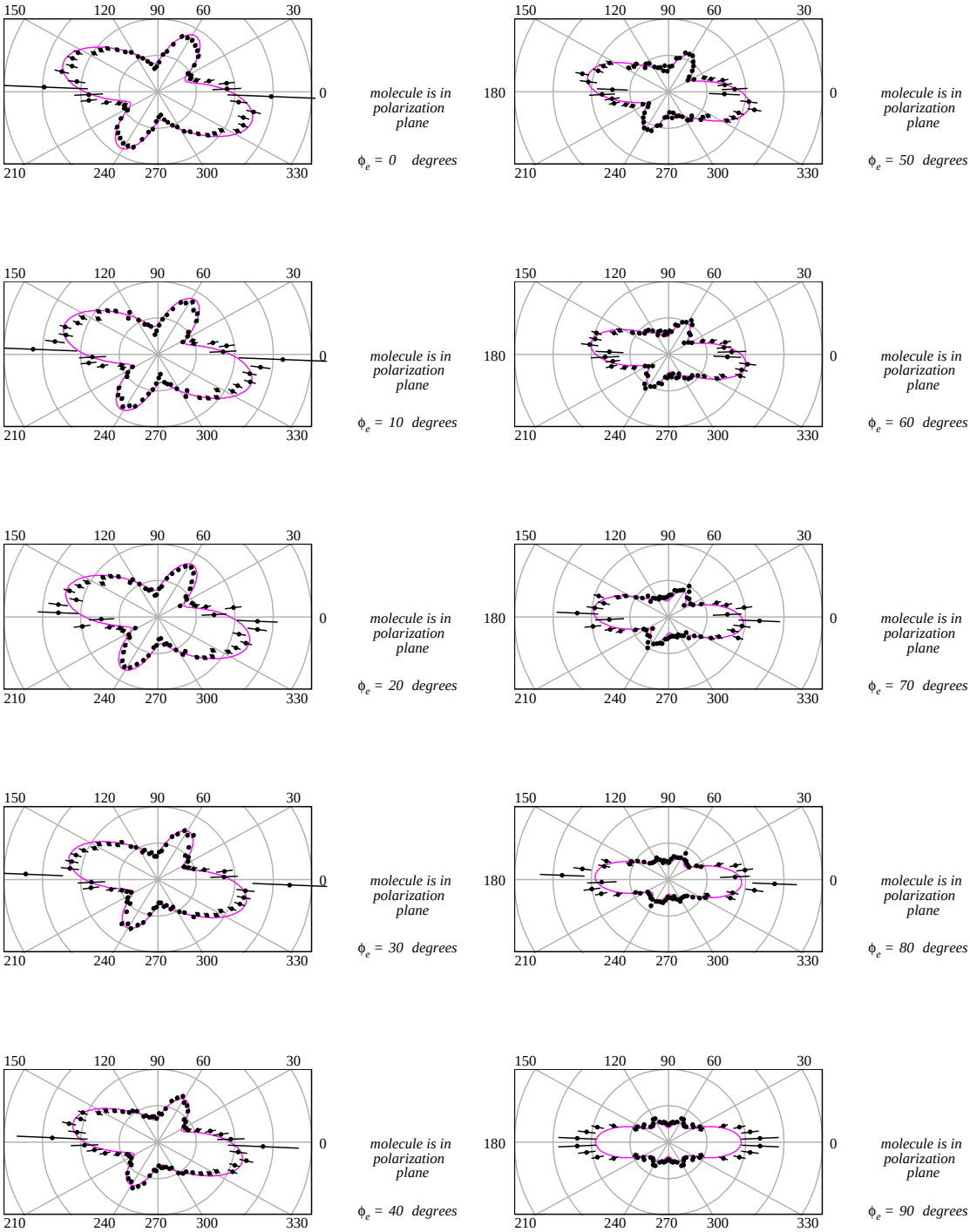

Figure 3.40: $f(\theta, \phi, 0)$ Angular Distribution Fit for 295eV Circular Light

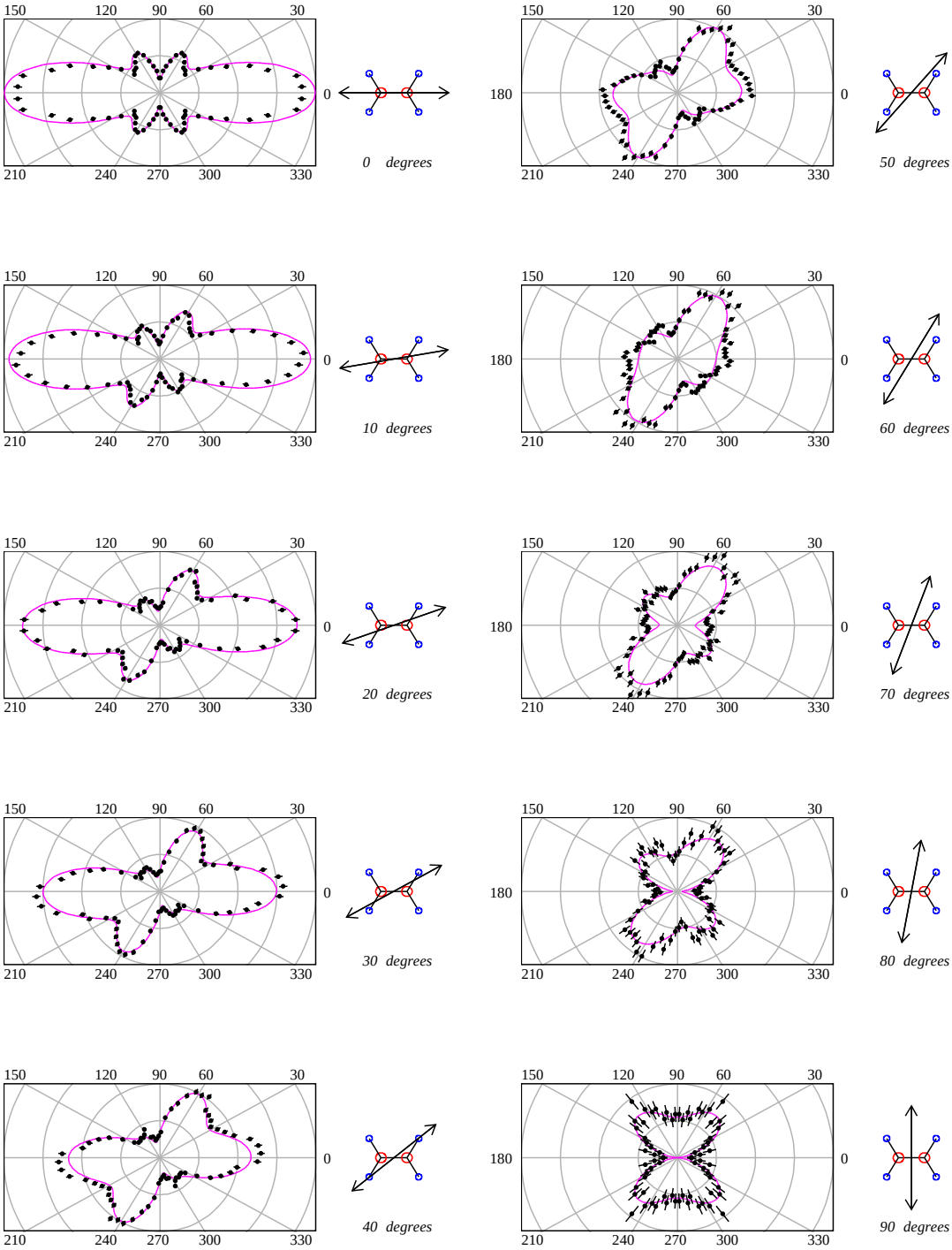

Figure 3.41: $f(\theta, 0, \theta')$ Angular Distribution Fit for 302eV Circular Light. Black arrow shows the direction of the polarization.

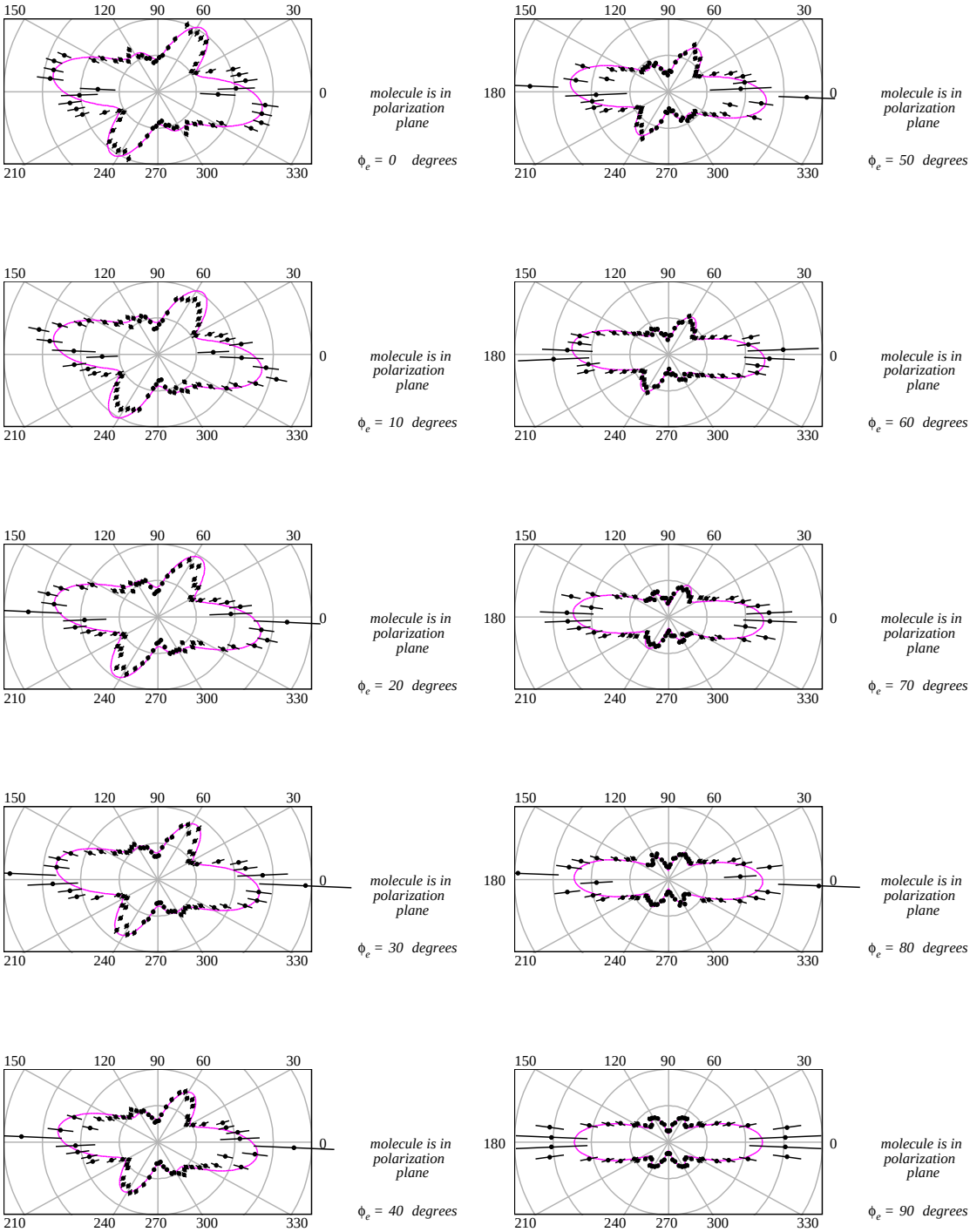

Figure 3.42: $f(\theta, \phi, 0)$ Angular Distribution Fit for 302eV Circular Light

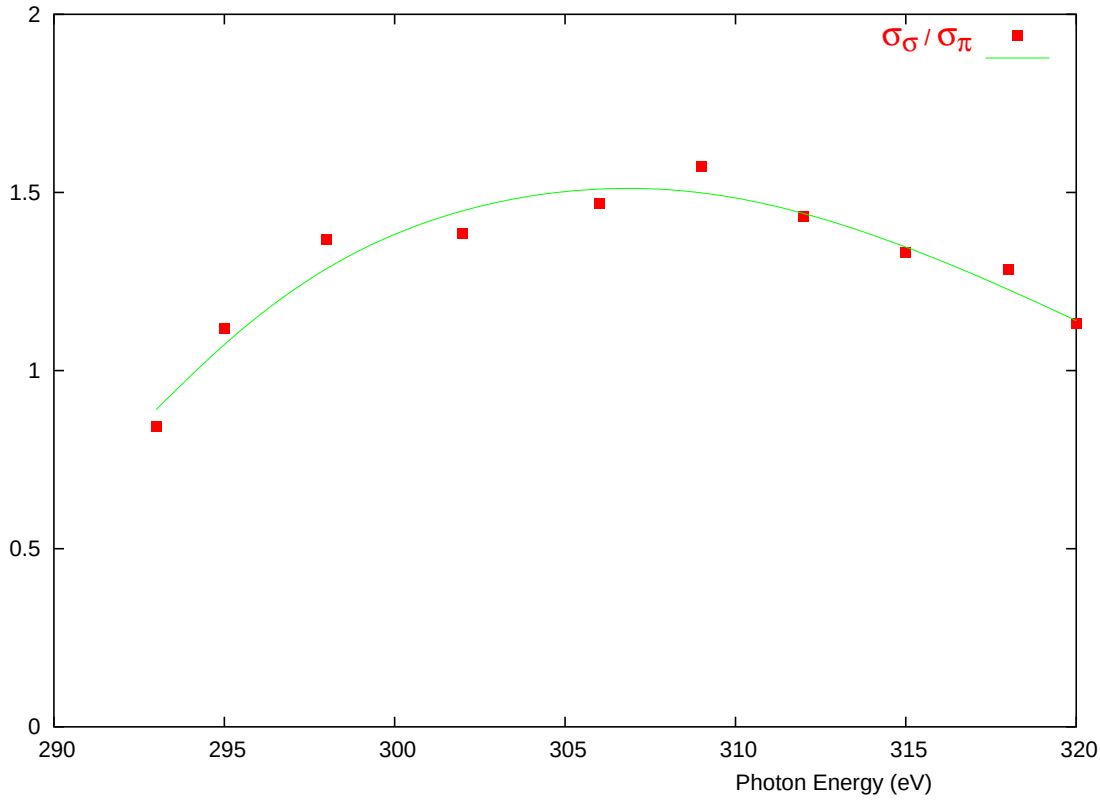

Figure 3.43: Ratio of the σ Cross Section to the π Cross Section for the Core Electron Photoionization of the Ethylene Molecule.

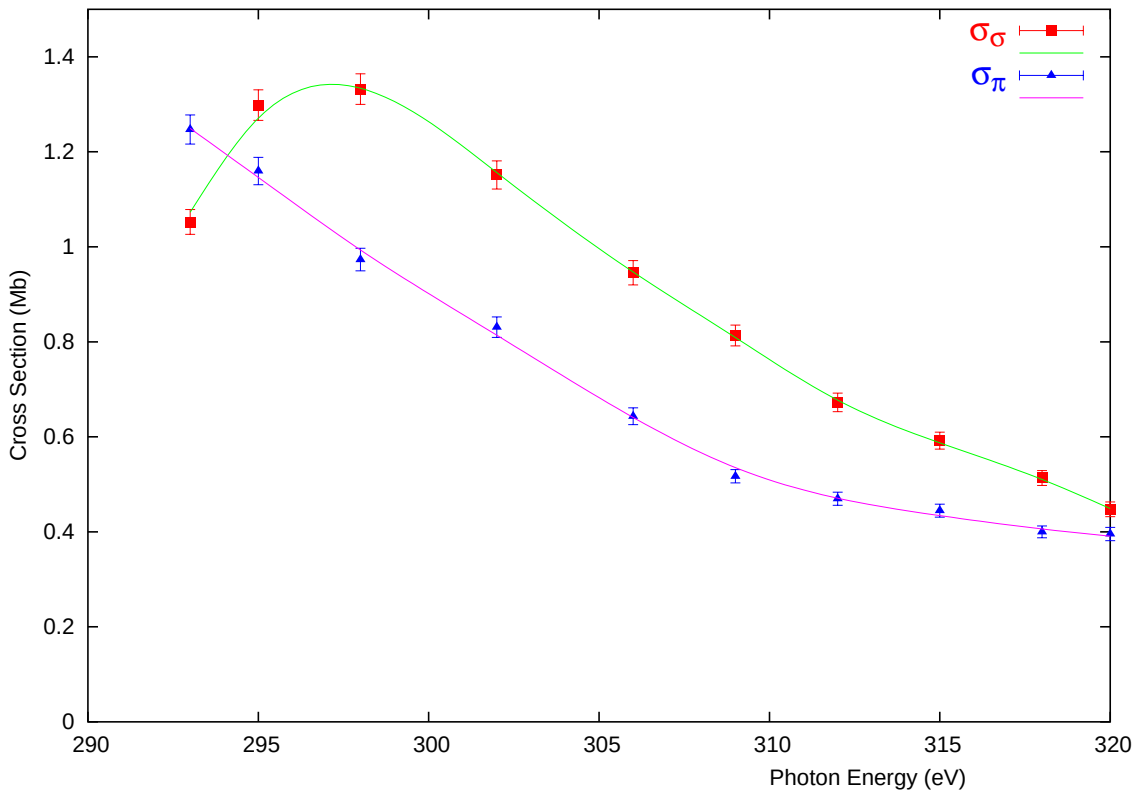

Figure 3.44: Absolute Values of the σ and π Cross Sections

respect to the complex amplitude of a spherical harmonic that is known to have no resonant behavior in the region of the photon energies involved. It is established that the π cross section has no resonances in this region and so any of the partial waves that contribute in it should not have one either. Measuring the phase of the A_3 with respect to the B_3 cannot be very reliable since the $Y_{3-1}(\theta)$ contribution is weak and using it causes high error bars in determining its phase. On the other hand, the amplitude of the B_1 derived from the fit seems to be reasonably large and stable. Figure 3.57 shows the resulting phase difference between A_3 and B_1 as a function of the photon energy obtained from two separate fitting results. The clear and similar phase shift of approximately π in value is observed. The rest

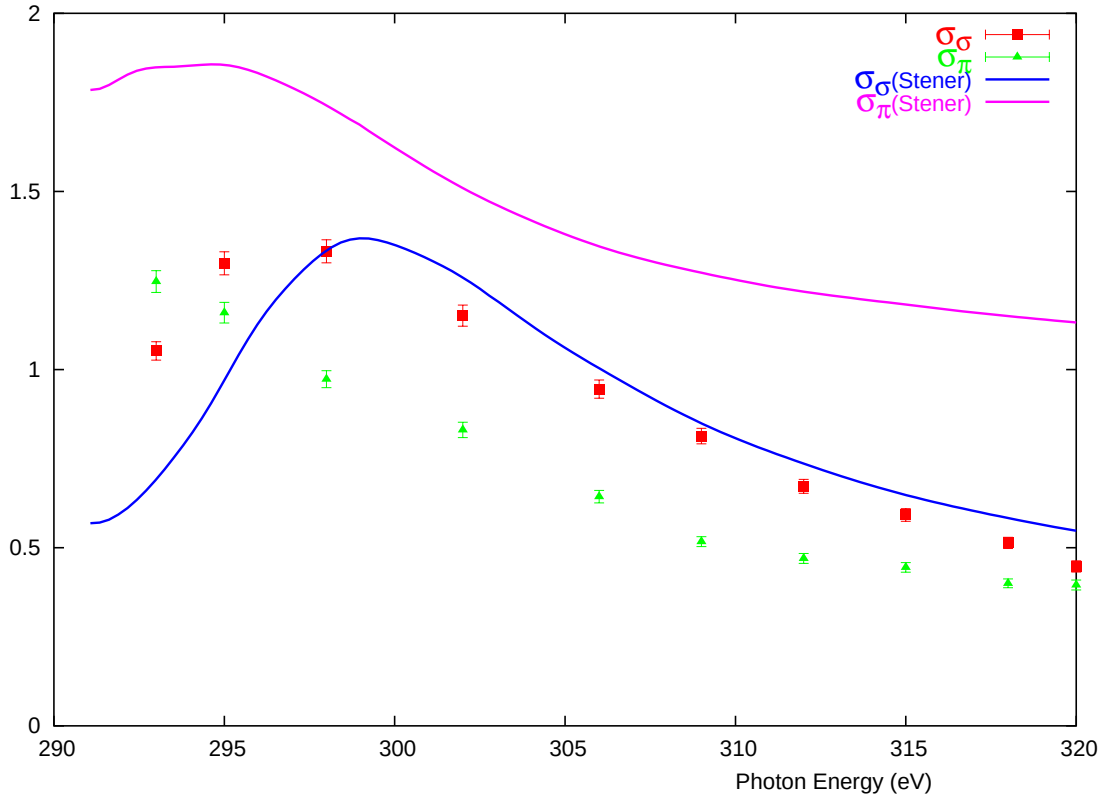

Figure 3.45: Comparison of the σ and π Cross Sections With Theory by Mauro Stener.

of the amplitudes and phase shift differences (due to the *gerade* initial state) obtained in the fitting procedure are shown in figures 3.58, 3.59. The connection between these amplitudes and the total cross section is given by a straightforward relationship:

$$\sigma_{\text{total}} = \sigma_\sigma + \sigma_\pi = \sum_l A_l^2 + \sum_l B_l^2$$

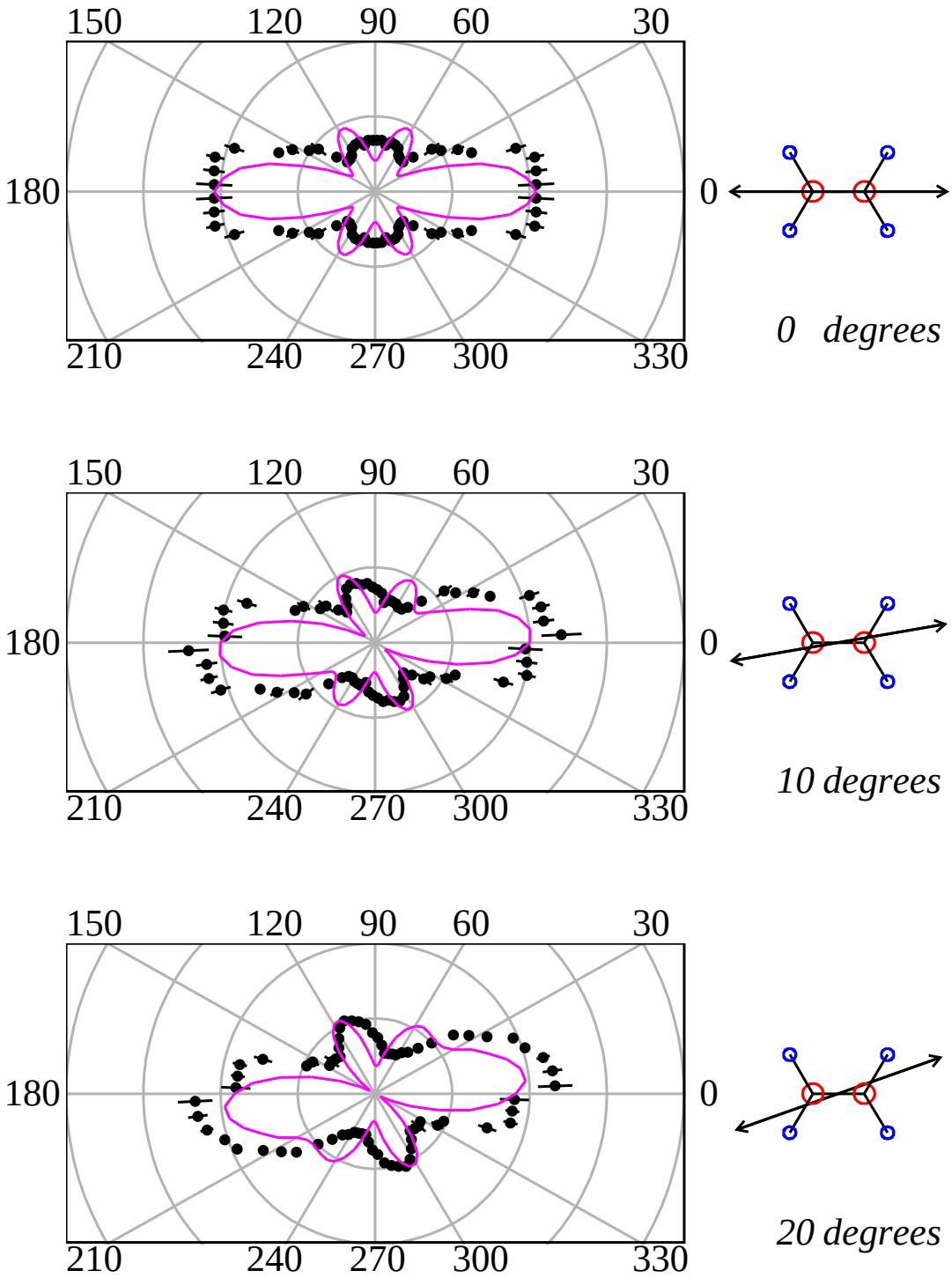

Figure 3.46: C_2H_4 Calculated Angular Distributions for 293eV Photon Energy (part 1)

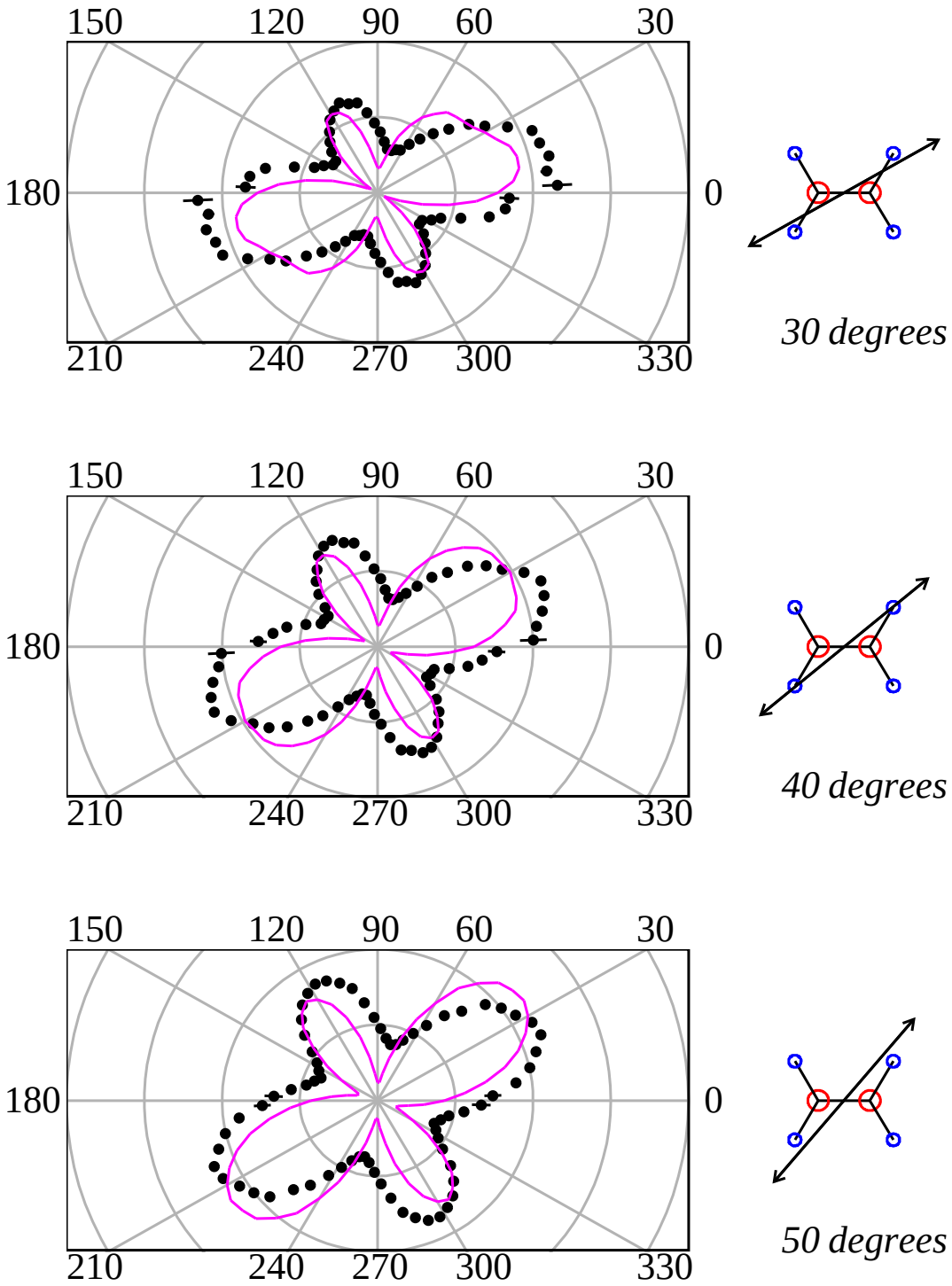

Figure 3.47: C_2H_4 Calculated Angular Distributions for 293eV Photon Energy (part 2)

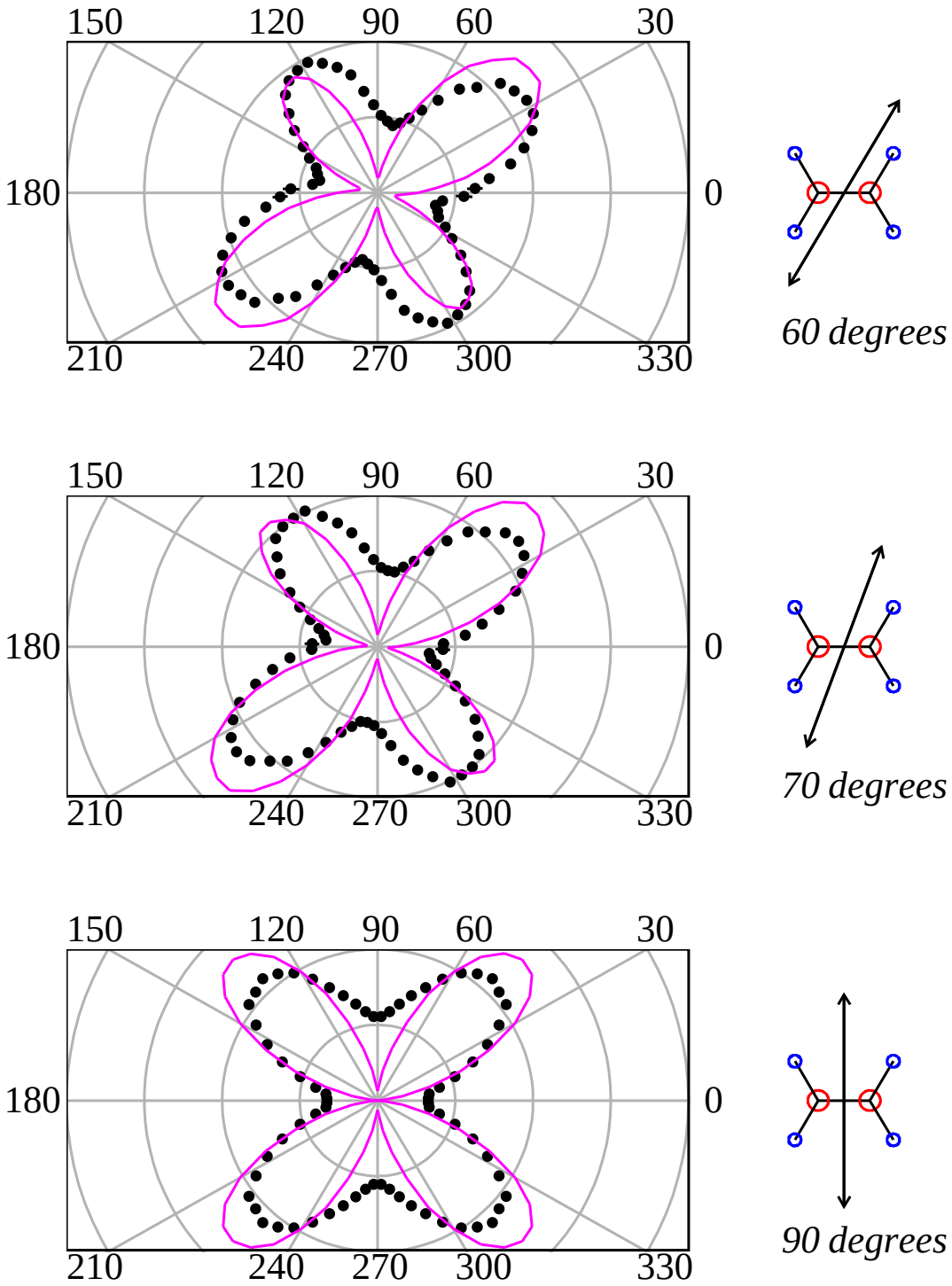

Figure 3.48: C_2H_4 Calculated Angular Distributions for 293eV Photon Energy (part 3)

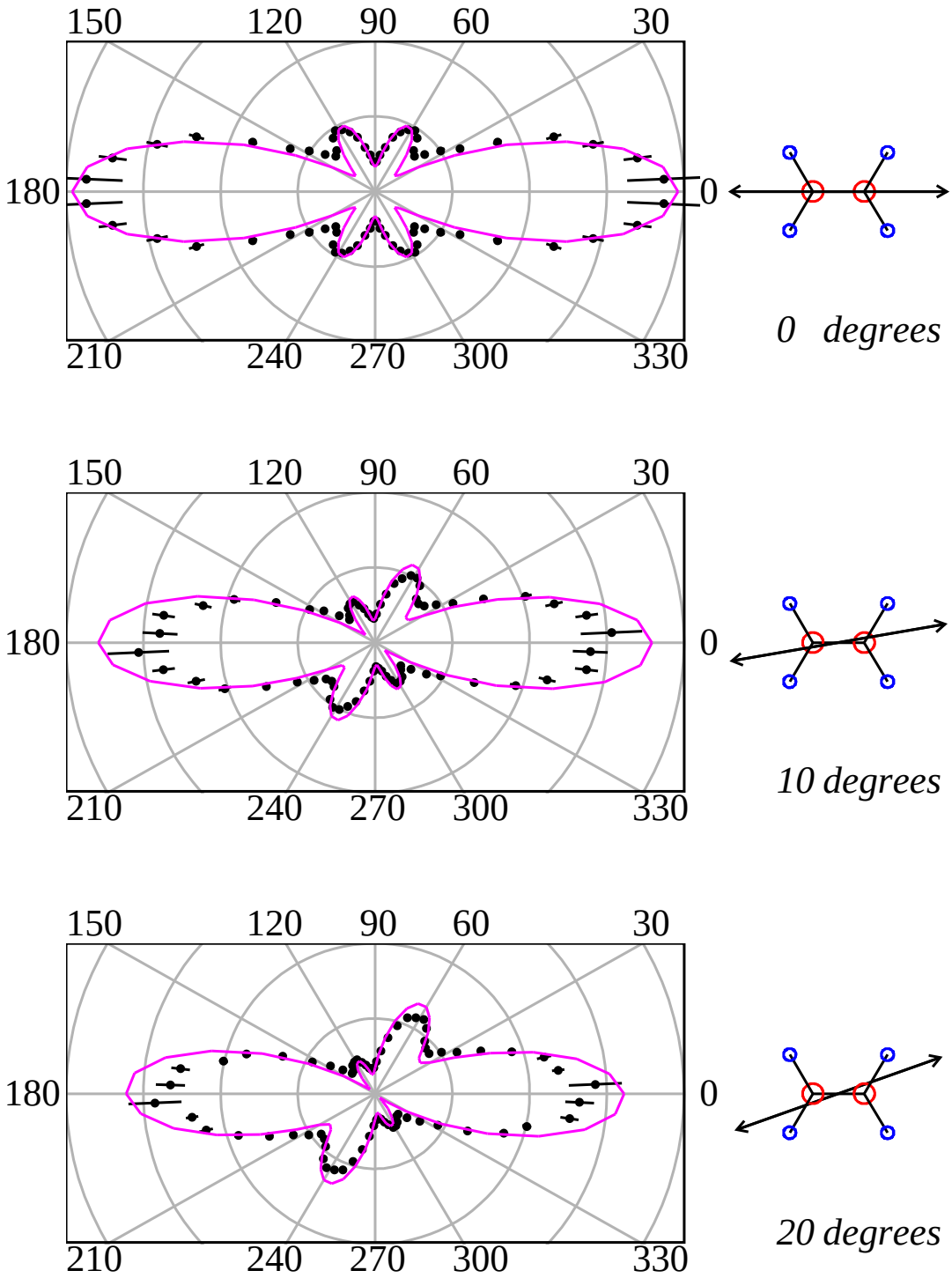

Figure 3.49: C_2H_4 Calculated Angular Distributions for 302eV Photon Energy (part 1)

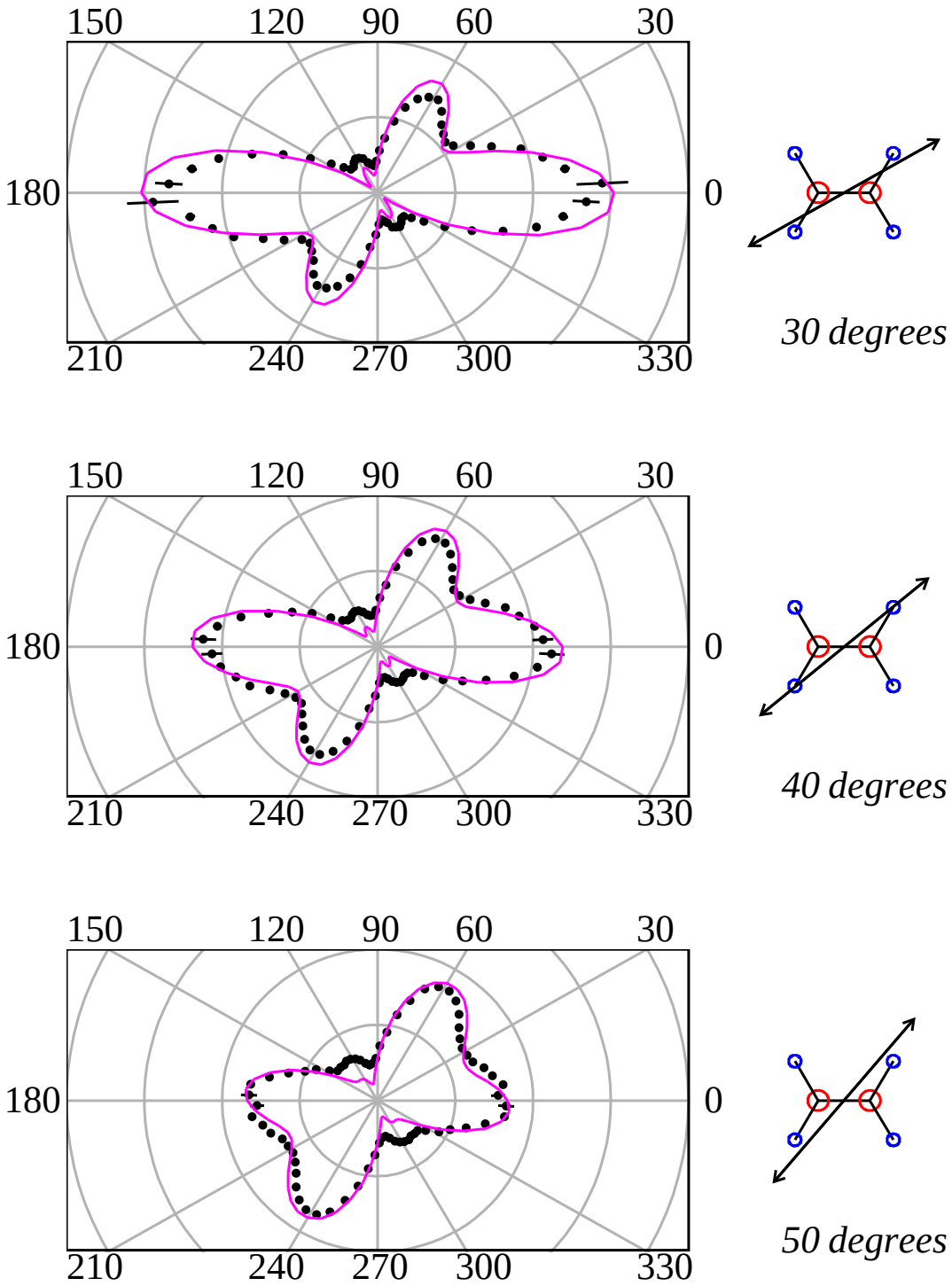

Figure 3.50: C_2H_4 Calculated Angular Distributions for 302eV Photon Energy (part 2)

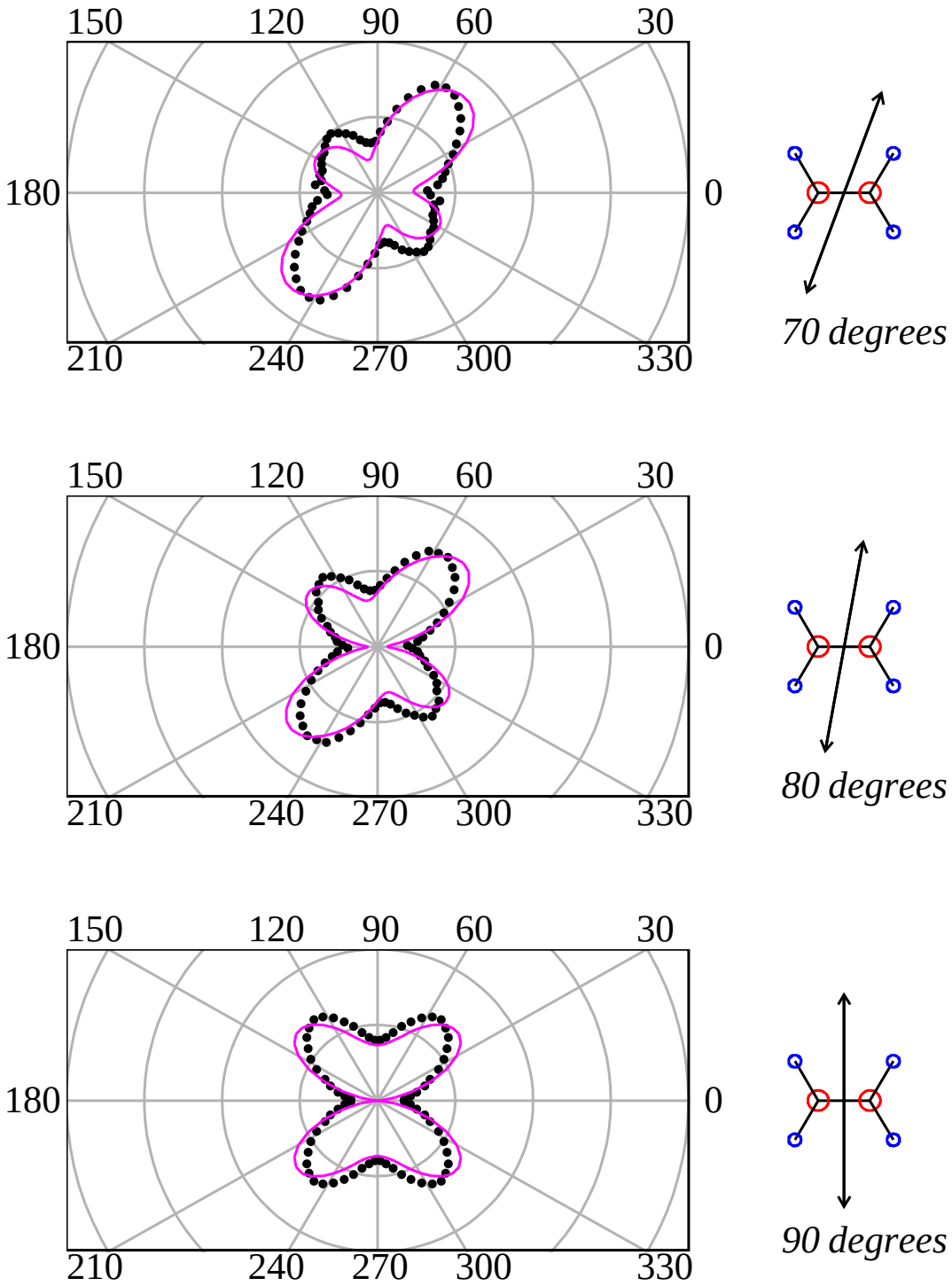

Figure 3.51: C_2H_4 Calculated Angular Distributions for 302eV Photon Energy (part 3)

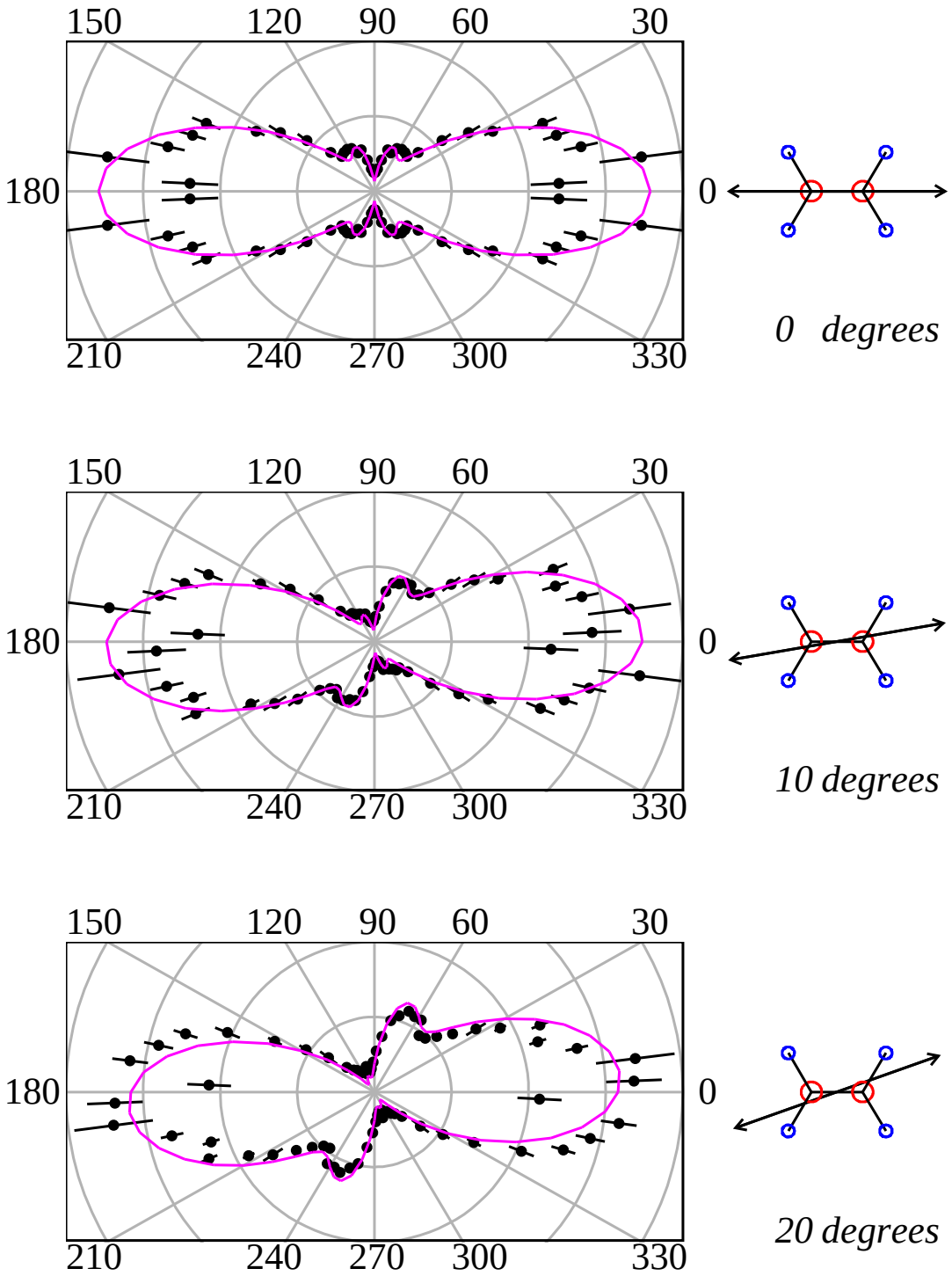

Figure 3.52: C_2H_4 Calculated Angular Distributions for 318eV Photon Energy (part 1)

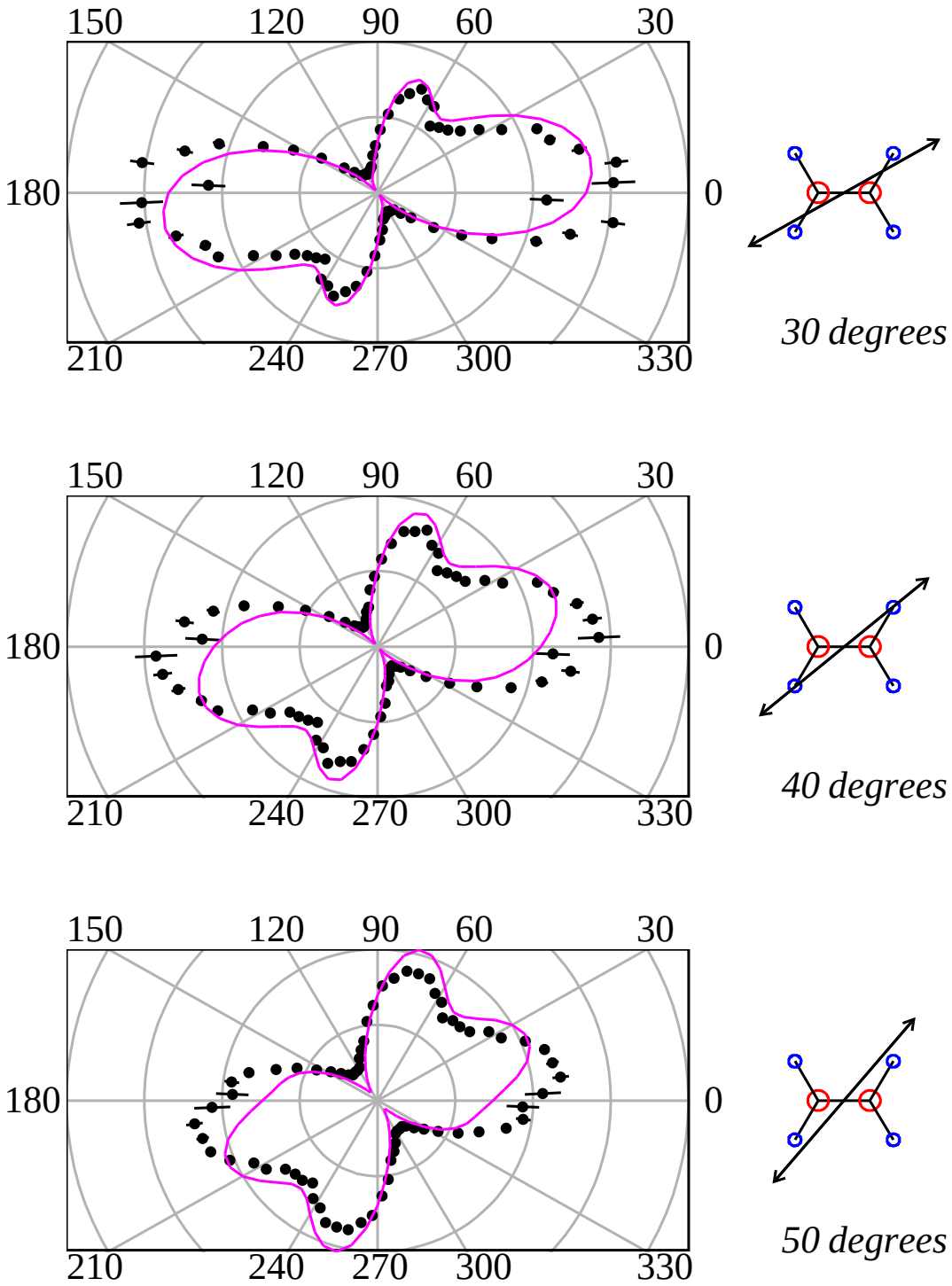

Figure 3.53: C_2H_4 Calculated Angular Distributions for 318eV Photon Energy (part 2)

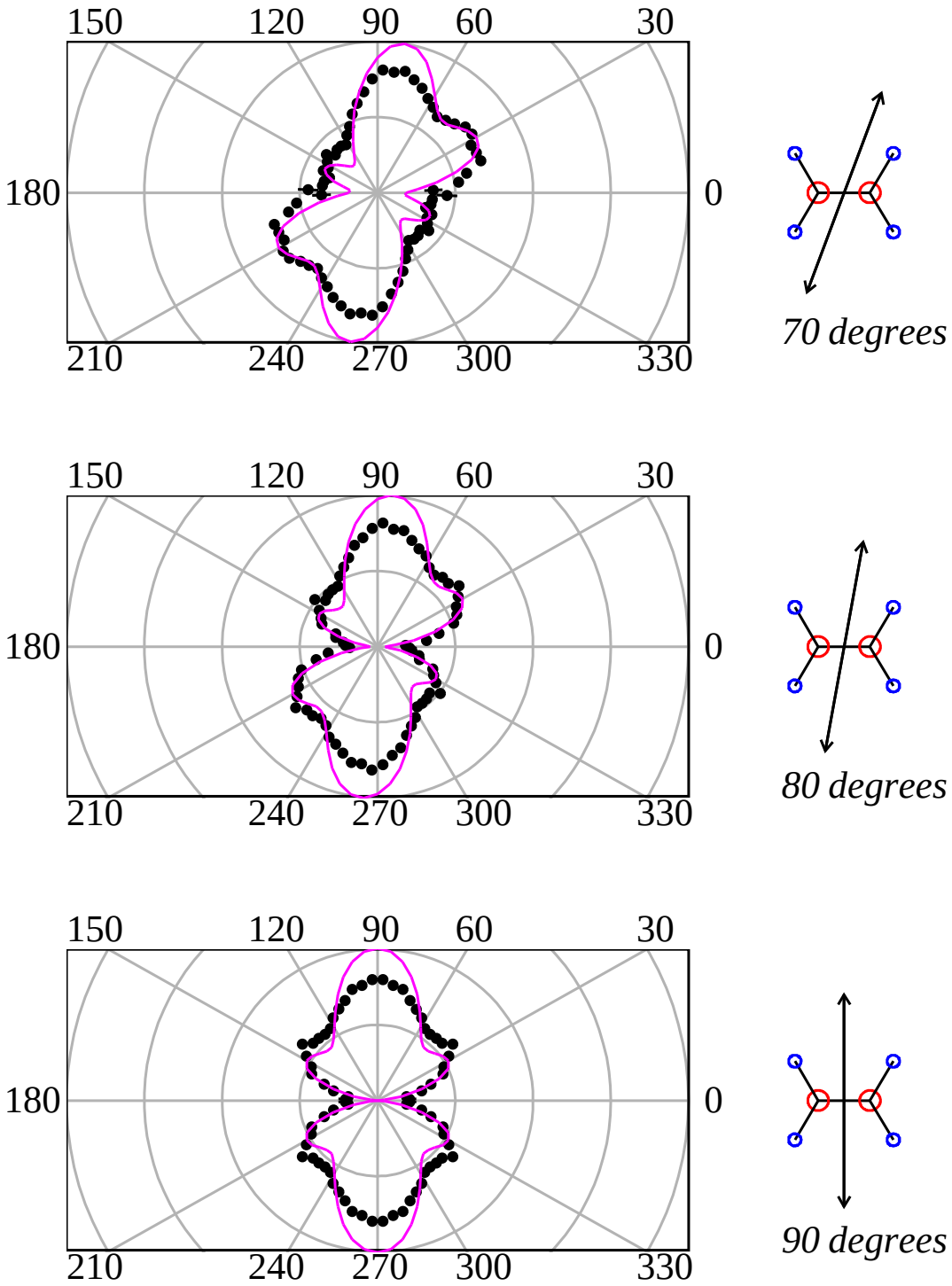

Figure 3.54: C_2H_4 Calculated Angular Distributions for 318eV Photon Energy (part 3)

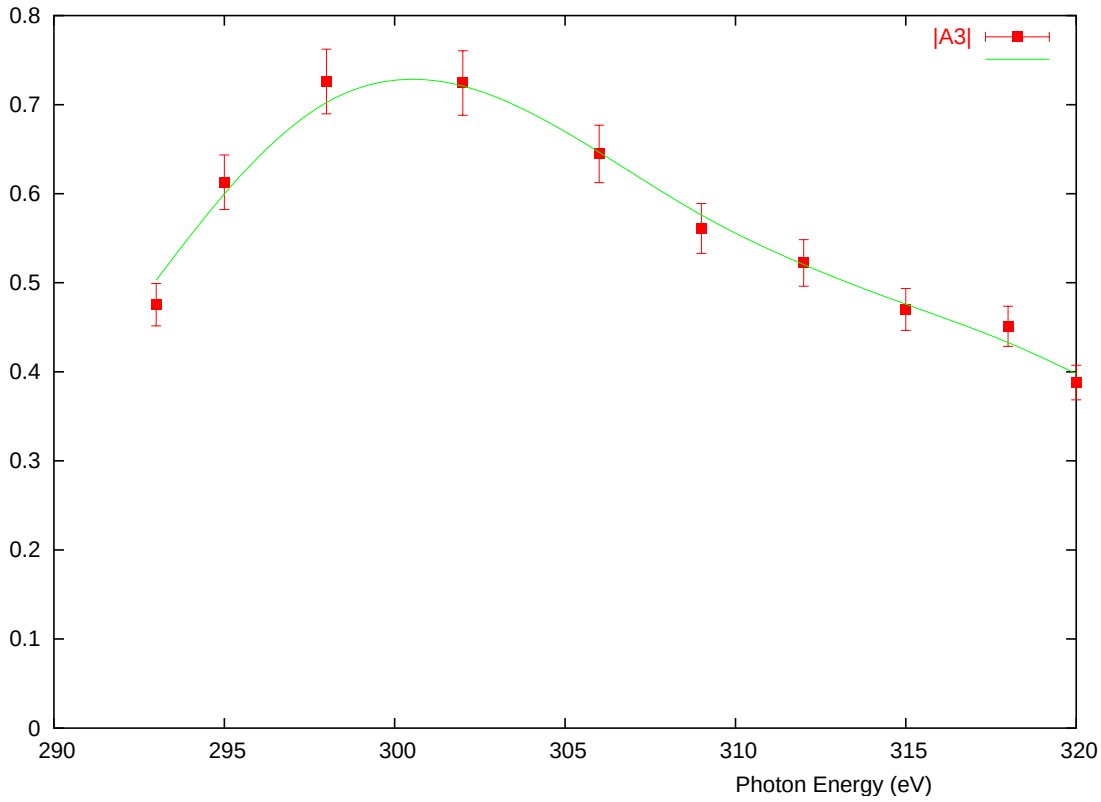

Figure 3.55: Absolute f-wave Amplitude as a Function of the Photon Energy

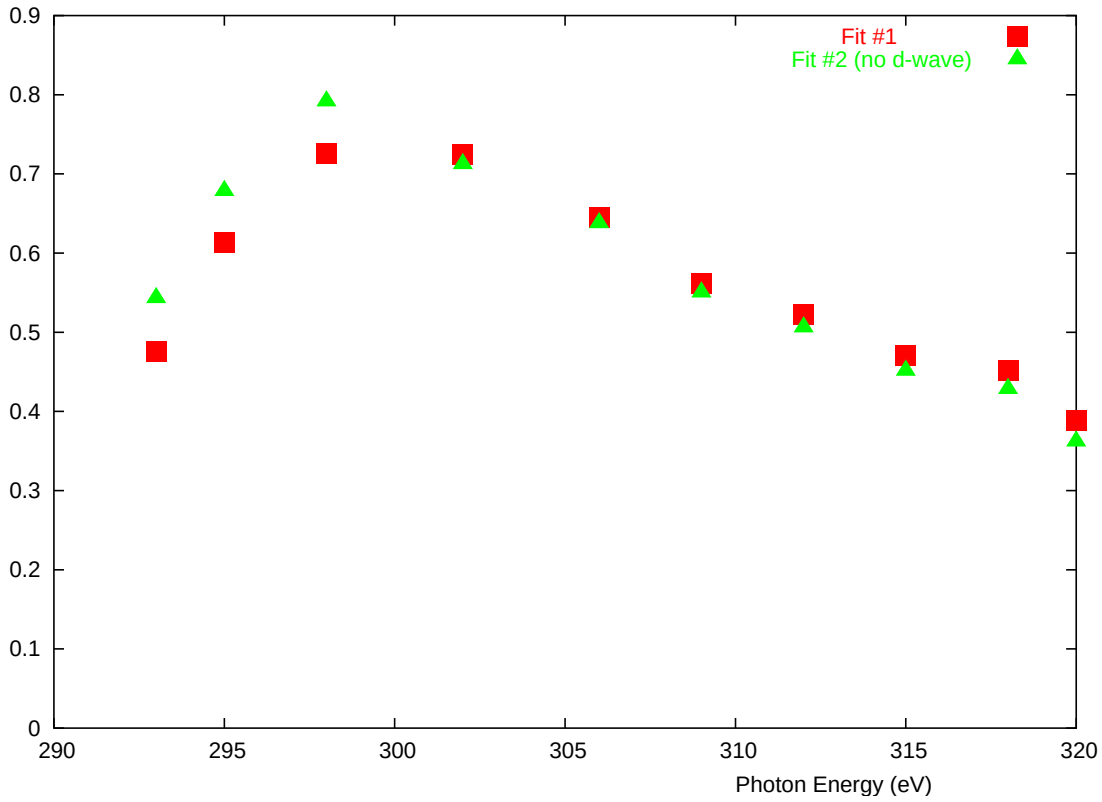

Figure 3.56: Comparison of f-wave Amplitudes from Different Fits

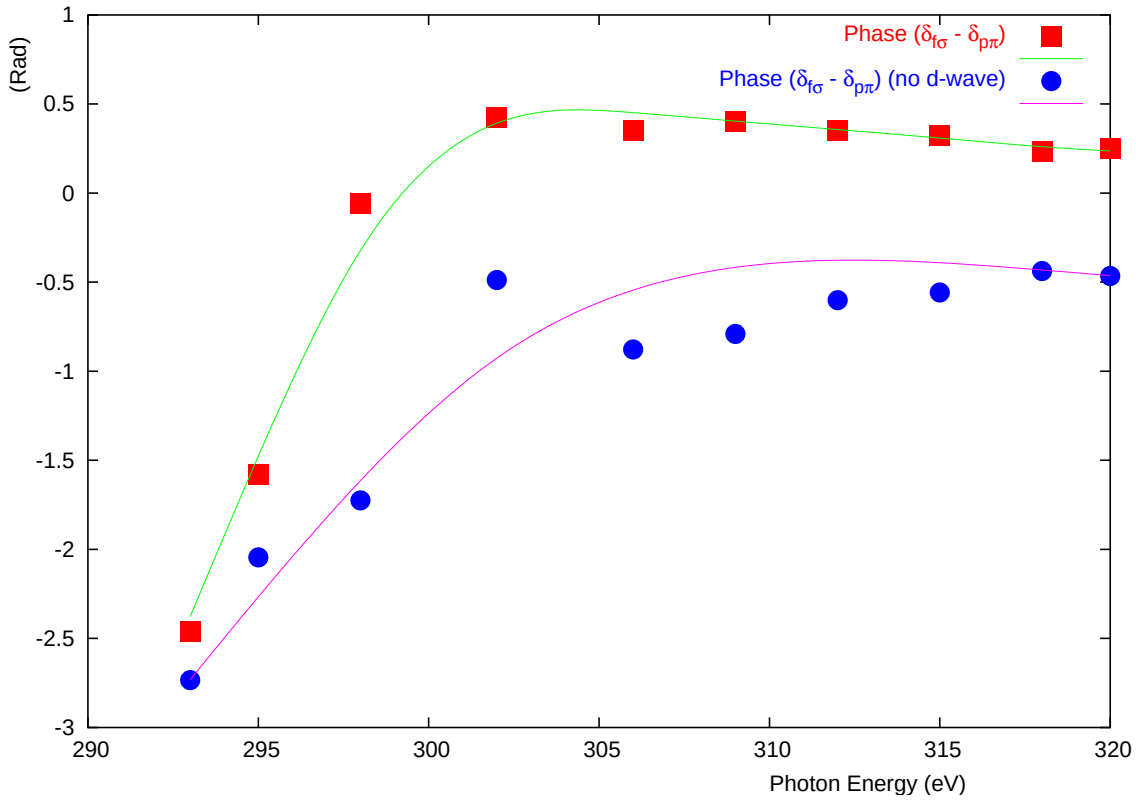

Figure 3.57: Phase difference between A_3 and B_1 Complex Amplitudes Obtained from two different fitting results

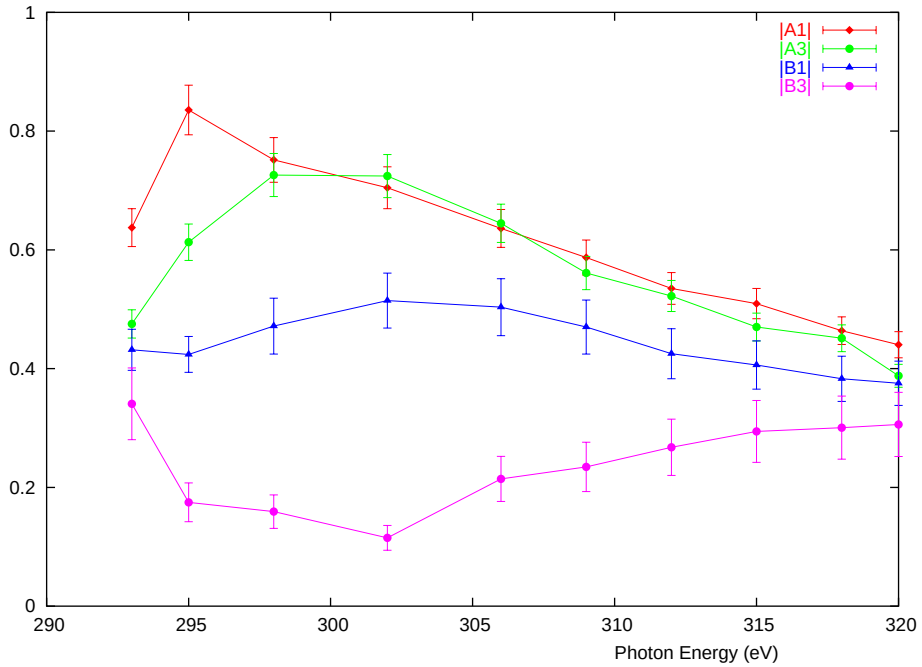

Figure 3.58: Amplitudes of the Partial Waves Contributing to the Total Cross Section due to the *gerade* Initial K-shell Electron State

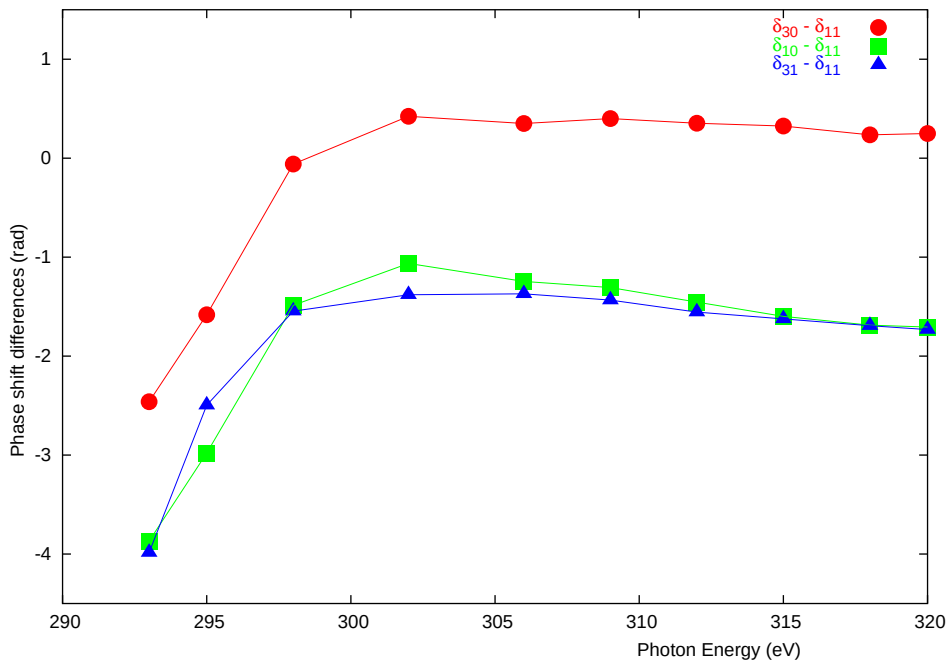

Figure 3.59: Phase Shift Differences of the Partial Waves due to the *gerade* Initial K-shell Electron State

Chapter 4

Electrons as a Clock

One of the most important problems of quantum mechanics is measurement of the time scales for different subatomic reactions and the durations of the numerous processes involved. The time-dependent Schrödinger equation is the basic tool for the theorists and it is often associated with months of computer calculations even for the simplest systems. Whether it is the lifetime of a certain state or a time parameter that describes the dynamics of an atomic or a molecular system, these are not just pure basic research concepts. These are also very important in industry, medicine and even everyday life. The process of carbon dating, for example, has been used by scientists and researchers from many different areas for decades; progress in controlling the duration of a stable nuclear plasma might one day provide us with an abundant and ecologically clean energy source.

Physicists and chemists are always trying to extend measurements and the control of time-dependent processes to shorter and shorter time scales. Recent advances in laser technologies combined with the atomic physics approaches have allowed the monitoring of atomic and molecular processes on a femtosecond time scale (see [19–21]).

The current chapter of this thesis is devoted to a special time–measuring technique. There are many standard approaches to measuring or calculating lifetimes and decay constants for excited states of molecules, atoms and nuclei. On the other hand, experiments that provide real–time information about molecular dynamics, constituent rearrangements and isomerization processes are rare, especially if the studied configuration does not exist in a neutral natural form. A technique that allows measuring the durations of such processes as well as determination of the lifetime of the long lived intermediate state is described next.

4.1 Acetylene/Vinylidene issue

Both acetylene and vinylidene[1] forms of C_2H_2 play very important roles in combustion processes and other organic reaction pathways. The isomerization of the acetylene into vinylidene has been extensively studied (see [22; 23]) for over two decades in both neutral [24–28] and ionic species [29] and for numerous excitation/ionization entrance channels. The species that will be covered in this work are the dications of C_2H_2 molecule in both isomer forms. Doubly charged positive ions of acetylene and vinylidene have been heavily investigated through various means [30–36]. A comprehensive *ab initio* study of the $C_2H_2^{++}$ molecular ion by Duflot *et al.* [37] provided a very detailed interpretation of the photoelectron-photoion-photoion coincidence (PEPIPICO) experimental data [36; 38] and a description of the decay pathways for this isomerization as well as for other photo dissociation channels.

[1] Analyzed data files related to this section can be found in the folder "pawfiles/acetylen" of the attached CD, with the FORTRAN code being in folder "programs".

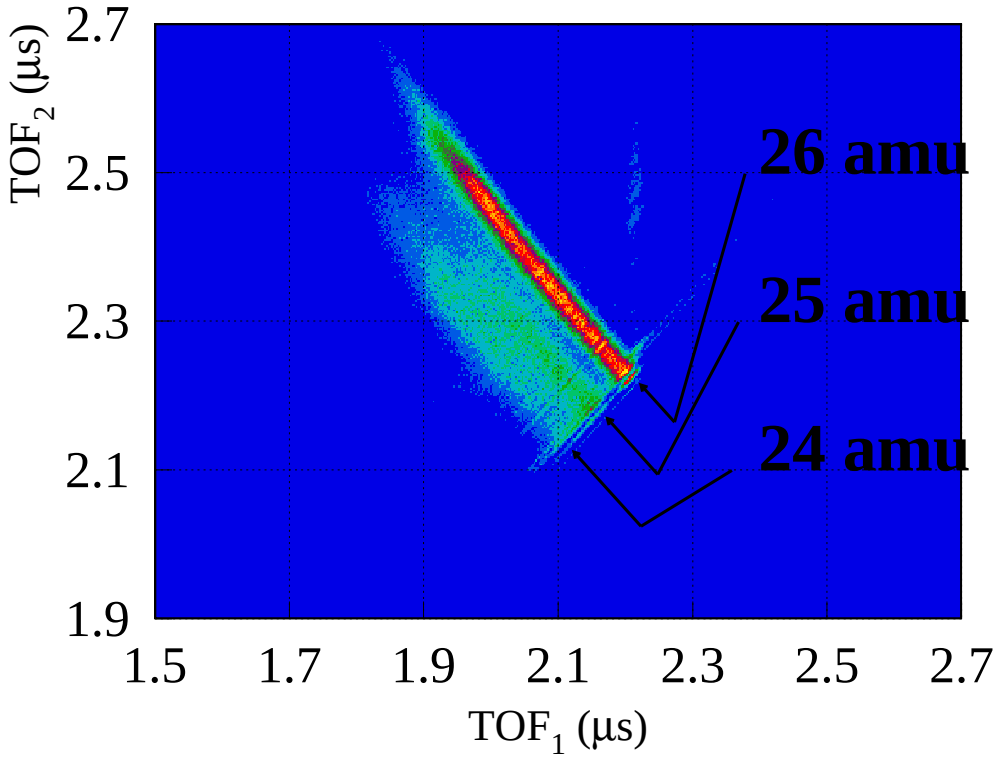

Figure 4.1: PIPICO Spectrum of the Acetylene/Vinylidene Breakup Channels

The production of acetylene and vinylidene dications covered in this work was accomplished through the photoionization of a carbon k-shell electron followed by Auger decay as described in chapter 2. The presence of vinylidene was first discovered (see appendix I) while analyzing strange features of the momentum spectrum of the exploding recoils(see fig. I.1). Note that the PIPICO spectrum for the breakup of the $C_2H_2^{++}$ molecular ion does not clearly show the vinylidene as a separate channel. The separation of the different channels along the diagonal seen in figure 4.1 only works well when the sum of two recoil masses is unique. By determining the fragmentation channel in the case of the vinylidene (V), the total mass (12 a.m.u+14 a.m.u=26 a.m.u.) is the same as that for the acetylene (A). Ideally

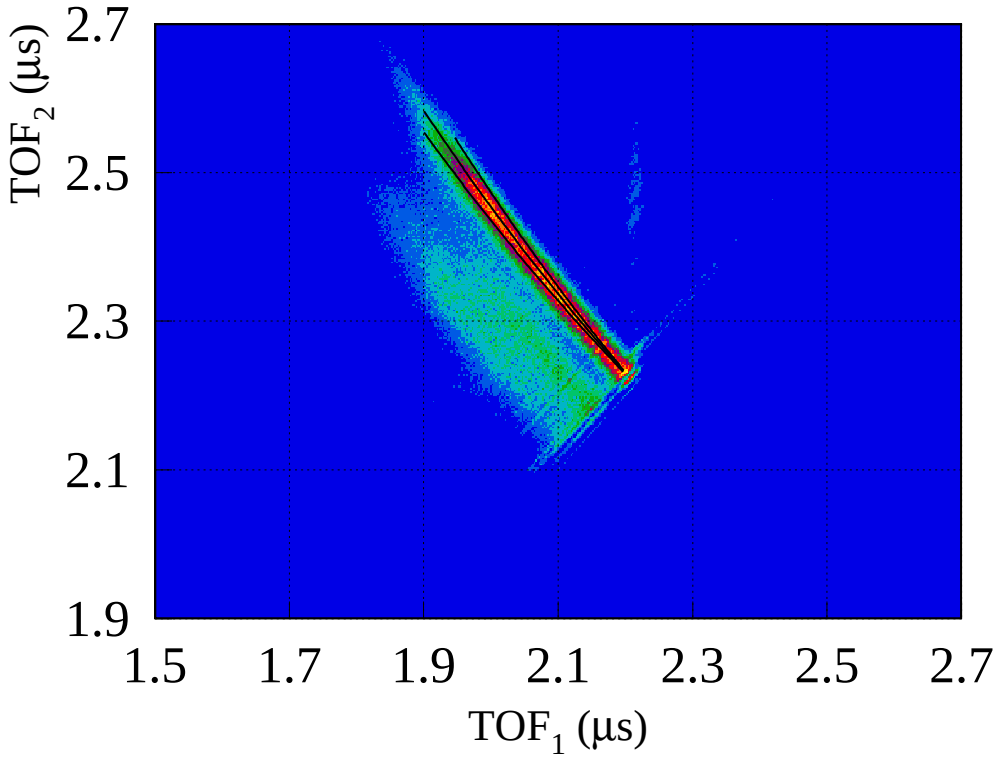

Figure 4.2: Labeled PIPICO Spectrum of the Acetylene/Vinylidene Breakup Channels: Diagonal black line in the middle corresponds to acetylene breakup; V-shape line around it — vinylidene breakup.

even breakup channels of the same total mass but different mass of individual recoils should be separable. In this case the V-shape of the stripe on fig. 4.2 expected from the asymmetric mass breakup, that corresponds to the vinylidene configuration, is so narrow that it completely overlaps with the acetylene stripe.

Other evidence of the rearrangement of acetylene into the vinylidene dication before dissociation can be obtained from analysis of the breakup channel found at the lower left corner of the C_2H_2 PIPICO spectrum 3.9. An enlarged picture of this channel is shown on fig. 4.3. It represents the events in which two protons were registered by the recoil detector. These two protons can be a random coincidence, i.e., they originated from the dissociation

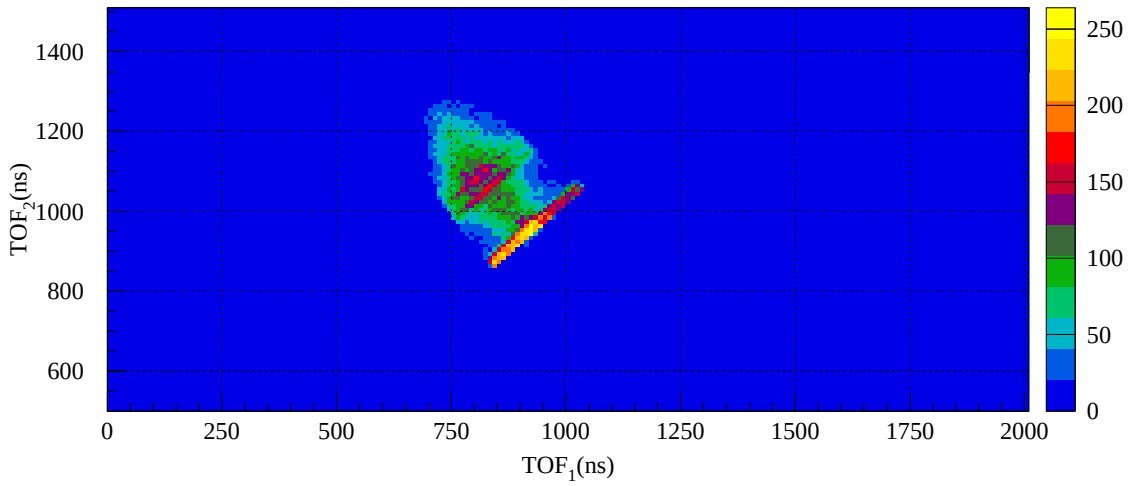

Figure 4.3: C_2H_2 Proton + Proton PIPICO Coincidence

of two separate molecular ions. They can also be a result of breaking both C–H bonds of a single acetylene or vinylidene dication. Figure 4.4 shows the relative angle between the proton momentum vectors in this breakup channel. The corresponding polar plot of this angular distribution is given by fig. 4.5. It is clear that the random coincidence proton pairs should contribute a uniform background in these angular distributions. The very low level of this background supports the fact that most of the proton pairs are correlated and came from the same parent molecular ion. The large peak at $\pm 180°$ must correspond mostly to the hydrogen atoms blown off the acetylene dication, which causes them to fly back-to-back. However, the peak around $\pm 60°$ between the proton momentum vectors cannot be explained by the breakup of the acetylene configuration and can only come from the vinylidene ion. Only the dissociation of the vinylidene configuration into two protons and a positively charged CC^{+n} residual ion can force these protons to fly at such a small angle

with respect to each other.

The final separation of the A and V channels was done by using momentum conservation. The momentum vectors of the two recoils that come out of the $(C_2H_2)^{++}$ Coulomb explosion should be opposite and equal[2]. As is discussed in appendix I, the right set of recoil masses on an event–by–event basis cannot be known *a priori*. The separation procedure thus involved the test of all three possible sets: 12+14 (C^++CH_2^+ breakup), 13+13 (CH^++CH^+ breakup) and 14+12 (CH_2^++C^+ breakup with heavier particle registered first.). The momentum vectors were calculated for both particles in all three cases and their vector sum was compared to zero. The set of masses that gave the shortest length for this total momentum vector was chosen as the correct one and was used in all the further calculations for the parameters of this particular event. Figure 4.6 shows the momentum and kinetic energy release spectra as a result of this separation procedure. It was however decided to continue the analysis of these two channels by looking only at those recoils that have an angle $< 45°$ with respect to the x axis (polarization direction) since that is the region where the separation procedure was believed to give the most reliable results.

By choosing an even smaller subset of these data — the recoils that are now within 10° from the polarization direction — one can plot the photoelectron angular distribution (in a body-fixed-frame) which would correspond to the σ part of the cross section of the photoionization. The energy of the photons used in this experiment was 310eV (20eV above the carbon k-shell ionization potential) and was chosen from considerations of the f-wave

[2]The momenta carried away by the photoelectron and the Auger electrons were neglected in this procedure.

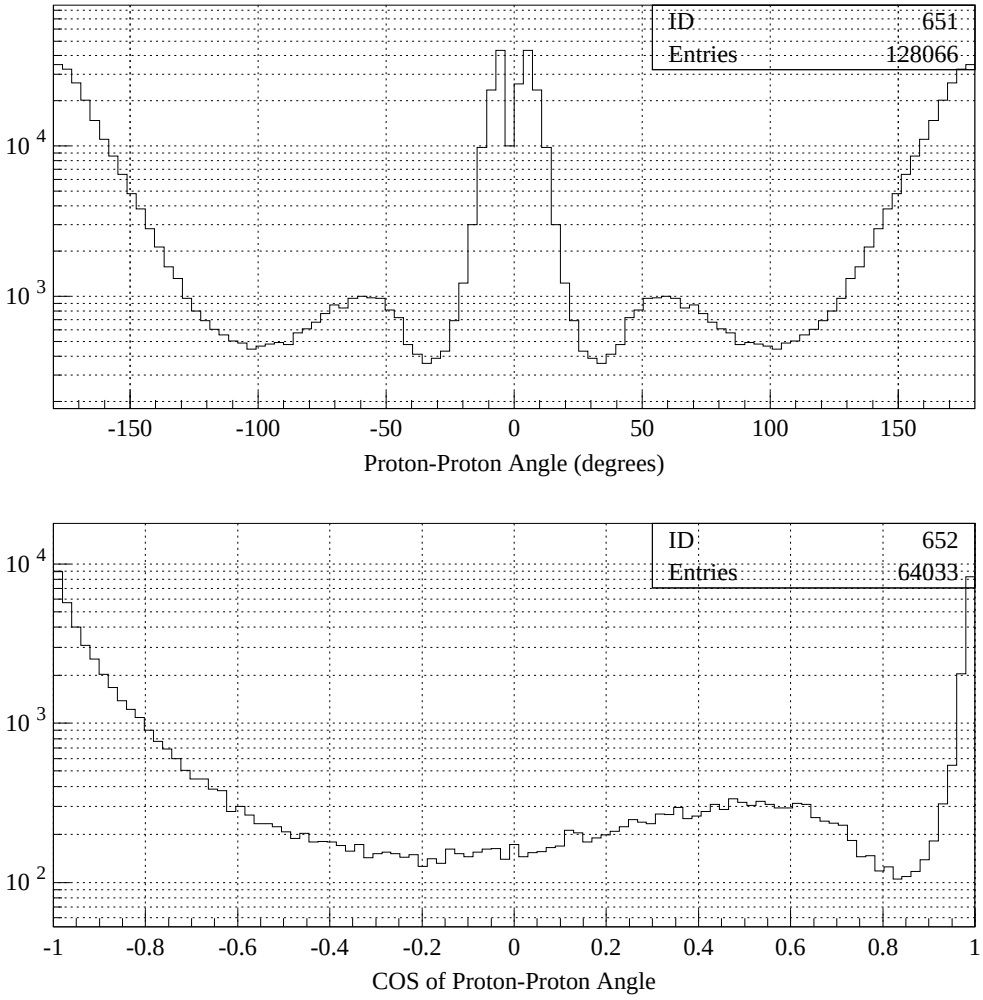

Figure 4.4: C_2H_2 Distribution of the Angle Between the Proton Momentum Vectors

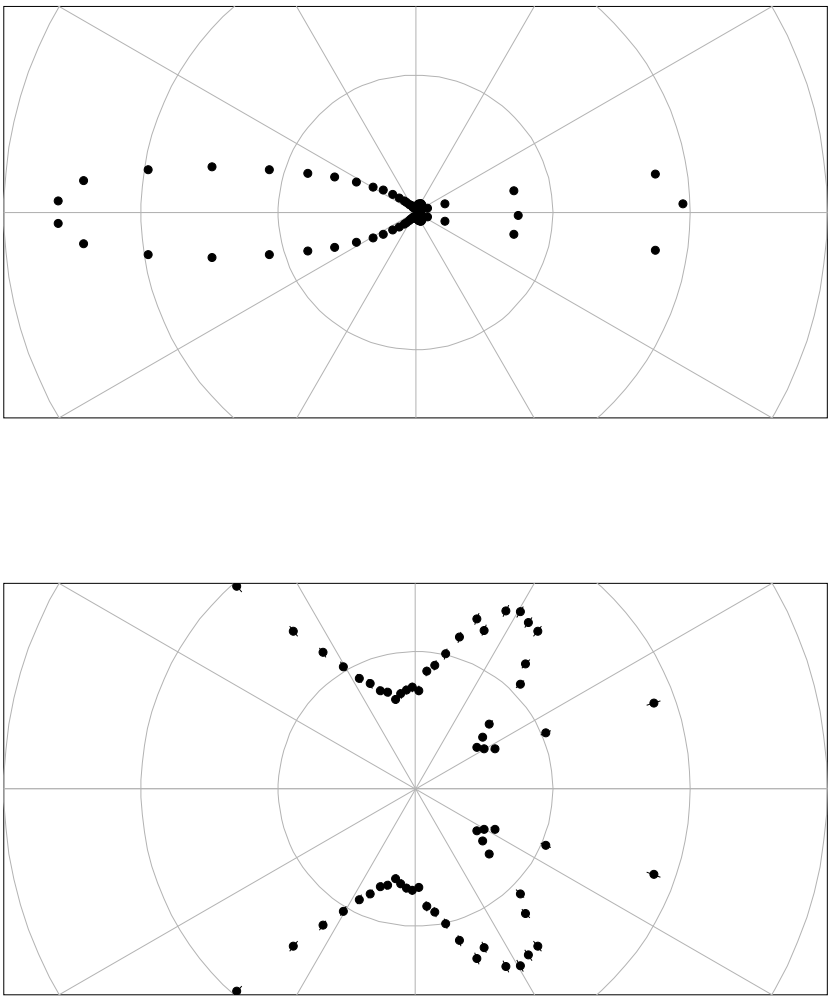

Figure 4.5: C_2H_2 polar plot of the angle between the proton momentum vectors (top) and the magnification of its fine features (bottom).

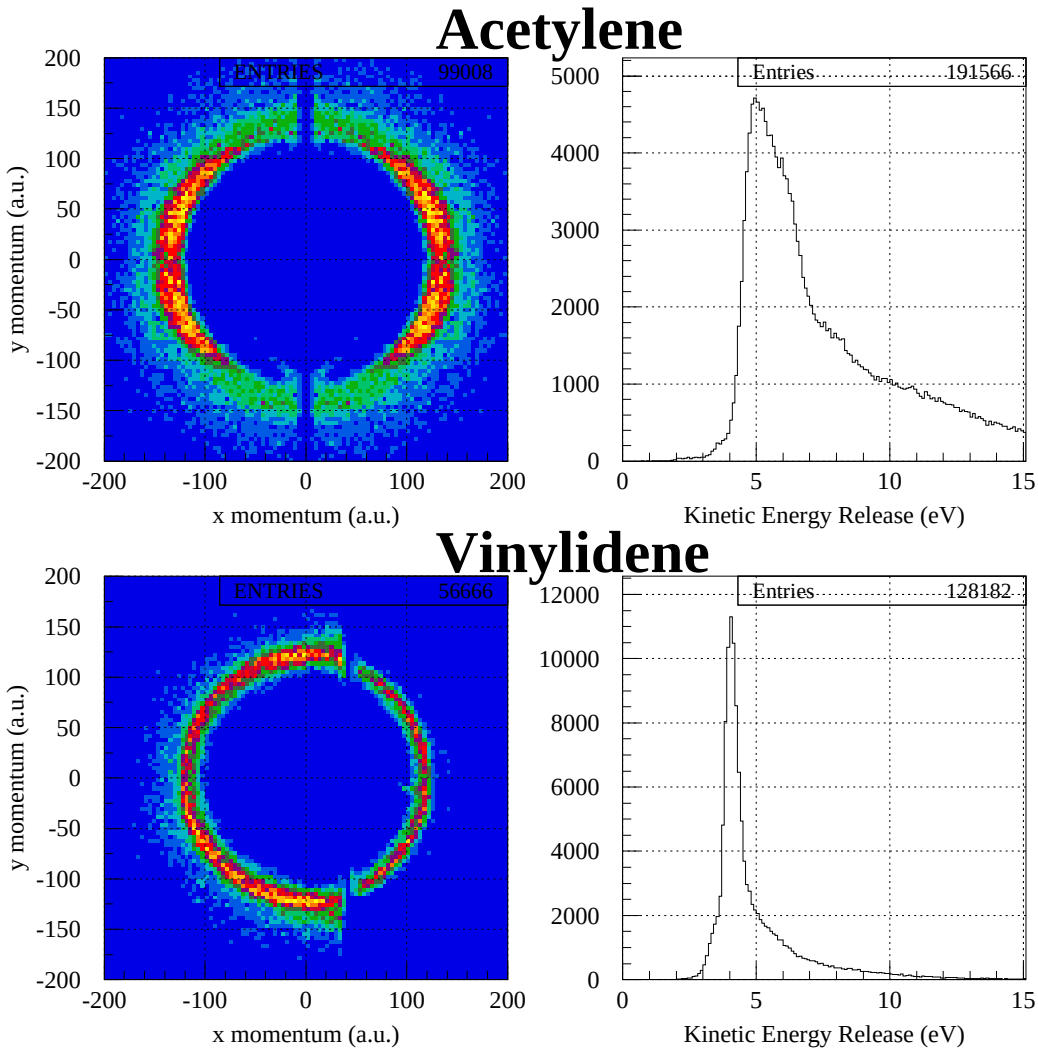

Figure 4.6: Momentum and Kinetic Energy Release spectra for Separated Acetylene and Vinylidene Channels

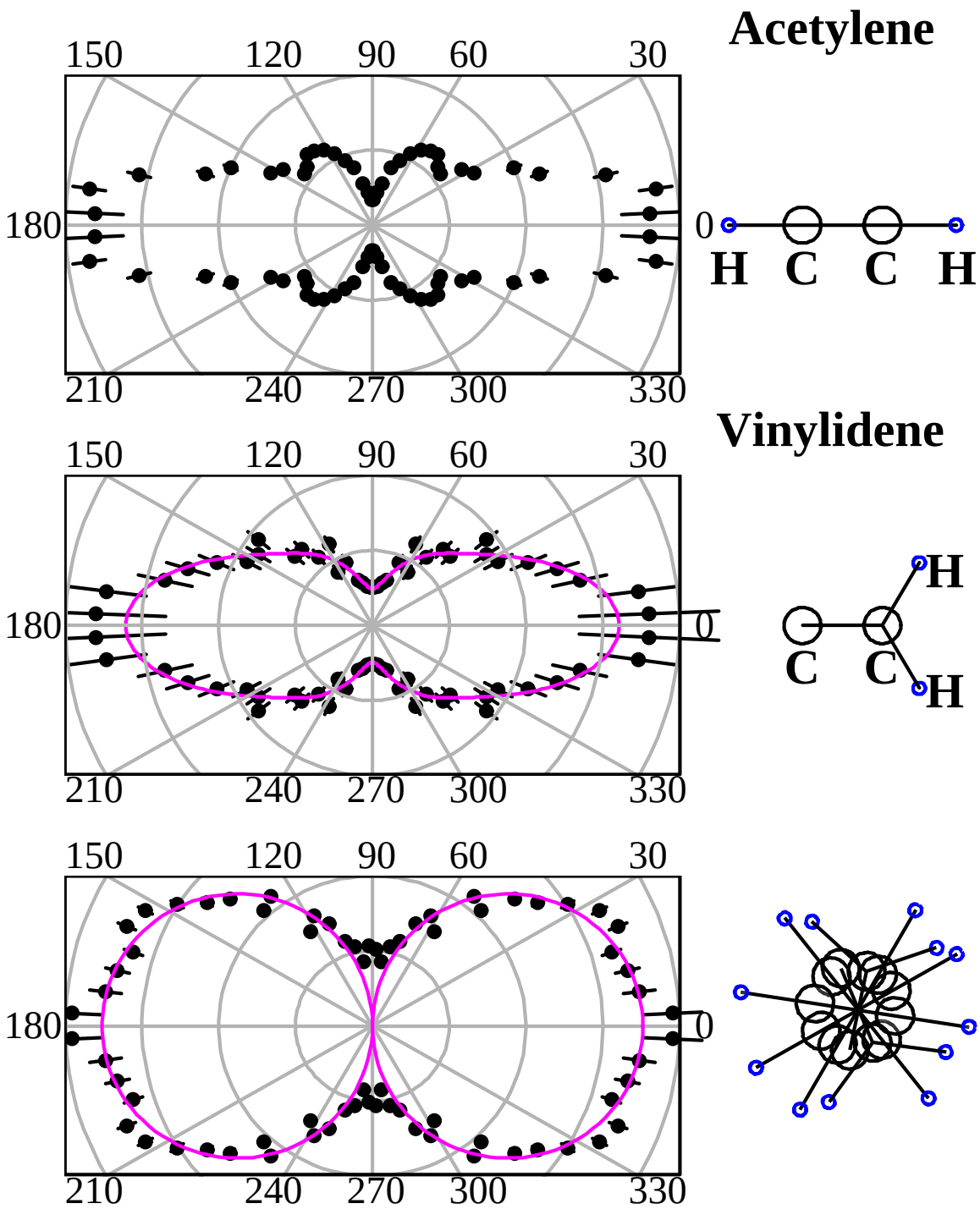

Figure 4.7: Photo-Electron Angular Distributions Comparison for Acetylene Breakup Channel (top), Vinylidene (middle), and Uncorrelated Laboratory Frame Electrons (bottom). In all three cases the x-ray polarization is left-to-right.

resonance position calculated by Haack [7]. While no conclusive study of the f-wave shape resonance in acetylene was attempted, the observed sharp features of the electron angular distribution in the A case (see top section of fig. 4.7), explained by a strong $l = 3$ harmonic contribution, was critical to the study discussed in this chapter.

As was mentioned in section 2.1, the photoionization process is very fast even at lower excess energies than the 20eV used for this part of the experiment. The photoelectron leaves long before the molecule "decides" whether or not to isomerize. Thus the actual photoelectron angular distribution is fixed by the initial alignment of the molecule at the time of the emission of the electron. However, the distribution obtained using the axial recoil approximation for the A and V channels are different, as seen in fig. 4.7. The middle part of figure 4.7 represents the angular distribution for the vinylidene breakup and its features are obviously "washed out" compared to the acetylene case (top of the fig. 4.7). This is explained by the fact that the axial approximation extraction of the C–C bond direction (molecular orientation) from the Coulomb explosion returns the orientation of the molecule at the time of the Coulomb explosion and this may differ from what it was when the photoelectron left the system. The washout in the angular distribution means that the molecule had a chance to rotate somewhat before it exploded. On the other hand, the bottom part of figure 4.7 represents the electron distribution in the laboratory frame. This was shown to represent the case of an infinitely long washout, i.e., the result one would obtain if the molecules rotated by an infinitely large angle before they broke up. The V case distribution is clearly somewhere between the top and the bottom case.

To determine the average angle of rotation performed by the vinylidene molecules the following technique was used. Knowing that the acetylene distribution represents a "prompt" breakup, and thus the primary photoelectron angular distribution relative to the target molecule; one can simulate the rotation observed for the V channel.

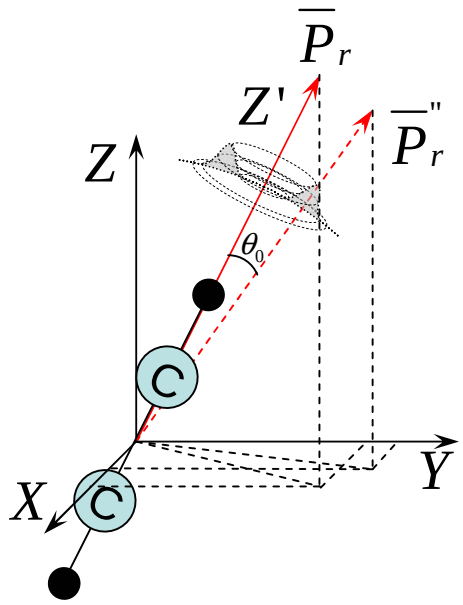

To simulate this rotation the data in the A channel were analyzed and sorted the same way as used in generating fig. 4.7(top) except that before plotting it the orientation of the molecule was changed by a random angle. The value of this angle was given by the Gaussian centered around θ_0 with a spread of 20% of the peak position[3]. To choose the direction of the rotation a transfer to a new system of coordinates was performed. A system in which the direction of the z-axis was along the original direction of the molecule $\bar{P}_r$ was used. The direction of the molecule, $\bar{P'}_r$, was then set to have a longitudinal angle θ_0 and an azimuthal angle chosen randomly between 0 and 2π. When the new angular distribution is created it is compared to that measured for the V channel distribution by fitting both of the data sets with a Legendre polynomial series and measuring the χ^2 of the fit to the V data (see fig. 4.8). Figure 4.9 presents the fitting results for several values of θ_0 for comparison[4]. Recall that it was decided that the reliable data for the A channel (molecular orientations) lies within a

[3]The results of the further analysis were found to be not very sensitive to this value.
[4]The movie of this fitting procedure can also be found in the folder "thesis/movies" of the attached CD.

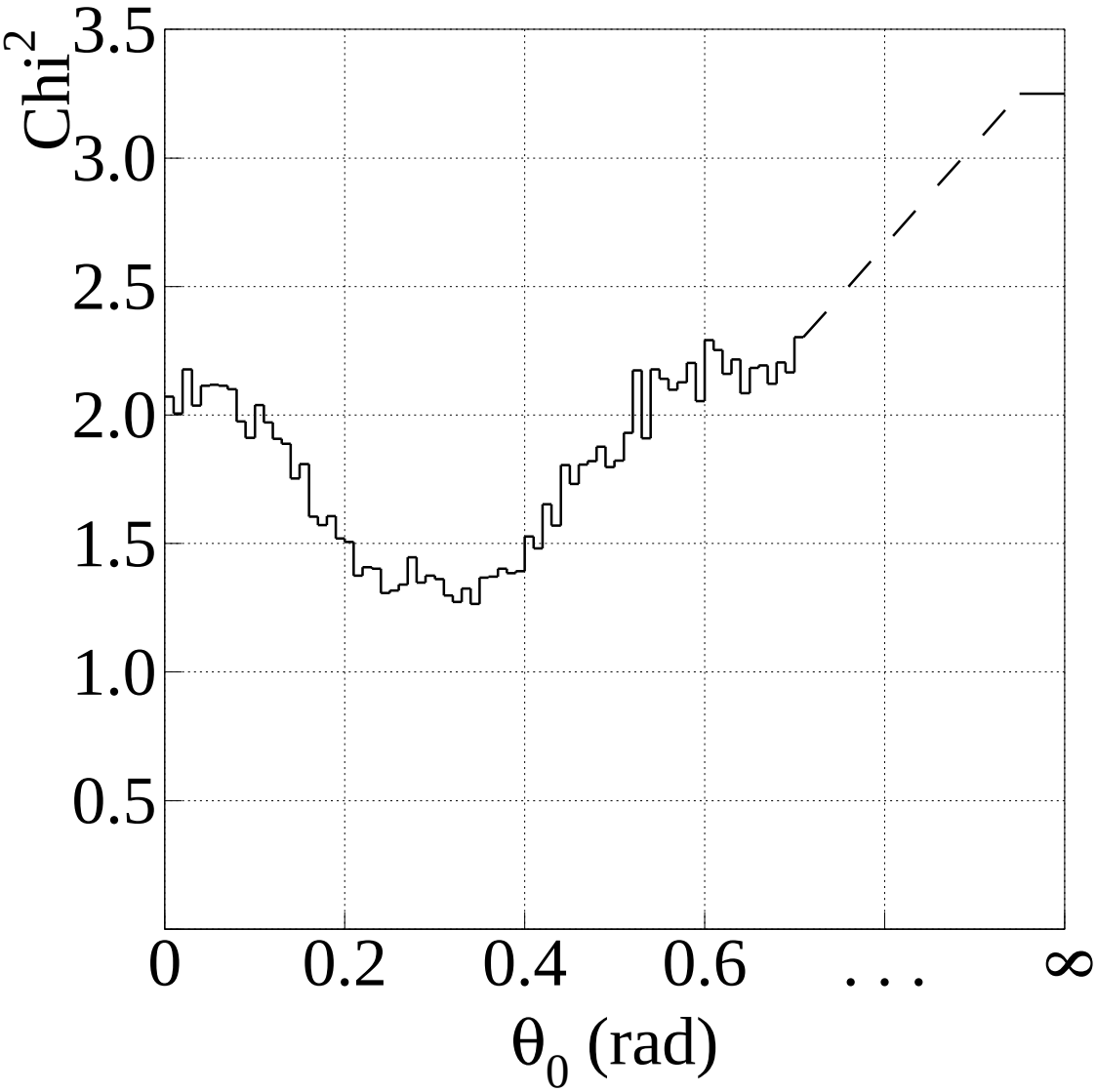

Figure 4.8: χ^2 as a Function of the Rotation Angle for the Vinylidene Electron Angular Distribution Fitting

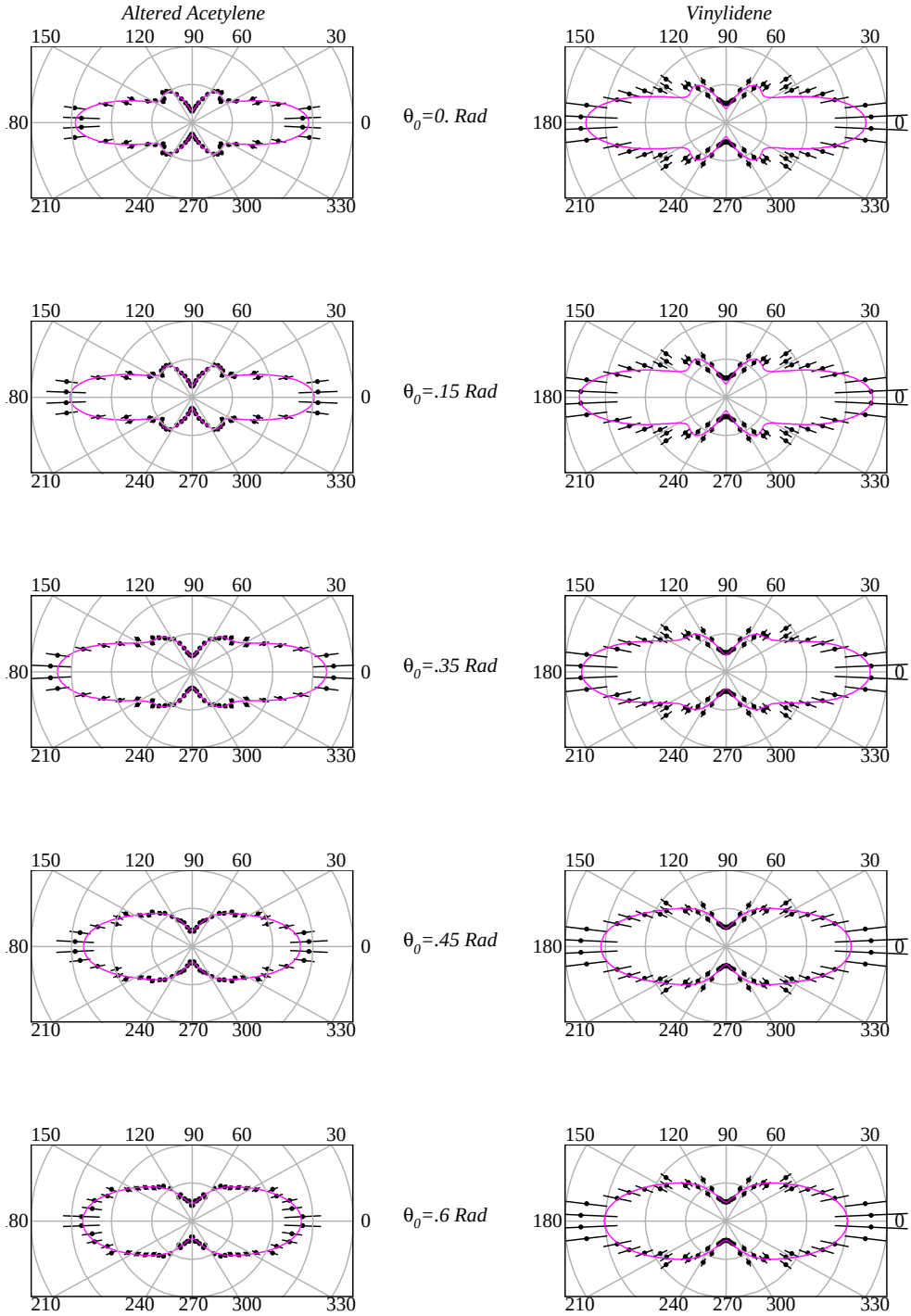

Figure 4.9: Fitting Results For Different Rotation Angles

45° angle from the laboratory x-axis. This limits the rotation simulation process to $\theta_0 \leqslant 45°$, since at higher values of θ_0 the "questionable" events might get mixed into the analysis. This point is reflected by the dashed line on fig. 4.8. The value at infinity is obtained by fitting the bottom part of figure 4.7 to the V channel distribution. This χ^2 distribution has a clear minimum at 0.33 ± 0.03 rad.

It is tempting to immediately attribute this angle to the product of the initial angular velocity of the molecule, due to a finite angular momentum value, and the time between the Auger decay (main contributor to this angular momentum) and the final Coulomb explosion of the V form of the dication. However, it is important to remember that some rotation of the angle of the C–C bond inevitably accompanies the rearrangement from the A to the V configuration, even if the jump of the hydrogen atom were instantaneous. The minimum rotation consistent with the mass rearrangement depends on the path the H atom follows in proceeding from its initial position on one end of the dication to its final location at the other end. If it goes straight down the C–C axis, no rotation is required; however, this is a very unlikely path. The details of the transition states through which the dication is expected to isomerize are described by Duflot *et al.* [37], and resemble more closely a tangential path around the center of mass of the system (see fig. 4.10).

The result of a model calculation for a tangential path of the hydrogen was presented in [39] and resulted in a predicted rotation angle 0.38rad due to an (infinitely fast) mass rearrangement[5]. Here the result of more precise calculations from appendix J is used in a

[5]The results of the Letter [39] were also covered in [40] by Charles Day.

more detailed analysis of the duration and nature of different events (see fig. 4.12) involved between the ejection of the photoelectron and the final Coulomb explosion of the dication $C_2H_2^{++}$. The angle of the C–C bond rotation due to the isomerization $\theta_I = 0.42 \pm 0.013$ rad, obtained in appendix J, represents the average of the result from three calculations, identical in their nature, performed for fixed but different values of C–C and C–H bond lengths. These different values correspond to the three transition states of the $C_2H_2^{++}$ ion involved in the isomerization process. The explanation of the fact that the result for θ_I(0.42rad) is slightly higher than the value obtained from the simulation for θ_0 (0.33rad) can be partially explained by the following consideration. The trans bent geometry of the acetylene dication (see top part of fig. 4.12) with the C–C–H angle equal to 128.3° was proposed by Duflot in [37] as an intermediate state before its dissociation into two CH^+ ions. It was not presumed here that this is the only possible pathway for the acetylene dication dissociation, but it needs to be shown that even this pathway does not dramatically change the results of the analysis or its applicability. It is logical to assume that the change of the $C_2H_2^{++}$ linear ground state into this planar geometry is fast and must take around 10fs, close to the C–H bending vibration period (see [27; 36]). Any longer time would not be consistent with the sharpness of the angular distribution shown in the top part of fig. 4.7. This geometry change also inevitably causes the change of the C–C bond orientation of the dication equal to $\theta_V = 0.18 \pm 0.02$ rad (see appendix J). This angle (∼10°) might seem to be inconsistent with the sharpness of the acetylene photoelectron angular distribution fig. 4.7(top). However, the result of the similarly simulated rotation for the ethylene (C_2H_4) data (see in fig. 4.11) shows that this

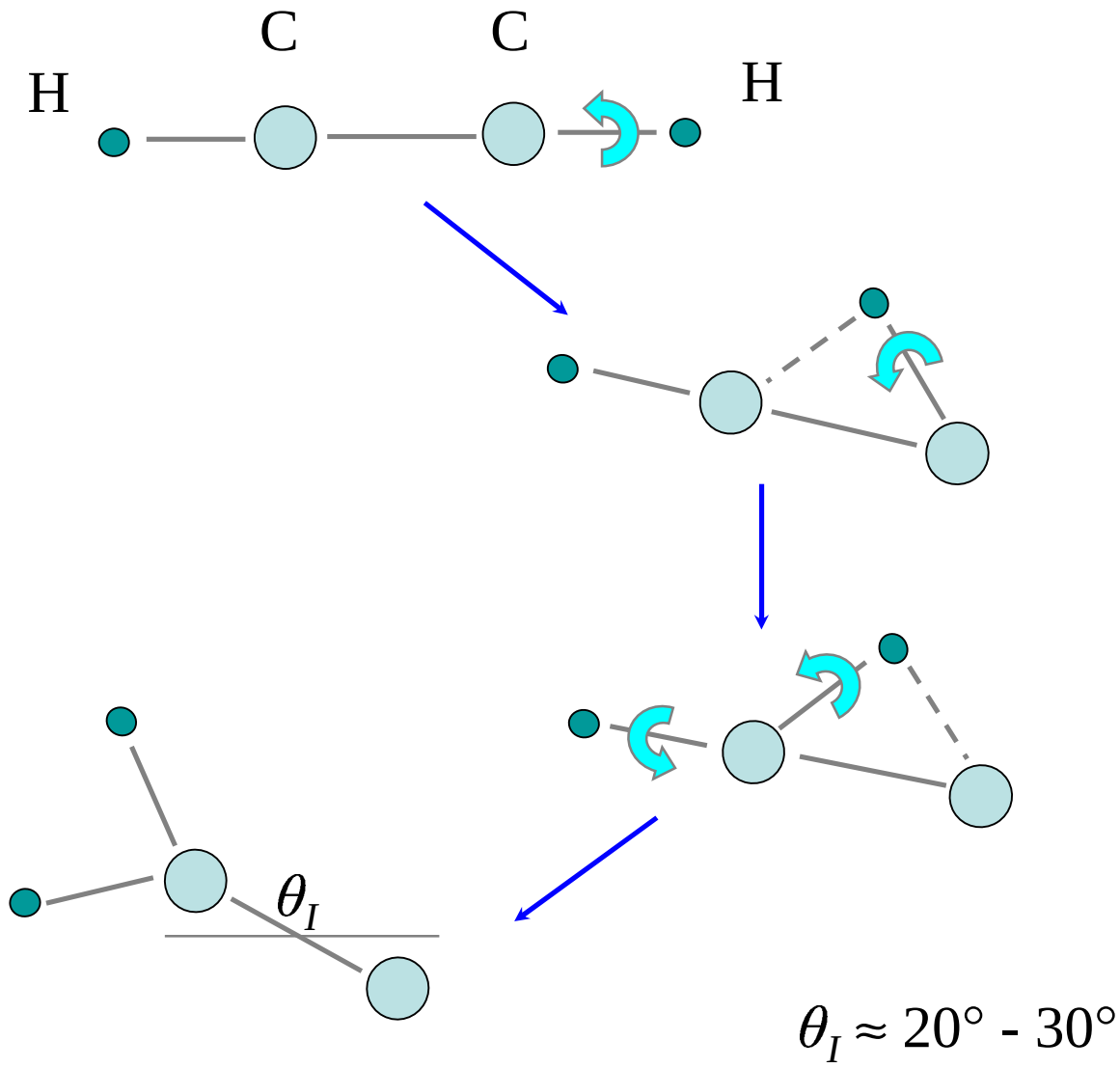

Figure 4.10: Steps of the Isomerization Process

rotation is not big enough to wash out the f-wave lobes. The combined effect of this rotation in acetylene and θ_0 might be in a better agreement with the θ_I.

On top of the $HCCH^{++} \rightarrow H_2CC^{++}$ isomerization process there is a rotation of the whole molecular ion due to the non-zero angular momentum of the system, originating from the Auger electron kick. The angle of this rotation will be denoted by $\theta_l = \sqrt{l(l+1)}\Delta t/I$. Here $l = \langle \mathbf{r_0} \times \mathbf{p_e} \rangle = r_0 p_e \langle \sin(\theta_{r_0 p_e}) \rangle \simeq 1/2 r_0 p_e$ the average angular momentum from the Auger decay (r_0 being the half distance between the carbon atoms), I is the moment of inertia of the system, and Δt is the time from the Auger decay to the Coulomb explosion (see fig. 4.12). The square of the angle θ_l can be obtained from the equality[6] $\theta_l^2 + \theta_I^2 = \theta_V^2 + \theta_0^2$ which reflects that the final rotation of the C–C bond in the case when the isomerization takes place is equal to the C–C bond rotations without the isomerization plus the simulated angle. Even with all this taken into account the value of $\theta_l^2 = \theta_V^2 + \theta_0^2 - \theta_I^2$ is slightly below zero ($0.18^2 + 0.33^2 - 0.42^2 = -0.0351$) which can only mean that θ_l must be zero within the error bars $\Leftrightarrow$ instantaneous isomerization process. The error bar analysis gives $\Delta(\theta_l^2) = \sqrt{(\partial(\theta_l)^2/\partial\theta_v \cdot \Delta\theta_v)^2 + (\partial(\theta_l)^2/\partial\theta_0 \cdot \Delta\theta_0)^2 + (\partial(\theta_l)^2/\partial\theta_I \cdot \Delta\theta_I)^2} = \sqrt{4(.18 \cdot .02)^2 + 4(.33 \cdot .03)^2 + 4(.42 \cdot .013)^2} = 0.0237$. Then taking $\theta_l \leqslant \sqrt{.0237} \simeq .15$ rad one can put an upper limit on $\Delta t = \theta_l I/\sqrt{l(l+1)}$ to be $4.2 \cdot 10^3$a.u. $\simeq 100 \cdot 10^{-15}$sec = 100fs (where it was assumed that $I = 9.5 \cdot 10^4$ a.u. and $l \simeq 1/2 r_0 p_e = 1/2 \cdot 1.2 \cdot 5$=3 a.u.).

[6]The proper formula for the addition of angles of independent rotations can be obtained from the addition of angular velocity vectors $\langle\theta\rangle = \langle|\int_{\Delta t} \bar{\boldsymbol{\omega}} dt|\rangle = \langle|\int_{\Delta t}(\bar{\boldsymbol{\omega}}_1 + \bar{\boldsymbol{\omega}}_2)dt|\rangle = \sqrt{|\int_{\Delta t} \bar{\boldsymbol{\omega}}_1 dt|^2 + |\int_{\Delta t} \bar{\boldsymbol{\omega}}_2 dt|^2 + \langle \int_{\Delta t} \bar{\boldsymbol{\omega}}_1 dt \cdot \int_{\Delta t} \bar{\boldsymbol{\omega}}_2 dt \rangle}$ where the dot product is averaged over the angle between the resulting vectors and thus is equal to zero, so $\langle\theta\rangle = \sqrt{|\int_{\Delta t} \bar{\boldsymbol{\omega}}_1 dt|^2 + |\int_{\Delta t} \bar{\boldsymbol{\omega}}_2 dt|^2} = \sqrt{\theta_1^2 + \theta_2^2}$.

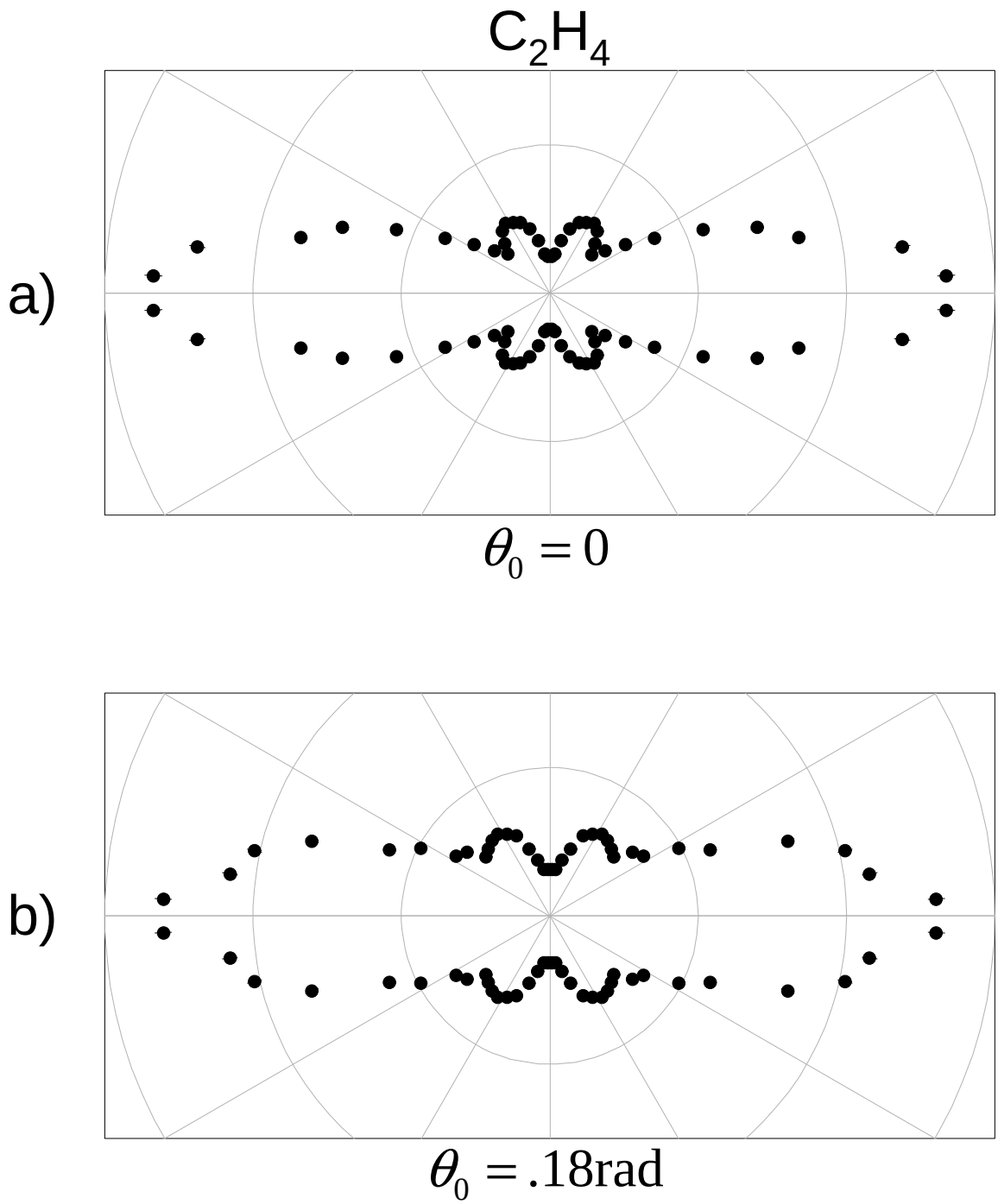

Figure 4.11: Ethylene photoelectron angular distribution for the horizontally oriented molecule (parallel to the polarization direction of the 302eV photons). Top — original data — no rotation. Bottom — electron angular distribution for simulated rotation of the molecule by .18rad ($\sim 10°$).

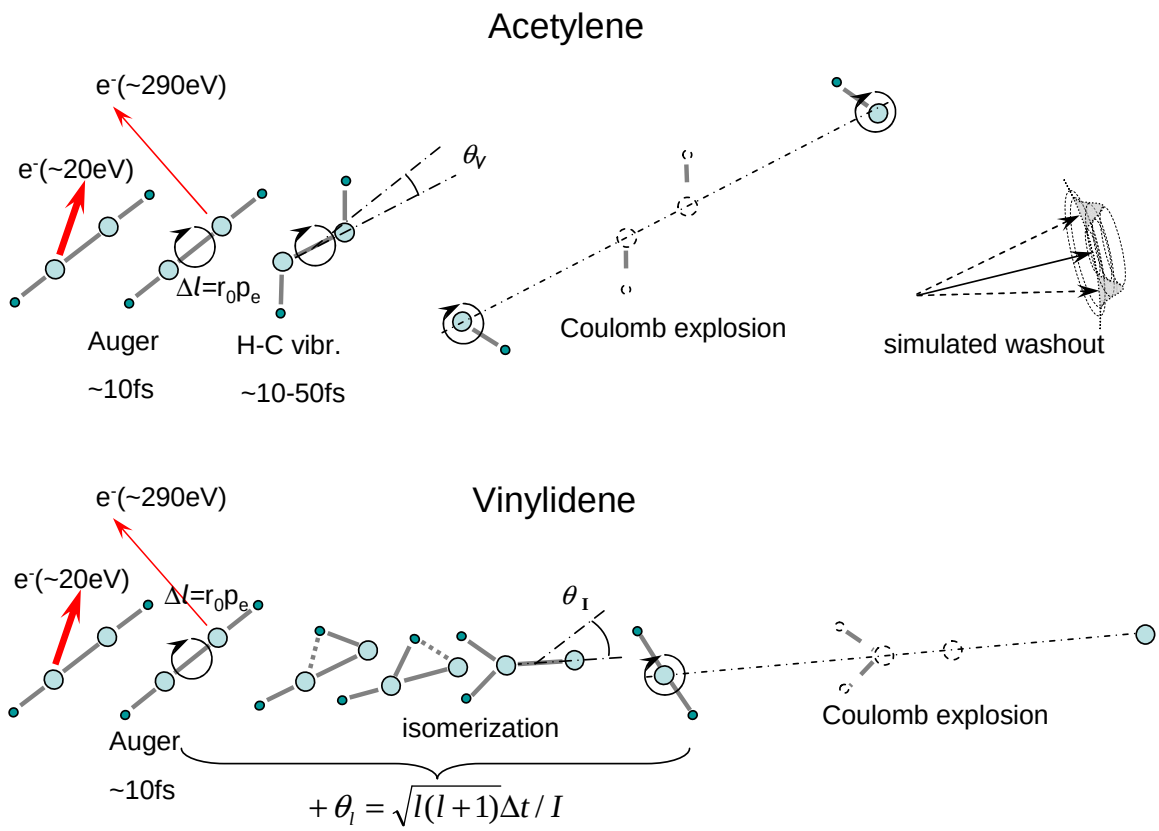

Figure 4.12: Event Sequence For Acetylene and Vinylidene Breakup Channels

Recall again that Δt is the time between the Auger decay[7] and the Coulomb explosion which means that both the duration of the isomerization process and the lifetime of the vinylidene dication are within this time interval and thus are limited by its value of <100fs.

[7]A higher value of the angular momentum, for example due to the finite initial target gas temperature, would result in even shorter Δt.

Chapter 5

Summary

In this thesis a detailed experimental study of k-shell photoionization of the hydrocarbons C_2H_2 and C_2H_4 was presented. The experiment was conducted by using the cold-target-recoil-ion-momentum-spectroscopy (COLTRIMS) setup with 4π solid angle detection capability. In this kinematically complete experiment the positions and the times-of-flight of both molecular ion recoils and the photoelectron were measured and converted into the corresponding 3d momentum vectors. The high electron and recoil momentum resolution in the experiment provided the means of selecting particular reaction channels corresponding to well defined energies of the reaction products. The kinetic energy release of hydrocarbon molecules was found to be monoenergetic with the peak position near 5eV total recoil energy ($\pm$2eV depending on the particular molecule and breakup channel). The photoelectron energy distribution was found to have a main peak at the position defined by the difference between the photon energy and the k-shell ionization potential, and several satellite peaks at lower energies corresponding to different excited states of the residual molecular ion. The analysis concentrated on processes corresponding to electrons in the main peak only; thus

the satellites were not studied in this work and were properly gated out. The dissociation of the molecular dication, created by the photo-ionization of the k-shell electron and the following Auger decay, was used to determine the molecular orientation at the time of the photoelectron emission, using the axial recoil approximation. This allowed the measurement of the photoelectron angular distributions in the molecular frame. The experiment was performed over a range of photon energies from 293eV to 320eV. The photoelectron angular distributions as well as total and partial cross sections for k-shell photoionization were obtained as a function of energy in the case of the ethylene molecule (C_2H_4). The photoelectron angular distributions were fitted by a function resembling the theoretical differential cross section in general form. The set of dipole transition matrix elements was extracted. The amplitude of the matrix element corresponding to the contribution of the $l = 3$ partial wave exhibits a resonance behavior around 300eV photon energy. It was determined that due to the symmetry of the studied system (C_2H_4) not all the matrix elements (amplitudes and phases) can be determined uniquely. A direct comparison between the theoretical body-fixed frame angular distribution (by M. Stener) and the present results showed good agreement.

In case of the C_2H_2 molecule it was determined that both isomers — acetylene and vinylidene — of the doubly charged molecular ion contribute to the final quasi-symmetric breakup channel (CH^++CH^+;C^++CH_2^+). The analysis of the photoelectron angular distributions corresponding to these different breakup channels revealed an important difference. The molecular rotation before the dissociation in the case of vinylidene was found to be substantially larger than in the case of the acetylene. This was inferred from the washout of the

corresponding photoelectron angular distribution. A special technique was used to extract the angle of rotation of the vinylidene dication. It was found to be 19±2° with respect to the similarly measured acetylene C–C bond orientation. By subtracting the rotational contribution of the C–C bond due to the isomerization process and assuming the initial angular momentum of the molecular ion to be defined by the Auger electron kick, an upper bound for the isomerization time and the lifetime of the vinylidene dication was determined to be 100fs.

Proposals for the future experiments studying the molecular structure and fragmentation pathways of the hydrocarbons include laser pump-probe experiments. With the current advances in laser techniques it is believed that a time step resolution of 10fs can be achieved in the study of the acetylene isomerization process, for example.

Appendix A

ALS Beam Lines Specifications

Table A.1: **Beamline 9.3.2 Specifications**

Source characteristics	Bend magnet
Energy range	30-1400 eV
Monochromator	SGM (gratings: 100, 600, 1200 lines/mm)
Calculated flux (1.9 GeV, 400 mA)	1011 photons/s/0.1%BW at 400 eV
Resolving power (E/DE)	3000 typical, 8000 max (with 10-μm slits)
Spatial resolution	0.5 x 1 mm

Table A.2: **Beamline 4.0.2 Specifications**

Source characteristics	5.0-cm-period elliptical polarization undulator (EPU5)
Energy range	52-1900 eV
Monochromator	Variable-included-angle PGM
Calculated flux (1.9 GeV, 400 mA)	1 x 1013 photons/s/0.1%BW at 800 eV [Value reported is the merit function, flux = total flux x (degree of circular polarization)^2.]
Resolving power (E/DE)	5,000-10,000 (at source-size limit; energy-dependent) >25,000 (64 eV, 10-mm entrance/exit slits)
Special notes	Polarization is user selectable; linear polarization continuously variable from horizontal to vertical; left and right elliptical (or circular) polarization.

Appendix B

Extraction of the Jet Parameters From the Experimental Data

Theoretical calculation of the gas jet temperature and velocity even for atomic gases is mainly based on a semi-empirical formulae and certain tabulated functions (see [41–43]). Extending this calculation to molecular gases would be much less reliable. Another approach to this problem is to extract all critical information straight from the experimental data.

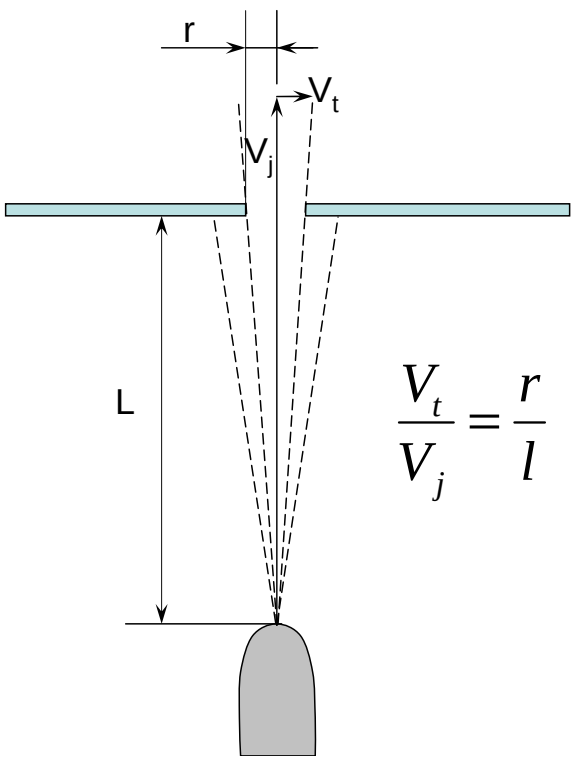

It is clear that jet has different temperatures for different degrees of freedom. The temperature of the transverse motion[1] is minimized by what is called "geometrical cooling". The aperture, the size of which is very small compared to the distance to the nozzle (see section 2.2 for exact numbers), cuts the transverse velocity down to the small fraction of common jet velocity V_j. V_j is related to the temperature of that direction in general defined by the thermodynamics of the gas expansion, pressures in the system, etc. It can be measured in several ways.

The first way uses the single ionization process. It is quite common for the photon beam to create many singly ionized molecular ions even at the high photon energies. This usually creates a bright spot of events a little above the detector center. On the other hand the x-rays passing through the spectrometer ionize the molecules not just in the jet but also from the background gas. This creates a low intensity stripe of the "hot gas" on the detector (see fig. B.1). The center of the stripe defines the y-position of the x-ray and gas jet intersection. By measuring the position of the single ionization spot with respect to the hot gas stripe and dividing it by the corresponding time of flight, the jet velocity V_j can be calculated. From figure B.1, for example, the distance is 3mm and the time-of-flight is $3\mu s$ which yields the $V_j \approx (5 \pm 2) \cdot 10^{-4}$a.u.

The initial y position does not have to be identified with the gas that will be used for the target in the main experiment. As a matter of fact none of the experimental setup parameters need to be set to their final values. The stripe can be created with the most convenient

[1]Here the word "transverse" refers to the motion in the plane perpendicular to the jet direction.

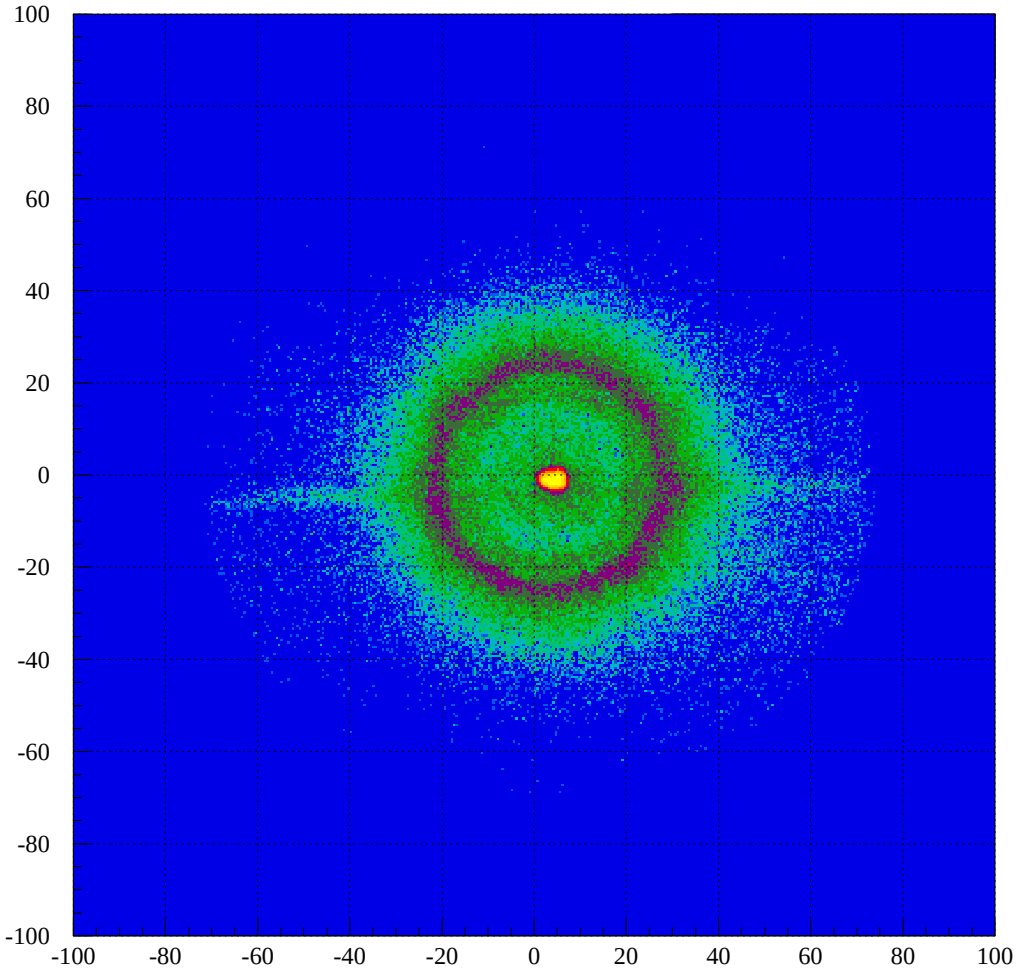

Figure B.1: Hot Gas Stripe on the Recoil Detector in the C_2H_2 experiment.

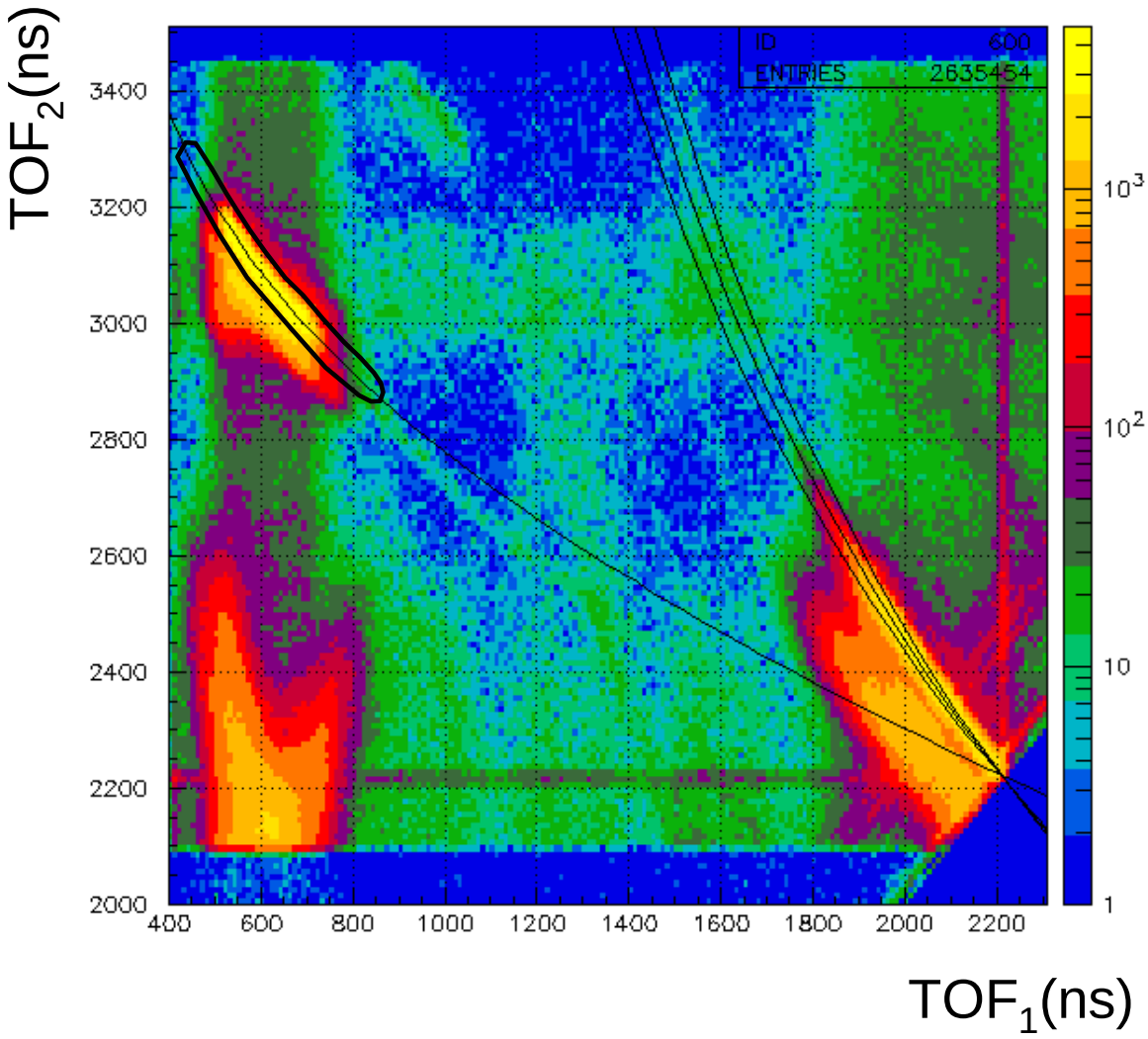

Figure B.2: PIPICO Gate for the C_2H_2 Deprotonation Reaction.

gas, spectrometer electric and magnetic field and the photon energy. This position is only defined by the x-ray beam height and does not change when any of the above parameters are adjusted. The single ionization spot, obviously, has to be measured with the gas whose jet velocity needs to be determined.

The other technique of measuring the initial y position together with the average jet velocity is based on the specific nature of the hydrocarbon molecule and its particular breakup

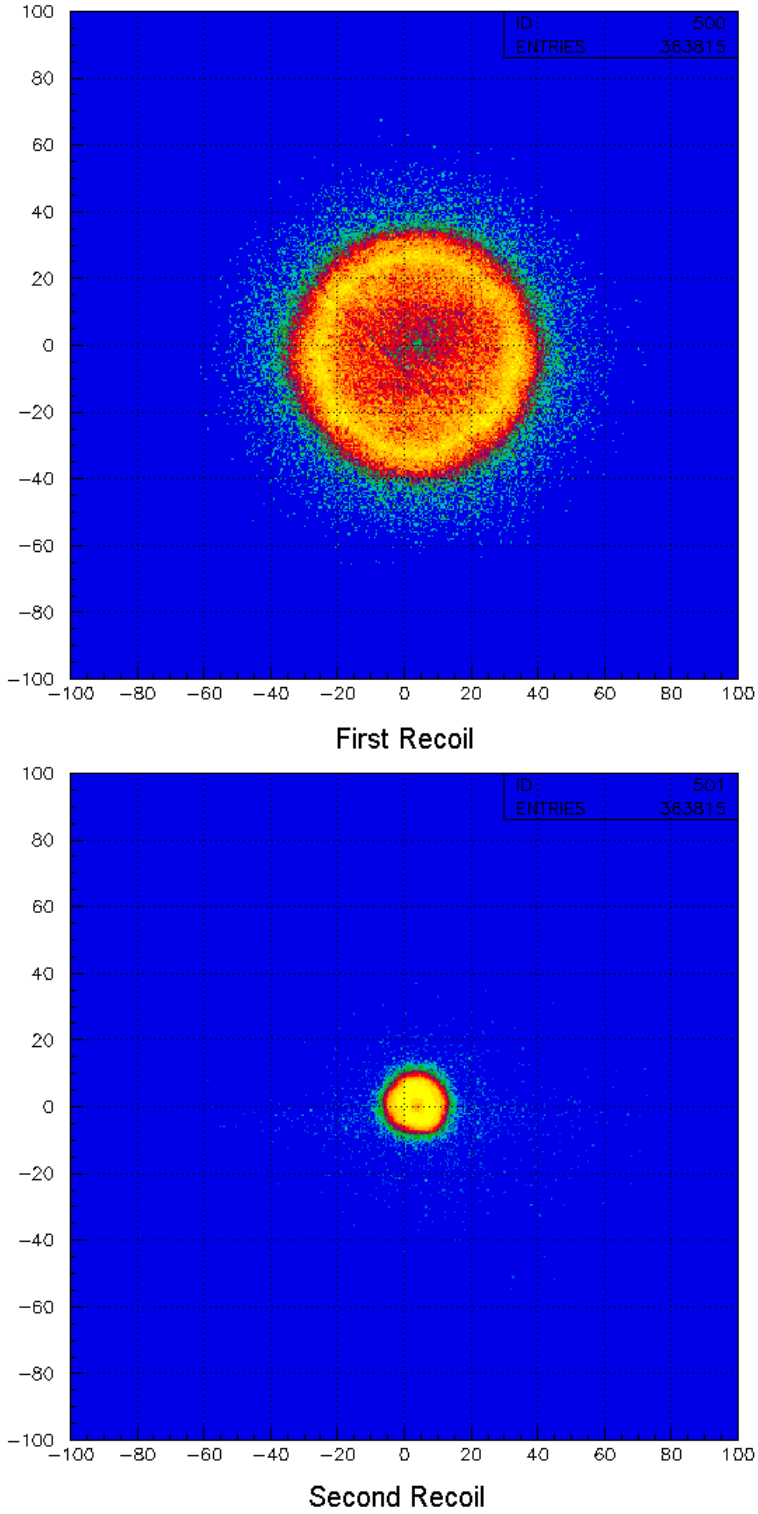

Figure B.3: C_2H_2 Deprotonation Reaction Position Spectra.

channel. This method uses the difference in position of recoils of different masses. It was observed that the deprotonation reaction dominates the rest of the breakup channels in the K-shell photoionization reaction of any hydrocarbon molecule (see table 3.1). In this case after the Coulomb explosion the proton has a time-of-flight about 5 times shorter than the residual molecule. Thus, it shifts up due to the common jet velocity considerably less than the second recoil, as seen from figure B.3 (the breakup channel gate is shown in fig. B.2). By measuring the central position of both recoil distributions and their times-of-flight the jet velocity and the x-ray height can be determined with a very good precision. First let us assume that all the positions are known. Then for the recoils that start with only the jet velocity:

$$\begin{cases} V_j \cdot t_1 = y_1 - y_0 & t_1 \text{ and } t_2 \text{ — time-of-flight of the first and second recoil} \\ V_j \cdot t_2 = y_2 - y_0 & y_1 \text{ and } y_2 \text{ are their positions on the detector} \end{cases}$$

After solving for V_j and y_0 one gets:

$$\boldsymbol{V_j = \frac{y_2 - y_1}{t_2 - t_1}\ ;\ y_0 = \frac{y_2 t_1 - y_1 t_2}{t_2 - t_1}} \tag{B.1}$$

The values of y_1 and y_2 are nothing else but the centers of the corresponding recoil position distributions as marked on figure B.4, and the value for t_1 and t_2 are equal to the times-of-flight of zero–momentum recoils of a proper mass. The calculation for the shown example of C_2H_2 deprotonation yields

$V_j = 900m/s \pm 100m/s = (4.1 \pm .4) \cdot 10^{-4}$a.u.

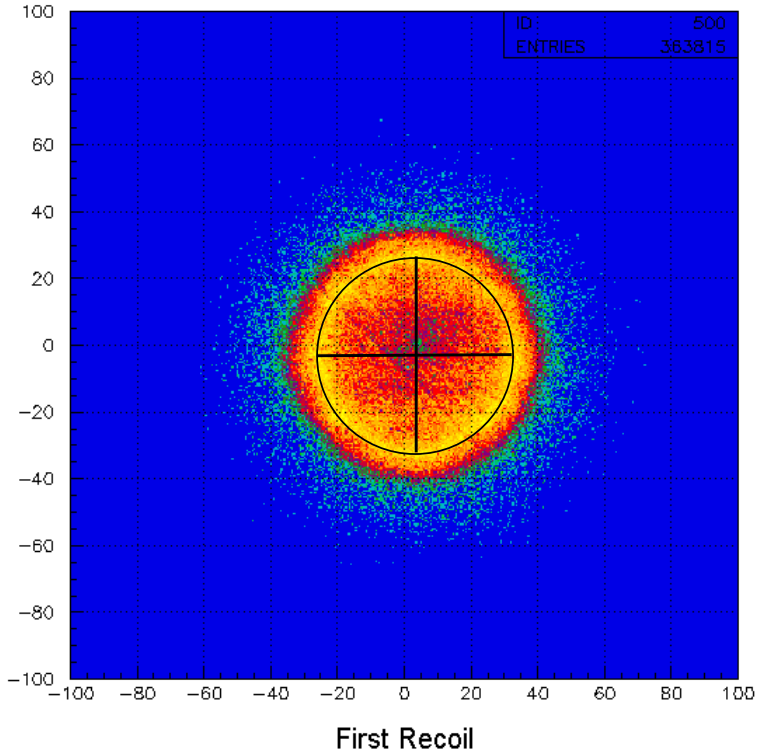

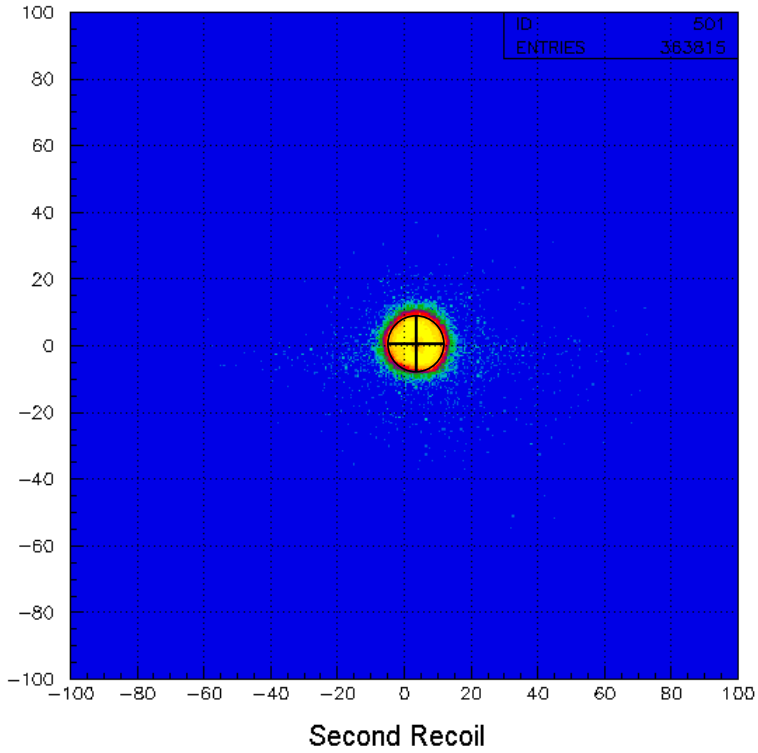

Figure B.4: C_2H_2 Deprotonation Reaction Position Spectra with Marked Centers.

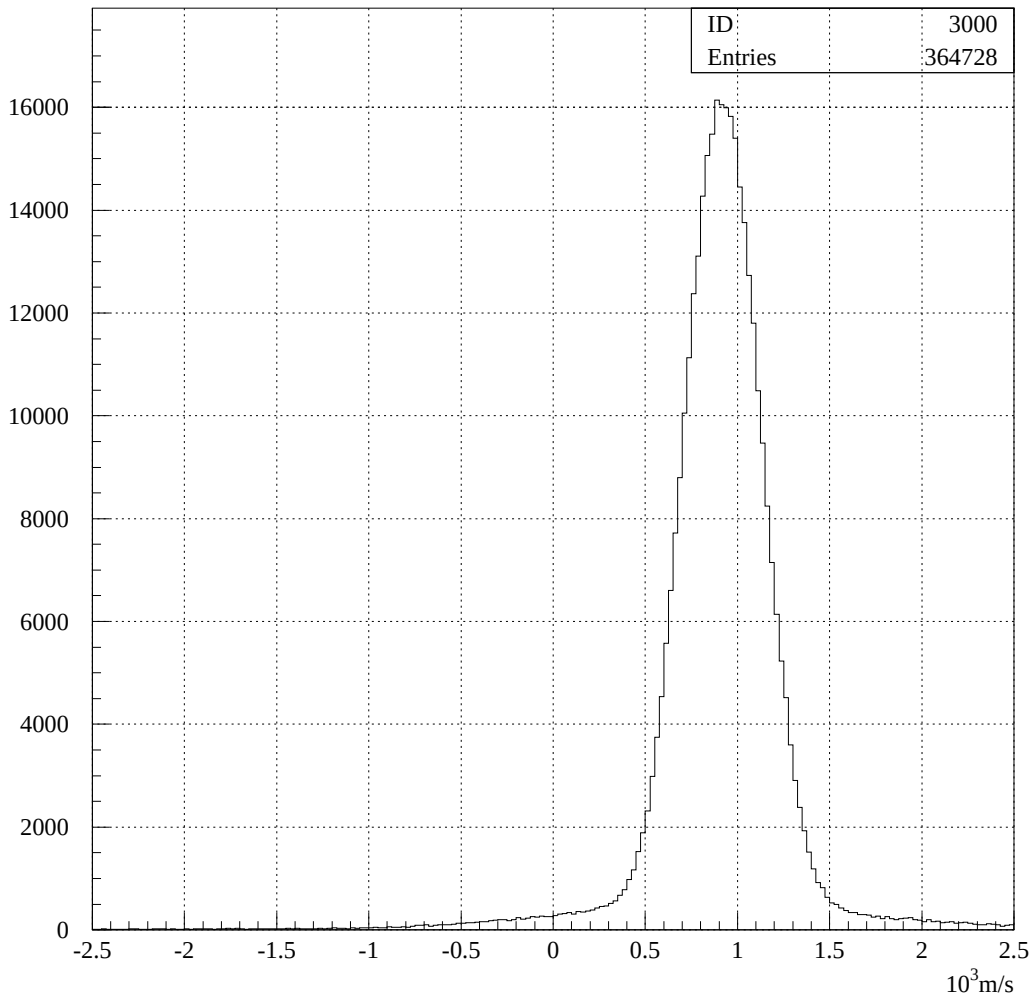

Figure B.5: Y Component of the Center-of-Mass Velocity Distribution for C_2H_2.

Yet another technique of measuring V_j provides not only its value but also gives the whole distribution which would define the temperature of the gas[2] if there were no Auger electron kick. The recoil momentum calculation part of section 2.3 discusses the technique of calculating the relative momentum of two recoils independent of V_j assuming the momentum conservation in the center-of-mass frame. Starting from the same assumption the velocity of the center of mass also can be calculated:

$$\begin{cases} P_{1y} = (\triangle y_1/t_1 - V_c)m_1 \\ P_{2y} = (\triangle y_2/t_2 - V_c)m_2 \end{cases} \Rightarrow \quad (\triangle y_1/t_1 - V_c)m_1 = -(\triangle y_2/t_2 - V_c)m2$$

So the final result for the V_c is

$$\boldsymbol{V_c = (\frac{m_2 \triangle y_2}{t_2} + \frac{m_1 \triangle y_1}{t_1})/(m_2 + m_1)} \tag{B.2}$$

The typical V_c distribution is shown in figure B.5, and it is clearly centered at $V_j = 900$ms which agrees with the previous calculation. The distribution of V_c is due to the Auger electron momentum and the initial temperature of the gas. From the width of the distribution the upper bound on this temperature is $\sim 100K$.

[2]Namely it would be the temperature of the gas in the jet direction as well as the temperature of all rotational and vibrational degrees of freedom

Appendix C

Delay Line Detectors

State-of-the-art delay line position sensitive detectors (PSD) are essential for the present COLTRIMS experiments. Multi-hit data collection and analysis is an inseparable part of most of these experiments. The experiment covered by this thesis, for example, involved the collection of at least three particles per event, out of which at least two were registered on the same detector.

The main principle of these detectors[1] (see fig. C.1, C.3, and C.4) is the timing information obtained by collecting the signals from two (or three) overlapping layers of wires, wound to make a few hundred turns. The layer with vertical turns provides the x-coordinate information, and the layer with horizontal turns — y-coordinate of the hit[2]. When a particle hits the detector system, it sets off an electron avalanche in the multi-channel plates. These multi-channel plates (MCP) work like a regular photomultiplier. The electron cloud created

[1]All of the detectors used in the presented experiment were RoentDek Delay Line position sensitive detectors. Most of the figures in this appendix were adapted from the RoentDek Position Sensitive Detector Manual that can be obtained from http://www.roentdek.com/ web page, where the reader can find more technical information and details on the specific detector parameters, detector use and assembly not covered here.

[2]Hex anode detectors have three overlapping layers at 60° with respect to each other and provide redundant position information.

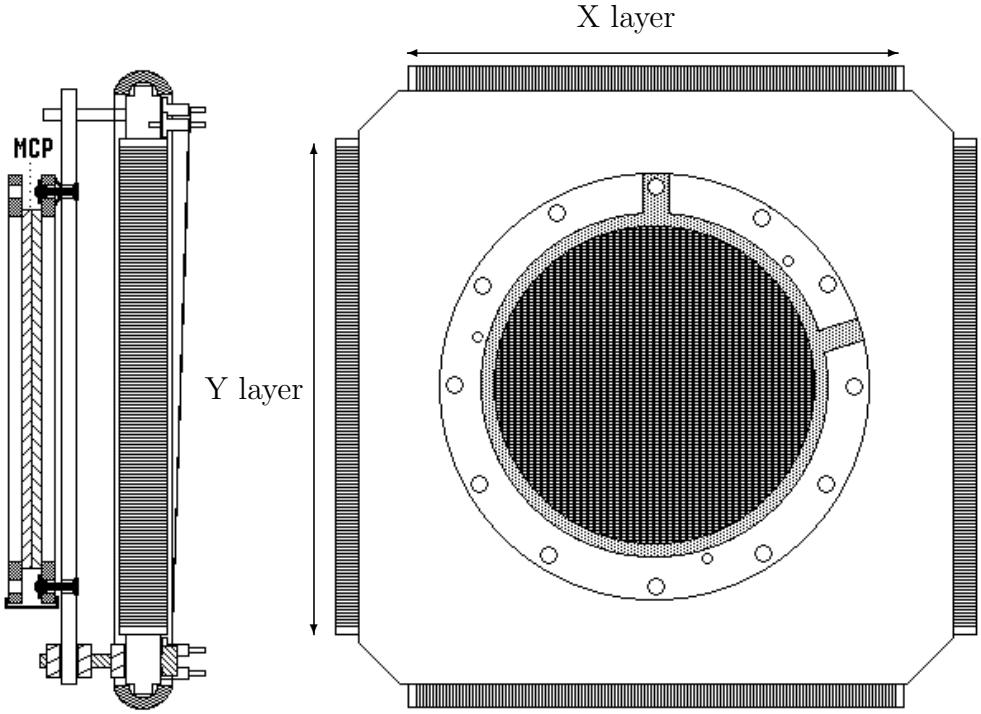

Figure C.1: **Schematics of the RoentDek Delay Line Detector Assembly.**

by them hits the wire turns of the anode and creates a pulse of current traveling in these wires from the position of the hit towards both ends of each wire. The time it takes for this pulse to travel to the end of the wire and to get registered by the electronics[3] is proportional to the distance from the hit position to the corresponding edge of the detector and thus proportional to the corresponding coordinate of the hit. The signals from opposite edges of the detector are in this sense redundant and used together to increase the accuracy and to eliminate noise when possible. The equations for the coordinates used in case of the square

[3]This pulse is processed by the differential amplifiers for the noise reduction. For that reason there are actually two parallel wires wound for each direction. One of these has about 50V higher potential applied so that the electron cloud gets attracted much more to it than to its neighbor. This insures that only one wire carries the actual signal and the other carries only the electronic noise which should be identical for both and is taken care of by the differential amplifiers.

anode detectors are

$$X = k(t_r - t_l) \ ; \ Y = k(t_t - t_b) \tag{C.1}$$

where t_l, t_r, t_b, and t_t are the timing signals from left, right, top, and bottom edges of the detector, respectively, and k is the conversion constant (usually in mm/ns) extracted from the mask detector calibration. The arrival of the pulse to the particular edge of the detector serves as a stop signal for the proper time interval. The start signal[4] is the same for all four timings and is taken off the MCP; it is also used to obtain the time-of-flight information. The position and the time-of-flight resolution of these detectors is usually defined by the electronics used to register all the signals. The best resolution of the time-of-flight is around 25 picoseconds and is mostly defined by the MCP parameters. The position resolution of the detectors themselves is around 0.1mm (see fig. C.2). In spite of the fact that the wire turns are about 0.5mm from each other the resolution is usually much better than that. This is explained by the fact that the electron cloud is spread enough to hit several turns at the same time by creating a pulse in each wire loop. These pulses overlap and create a Gaussian shape pulse of about 10 nanoseconds duration with the peak position not necessarily in the exact discreet position of any of the wire loops. The detection efficiency of these PSD systems is around 10 -20% and is defined by the performance of the multi-channel plates .

The main feature that distinguishes delay line detectors from most of the other types of PSD's is its multi-hit capability. This brings up another parameter that describes the

[4]Any common signal can actually be used for the start of the position signals — when the difference is taken ($t_r - t_l$ or $t_t - t_b$), the arbitrary relative start time cancels out.

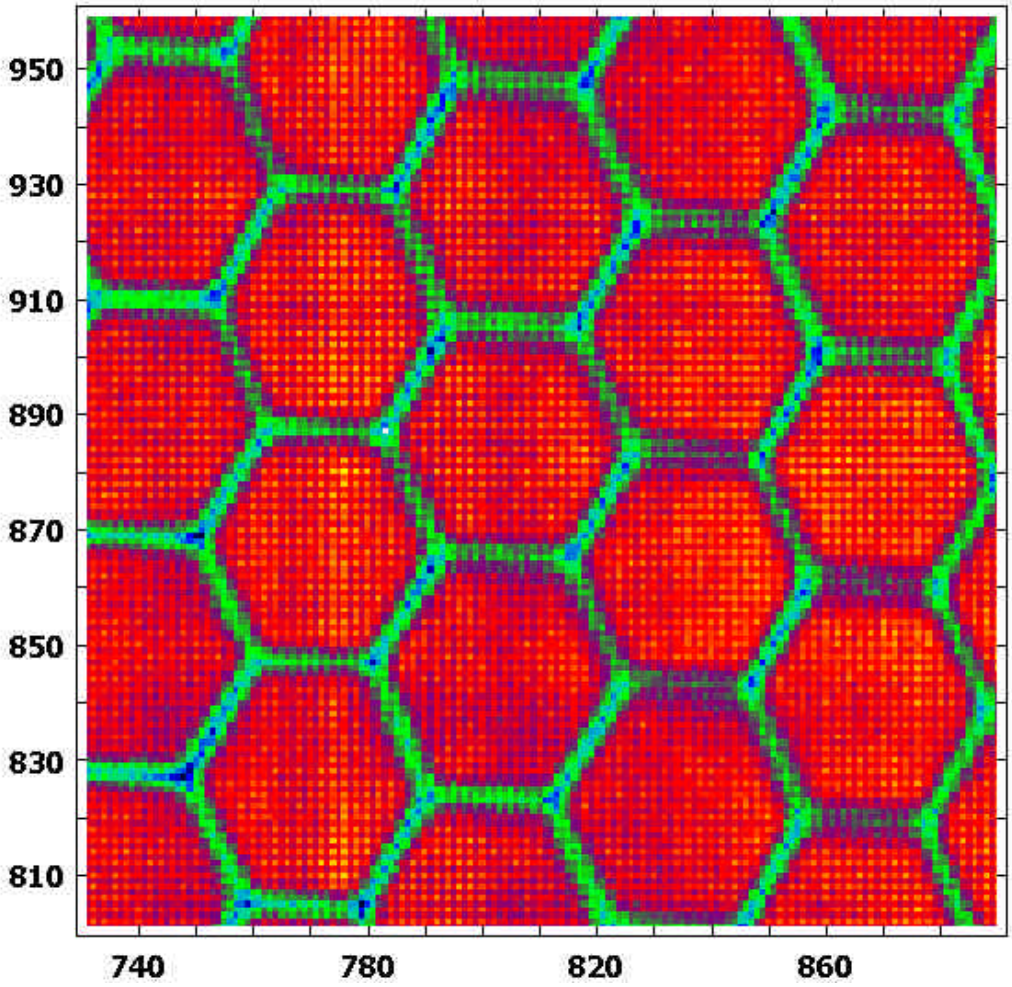

Figure C.2: Enlargement of a shadow mask image, obtained by a DLD80 (80mm) detector. The hexagons are 3 mm wide, the obstacles have a 0.2 mm width. One channel corresponds to approximately 0.08 mm.

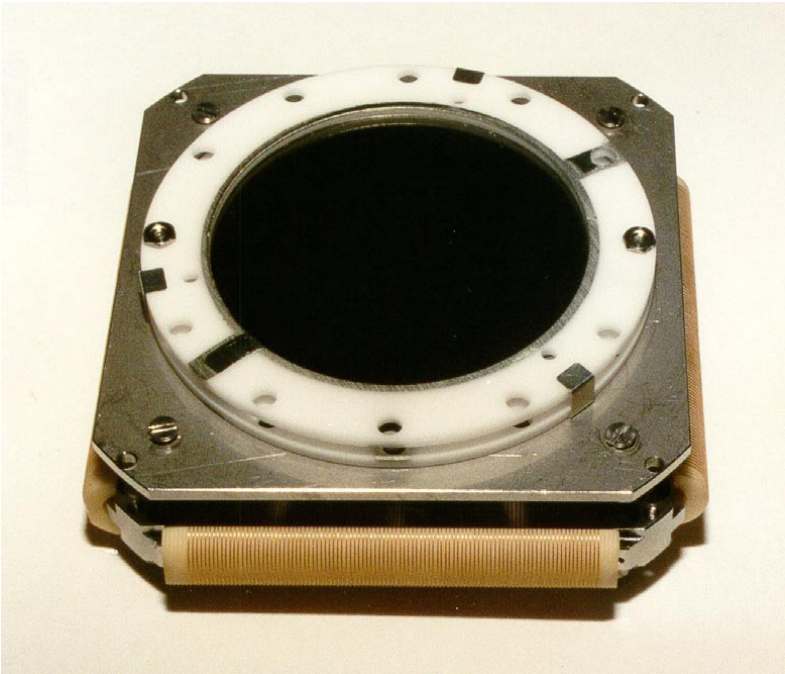

a)

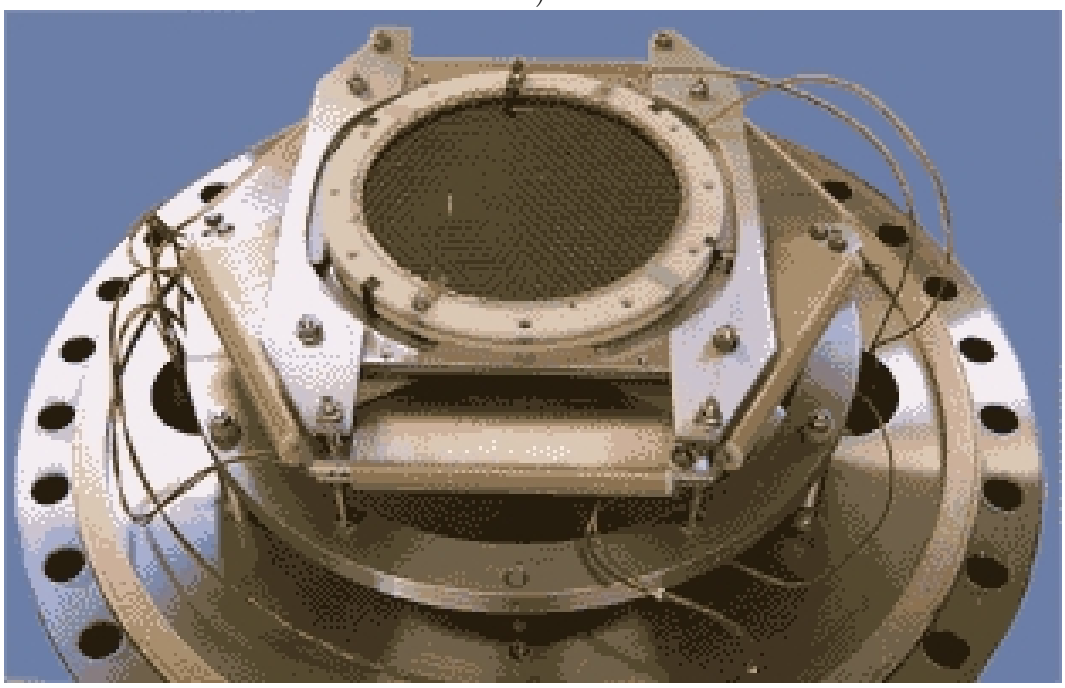

b)

Figure C.3: **RoentDek Delay Line Detectors.** Assembly of the a) square and b) hex anode delay line detectors.

delay line detector performance — its pulse-pair-resolution. For the electronics used in this experiment (the RoentDek detectors) this is around 10 nanoseconds. This means that if two particles hit the detector within this time period only one time-of-flight signal will be registered and the position information of the second or even both particles would be questionable. Again this is defined by the electronics used to register and analyze these signals. The best available electronics today produce a dead time of about 10 nanoseconds. As long as there is at least one module that has this dead time in the device chain that processes these timing signals, the pulse-pair-resolution of the system will be at least this long.

An important detail about the hit position information extraction with delay lines is the constant value of the so called time-sum. The time it takes for a signal to get from the hit position to the edge of the detector (say left) is given by $t_l - t_{mcp}$ where t_{mcp} is the time of the MCP signal. The time defined by $(t_l - t_{mcp}) + (t_r - t_{mcp}) = t_l + t_r - 2t_{mcp}$ ($t_t + t_b - 2t_{mcp}$ for the Y coordinate) defines the time it takes for the signal to travel from one side of the detector to the other and is thus constant and equal to the length of the wire of the proper layer divided by the speed of light. Of course that is only true if the t_l and t_r (t_t and t_b) signals belong to the same hit. Checking the signals against this condition helps to assign proper X and Y coordinates to the corresponding time-of-flight and to eliminate signals due to noise. The typical value of the time-sum is equal in nanoseconds to the size of the detector in mm (80mm detector has ≈80ns time-sum, for example).

The fact that the time-sum is usually longer than 10ns means that besides the particles

that hit the detector within 10ns from each other one must take special care with the particles that hit within a time interval equal to or less than the time-sum. The following table is an example of the time signals for two particles hitting the detector with the time-sum equal to 80ns:

hit #	t_{mcp}	t_l	t_r	X
1	0ns	60ns	20ns	-40
2	20ns	30ns	90ns	60

Unfortunately in the real experiment signals from different wires are collected into separate independent channels of the multi-hit time-to-digital converter (MTDC), so after the event digitization one has a set of sorted arrays of signals. For the above example this set looks like:

t_{mcp}	t_l	t_r
0	30	20
20	60	90

If one just starts calculating the coordinate by using the ordered signals in the MTDC channels the result would be $X_1 = 20 - 30 = -10$ and $X_2 = 90 - 60 = 30$, which is incorrect!! The right procedure includes the time-sum check of every possible pair of signals. This is just a small part of the hit reconstruction procedure discussed in section 2.3.1.

The figure C.5 shows the position of the second hit that takes place within 10ns from the first one that hits the center of the detector. The white area is where the reconstruction of the second hit time and coordinate information is impossible. Compare the results obtained for the square anode and the hex anode. The better results obtained with the hex anode are due to the extra redundancy in the position information. The three layers of the hex anode

are labelled U, V, and W and the information about the position along the corresponding directions is obtained as (with proper time-sum conditions)

$$\begin{cases} U = t_{u2} - t_{u1} \\ V = t_{v2} - t_{v1} \\ W = t_{w2} - t_{w1} \end{cases} \quad ; \quad \begin{cases} sum_u = t_{u2} + t_{u1} - 2t_{mcp} \\ sum_v = t_{v2} + t_{v1} - 2t_{mcp} \\ sum_w = t_{w2} + t_{w1} - 2t_{mcp} \end{cases} \tag{C.2}$$

but now besides these there is an extra relationship[5]

$$U + V + W = 0 \tag{C.3}$$

It is clear that the coordinate information for these detectors can be obtained from any pair of layers.

For example, the use of the hex anode together with special electronics and reconstruction software can dramatically improve the result of the multi-electron detection experiment.

www.RoentDek.com web site can be visited for more performance boosting tips, tricks and suggestions on the delay line detectors.

[5]The signs in this relationship depend on the direction chosen for each layer.

a)

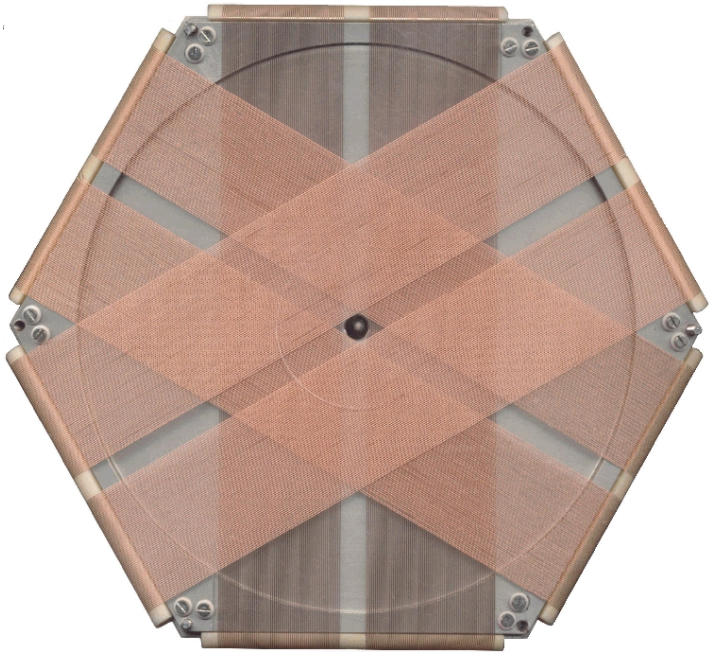

b)

Figure C.4: **Hex Delay Line Anodes.** a) Regular Hex anode HEX80, a delay-line anode with three layers for redundant multi-hit detection. b) Hex80/o - Hex anode with central hole 6.4mm diameter for primary beam transmission. The gap in each layer does not pose the problem due to redundant data obtained from the other two layers.

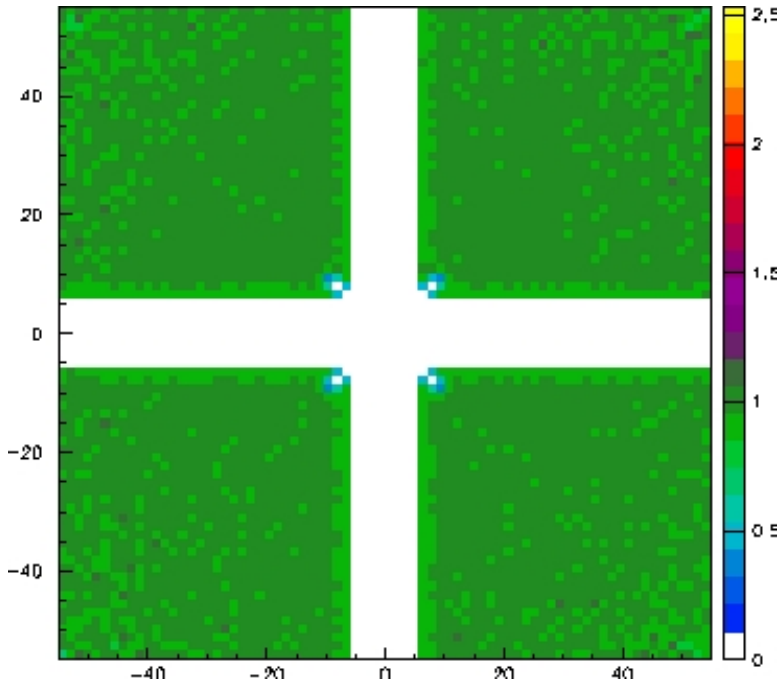

a)

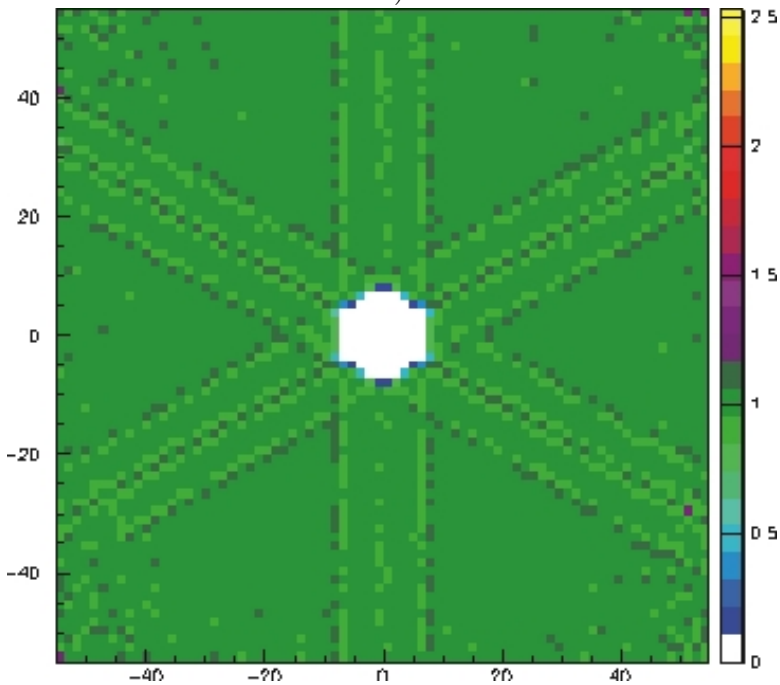

b)

Figure C.5: **Pulse Pair Resolution.** White area is where reconstruction of two hits is impossible due to the 10ns electronic dead-time in a) Square DL with Delta tpp = 2.5ns and b) Hexagonal DL with Delta tpp = 0ns.

Appendix D

Electron Momentum Reconstruction in the Magnetic Field

In this appendix two ways of calculating the electron transverse momentum are presented. While the first technique has been found to give a better physical picture of the process, the second one presents a much more precise derivation procedure resulting in the same system of equations for the final values of the momentum. All calculations have been done assuming that the electrons are moving in a constant magnetic field and the electric field is uniform in the transverse direction of the spectrometer, i.e., there are no electrostatic lens effects. Another assumption is that the electric field is parallel to the magnetic field. While the last condition is not always perfectly fulfilled the following equations easily can be extended to the case when the fields are not absolutely parallel, especially if the angle is small.

Intuitive Approach.

The final goal of this exercise is to get the initial electron transverse momentum (perpendicular to the magnetic field direction) as a function of the position of the hit on the detector and its time-of-flight. The transverse plane will be referred to as the XY plane[1] (the detector plane) and the magnetic field is assumed to go into the XY plane. Thus the electrons will move in counterclockwise direction. Respectively, the results for the opposite direction of the magnetic field will be referred to as the "clockwise" case.

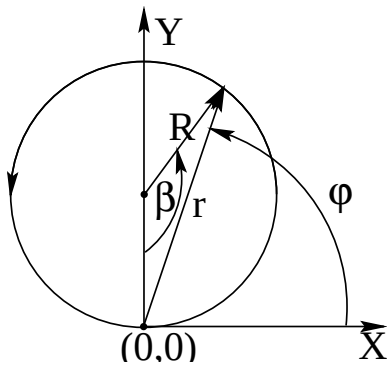

Let us start with the simple case — the electron initial momentum is along the positive X direction. Due to the Lorentz force the electron will be following a counterclockwise circular path in the Y>0 half plane. Recall that the electric field is always perpendicular to the XY plane and thus it does not affect the P_x and P_y components of the electron momentum. This is why the final equations for P_x and P_y do not have any explicit[2] dependence on the spectrometer electric field. The equation that describes the circle that the electron travels along is $r = 2R\sin\varphi$, where r and φ are the polar coordinates, and R is the

[1]The coordinate system chosen here for the convenience of the derivation is different from that used in the analysis section of this thesis. There the horizontal direction in the plane of the detector is taken to be the Z direction — the direction of light, vertical direction is Y, and the third direction is X — the direction of the electric field of the spectrometer, magnetic field and the X-ray polarization when the linearly polarized light is used. When dealing with the relative angular distributions such details as right-handedness of the coordinate system used should be very carefully taken care of when converting from the equations derived in this appendix to the equations used in the final analysis or the analyzing software programs.

[2]The position of the hit on the detector and the time-of-flight do depend on the spectrometer electric field. However, this dependence cancels out in the final values of P_x and P_y.

constant radius of the circle. From the basic geometry it can be shown that $\varphi = \beta/2$, where $\beta = \omega t$ and ω is the cyclotron frequency that can be found as follows:

$$\omega = \frac{V}{R} \ , \ \frac{V^2}{R} = \frac{F_l}{m} = \frac{qVB}{m} \ \Rightarrow \ V = \frac{qRB}{m} \ \Rightarrow \ \omega = \frac{qB}{m} = B\frac{e}{m_e} \ , \ P_\perp = RBe$$

where V is the value of the velocity in the XY plane, q is the charge of the particle, m is the mass of the particle, B is the value of the magnetic field, F_l is the Lorentz force and $P_\perp$ is the value of the electron momentum in the XY plane. Going back to the trajectory equation

$$r = 2R\sin\frac{\omega t}{2} \ \Rightarrow \ R = \frac{r}{2\sin\frac{\omega t}{2}} \ \Rightarrow \ P_\perp = \frac{rBe}{2\sin\frac{\omega t}{2}} = \frac{rm_e\omega}{2\sin\frac{\omega t}{2}}$$

The result is the value of the transverse electron momentum as a function of r, ω and t which can all be extracted from the measured parameters. This result does not depend on either the direction of the magnetic field nor the direction of the momentum, thus it only gives the its absolute value.

After a closer look at this expression, one will notice that if the electron makes one full circle and goes on the second one, that is $4\pi > \omega t > 2\pi$ the result becomes negative. This is an artifact caused by the original equation of the circle. Thus, to be exact, the expression should be

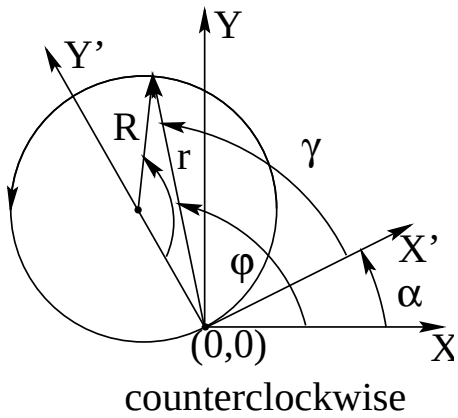

$$P_\perp = \frac{rm_e\omega}{2|\sin\frac{\omega t}{2}|} \tag{D.1}$$

Let us now consider the case when electron initial momentum has an angle α with respect to the X axis. This time $\gamma = \omega t/2$ and $\alpha = \varphi - \gamma \pm 2\pi$. As before $\varphi = \arctan\frac{Y}{X}$ — is the

polar angle[3]. Thus α is given by $\arctan\frac{Y}{X} - \frac{\omega t}{2} \pm 2\pi$. Now by means of equation D.1 one obtains

$$P_x = P_\perp \cdot \cos\alpha = P_\perp \cdot (\frac{X}{r}\cos\frac{\omega t}{2} + \frac{Y}{r}\sin\frac{\omega t}{2}) = \frac{m_e\omega}{2}(X\cot\frac{\omega t}{2} + Y)$$

Similarly, the expression for P_y is

$$P_y = \frac{m_e\omega}{2}(Y\cot\frac{\omega t}{2} - X)$$

So the final result for the ***counterclockwise*** direction of electron motion is

$$\begin{cases} P_x = \frac{m\omega}{2\sin\frac{\omega t}{2}}(X\cos\frac{\omega t}{2} + Y\sin\frac{\omega t}{2}) \\ P_y = \frac{m\omega}{2\sin\frac{\omega t}{2}}(Y\cos\frac{\omega t}{2} - X\sin\frac{\omega t}{2}) \end{cases} \Leftrightarrow \tag{D.2}$$

$$\Leftrightarrow \begin{cases} \boldsymbol{P_x = \frac{m_e\omega}{2}(X\cot\frac{\omega t}{2} + Y)} \\ \boldsymbol{P_y = \frac{m_e\omega}{2}(Y\cot\frac{\omega t}{2} - X)} \end{cases} \tag{D.3}$$

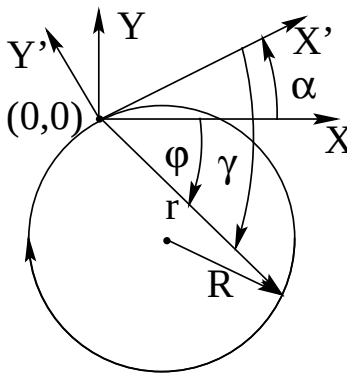

clockwise

By repeating this whole derivation procedure with the opposite magnetic field direction the result can be obtained for the ***clockwise*** direction of electron motion. After noticing that $\alpha = \gamma - \varphi \pm 2\pi$ and thus $\alpha = \arctan\frac{Y}{X} - \frac{\omega t}{2} \pm 2\pi$ the rest of derivation is identical

$$\begin{cases} \boldsymbol{P_x = \frac{m_e\omega}{2}(X\cot\frac{\omega t}{2} - Y)} \\ \boldsymbol{P_y = \frac{m_e\omega}{2}(Y\cot\frac{\omega t}{2} + X)} \end{cases} \tag{D.4}$$

[3]This formula gives the right result only in the top two quadrants; in the bottom two a special care should be taken.

These formulae work for all angles and all values of the time-of-flight, in spite of the fact that the absolute value sign in result D.1 was ignored and $arctan\frac{Y}{X}$ is not always equal to the polar angle φ. One can verify this by running simple checks with different values of electron momentum. It also follows from a more precise derivation that comes next.

Equations of Motion Approach.

Start with $e\,\overline{V} \times \overline{B} = m\overline{a} \;\Rightarrow\; \overline{a} = \overline{V} \times \overline{B}\, e/m$,

or after opening up the cross product with $\overline{B} = \begin{pmatrix} 0 \\ 0 \\ B \end{pmatrix} \Rightarrow$

$$\dot{V}_x = V_y \cdot \frac{eB}{m} \qquad \dot{V}_y = -V_x \cdot \frac{eB}{m} \tag{D.5}$$

Take the time derivative of the above

$$\ddot{V}_x = \dot{V}_y \cdot \frac{eB}{m} \qquad \ddot{V}_y = -\dot{V}_x \cdot \frac{eB}{m} \tag{D.6}$$

and substituting (D.5) into equations (D.6) one obtains

$$\ddot{V}_x + V_x \cdot \left(\frac{eB}{m}\right)^2 = 0 \qquad \ddot{V}_y + V_y \cdot \left(\frac{eB}{m}\right)^2 = 0$$

together with the following initial conditions

$$V_x|_{t=0} = V \cdot \cos\alpha \qquad V_y|_{t=0} = V \cdot \sin\alpha$$

the resulting velocities as a function of time are given

$$\begin{cases} V_x = V \cdot \cos(\alpha + \omega t) \\ V_y = V \cdot \sin(\alpha + \omega t) \end{cases} \qquad with \;\; \omega = \pm \frac{eB}{m}$$

As one can see, the direction of the rotation is not well defined from these equations — either positive or negative ω gives the good solution. So all the precautions that have been taken before to determine the direction of the rotation, are still in order.

Integrating the above velocities with the initial conditions on the coordinates $X|_{t=0} = 0$, $Y|_{t=0} = 0$ gives

$$\begin{cases} V_x = V \cdot \cos(\alpha + \omega t) \\ V_y = V \cdot \sin(\alpha + \omega t) \end{cases}$$

Some useful trigonometric formulae:
$\cos(\alpha \pm \beta) = \cos\alpha\cos\beta \mp \sin\alpha\sin\beta$
$\sin(\alpha \pm \beta) = \sin\alpha\cos\beta \pm \sin\alpha\cos\beta$
$1 - \cos(2\alpha) = 2\sin^2\alpha$
$\sin(2\alpha) = 2\sin\alpha\cos\alpha$
The last pair is the result of the first two in case $\alpha = \beta$

By means of the trigonometric formulae the above system of equations can be rearranged in the following way

$$\begin{cases} \omega X = V \cdot (\sin\alpha\cos(\omega t) + \cos\alpha\sin(\omega t) - \sin\alpha) \\ \omega Y = V \cdot (\cos\alpha - \cos\alpha\cos(\omega t) + \sin\alpha\sin(\omega t)) \end{cases}$$

The final goal is to get P_x and P_y as a function of coordinates on the detector X, Y, time-of-flight and the cyclotron frequency ω. Recall that $P_x = mV_x|_{t=0} = mV\cos\alpha$ and $P_y = mV_y|_{t=0} = mV\sin\alpha$. By substituting this into the above...

$$\begin{cases} m\omega X = P_y\cos(\omega t) + P_x\sin(\omega t) - P_y \\ m\omega Y = P_x - P_x\cos(\omega t) + P_y\sin(\omega t) \end{cases} \Leftrightarrow \begin{cases} m\omega X = P_y(\cos(\omega t) - 1) + P_x\sin(\omega t) \\ m\omega Y = P_x(1 - \cos(\omega t)) + P_y\sin(\omega t) \end{cases}$$

Now by converting to half the angle

$$\begin{cases} m\omega X = 2(P_y\sin(\omega t/2) + P_x\cos(\omega t/2))\sin(\omega t/2) \\ m\omega Y = 2(P_y\cos(\omega t/2) - P_x\sin(\omega t/2))\sin(\omega t/2) \end{cases}$$

Finally solving for P_x and P_y

$$\begin{cases} P_x = \frac{m\omega}{2\sin(\omega t/2)}(X\cos(\omega t/2) + Y\sin(\omega t/2)) \\ P_y = \frac{m\omega}{2\sin(\omega t/2)}(Y\cos(\omega t/2) - X\sin(\omega t/2)) \end{cases} \Rightarrow \tag{D.7}$$

$$\begin{cases} \boldsymbol{P_x = m\omega(X\cot(\omega t/2) + Y)/2} \\ \boldsymbol{P_y = m\omega(Y\cot(\omega t/2) - X)/2} \end{cases} \quad \boldsymbol{(counterclockwise)} \tag{D.8}$$

If the ω is replaced by $-\omega$ everywhere, one gets equations for the "clockwise" rotation, as in the direction of the electrons along their circular trajectory:

$$\begin{cases} \boldsymbol{P_x = m\omega(X\cot(\omega t/2) - Y)/2} \\ \boldsymbol{P_y = m\omega(Y\cot(\omega t/2) + X)/2} \end{cases} \quad \boldsymbol{(clockwise)} \tag{D.9}$$

Both t and ω can be extracted from the experimental data. The use of these formulae is the most convenient and does not accumulate large error bars.

Appendix E

Exact Wiggles Spectrum Curve Calculation

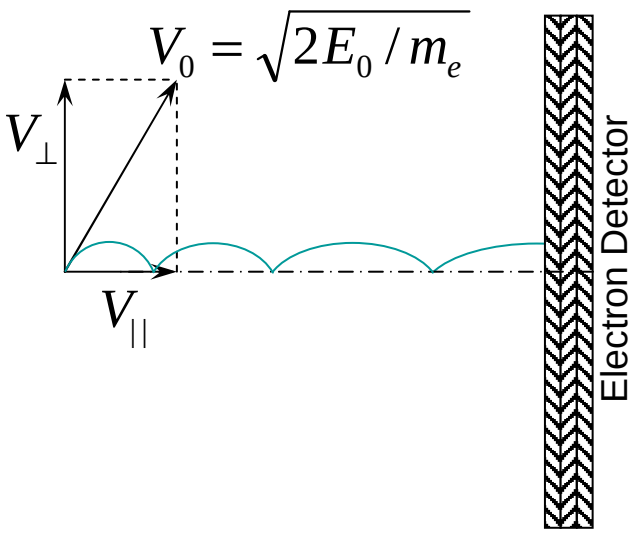

In addition to the technique described in the calibration part of section 2.3 there is another way to obtain the cyclotron period (or frequency), absolute time-zero and the electric field of the spectrometer at the same time. This could be done by fitting the wiggles spectrum obtained for the mono-energetic electron with the analytical curve, as done in the bottom part of figure 2.17. To obtain this analytical curve (the distance of the electron hit from the center of the detector as a function of its time-of-flight) let us first consider the simple case of a single acceleration region that electrons fly

through before they hit the detector. Equation D.1 can be rewritten as

$$r = 2\frac{V_\perp}{\omega}|\sin\frac{\omega t}{2}|$$

where t is the time-of-flight plotted along the x-axis of the wiggle spectrum, r is the distance plotted along its y-axis, ω is the cyclotron frequency, and $V_\perp$ is the initial electron velocity in the plane of the detector.

Next, $V_\perp$ needs to be expressed in terms of the known values:

$$V_\perp = \sqrt{\frac{2E_\circ}{m_e} - V_\parallel^2}$$

where $V_\parallel$ is the initial electron velocity along the field of the spectrometer, and $E_\circ$ is the electron initial energy. The $V_\parallel$ in turn can be derived from the time-of-flight and spectrometer parameters:

$$V_\parallel = \frac{S}{t} - \frac{\mathscr{E}e}{2m_e}t$$

where $\mathscr{E}$ is the spectrometer electric field. So the final result is

$$r = 2\frac{\sqrt{\frac{2E_\circ}{m_e} - (\frac{S}{t} - \frac{\mathscr{E}e}{2m_e}t)^2}}{\omega}|\sin\frac{\omega t}{2}| \tag{E.1}$$

or, if the absolute time-zero is fitted also:

$$r = 2\frac{\sqrt{\frac{2E_\circ}{m_e} - (\frac{S}{t-t_z} - \frac{\mathscr{E}e}{2m_e}(t-t_z))^2}}{\omega}|\sin\frac{\omega(t-t_z)}{2}| \tag{E.2}$$

This is the final form of the fitting function. As one can see, the list of fitting parameters includes ω, t_z, S, $\mathscr{E}$, and even $E_\circ$. A similar but more complicated formula can be obtained for the case of two acceleration regions. In that case the expression for $V_\parallel$ would be a solution

of the cubic equation (see Appendix F for a similar derivation). It is quite often the case that the time-of-flight spread of the electron distribution is much smaller than the time-of-flight of the zero-momentum electron, which usually is the central position of that distribution. Then equation E.2 can be approximated by:

$$\text{if } \triangle t \ll t_\circ \text{ then } r \approx 2\frac{\sqrt{\frac{2E_\circ}{m_e} - (\frac{\mathscr{E}e}{2m_e}(t-t_\circ))^2}}{\omega}|\sin\frac{\omega(t-t_z)}{2}| \tag{E.3}$$

where $t_\circ$ is the center of the distribution. This functional form will still work for the fitting process in most cases, but now it has an easily recognizable form: it is an equation of the circle times the oscillation equation. Another advantage of this formula is that, as long as the preceding condition holds, the formula works for any spectrometer design, no matter how many different field regions it has.

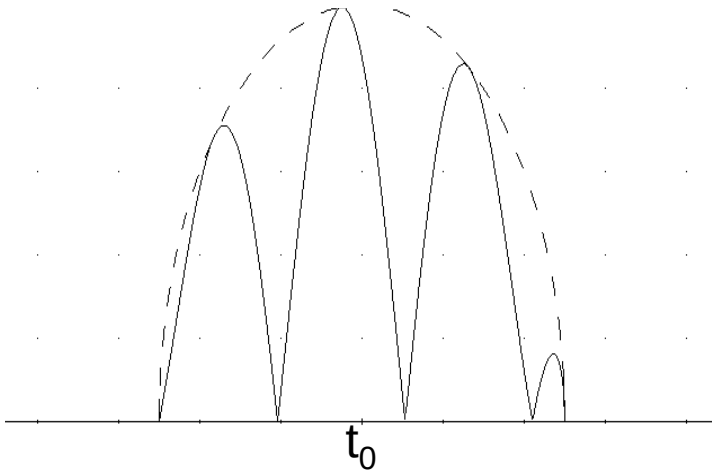

Appendix F

The PIPICO Spectrum Fitting

Most of the features (stripes and islands) of the PhotoIon-PhotoIon-Coincidence (PIPICO) spectrum can be fitted with analytical curves. There are a couple of rules of thumb that help in identifying the coincidence features. First of all the stripe should be relatively sharp — the recoils originating from any kind of Coulomb explosion or molecular dissociation are subject to momentum conservation.

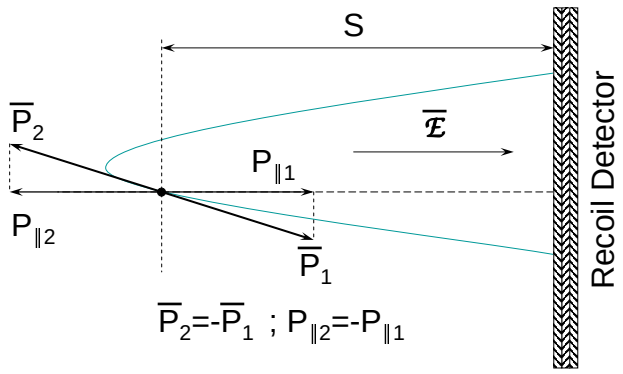

The features of the PIPICO spectrum are defined by the relationship between the times-of-flight of the recoils that originated from the breakup of the same molecule. These times-of-flight are defined by the initial velocities of these recoils in the lab frame, not the center-of-mass frame. The momentum conservation requirement can be applied to the lab frame momentum vectors only if they are reasonably close to the corresponding center-of-mass momenta, i.e., if the center-of-mass momentum before

the dissociation is much smaller than the relative momentum of recoils obtained during the dissociation. It is the component of the initial center-of-mass momentum along the time-of-flight direction that defines the width of the PIPICO spectrum stripes. If there are more than two recoils[1] of a similar momentum the picture will obviously get much more washed out.

Consider the symmetric Coulomb explosion that results in two recoils of the same mass m and charge q. From momentum conservation their velocities are of the same value and opposite sign. From now on the subscript $\|$ will be implicit since the only direction that is of interest in this section is the direction of the electric field. The equations for the distances traveled to the detector in a single acceleration region would be:

$$\begin{cases} S = vt_1 + at_1^2/2 \\ S = -vt_2 + at_2^2/2 \end{cases} \tag{F.1}$$

After adding and subtracting these two equations one obtains:

$$\begin{cases} v = a\triangle t/2 \\ 2S = -v\triangle t + a\triangle t^2/2 + at_1t_2 \end{cases} \quad \text{where } \triangle t = t_2 - t_1 \tag{F.2}$$

The top equation can be rewritten to get the well known "turn around" time $\triangle t = 2v/a$. Eliminating v from equations F.1, one obtains:

$$2S = -a\triangle t^2/2 + a\triangle t^2/2 + at_1t_2 \;\Rightarrow\; t_1t_2 = 2s/a$$

Or in the final fitting form:

$$\boldsymbol{t_2 = \frac{t_0^2}{t_1}} \;\text{ where } \boldsymbol{t_0 = \sqrt{\frac{2Sm}{Eq}}} \tag{F.3}$$

[1]The TOF_1/ TOF_2 picture for a three-particle breakup still looks quite sharp, but is not described by the present equations and, thus, does not agree very well with the derived fit (see L+M channel of fig. 3.9).

In this case t_0 is the time of flight of the zero-momentum recoil. For a more general case of recoils with masses m_1 and m_2 and charges q_1 and q_2 the system of equations F.1 will look as follows:

$$\begin{cases} S = Pt_1/m_1 + Eq_1t_1^2/(2m_1) \\ S = -Pt_2/m_2 + Eq_2t_2^2/(2m_2) \end{cases} \quad \text{given that } \; P_1 = -P_2 = P \text{ recoil momentum.}$$

Rewriting this to cancel out the momentum value:

$$\begin{cases} m_1S/t_1 = Pt_1 + Eq_1t_1/2 \\ m_2S/t_2 = -Pt_2 + Eq_2t_2/2 \end{cases} \Rightarrow \frac{S(m_1t_2 + m_2t_1)}{t_1t_2} = \frac{E}{2}(q_1t_1 + q_2t_2)$$

The last expression can be rewritten in a form of a simple quadratic equation:

$$t_2^2(Eq_2t_1) + t_2(Eq_1t_1^2 - 2Sm_1) - 2Sm_2t_1 = 0$$

The solution of which is:

$$\boldsymbol{t_2 = b + \sqrt{b^2 + \frac{2Sm_2}{Eq_2}}; \;\; b \equiv \frac{Sm_1}{t_1Eq_2} - \frac{q_1}{2q_2}t_1} \tag{F.4}$$

The FORTRAN function t1t2(tof,...) at the end of this chapter takes as an input the time-of-flight t_1 of the first recoil in *ns*, the electric field in *V/cm*, the spectrometer distance in *cm*, masses and charges of the first and second recoil in *a.m.u.* and *a.u.*, respectively, and returns the time-of-flight t_2 of the second recoil. The non-zero value of the "`shift`" parameter is sometimes useful for correcting for the short high-field region between the end of the spectrometer and the detector. This is just a first order correction, however.

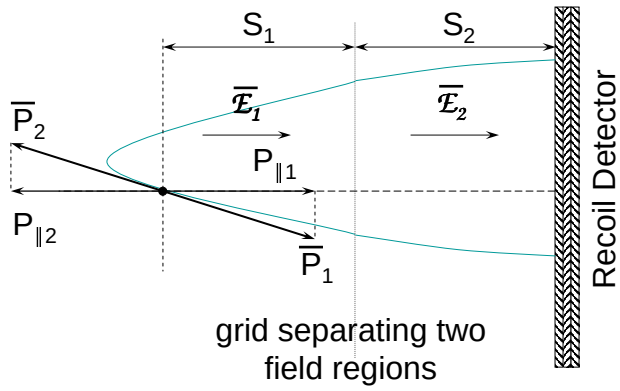

If more accurate results are desirable, the use of the function for the two electric field regions is recommended (see function pipico2(tof,...) below for example). The first step in its derivation would be the same as for any other spectrometer field configuration. It is also a procedure that always takes place in any COLTRIMS analysis anyway — calculation of the initial velocity (or the momentum) from the time-of-flight — whether it is an analytical solution, iteration function or a look up table. For the case of two acceleration regions it can be calculated exactly:

$$\begin{cases} S_1 = v_\circ t_1 + a_1 t_1^2/2 \\ S_2 = (v_\circ + a_1 t_1) t_2 + a_2 t_2^2/2 \\ t = t_1 + t_2 \end{cases} \tag{F.5}$$

Here $v_\circ$ is the initial velocity of the first recoil that needs to be found; S_1, S_2 are the lengths of the first and second region; t_1, t_2 are the times spent by the first recoil in the corresponding region; t is the total (measured) time-of-flight of the first recoil; a_1, a_2 are the proper accelerations of the first recoil given by $a_1 = E_1 q_1/m_1$ and $a_2 = E_2 q_1/m_1$. After canceling out $v_\circ$ and substituting $t - t_1$ for t_2:

$$\begin{cases} v_\circ = \frac{S_1}{t_1} - \frac{a_1 t_1}{2} \\ \frac{S_1}{t_1} = \frac{S_2}{t - t_1} - \frac{a_2 (t - t_1)}{2} - \frac{a_1 t_1}{2} \end{cases}$$

Rearranging the second equation yields:

$$t_1^3 + t_1^2 \frac{2a_2 - a_1}{a_1 - a_2} t + t_1 \frac{2S_2 + 2S_1 - a_2 t^2}{a_1 - a_2} - \frac{2S_1 t}{a_1 - a_2} = 0$$

The roots of this equation can by found by using the standard cubic equation solutions formulae (see the function cubic(a,b,c) of file pipico.f below). Care should be taken to choose the proper root. Also, if using a computer program to calculate the final root values, the error will be minimized if the answer is calculated in units of $t_\circ$ (time-of-flight of zero momentum recoil), i.e., making the substitution $t_1 = xt_\circ$, and then solving for x. The FORTRAN function below takes care of all of these nuances. The function also can be used for calculation of the electron initial velocity in a time-focussing spectrometer.

After the value of t_1 is found from $v_\circ$ by using the top equation from F.5, the initial velocity of the second recoil is given by $v_\circ \frac{m1}{m2}$. Given the initial velocity, the calculation of the time-of-flight for the second recoil is trivial. Figure F.1 shows the PIPICO spectrum with all the breakup channels fitted with the curves generated by the function pipico(tof,...) for different recoil masses.

file t1t2.f

```
      function t1t2(tof,mu1,mu2,qu1,qu2,dist,field,shift)

      real tof, mu1, mu2, qu1, qu2, shift, dist, field
      real x, xshift, yshift, m1, m2, q1, q2, z, s, E

c     print *,dist,field,shift
```

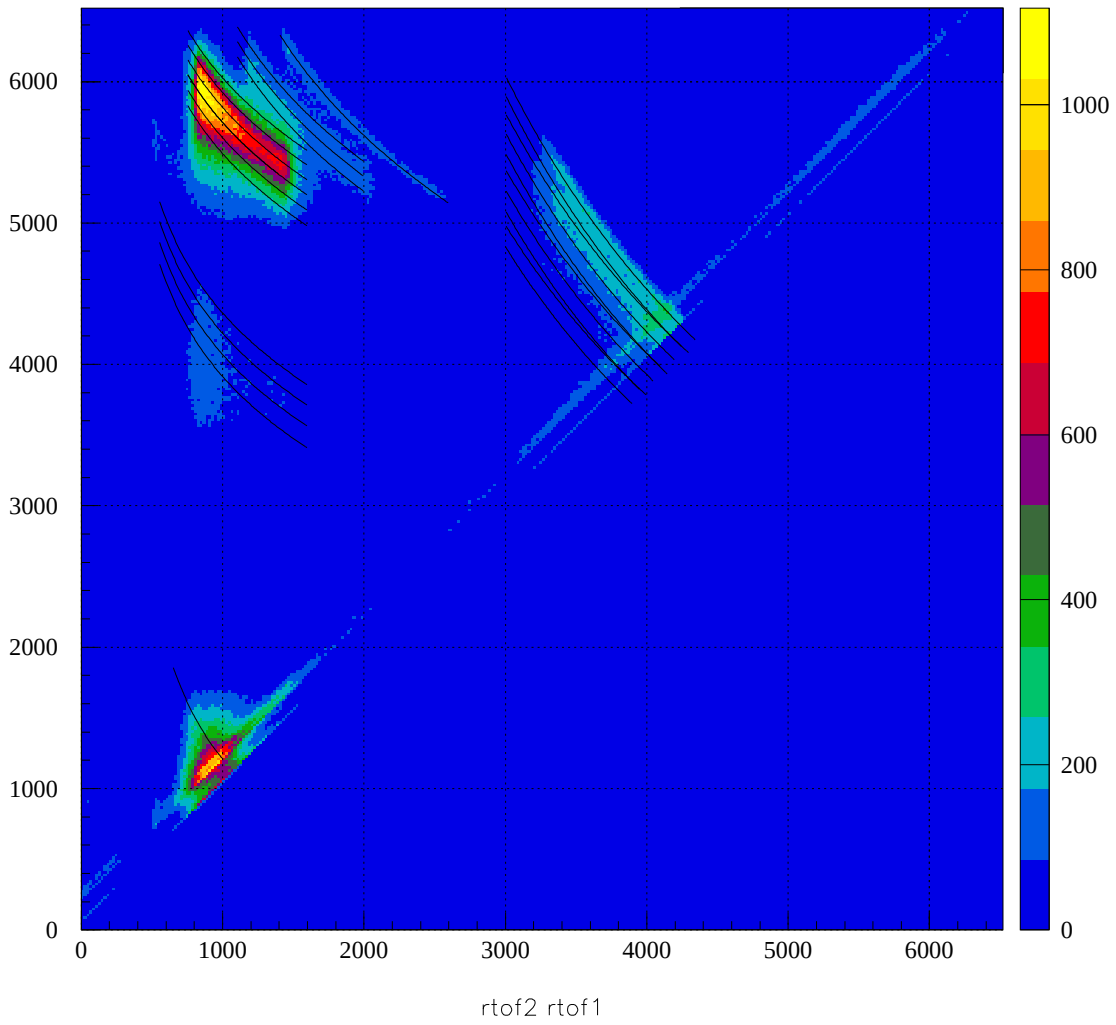

Figure F.1: C_2H_6 PIPICO With Analytical Curves.

```
      E = field*100.
      s = dist/100.
      xshift=shift*sqrt(mu1/qu1)
      yshift=shift*sqrt(mu2/qu2)
      m2=mu1*1.661E-27
      m1=mu2*1.661E-27
      q1=qu1*1.60322E-19
      q2=qu2*1.60322E-19

      x=(tof-xshift)*1.E-9
c     x=(tof/shift)*1.E-9
      if(m1.eq.m2.and.q1.eq.q2)then
          t1t2 = 2*s*m1/(q1*E*x)
      else
          z=s*m1/(q2*E*x)-q1*x/(2.*q2)
          t1t2=z+sqrt(2.*s*m2/(q2*E)+z**2)
      endif
      t1t2=(t1t2*1.E9 + yshift)
c     t1t2=t1t2*1.E9*shift

      end
```

file pipico2.f

```
      function pipico2(tof,mu1,mu2,qu1,qu2,dist1,F1,dist2,F2,sh)
      implicit none
      real tof, mu1, mu2, qu1, qu2, shift, dist1, dist2, F1, F2, sh
      real m1, m2, q1, q2, z, s1, E1, s2, E2, pipico2
      real a1, a2, v1, v2, t, t1, t2  ! derived
      double precision cubic  ! function
c     real cubic  ! function
c     real time

c     print*,dist1,f1,dist2,f2,sh

      E1 = F1*100.    ! to get v/m
      s1 = dist1/100.  ! to get m
```

```
      E2 = F2*100.    ! to get v/m
      s2 = dist2/100.  ! to get m
      m1=mu1*1.661E-27
      m2=mu2*1.661E-27
      q1=qu1*1.60322E-19
      q2=qu2*1.60322E-19
      a1 = E1*q1/m1 ! acc. first ion, first region
      a2 = E2*q1/m1 ! acc. first ion, second region
      t=(tof-sh)*1.E-9
      t1 = cubic(t*(2*a2-a1)/(a1-a2),
     *             (2*s1+2*s2-a2*t*t)/(a1-a2),t*2*s1/(a2-a1))
c     print *,'t',t,t1
      v1 = s1/t1-a1*t1/2
      v2 = -m1*v1/m2
c     print *,'v', v1,v2,a1,a2,s1,s2
      a1 = E1*q2/m2 ! acc. second ion, first region
      a2 = E2*q2/m2 ! acc. second ion, second region
      t2 = (sqrt(v2*v2+2*a1*s1+2*a2*s2) - sqrt(v2*v2+2*a1*s1))/a2
     *     + (sqrt(v2*v2+2*a1*s1)-v2)/a1
      pipico2=(t2*1.E9 + sh)
c     print *,t2,pipico2
      end

C*****************************************************************
      double precision function cubic(a,b,c)
c     the real root of the cubic equation with coefficient 1,a,b,c
C*****************************************************************

c     MAKE SURE TO CHOOSE THE RIGHT ROOT IN CASE OF 2 OR 3 REAL
      implicit none
      real a, b, c
      double precision n, aa, bb, cc, q, r, d, s, t, z, z2, z3, PI
      PI = 3.14159265359
c     print *, a, b, c
          n = EXP(((log(sqrt(a*a))+2*log(sqrt(b*b))
     *            +3*log(sqrt(c*c))))/14.)
      aa = a/n
          bb = b/n**2
          cc = c/n**3
c     print *, '*', n, aa, bb, cc
      q = (3.*bb-aa*aa)/9.
      r = (9.*aa*bb-27.*cc-2.*aa*aa*aa)/54.
```

```
      d = q*q*q + r*r
c     print *,q,r,d
      if(d.le.0.)then
           t = acos(r/sqrt(-q*q*q))
           z3 = 2.*sqrt(-q)*cos(t/3.) - aa/3 !real root #1 right most
           z2 = 2.*sqrt(-Q)*cos((T+2.*PI)/3.) - aa/3.; ! real root #2
           z = 2.*sqrt(-Q)*cos((T+4.*PI)/3.) - aa/3.; ! real root #3 same if D=0
c          print *,'all real', n*z, n*z2, n*z3
      else
           if(r+sqrt(d).gt.0.) then
          s = (R+sqrt(D))**(1./3.)
           else
          s = -(-R-sqrt(D))**(1./3.)
           endif
           if(r-sqrt(d).gt.0.) then
          t = (R-sqrt(D))**(1./3.)
           else
          t = -(-R+sqrt(D))**(1./3.)
           endif
           z = s + t - aa/3.
      endif
      cubic = z*n
      end
```

Appendix G

Fitting Photo-Electron Angular Distribution

Fitting Function Form

The form of the fitting function used for extracting the complex amplitudes can be obtained from the simplified treatment of the photo-effect phenomenon in molecules.

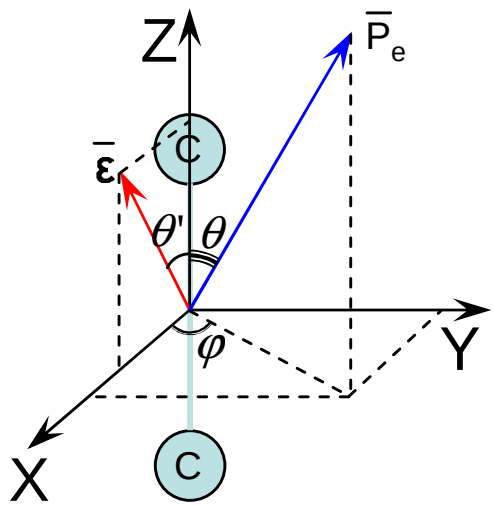

The standard approach is to treat the problem using perturbation theory. In the electric dipole approximation the cross section for the photoionization process is proportional to the square of the transition matrix element — $\langle\psi_b|\hat{\boldsymbol{\varepsilon}}\cdot\bar{\mathbf{r}}|\psi_a\rangle^2$ — for a transition from the ground state (of the core electron in this case) to a continuum wave function. ψ_b and ψ_a are the final and the initial states of the electron, respectively. In the body-fixed-frame coordinate system the electric dipole operator for linearly polarized light with polarization direction in

the XZ plane can be rewritten as

$$\left(\frac{4\pi}{3}\right)^{1/2}\left(Y_1^0(\hat{\mathbf{r}})\cos\theta' + 1/\sqrt{2}\cdot\left(Y_1^{-1}(\hat{\mathbf{r}}) - Y_1^1(\hat{\mathbf{r}})\right)\sin\theta'\right)r \tag{G.1}$$

where θ' is the longitudinal angle of the polarization direction. Since the molecular potential is cylindrically symmetric, m is a good quantum number and the initial state of the k-shell orbital, from which the electron is removed, in general can be expanded as

$$\psi_a = \sum_{l=0}^{\infty} R_{al}(r) Y_l^0(\hat{\mathbf{r}}) \tag{G.2}$$

The final state of the ejected photoelectron is a continuum wavefunction $\psi_p^{(-)}(\bar{\mathbf{r}})$ constructed in such a way that in the asymptotic region of large r it represents the superposition of the plane wave propagating in the direction of the photoelectron momentum $\boldsymbol{p}$ and a converging spherical wave. It is convenient to first present this function as (see expression (5) of [14])

$$\psi_p^{(-)} = \frac{1}{\sqrt{p}}\sum_{l,\lambda} F_{pl\lambda}(\bar{\mathbf{r}}) i^l e^{-i\eta_l} (Y_l^\lambda(\hat{\mathbf{p}}))^* \tag{G.3}$$

where η_l are the Coulomb phase shifts. The functions $F_{pl\lambda}(\bar{\mathbf{r}})$ do not depend on the direction of the electron momentum $\boldsymbol{p}$ and are the complex conjugate of solutions of the following Schrödinger equation multiplied by a constant factor — $F_{pl\lambda}(\bar{\mathbf{r}}) = C_{l\lambda}\cdot\psi^*_{pl\lambda}(\bar{\mathbf{r}})$

$$\left(\frac{p^2}{2} + \nabla^2 - U(\bar{\mathbf{r}})\right)\psi_{pl\lambda}(\bar{\mathbf{r}}) = 0 \tag{G.4}$$

where $U(\bar{\mathbf{r}})$ is the "frozen" potential seen by the photoelectron due to the nuclei and $N-1$ electrons of the molecule. By going to the asymptotic region of high r this potential can be

replaced by a central potential. The $\psi_p^{(-)}$ will become

$$\frac{1}{\sqrt{p}}\sum_{l,\lambda} C_{l\lambda} i^l e^{-i\eta_l} R_{pl}(r) Y_l^\lambda(\hat{\mathbf{r}})(Y_l^\lambda(\hat{\mathbf{p}}))^* \tag{G.5}$$

where $R_{pl}(r)$ are the radial functions that are solutions of the asymptotic Schrödinger equation

$$\frac{1}{r^2}\frac{d}{dr}\left(r^2\frac{dR_{pl}(r)}{dr}\right) + \left(p^2 - \frac{l(l+1)}{r^2} - 2u(r)\right) R_{pl}(r) = 0, \quad \text{where} \quad u(r) = \lim_{r\to\infty} U(\bar{\mathbf{r}}) \tag{G.6}$$

On the other hand this asymptotic form should be given by a superposition of the plane wave and the converging spherical wave

$$e^{i\bar{\mathbf{k}}\cdot\bar{\mathbf{r}}} + \frac{f(k,\theta_r)}{r}e^{-ikr}\ ; \text{where } \bar{\mathbf{k}} = \frac{\bar{\mathbf{p}}}{\hbar}\ , \text{or just } \bar{\mathbf{k}} = \bar{\mathbf{p}} \text{ in a.u.} \tag{G.7}$$

It can be shown (see section 123 of [44] for example) that by setting these two forms equal to each other the values of $C_{l\lambda}$ can be found to be simply 4π.

Another look at equation G.4 can reveal other important properties of functions $\psi_{pl\lambda}(\bar{\mathbf{r}})$. The potential $U(\bar{\mathbf{r}})$ for the linear molecule can be rewritten as $U(r,\theta_r)$ if the Z axis is taken to be along the molecule, which means that the projection of the angular momentum on the Z axis is a good quantum number and the solution of equation G.4 can be represented by $\psi_{pl\lambda}(\bar{\mathbf{r}}) = \Psi_{pl\lambda}(r,\theta_r)\cdot\Phi_\lambda(\phi_r)$ where $\Phi_\lambda(\phi_r) = e^{i\lambda\phi}/\sqrt{2\pi}$. Now that function $\Psi_{pl\lambda}(r,\theta_r)$ does not depend on angle ϕ_r it can be expanded in terms of Legendre polynomials:

$$\psi_{pl\lambda}(\bar{\mathbf{r}}) = \Phi_\lambda(\phi_r)\sum_{l'} \mathcal{C}_{pl\lambda l'}\mathcal{R}_{p\lambda l'}(r) P_{l'}(\cos\theta_r) \tag{G.8}$$

where $\mathcal{C}_{pl\lambda l'}$ are some constants and $\mathcal{R}_{p\lambda l'}(r)$ are some radial functions. The final form of the

$\psi_p^{(-)}$ can now be written as

$$\psi_p^{(-)} = \frac{4\pi}{\sqrt{p}} \sum_{l,\lambda} i^l e^{-i\eta_l} (Y_l^\lambda(\hat{\mathbf{p}}))^* \Phi_\lambda(\phi_r) \sum_{l'} \mathcal{C}_{pl\lambda l'} \mathcal{R}_{p\lambda l'}(r) P_{l'}(\cos\theta_r) \tag{G.9}$$

Finally, note that if the molecule is symmetric, i.e., $U(r,\theta_r) = U(r,\pi-\theta_r)$ than the wavefunctions $\psi_{pl\lambda}(\bar{\mathbf{r}})$ in G.8 should have a definite symmetry too. This means that expansion G.8 can have only odd or only even Legendre polynomials. To satisfy the asymptotic form of the final electron state given by G.7 (see (123,9) of [44]) the function $\psi_p^{(-)}$ should be given by

$$\begin{aligned}\psi_p^{(-)} = \frac{4\pi}{\sqrt{p}} \Bigg(&\sum_{\text{even } l,\lambda} i^l e^{-i\eta_l} (Y_l^\lambda(\hat{\mathbf{p}}))^* \Phi_\lambda(\phi_r) \sum_{\text{even } l'} \mathcal{C}_{pl\lambda l'} \mathcal{R}_{p\lambda l'}(r) P_{l'}(\cos\theta_r) + \\ &+ \sum_{\text{odd } l,\lambda} i^l e^{-i\eta_l} (Y_l^\lambda(\hat{\mathbf{p}}))^* \Phi_\lambda(\phi_r) \sum_{\text{odd } l'} \mathcal{C}_{pl\lambda l'} \mathcal{R}_{p\lambda l'}(r) P_{l'}(\cos\theta_r) \Bigg)\end{aligned} \tag{G.10}$$

i.e., the symmetry of the $Y_l^\lambda(\hat{\mathbf{p}})$ should be matched by the symmetry of the $\psi_{pl\lambda}(\bar{\mathbf{r}})$ since in the asymptotic region their product becomes $R_{pl}(r) Y_l^\lambda(\hat{\mathbf{r}})(Y_l^\lambda(\hat{\mathbf{p}}))^*$ (see expression G.5).

Now by substituting G.9 (or G.10), G.2 into the formula for transition matrix element gives:

$$\langle \psi_p^{(-)} | \hat{\boldsymbol{\varepsilon}} \cdot \bar{\mathbf{r}} | \psi_a \rangle = \frac{4\pi}{\sqrt{p}} \sum_{l,\lambda} i^l Y_l^\lambda(\hat{\mathbf{p}}) \left(d_{l\lambda}^z e^{i\delta_{l\lambda}} \cos\theta' + d_{l\lambda}^x e^{i\delta_{l\lambda}} \sin\theta' \right) \tag{G.11}$$

where

$$\langle \psi_{pl\lambda}(\bar{\mathbf{r}})^* | x | \psi_a \rangle = d_{l\lambda}^x e^{i\tau_{l\lambda}} \quad , \quad \langle \psi_{pl\lambda}(\bar{\mathbf{r}})^* | y | \psi_a \rangle = d_{l\lambda}^y e^{i\tau_{l\lambda}} \quad , \quad \langle \psi_{pl\lambda}(\bar{\mathbf{r}})^* | z | \psi_a \rangle = d_{l\lambda}^z e^{i\tau_{l\lambda}} \tag{G.12}$$

and $\tau_{l\lambda}$ is the short range phase shift and $\delta_{l\lambda} = \tau_{l\lambda} + \eta_l$ is the total phase shift. The term $\langle \psi_{pl\lambda}(\bar{\mathbf{r}})^* | y | \psi_a \rangle$ is not present in the case of linearly polarized light due to the choice of the specific coordinate system, but is present in the case of circularly polarized light — see below.

The more explicit form of the $d^z_{l\lambda}\exp(i\tau_{l\lambda})$ is given by

$$\begin{aligned} d^z_{l\lambda}\exp(i\tau_{l\lambda}) &= \int \Phi^*_\lambda(\phi_r)\sum_{l'}\mathcal{C}^*_{pl\lambda l'}\mathcal{R}_{p\lambda l'}(r)P_{l'}(\cos\theta_r)Y^0_1(\hat{\mathbf{r}})\sum_{l''}R_{al''}(r)Y^0_{l''}(\hat{\mathbf{r}})d\bar{\mathbf{r}} = \\ &= \sum_{l'}\sum_{l''}\sqrt{\frac{2l+1}{2}}\mathcal{C}^*_{pl\lambda l'}\int \Phi^*_\lambda(\phi_r)\Phi_0(\phi_r)\Phi_0(\phi_r)d\phi_r\times \\ &\times\int \mathcal{R}_{p\lambda l'}(r)R_{al''}(r)r^2dr\int P_{l'}(\cos\theta_r)P_1(\cos\theta_r)P_{l''}(\cos\theta_r)d(\cos\theta_r) = \\ &= \sum_{l'}\sum_{l''}\sqrt{\frac{2}{2l+1}}\mathcal{C}^*_{pl\lambda l'}\int \mathcal{R}_{p\lambda l'}(r)R_{al''}(r)dr\,\delta_{\lambda 0}\,\delta_{l'(l''\pm 1)} \end{aligned} \tag{G.13}$$

A similar result can be obtained with the second part of electric dipole operator (G.1) corresponding to $x \propto Y^{-1}_1(\hat{\mathbf{r}}) - Y^1_1(\hat{\mathbf{r}})$. The $\delta_{\lambda 0}$ in the result G.13 ensures that the only $Y^\lambda_l(\hat{\mathbf{p}})$ contributing in transition element G.11 (due to Y^0_1) are with $\lambda = 0$ and $\lambda = \pm 1$ (due to $Y^{\pm 1}_1$); this is also used here to drop the x, y and z superscripts so that $d_{l0} := d^z_{l0}$ and $d_{l1} := d^x_{l1} = d^y_{l1}$. Expression G.11 can be simplified as

$$\begin{aligned} \langle\psi^{(-)}_p|\hat{\boldsymbol{\varepsilon}}\cdot\bar{\mathbf{r}}|\psi_a\rangle &= \frac{4\pi}{\sqrt{p}}\sum_l i^l\left(Y^0_l(\hat{\mathbf{p}})d_{l0}e^{i\delta_{l0}}\cos\theta' + \frac{Y^{-1}_l(\hat{\mathbf{p}}) - Y^1_l(\hat{\mathbf{p}})}{\sqrt{2}}d_{l1}e^{i\delta_{l1}}\sin\theta'\right) = \\ &= \sum_l\left(Y^0_l(\hat{\mathbf{p}})A_l\cos\theta' + (Y^{-1}_l(\hat{\mathbf{p}}) - Y^1_l(\hat{\mathbf{p}}))\frac{B_l}{\sqrt{2}}\sin\theta'\right) \end{aligned} \tag{G.14}$$

where all the constant factors have been put into A_l and B_l, i.e., $i^l d_{l0}\exp(i\delta_{l0})4\pi/\sqrt{p} = A_l$ and $i^l d_{l1}\exp(i\delta_{l1})4\pi/\sqrt{p} = B_l$

In the case of a diatomic heteronuclear molecule such as CO all values of angular momentum are present in the initial state of the electron. Thus the equation for the general form of the differential cross section is

$$\frac{d^2\sigma}{dkd\Omega} \propto \left|\sum_l\left(A_l(k)Y^0_l(\hat{\mathbf{k}})\cos\theta' + \frac{B_l(k)}{\sqrt{2}}\left(Y^{-1}_l(\hat{\mathbf{k}}) - Y^1_l(\hat{\mathbf{k}})\right)\sin\theta'\right)\right|^2 \tag{G.15}$$

For symmetric molecules that have a definite parity the *gerade* and *ungerade* initial states can be separated. The $\delta_{l'(l''\pm 1)}$ in (G.13) shows that the electric dipole transition is only

possible between the states with opposite symmetry, i.e., the only transitions possible are $g \to u$ or $u \to g$ and they do not couple with each other. It follows that in case of a *gerade* initial state, which has contributions only from the even spherical harmonics, the final state will be of *ungerade* symmetry and have only odd l values.

$$\left.\frac{d^2\sigma}{dkd\Omega}\right|_g \propto \left|\sum_{l_{odd}} A_l(k) Y_l^0(\hat{\mathbf{k}}) \cos\theta' + \sum_{l_{odd}} \frac{B_l(k)}{\sqrt{2}} \left(Y_l^{-1}(\hat{\mathbf{k}}) - Y_l^1(\hat{\mathbf{k}})\right) \sin\theta'\right|^2$$

similarly the result is obtained for the *ungerade* initial state

$$\left.\frac{d^2\sigma}{dkd\Omega}\right|_u \propto \left|\sum_{l_{even}} A_l(k) Y_l^0(\hat{\mathbf{k}}) \cos\theta' + \sum_{l_{even}} \frac{B_l(k)}{\sqrt{2}} \left(Y_l^{-1}(\hat{\mathbf{k}}) - Y_l^1(\hat{\mathbf{k}})\right) \sin\theta'\right|^2$$

If the initial state of the electron cannot be resolved the contributions of both cross sections should be added incoherently

$$\begin{aligned}\left.\frac{d^2\sigma}{dkd\Omega}\right|_{sym} \propto & \left|\sum_{l_{odd}} A_l(k) Y_l^0(\hat{\mathbf{k}}) \cos\theta' + \sum_{l_{odd}} \frac{B_l(k)}{\sqrt{2}} \left(Y_l^{-1}(\hat{\mathbf{k}}) - Y_l^1(\hat{\mathbf{k}})\right) \sin\theta'\right|^2 + \\ & + \left|\sum_{l_{even}} A_l(k) Y_l^0(\hat{\mathbf{k}}) \cos\theta' + \sum_{l_{even}} \frac{B_l(k)}{\sqrt{2}} \left(Y_l^{-1}(\hat{\mathbf{k}}) - Y_l^1(\hat{\mathbf{k}})\right) \sin\theta'\right|^2\end{aligned} \tag{G.16}$$

The cross section for the case of the circular polarization can be similarly obtained by starting with the appropriate form of the electric dipole operator given by

$$\begin{aligned}\hat{\boldsymbol{\varepsilon}} \cdot \bar{\mathbf{r}} &= \frac{1}{\sqrt{2}}(\pm\hat{e}_1 - i\hat{e}_2) \cdot \bar{\mathbf{r}} = \frac{1}{\sqrt{2}}\left(\pm\left(\hat{z}\cos\theta' + \hat{y}\sin\theta'\right) - i\hat{x}\right) \cdot \bar{\mathbf{r}} = \\ &= \frac{1}{\sqrt{2}}\left(\frac{4\pi}{3}\right)^{1/2} \left(\pm Y_1^0(\hat{\mathbf{r}})\cos\theta' \pm \frac{i}{\sqrt{2}}\left(Y_1^1(\hat{\mathbf{r}}) + Y_1^{-1}(\hat{\mathbf{r}})\right)\sin\theta' - \frac{i}{\sqrt{2}}\left(Y_1^{-1}(\hat{\mathbf{r}}) - Y_1^1(\hat{\mathbf{r}})\right)\right) r\end{aligned}$$

where the $\pm$ sign corresponds to the handedness of the photon. The body-fixed coordinate system in this case is chosen according to the following sketch.

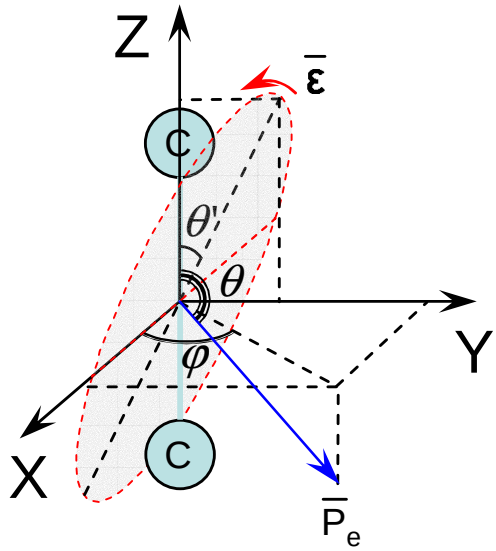

Here the polarization plane passes through the X axis and at the angle θ' with respect to the Z axis.

After repeating the same procedure with the above electric dipole operator the general form of the cross section for the diatomic heteronuclear molecule yields

$$\begin{aligned}\frac{d^2\sigma}{dkd\Omega} \propto \frac{1}{2}\Bigg|\sum_l A_l(k)Y_l^0(\hat{\mathbf{k}})\cos\theta' + \\ + i\sum_l \frac{B_l(k)}{\sqrt{2}}\left(\left(Y_l^{-1}(\hat{\mathbf{k}}) + Y_l^1(\hat{\mathbf{k}})\right)\sin\theta' \pm \left(Y_l^{-1}(\hat{\mathbf{k}}) - Y_l^1(\hat{\mathbf{k}})\right)\right)\Bigg|^2\end{aligned} \tag{G.17}$$

or for the symmetric molecule

$$\begin{aligned}\left.\frac{d^2\sigma}{dkd\Omega}\right|_{sym} \propto \frac{1}{2}\Bigg|\sum_{l_{odd}}\Big(A_l(k)Y_l^0(\hat{\mathbf{k}})\cos\theta' + \\ + \sum_{l_{odd}} i\frac{B_l(k)}{\sqrt{2}}\left(\left(Y_l^{-1}(\hat{\mathbf{k}}) + Y_l^1(\hat{\mathbf{k}})\right)\sin\theta' \pm \left(Y_l^{-1}(\hat{\mathbf{k}}) - Y_l^1(\hat{\mathbf{k}})\right)\right)\Bigg|^2 + \\ + \frac{1}{2}\Bigg|\sum_{l_{even}}\Big(A_l(k)Y_l^0(\hat{\mathbf{k}})\cos\theta' + \\ + \sum_{l_{even}} i\frac{B_l(k)}{\sqrt{2}}\left(\left(Y_l^{-1}(\hat{\mathbf{k}}) + Y_l^1(\hat{\mathbf{k}})\right)\sin\theta' \pm \left(Y_l^{-1}(\hat{\mathbf{k}}) - Y_l^1(\hat{\mathbf{k}})\right)\right)\Bigg|^2\end{aligned} \tag{G.18}$$

One factor that can cause higher m values to appear in the final cross-section form is the nonlinearity of the molecule, for example in the case of C_2H_4 and C_2H_6 molecules. Since there is no symmetry with respect to the rotation about the Z axis, m is not a good quantum number anymore. Thus the expansion of the initial core electron state G.2 should also be summed over different values of m. For these configurations the final state of the residual molecule can also have nonzero angular momentum along the Z axis due to the rotation of the sticking–out hydrogen atoms. It follows from angular momentum conservation that the photo-electron should thus be carrying out an angular momentum equal and opposite ($\pm$ the photon angular momentum) to the angular momentum of the molecule, which can have any value and not just $0; \pm 1$.

In the analysis of the C_2H_4 molecule the potential was approximated by the cylindrically symmetric one, e. i., treated as if the molecule were linear. The formula G.16 was considered sufficient to obtain quantitatively reasonable results. This assumption is also supported by the acceptable results of the fitting procedure, see figures 3.30–3.38.

Ambiguity of the Spherical Harmonics Fitting Results.

The results obtained by fitting the experimental photo-electron angular distributions with the function form G.15 were found not to be unique. To understand the source of this ambiguity it is convenient to expand the square in G.15 and rewrite it in the form

$$\sum_{l=0}^{2l_{max}} \left(C_l P_l(\cos\theta)\cos^2\theta' + B_l P_l(\cos\theta)\cos\phi\sin 2\theta' + D_l P_l(\cos\theta)\cos^2\phi\sin^2\theta' \right) \qquad \text{(G.19)}$$

which is similar to the functional forms used in [13–15]. In this representation parameters

C_l's, D_l's, and E_l's corresponding to the experimental distributions should be unique since they are contributions of the independent orthogonal functions of θ, ϕ, and θ'. These parameters are in turn second-order functions of A_l's and B_l's of G.15. Expression G.19 is not an appropriate fitting function form, however. From the comparison of functional forms G.15 and G.19 it can be seen that the number of parameters C_l's, D_l's, and E_l's is larger than that of A_l's and B_l's for a given number l_{max}, i.e., C_l's, D_l's, and E_l's are not completely independent.

After solving the equations that relate C_l's, D_l's, and E_l's with A_l's and B_l's exactly, the following conclusions were made:

1) In case of non-symmetric linear molecule (e.g., CO) for each set of values for A_l's and B_l's there are another three sets that yield identical values for C_l's, D_l's, and E_l's. One is just the complex conjugate of the first set, the other two correspond to sign flip of the relative phase between the σ and π cross sections and can be eliminated by fitting the experimental data obtained in the case of circular polarization. In either case all four sets should give the same absolute values of the spherical harmonic amplitudes and only differ by values of their phases.

2) In case of symmetric linear molecule (e.g., N_2, C_2H_2, C_2H_4) the two contributions (*gerade* and *ungerade* — see formula G.16) to total cross sections are both even functions of $\cos\theta$ and are not, in general, independent. Thus for any set of values of A_l's and B_l's an infinite number of different sets can be found, each resulting in the same values of C_l's, D_l's, and E_l's. The use of the data obtained in the case of circular polarization eliminates

most of these sets so that only a finite number of them remain valid. However, the values of A_l's and B_l's in these remaining sets can be, in general, sufficiently different to make even the absolute values of the spherical harmonic amplitudes vary appreciably from set to set. The number of these sets, although finite, goes up with the value of l_{max} which truncates the expansion in G.19 or G.15.

It was also found that the best least square fit of the experimental data does not necessarily correspond to the unique set of C_l's, D_l's, and E_l's either. The χ^2 of the fit is a function of the high number of fitting parameters and can have a lot of local minima in the corresponding n-dimensional space. For a sophisticated fitting function form the value of χ^2 in one of these local minima can be very close to the one corresponding to the true best fit. This difference can be within the finite error bars of the experimental data and thus absolutely inconclusive. This can result in non-unique values of the fitting parameters even for the analysis of the CO molecule.

Tables G.1 and G.2 present two sets of C_2H_4 angular distribution fitting parameters obtained for different initial values. The second set also has the d-wave σ cross-section contribution fixed at zero.

Table G.1: **C_2H_4 fitting results #1**

$h\nu$ (eV)	A_0	A_2		B_2		A_1	A_3		B_1		B_3	
		real	imag.	real	imag.		real	imag.	real	imag.	real	imag.
293	-1.759E-01	3.892E-01	-2.436E-01	2.356E-01	5.303E-01	-4.204E-01	5.142E-02	-3.092E-01	-2.408E-01	2.147E-01	2.240E-01	2.591E-02
295	-3.104E-01	2.682E-01	-2.934E-01	2.480E-01	5.048E-01	-5.330E-01	6.835E-02	-3.849E-01	-2.686E-01	-4.376E-02	1.045E-01	-5.490E-02
298	-3.110E-01	1.053E-01	-2.940E-01	-1.577E-01	4.342E-01	-4.950E-01	6.849E-02	-4.733E-01	3.693E-02	-4.361E-01	1.048E-01	6.281E-03
302	-3.850E-01	9.295E-02	-1.592E-01	-1.462E-01	3.961E-01	-5.005E-01	4.388E-02	-5.126E-01	2.261E-01	-4.062E-01	7.961E-02	2.612E-02
306	-3.535E-01	3.922E-02	-1.364E-01	-9.694E-02	3.018E-01	-5.047E-01	-1.482E-02	-5.113E-01	1.718E-01	-5.100E-01	1.693E-01	2.119E-02
309	-3.792E-01	4.155E-02	-8.216E-02	-6.874E-02	2.614E-01	-5.091E-01	-6.789E-02	-4.816E-01	1.450E-01	-5.387E-01	2.025E-01	2.579E-02
312	-3.656E-01	5.113E-02	-3.266E-02	-6.639E-02	2.388E-01	-5.007E-01	-1.165E-01	-4.746E-01	6.479E-02	-5.550E-01	2.497E-01	2.508E-02
315	-3.236E-01	1.148E-01	6.751E-02	-7.803E-02	2.221E-01	-5.005E-01	-1.588E-01	-4.335E-01	-1.523E-02	-5.637E-01	2.890E-01	7.421E-03
318	-2.960E-01	1.127E-01	7.729E-02	-1.042E-01	2.024E-01	-4.854E-01	-1.630E-01	-4.430E-01	-6.557E-02	-5.590E-01	3.146E-01	1.747E-03
320	-2.850E-01	1.454E-01	1.198E-01	-8.745E-02	2.008E-01	-4.795E-01	-1.586E-01	-3.916E-01	-7.752E-02	-5.677E-01	3.333E-01	8.218E-03

Table G.2: **C_2H_4 fitting results #2** ($|A_2| = 0$)

$h\nu$ (eV)	A_0	B_2		A_1	A_3		B_1		B_3	
		real	imag.		real	imag.	real	imag.	real	imag.
293	-5.919E-01	-2.954E-03	-3.341E-01	-1.901E-01	-2.873E-01	-2.140E-01	5.530E-01	1.329E-01	1.616E-01	-1.770E-01
295	-5.040E-01	-1.162E-01	-3.861E-01	-4.015E-01	-6.771E-02	-4.274E-01	4.957E-01	1.642E-01	1.152E-01	-1.610E-02
298	-4.705E-01	9.377E-02	-4.607E-01	-4.171E-01	2.886E-02	-5.206E-01	4.310E-01	9.180E-02	2.004E-03	-3.414E-02
302	-4.911E-01	-1.522E-01	2.955E-01	-4.753E-01	3.401E-02	-5.048E-01	2.650E-01	-4.276E-01	1.520E-01	4.254E-02
306	-4.390E-01	-1.512E-01	9.780E-07	-4.619E-01	-4.694E-02	-5.039E-01	4.312E-01	-4.290E-01	1.603E-01	1.818E-02
309	-4.502E-01	-1.125E-01	2.087E-06	-4.687E-01	-9.408E-02	-4.677E-01	3.443E-01	-5.087E-01	1.855E-01	2.635E-02
312	-4.350E-01	-1.013E-01	8.265E-08	-4.624E-01	-1.351E-01	-4.540E-01	1.867E-01	-5.737E-01	2.474E-01	2.883E-02
315	-4.663E-01	-3.516E-02	5.594E-06	-4.171E-01	-2.128E-01	-3.891E-01	3.726E-02	-6.087E-01	2.874E-01	-1.504E-02
318	-4.343E-01	-6.069E-02	6.487E-06	-4.219E-01	-2.053E-01	-3.984E-01	-2.293E-02	-6.025E-01	3.142E-01	-1.626E-02
320	-4.687E-01	2.172E-02	-1.532E-04	-3.897E-01	-2.357E-01	-3.161E-01	-1.069E-01	-6.032E-01	3.294E-01	-4.737E-02

Appendix H

Plotting the Experimental Angular Distributions in the Case of Linear Polarization

The angular distributions of the photoelectrons are usually presented as a function of two variables θ and θ'. These are the angles between the electron momentum and the molecular axis, and between the molecular axis and the X-ray polarization direction, respectively. Planar polar plots of these angular distributions provide a means to visualize the underlying three dimensional ones. The dependence of $f(\theta, \phi, \theta')$ on the photoelectron azimuthal angle ϕ is usually dropped by choosing the orientation when $\phi = 0°$ (or $\phi = 90°$ in case of the circularly polarized light). Figure 3.1 shows the distribution $f_l(\theta, \theta')$ as a two dimensional plot. Another reason why the two-dimensional representation of the linear polarization data is sufficient is that the information obtained from events with $\phi \neq 0°$ is redundant. In this appendix it will be shown how to sort these events to accomplish their proper projection into the $\phi = 0°$ plane. This procedure greatly increases the statistics and enhances the quality of the resulting distributions.

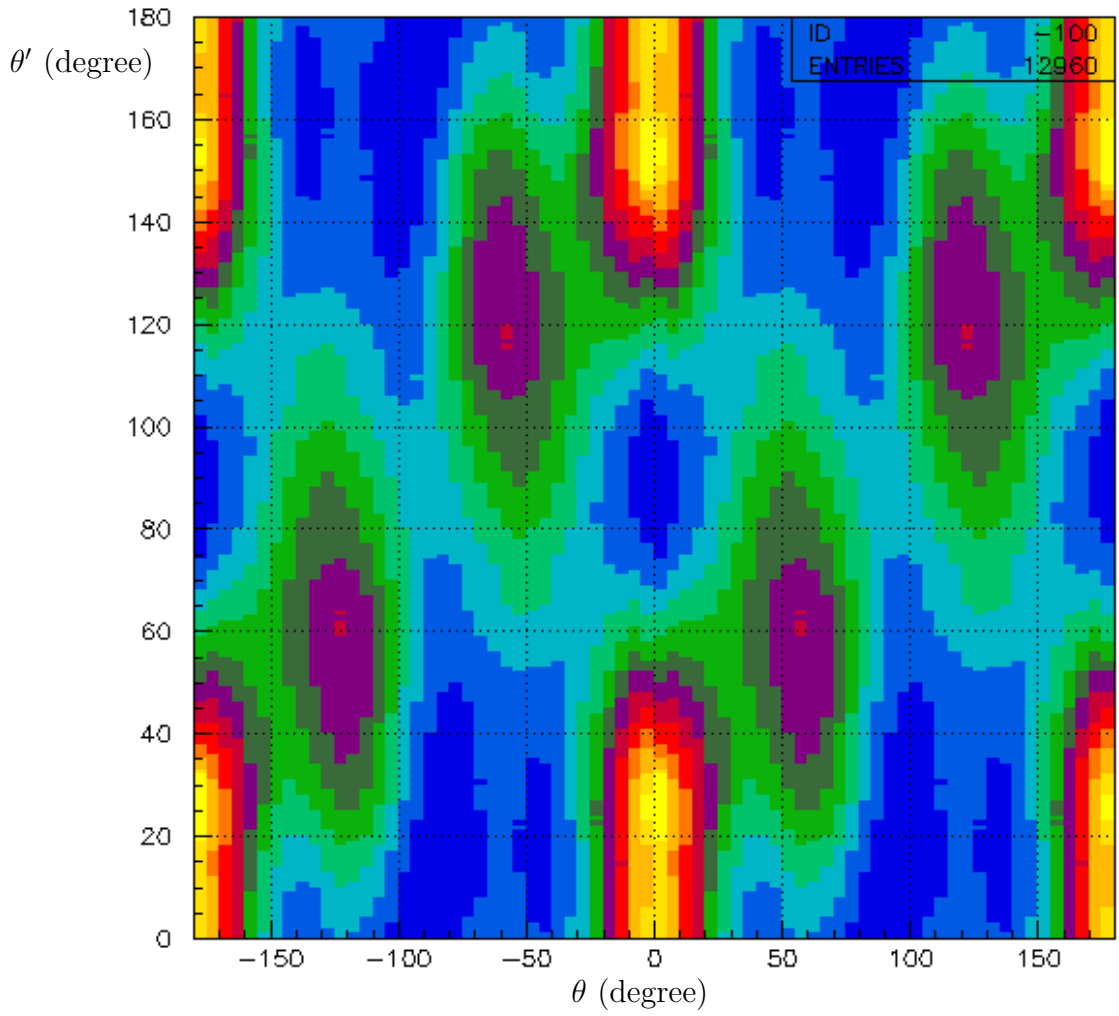

Figure H.1: $f_l(\theta, \theta')$ for the 302eV X-rays on the C_2H_4 Molecule.

The trivial starting point in producing the electron angular distribution for $\phi = 0$ is to confine the analysis to a single plane (XZ plane of the laboratory frame (see fig. 2.5), for example). In this case a gate condition is set to require that the electron and the molecule lie in that plane, i.e., the electron and recoil momentum components perpendicular to this analysis plane are less than a certain small fraction of the total momentum value. This accepts particles from a finite solid angle around this plane to ensure that statistics in the resulting distributions are still appreciable. The angles between different particles in this plane can be calculated by measuring the angle between the projections of their momenta onto the plane. In spite of the fact that these projections are very close to the actual total momentum vector (due to the gate discussed above) the use of the total momentum vectors would treat the situations with small angles between the molecule and the polarization direction unfairly and would create artificial dips in the angular distributions. The resulting number of counts in such a limited analysis would be proportional to the value of the allowed solid angle squared. This is clearly not the most efficient procedure since in general it discards well over 90% of the collected data.

For example, if the analysis plane is defined by the polarization axis (which coincides with the X-axis of the laboratory frame) and the molecular orientation (that can be in any direction), the bins[1] of the 2d histogram that represents the function $f(\theta, \theta')$ should be incremented not by 1 every time one gets a hit but by $1/\sin\theta'$ to normalize the function to the solid angle of the molecular orientation direction. Another identically set up 2d histogram

[1]The bins of the corresponding histograms were taken to be of uniform size if measured in units of angle — either degrees or radians.

is always incremented by the square of the above weight value. When the analysis of the whole data set is complete this second histogram represents the array of squares of the error bars for function $f(\theta, \theta')$. The main part of the histogram $f(\theta, \theta')$ has much better statistics compared to the case of a single plane. This is achieved at the expense of large error bars for $\theta' \simeq 0$ (region of the smallest solid angle) due to the nature of the $1/\sin\theta'$ weight function.

A more sophisticated analysis can be performed to obtain σ and π cross sections with higher statistics and even their relative phase information in the case of the linear polarization if the general form of the cross section is given by formulae G.15 or G.16. As a matter of fact these formulae can be relaxed even further and the analysis will still work. As long as the differential cross section has the form[2]:

$$|A(\theta)\cos\theta' + B(\theta)\sin\theta'\cos\phi|^2 \tag{H.1}$$

all parts of the following analysis should work just as well. Here the functions $A(\theta)$ and $B(\theta)$ are some arbitrary complex functions of θ (θ, θ', and ϕ are the same angles as in G.15, G.16, or 3.1). It is clear that $\sigma_\sigma \propto \int |A(\theta)|^2 \sin\theta d\theta$ and $\sigma_\pi \propto \int |B(\theta)|^2 \sin\theta d\theta$ and after integration of H.1 over Ω and Ω' one gets the total cross section $\sigma_{total} = \sigma_\sigma + \sigma_\pi$.

The idea behind the technique is to use all possible angles of electrons and molecular orientations in the final result. The simplest way to do this is to integrate the differential cross section H.1 over ϕ:

$$\int_0^{2\pi} |A(\theta)\cos\theta' + B(\theta)\sin\theta'\cos\phi|^2 \, d\phi = 2\pi \, |A(\theta)\cos\theta'|^2 + \pi \, |B(\theta)\sin\theta'|^2$$

[2]It is trivial to show that all the derivations will also work for the more general cross-section form given by $\sum_i |A_i(\theta)\cos\theta' + B_i(\theta)\sin\theta'\cos\phi|^2$.

That means if one sorts all the data into a two dimensional histogram (with the weight function $\frac{1}{|\sin\theta\sin\theta'|}$) according to the values of θ and θ', ignoring the value of ϕ, one will get the above function of two variables. The only disadvantage of this approach is that it completely loses the relative phase information between $A(\theta)$ and $B(\theta)$ functions.

The way to preserve the phase information and still use all the data involves the sorting of data into a two dimensional histogram as before but by using a special weight function that now depends on ϕ. Before this function is obtained let us consider a much simpler case first to prepare the ground for the similar but more involved derivation.

Suppose that some distribution $\frac{\partial N}{\partial\Omega}$ is measured and suppose that this distribution is independent of azimuthal angle ϕ so that the solid angle differential can be written as $d\Omega = d(2\pi\cos\theta)$. The standard approach is to sort the data with the unity weight function into the histogram with the bins defined by $\Delta\Omega \propto \Delta(\cos\theta)$ =const. That way the resulting $\frac{\partial N}{\partial\Omega}$ distribution is plotted as a function of Ω or $\cos\theta$. Sometimes it is needed to have this function plotted as a function of θ, that is with bins defined by $\Delta\theta$ =const instead of $\Delta(\cos\theta)$ =const. For example, when the data are represented in the form of a polar plot it is more convenient if the points are plotted every 5 or every 10 degrees. The following reasoning shows how to sort the data to obtain the $\frac{\partial N}{\partial\Omega}$ distribution as a function of θ.

$$\frac{\partial N(\Omega)}{\partial\Omega} \propto \left.\frac{\Delta N}{\Delta\cos\theta}\right|_{\text{exper. data}} \Rightarrow \left.\frac{\partial N(\Omega)}{\partial\Omega}\Delta\cos\theta \propto \Delta N\right|_{\theta:\,\cos\theta\propto\Omega} \Rightarrow$$

$$\Rightarrow \left.\frac{\partial N(\Omega)}{\partial\Omega}\sin\theta\Delta\theta \propto \Delta N\right|_{\theta:\,\cos\theta\propto\Omega} \Rightarrow f(\theta) := \left.\frac{\partial N}{\partial\Omega}\right|_{\Omega\propto\cos\theta} \propto \left.\frac{\Delta N}{\Delta\theta}\,\frac{1}{\sin\theta}\right|_{\text{exper. data}}$$

which means that whenever a hit appears in the range $\theta \pm \Delta\theta/2$ (with a constant value of $\Delta\theta$) the appropriate channel of the histogram should be incremented by $1/|sin\theta|$ and not just by 1.

Now consider the cross section given by H.1:

$$\frac{1}{\sin\theta\sin\theta'}\frac{\partial^3 N}{\partial\phi\partial\theta\partial\theta'} \propto \frac{1}{\sin\theta\sin\theta'}\left.\frac{\Delta N}{\Delta\phi\Delta\theta\Delta\theta'}\right|_{\text{exper. data}} = f(\theta,\theta',\phi) =$$
$$= \left|A(\theta)\cos\theta' + B(\theta)\sin\theta'\cos\phi\right|^2$$

The objective here is to sort all the data (including all values of ϕ) into the 2d histogram in such a way that it represents the distribution given by the function $g(x,y)$ such that:

$$g(\theta,\theta') = f(\theta,\theta',\phi)|_{\phi=0} = \left|A(\theta)\cos\theta' + B(\theta)\sin\theta'\right|^2$$

Let us start with the following, assuming some fixed value of ϕ first:

$$\frac{1}{\sin\theta\sin\theta'}\frac{\Delta N}{\Delta\phi} = \left|A(\theta)\cos\theta' + B(\theta)\sin\theta'\right|^2 \Delta\theta\Delta\theta'$$

Now let us change the θ and θ' variables to x and y so that $x=\theta$, $\cos y = \frac{\cos\theta'}{\sqrt{\cos^2\theta'+\sin^2\theta'\cos^2\phi}}$ and $\sin y = \frac{\sin\theta'\cos\phi}{\sqrt{\cos^2\theta'+\sin^2\theta'\cos^2\phi}}$. Then the above result could be rewritten as

$$\frac{1}{\sin\theta\sin\theta'}\frac{\Delta N}{\Delta\phi} = \left|A(x)\cos y + B(x)\sin y\right|^2\left(\cos^2\theta' + \sin^2\theta'\cos^2\phi\right)\left\|\begin{matrix}\frac{\partial\theta}{\partial x} & \frac{\partial\theta'}{\partial x}\\ \frac{\partial\theta}{\partial y} & \frac{\partial\theta'}{\partial y}\end{matrix}\right\|\Delta x\Delta y \Rightarrow$$

$$\Rightarrow \frac{1}{\sin\theta\sin\theta'\left(\cos^2\theta' + \sin^2\theta'\cos^2\phi\right)}\frac{\Delta N}{\Delta\phi}\frac{\partial y}{\partial\theta'} = \left|A(x)\cos y + B(x)\sin y\right|^2\Big|_{\substack{x=\theta\\ y=h(\theta',\phi)}}\Delta x\Delta y$$

where

$$y = h(\theta',\phi) = \begin{cases}\arctan\left(\tan\theta'\cos\phi\right) & \text{if } \cos\theta' > 0\\ \pi + \arctan\left(\tan\theta'\cos\phi\right) & \text{otherwise}\end{cases} \Rightarrow \frac{\partial y}{\partial\theta'} = \frac{\cos\phi}{\cos^2\theta' + \sin^2\theta'\cos^2\phi}$$

so finally one gets

$$g(x,y)\Big|_{\substack{x=\theta\\ y=h(\theta',\phi)}} = f(x,y,0)\Big|_{\substack{x=\theta\\ y=h(\theta',\phi)}} =$$
$$= |A(x)\cos y + B(x)\sin y|^2 = \frac{\cos\phi}{\sin\theta\sin\theta'\left(\cos^2\theta' + \sin^2\theta'\cos^2\phi\right)^2}\frac{\Delta N}{\Delta\phi\Delta x\Delta y}\Bigg|_{\substack{x=\theta\\ y=h(\theta',\phi)}}$$

Thus the sorting process includes calculating the x and y coordinates for every hit (as a function of corresponding θ, θ', and ϕ) and incrementing the proper channel of the 2d histogram by the weight equal to

$$\left|\frac{\cos\phi}{\sin\theta\sin\theta'\left(\cos^2\theta' + \sin^2\theta'\cos^2\phi\right)^2}\right| \tag{H.2}$$

This can be thought of as if the angular distribution in the plane determined by a given value of ϕ is similar to the one with $\phi = 0$ but shrunk along the $\theta' = 90°$ direction according to the value of $\cos\phi$. This sorting technique reverses this shrinking effect and rotates the result to the $\phi = 0$ plane.

In this experiment the validity of the use of this sorting was checked by comparing the angular distributions obtained for different small segments of ϕ with each other and with the result for $\phi = 0$ plane. The distributions were found to be identical within the error bars. This brings up the other advantage of using this formula. It is clear that since the resulting distribution $g(x,y)$ is independent of ϕ the weight function H.2 can be multiplied by any function of ϕ (it cannot be a function of any other angle!!) to favor or to lower the effect of a certain range of azimuthal angles. This will only affect the error bars of the resulting distribution and will not change its shape. For example, the error bars on the π part of the cross section ($\theta' \to 90°$) blows up for $\phi \to 90°$ since the weight function becomes

$\rightarrow \left|\frac{1}{\sin\theta\sin\theta'\cos^3\phi}\right|$. One might consider multiplying it by $\cos^3\phi$ to compensate for this or even setting the gate on the range of ϕ to exclude this case entirely.

As was mentioned above, this kind of data sorting[3] is very error-prone, since it involves first the calculation of all the original angles θ, θ', and ϕ, and then their conversions to x and y. All of that is done in some arbitrarily oriented system of coordinates. Many vector products are involved; special attention must be paid to the signs of all the angles, etc. Thus this part of the analysis should be performed with special care, and none of the details should be ignored. "Erroneous results are to be expected otherwise".

[3]The FORTRAN code for the proper sorting procedure can be found in the folder "programs" of the attached CD.

Appendix I

Acetylene/Vinylidene Momentum Picture Interpretation

The unusual character of the momentum plot obtained by assuming a 13/13 symmetric breakup of acetylene, seen from the comparison of figures 3.13 and 3.14, can be explained by the presence of mass 12 a.m.u. and 14 a.m.u. recoils in the spectrum as shown in the bottom part of fig. I.1. The usual technique of separating the different recoil breakup channels by gates on the PIPICO spectrum does not give very good results in this case because the total mass of both recoils is equal to 26 a.m.u., the same as for mass 13-13 a.m.u. recoils. This puts both of these channels right on top of each other in terms of the position along the diagonal of the PIPICO spectrum (see fig. 4.1). The small Δm=1 a.m.u. does not suffice to separate these channels since the difference in curvature of the PIPICO stripes for CH^+ + CH^+ and CH_2^+ + C^+ breakup is very small and can be seen only with a very high spectrometer extraction field which would cause a very poor electron momentum resolution. Thus the only spectra in which the presence of the vinylidene dication breakup is obvious are the momentum plots.

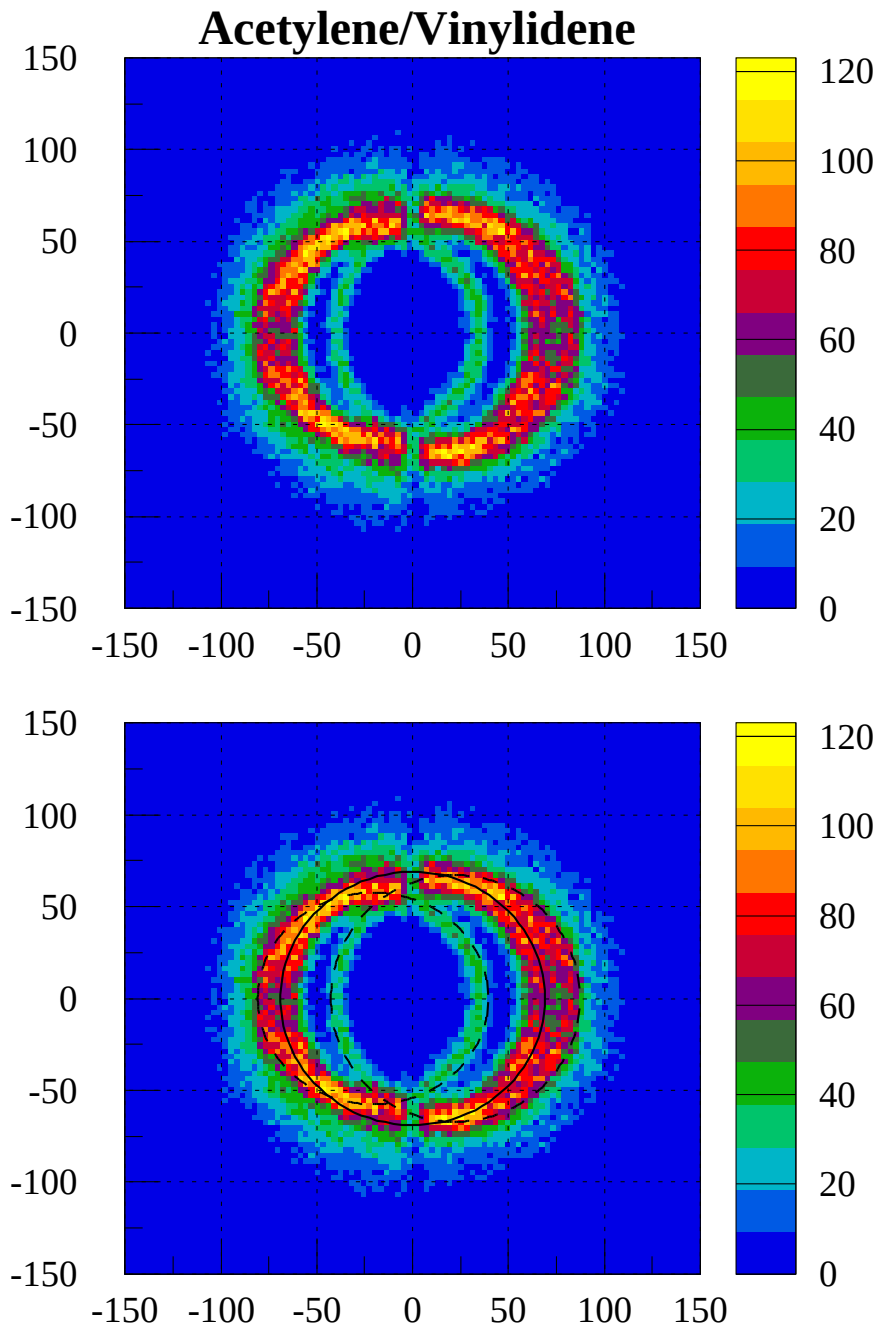

Figure I.1: Y vs X Momentum Plot of the Symmetric Molecular Breakup after k-shell photoionization of Acetylene (top) and with the calculated positions for the different mass recoils (bottom).

To understand these shapes it is important to remember that the X momentum component of the spectra in fig. I.1 is calculated from the time-of-flight of the particle, and the Y component is calculated from the Y position on the detector as follows:

$$\begin{cases} P_x = \frac{Sm}{t} - \frac{Eqt}{2} \\ P_y = \frac{my}{t} \end{cases}$$

When these calculations were performed to obtain the momentum plots in fig. I.1 it was originally assumed (mistakenly) that only mass 13 a.m.u. recoils were present. Let us consider what happens when the recoil momenta are mis-analyzed due to the incorrect mass assignments. Let $\bar{P}$ and m be recoil ion's momentum and mass and $\bar{P}'$ and m' be the calculated ones with P'_x, P'_y and P'_z being corresponding momentum components (S — is the flight distance, E — spectrometer electric field, and q — recoil charge):

$$\begin{cases} P'_x = \frac{Sm'}{t} - \frac{Eqt}{2} = \frac{Sm}{t} - \frac{Eqt}{2} + \frac{\Delta m S}{t} \simeq \frac{Sm}{t} - \frac{Eqt}{2} + \frac{\Delta m S}{t_0} \\ P'_y = \frac{m'y}{t} = \frac{m'}{m}\frac{my}{t} = \frac{m'}{m}P_y \end{cases} \Rightarrow$$

$$\begin{cases} \boldsymbol{P'_x = P_x + \Delta m \frac{S}{t} \simeq P_x + \Delta m \frac{S}{t_0}} \\ \boldsymbol{P'_y = \frac{m'}{m} P_y} \\ \boldsymbol{P'_z = \frac{m'}{m} P_z} \end{cases} \tag{I.1}$$

where the approximation was made for simplicity that $t = t_0 + \Delta t \approx t_0$ with t_0 being the peak position of the time-of-flight distribution. This is often the case because the spread of the distribution is much smaller than the position of the peak $\Rightarrow t_0 \gg \Delta t$ and thus t in the denominator can be replaced by t_0. Equation I.1 shows how the momentum sphere calculated from the experimental data will be distorted if the wrong value of the mass is used in the calculation.

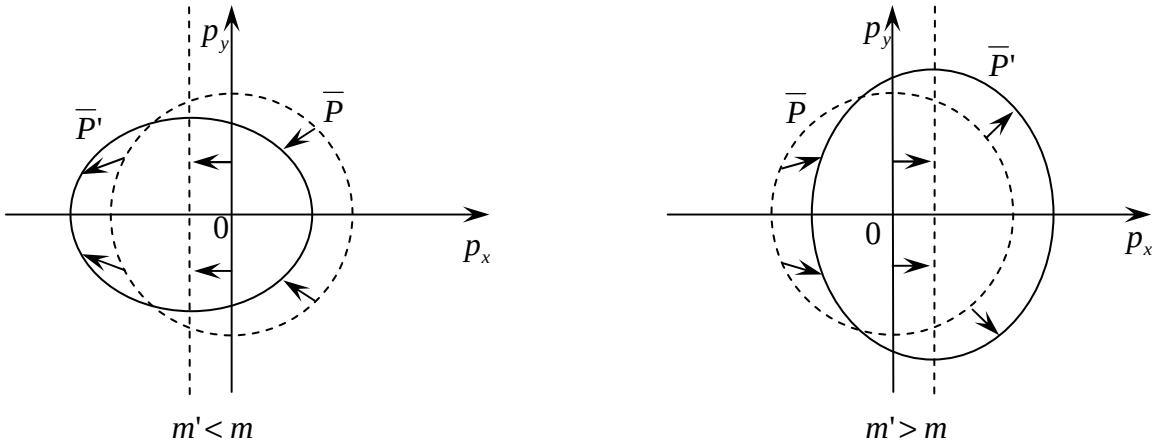

For example, if the value of the $\Delta m = m' - m$ is positive or $m' > m$ then the momentum sphere will be shifted towards the positive values of p_x by approximately $\Delta m/t_0$, and it is stretched along the p_y and p_z axes by a factor of m'/m, or in the case when $m' = 13$ a.m.u. and $m = 12$ a.m.u., by about 8% as shown in the schematics ($\bar{P}$ represented by dashed lines, and $\bar{P}'$ — by solid curves). Similarly the case of $m' = 13$ a.m.u. and $m = 14$ a.m.u. the momentum sphere will get shifted by $\sim S/t_0$ in the negative direction of p_x and shrunk along p_y and p_z by about 8%.

If all three masses 12, 13, and 14 a.m.u. are present in the data the resulting momentum spheres[1] overlapping as shown in the bottom part of fig. I.1 by solid and dashed black lines on top of the experimental data. The perfect agreement shows clearly that the strange momentum spectra result from recoils of different mass (12 and 14) being mixed with the main channel (13 plus 13).

[1]The slight difference in the kinetic energy release (see fig. 4.6) is also taken into account here when calculating the positions of the circles corresponding to different masses.

Appendix J

Calculation Of C–C bond rotation in the Isomerization Process

The calculation process covered in this appendix is quite long and tedious although simple in principle. It will be presented in detail for the simplest case of symmetric C–H bonds vibration and only the final analytical result will be given for different steps of the proposed isomerization process.

C–C Bond Rotation in the Symmetric C–H Bending

The logical choice of the coordinate system is the one where the center of mass is at rest:

$$\sum_i m_i \dot{\bar{\mathbf{r}}}_{\mathbf{i}} = 0$$

Taking the center of mass for the center of the coordinate system ensures that the angular momentum of the system is constant in the absence of external torques and can be set to zero for the purpose of this calculation. The position of the center of mass for the particular case in hand is trivial and is always the mid point between two carbons. In general however it might be a function of angles and bond lengths of the corresponding molecular ion and

should be found from the following equations:

$$\sum_i m_i x_i = 0 \ ; \ \sum_i m_i y_i = 0$$

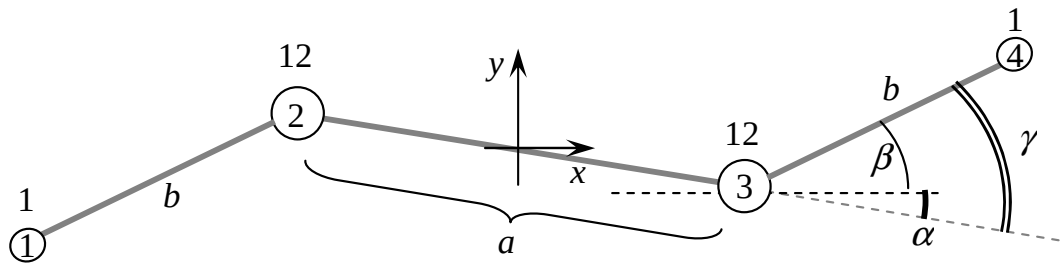

In this particular case one has for the coordinates of the four nuclei the following:

$$\begin{cases} x_1 = -\left(\frac{1}{2}a\cos\alpha + b\cos\beta\right) \\ y_1 = \frac{1}{2}a\sin\alpha - b\sin\beta \end{cases} ; \begin{cases} x_2 = -\frac{1}{2}a\cos\alpha \\ y_2 = \frac{1}{2}a\sin\alpha \end{cases}$$

$$\begin{cases} x_3 = \frac{1}{2}a\cos\alpha \\ y_3 = -\frac{1}{2}a\sin\alpha \end{cases} ; \begin{cases} x_4 = \frac{1}{2}a\cos\alpha + b\cos\beta \\ y_4 = -\frac{1}{2}a\sin\alpha + b\sin\beta \end{cases}$$

Where a and b are the bond lengths and α and β are the corresponding angles to the horizontal as shown in schematics. The angle $\gamma = \alpha + \beta$ is the angle between the C–C bond and C–H bond. The final goal is to find α as a function of γ since that is the parameter that usually describes the geometry of the ion structure.

Table J.1: **Angle of the C–C Bond in Trans Bend Geometry of Acetylene Dication.** In all four cases α is calculated for $\gamma = 51.7°$ see [37]

State	$^3\Sigma_g^-$	$^3\Delta_g$	$^1\Sigma_g^+$	^1A_g
a	2.308Å	1.344Å	1.378Å	1.365Å
b	1.145Å	1.137Å	1.134Å	1.135Å
$\boldsymbol{\alpha}$	.106 rad	.208 rad	.201 rad	.2035 rad

Now the angular momentum conservation will come into play:

$$\begin{aligned}
\overline{L}(t) = \text{const} = 0 = \sum_i \bar{\mathbf{r}}_\mathbf{i} \times \left(m_i \dot{\bar{\mathbf{r}}}_\mathbf{i}\right) = \sum_i m_i \left(x_i \dot{y}_i - \dot{x}_i y_i\right) = \\
= \left(-\left(\frac{1}{2}a\cos\alpha + b\cos\beta\right)\left(\frac{1}{2}a\cos\alpha\dot{\alpha} - b\cos\beta\dot{\beta}\right) - \right. \\
- \left(\frac{1}{2}a\sin\alpha\dot{\alpha} + b\sin\beta\dot{\beta}\right)\left(\frac{1}{2}a\sin\alpha - b\sin\beta\right) + \\
\left. + 12\left(-\frac{1}{4}a^2\cos^2\alpha\dot{\alpha} - \frac{1}{4}a^2\sin^2\alpha\dot{\alpha}\right)\right) 2 = \\
= 2\left(b^2\dot{\beta} - \frac{a^2}{4}\dot{\alpha} + \frac{1}{2}\cos\left(\alpha+\beta\right)(\dot{\beta} - \dot{\alpha}) - 3a^2\dot{\alpha}\right) = \\
= \left(2b^2 + ab\cos\gamma\right)\dot{\gamma} - \left(2b^2 + \frac{13}{2}a^2 + 2ab\cos\gamma\right)\dot{\alpha}
\end{aligned}$$

where the masses of the nuclei were substituted as 1 a.m.u. and 12 a.m.u., also $\dot{\beta} - \dot{\alpha}$ was replaced by $\dot{\gamma} - 2\dot{\alpha}$ in the final result. After the separation of the derivatives:

$$\dot{\alpha} = \frac{2b^2 + ab\cos\gamma}{2b^2 + 7.5a^2 + 2ab\cos\gamma}\dot{\gamma} \;\Rightarrow \int d\alpha = \int \frac{2b^2 + ab\cos\gamma}{2b^2 + 7.5a^2 + 2ab\cos\gamma}d\gamma$$

The final result after the integration is given by:

$$\alpha = \frac{\gamma}{2} + \frac{4b^2 - 13a^2}{\sqrt{13a^2 - 4ab + 4b^2}\sqrt{13a^2 + 4ab + 4b^2}}\arctan\left(\frac{\sqrt{13a^2 - 4ab + 4b^2}}{\sqrt{13a^2 + 4ab + 4b^2}}\tan\frac{\gamma}{2}\right)$$

Table J.1 gives the values of α calculated by means of the above formula for four different sets of values of a and b parameters corresponding to the four lowest states of the acetylene dication described in [37]. The averaging over these four states gives the final result $\boldsymbol{\alpha} =$ $\mathbf{.180 \pm .02}$ rad $= \mathbf{10.3^\circ \pm 1.14^\circ}$.

C–C Bond Rotation During the Acetylene→Vinylidene Isomerization.

The isomerization process is assumed to proceed through a tangential hydrogen atom motion. It first moves around the right carbon atom and when it gets about half way in between the carbons it becomes attached to the left one and moves around it. At some point the second hydrogen starts feeling the first one and they both are assumed to move to their final location on the left carbon with the angle between them kept constant and equal.

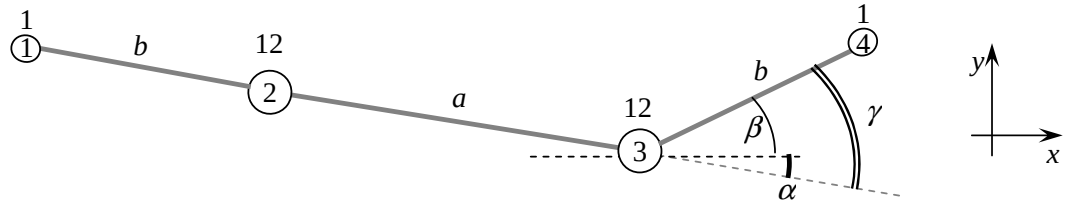

The first stage of the rearrangement gives the following result (see schematics for details on the parameter definitions):

$$\alpha = \frac{\gamma}{2} - \frac{\sqrt{13}\, a(13a+2b)}{\sqrt{169a^2+48b^2}\sqrt{13a^2+4ab+4b^2}} \arctan\left(\frac{\sqrt{169a^2+48b^2}}{\sqrt{13}\sqrt{13a^2+4ab+4b^2}} \tan\frac{\gamma}{2}\right)$$

The resulting numerical values given for three different sets of parameters (see [37])

a	1.2164Å	1.3447Å	1.3905Å
b	1.0625Å	1.1366Å	1.1391Å
$\boldsymbol{\gamma} = \pi - \mathrm{acos}(\frac{a}{2b})$	2.1803 rad	2.2038 rad	2.2273 rad
$\boldsymbol{\alpha}$	.2133 rad	.2051 rad	.1974 rad

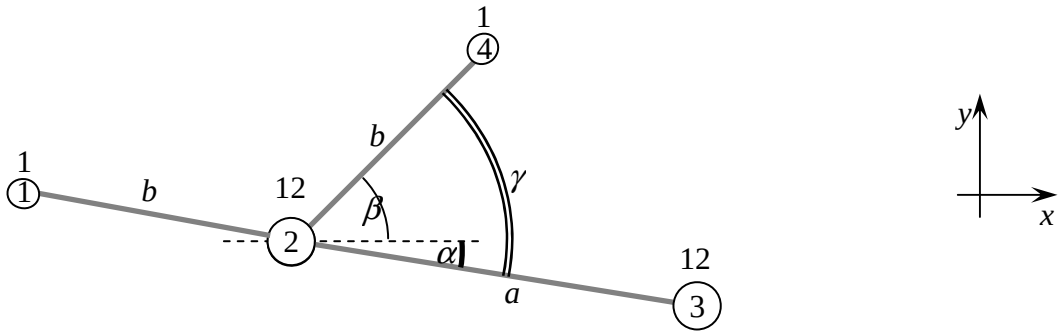

The result for the C–C bond rotation in the second stage of isomerization is

$$\alpha = \frac{\gamma}{2} - \frac{\sqrt{6}\, a(7a+b)}{\sqrt{7a^2+2ab+2b^2}\sqrt{42a^2+13b^2}} \arctan\left(\sqrt{6}\frac{\sqrt{7a^2+2ab+2b^2}}{\sqrt{42a^2+13b^2}} \tan\frac{\gamma}{2}\right)\Bigg|_{\gamma_d}^{\gamma_u}$$

The following table gives the results for the three already established states for $\gamma_u = 61.97°$:

a	1.2164Å	1.3447Å	1.3905Å
b	1.0625Å	1.1366Å	1.1391Å
$\boldsymbol{\gamma_d} = \mathrm{acos}(\frac{a}{2b})$	.9613 rad	.9378 rad	.9143 rad
$\boldsymbol{\alpha}$	.00776 rad	.008631 rad	.009356 rad

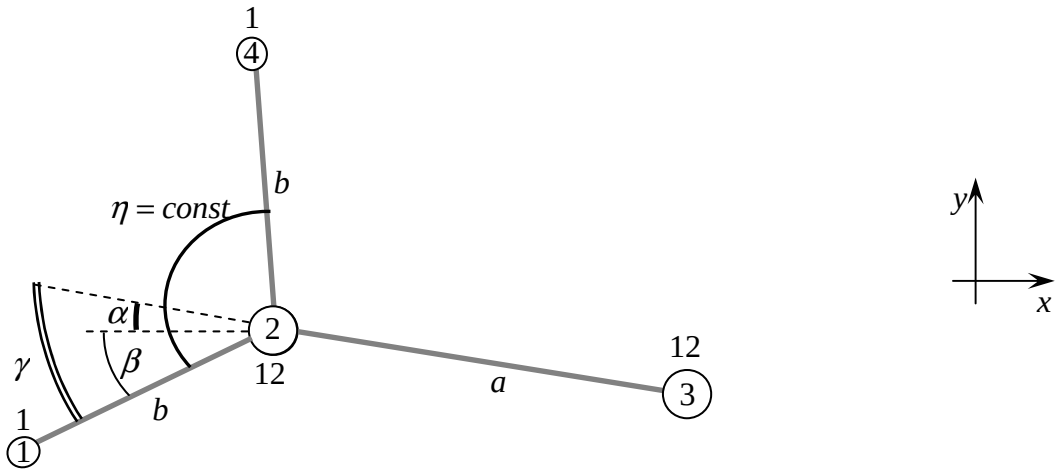

The resulting formula for the third stage of the isomerization is

$$\alpha = \frac{\gamma}{2} - \frac{\eta}{4} - \frac{b^2\cos\eta + 84a^2 - 25b^2}{\sqrt{b^4\cos^2\eta - 2b^2(228a^2+25b^2)\cos\eta + 7056a^4 + 3912a^2b^2 + 625b^4}} \times$$
$$\times \arctan\left(\sqrt{\frac{b^2\cos\eta + 24ab\cos\frac{\eta}{2} - 84a^2 - 25b^2}{b^2\cos\eta - 24ab\cos\frac{\eta}{2} - 84a^2 - 25b^2}} \tan\left(\frac{\gamma}{2} - \frac{\eta}{4}\right)\right)\Bigg|_{\gamma=0}^{\gamma=\eta/2}$$

given that $\eta = 118.03°$ the table of the numerical results is

a	1.2164Å	1.3447Å	1.3905Å
b	1.0625Å	1.1366Å	1.1391Å
$\boldsymbol{\alpha}$	.21914 rad	.20933 rad	.20032 rad

The combined result of the above three steps of the isomerization process is given in table J.2. The final value of the C–C bond rotation angle after the isomerization averaged over the three listed states is given by $\mathbf{0.423 \pm 0.013\ rad} = \mathbf{23.8° \pm 0.8°}$.

Table J.2: **Angle of the C–C Bond in the Vinylidene Dication (see [37]).**

State	${}^1\Sigma_g^+$ (C_2H_2)	${}^3\Sigma_g^-$ ($C_2H_2^{++}$)	${}^1B_1$(H_2CC^{++})
a	1.2164Å	1.3447Å	1.3905Å
b	1.0625Å	1.1366Å	1.1391Å
$\boldsymbol{\alpha}$	.44019 rad	.423041 rad	.407116 rad

References

[1] H. Goldstein, *Classical Mechanics*, 2nd ed. (Addison-Wesley Publishing Company, Inc., Philippines, 1980).

[2] T. Jahnke *et al.*, Phys. Rev. Lett. **88**, 073002 (2002).

[3] T. Weber *et al.*, J. Phys. B **34**, 3669 (2001).

[4] A. Landers, T. Weber, I. Ali, A. Cassimi, M. Hattass, O. Jagutzki, A. Nauert, T. Osipov, A. Staudte, M. H. Prior, H. Schmidt-Böcking, C. L. Cocke, and R. Dörner, Phys. Rev. Lett. **87**, 013002 (2001).

[5] T. Osipov, Bachelor's Thesis, University of Nevada, Reno, 1998.

[6] J. L. Dehmer, D. Dill, and S. Wallace, Phys. Rev. Lett. **43**, 1005 (1979).

[7] N. Haack, G. Ceballos, H. Wende, K. Baberschke, D. Arvanitis, A. L. Ankudinov, and J. J. Rehr, Phys. Rev. Lett. **84**, 614 (2000).

[8] B. Kempgens, H. M. Köppe, A. Kivimäki, M. Neeb, K. Maier, U. Hergenhahn, and A. M. Bradshaw, Phys. Rev. Lett. **79(1)**, 35 (1997).

[9] J. L. Dehmer and D. Dill, Phys. Rev. Lett. **35**, 213 (1975).

[10] J. Berkowitz, Photoabsorption, Photoionisation and Photoelectron Spectroscopy (New York: Academic) (1979).

[11] M. N. Piancastelli, T. A. Ferrett, D. W. Lindle, L. J. Medhurst, P. A. Heimann, S. H. Liu, and D. A. Shirley, J. Chem. Phys. **94**, 3004 (1989).

[12] A. L. D. Kilcoyne, M. Schmidbauer, A. Koch, K. J. Randall, and J. Feldhaus, J. Chem. Phys. **98(9)**, 6735 (1993).

[13] S. Motoki, J. Adachi, Y. Hikosaka, K. Ito, M. Sano, K. Soejima, A. Y. G. Raseev, and N. A. Cherepkov, J. Phys. B: At. Mol. Opt. Phys. **33**, 4193 (2000).

[14] S. Motoki, J. Adachi, K. Ito, K. Ishii, K. Soejima, A. Yagishita, S. K. Semenov, and N. A. Cherepkov, J. Phys. B: At. Mol. Opt. Phys. **35**, 3801 (2002).

[15] N. A. Cherepkov, G. Raseev, J. Adachi, Y. Hikosaka, K. I. S. Motoki, M. Sano, K. Soejima, and A. Yagishita, J. Phys. B: At. Mol. Opt. Phys. **33**, 4213 (2000).

[16] A. Ehresmann, H. Liebel, H. Schmoranzer, B. Z. S. Kammer, K.-H. Schartner, P. V. Demekhin, and V. L. Sukhorukov, J. Phys. B: At. Mol. Opt. Phys. **36**, 3669 (2003).

[17] E. Ohrendorf, H. Köppel, and L. Cederbaum, J. Chem. Phys. **91(3)**, 1734 (1989).

[18] E. Ohrendorf, F. Tarantelli, and L. Cederbaum, J. Chem. Phys. **92(5)**, 2984 (1990).

[19] H. Niikura, F. Legare, R. Hasbani, A. D. Bandarauk, M. Y. Ivanov, D. M. Villeneuve, and P. B. Corkum, Nature (London) **417**, 917 (2002).

[20] H. Niikura, F. Legare, R. Hasbani, M. Y. Ivanov, D. M. Villeneuve, and P. B. Corkum, Nature (London) **421**, 826 (2003).

[21] A. S. Alnaser, T. Osipov, E. P. Benis, A. Wech, B. Shan, C. L. Cocke, X. M. Tong, and C. D. Lin, Phys. Rev. Lett. **91**, 163002 (2003).

[22] A. H. Laufer, J. Chem. Phys. **73**, 49 (1980).

[23] A. Fahr and A. H. Laufer, J. Chem. Phys. **83**, 908 (1985).

[24] K. Ervin, J. Ho, and W. Lineberger, J. Chem.Phys. **91**, 5974 (1989).

[25] T. Carrington Jr., L. Hubbard, H. F. Schaerfer, and W. H. Miller, J. Chem. Phys. **80**, 4347 (1984).

[26] H. K. Srivastava, A. Conjusteau, H. Mabuchi, A. Callegari, K. K. Lehmann, G. Scoles, M. L. Silva, and R. Field, J. Chem. Phys. **113**, 7376 (2000).

[27] N. Chang, M. Shen, and C. Yu, J. Chem. Phys. **106**, 3237 (1996).

[28] J. Levin, H. Feldman, A. Baer, D. Ben-Hamu, O. Heber, D. Zajfman, and Z. Vager, Phys. Rev. Lett. **81**, 3347 (1998).

[29] M. J. Jensen, U. Pedersen, and L. H. Andersen, Phys. Rev. Lett. **84**, 1128 (2000).

[30] T. Ast, J. H. Beynon, and R. Cooks, Org. Mass. Spectrom. **6**, 749 (1972).

[31] J. R. Appling, B. E. Jones, L. E. Abbey, D. E. Bostwick, and T. F. Moran, Org. Mass. Spectrom. **18**, 282 (1983).

[32] R. R. Rye, T. E. Madey, J. E. Houston, and P. H. Holloway, J. Chem. Phys. **69**, 1504 (1978).

[33] M. Thompson, P. A. Hewitt, and D. S.Wooliscroft, Anal. Chem. **48**, 1336 (1976).

[34] J. Appel, J. Durup, F. C. Fehsenfeld, and P. Fournier, J. Phys. B **7**, 406 (1974).

[35] S. R. Andrews, F. Harris, and D. E. Parry, Chem. Phys. **166**, 69 (1992).

[36] R. Thissen, J. Delwiche, J. Robbe, D. Duflot, J. P. Flament, and J. H. D. Eland, J. Chem. Phys. **99**, 6590 (1993).

[37] D. Duflot, J.-M. Robbe, and J.-P. Flament, J. Chem. Phys. **102**, 355 (1994).

[38] R. Thissen, Ph.D. Thesis, Université de Lieġe, Belgium, 1993.

[39] T. Osipov, C. L. Cocke, M. H. Prior, A. Landers, O. J. Th.Weber, L. Schmidt, H. Schmidt-Böcking, and R. Dörner, Phys. Rev. Lett. **90**, 233002 (2003).

[40] C. Day, Phys. Today **19**, 19–21 (2003).

[41] D. R. Miller, in *Atomic and Molecular Beam Methods*, edited by G. Scoles, D. Bassi, U. Buck, and D. Lainé (Oxford University Press, New York, 1988), Vol. 14.

[42] G. Brusdeylins, J. Toennies, and R. Vollmer, Perugia 98 (1989).

[43] L. Pedemonte, G. Bracco, and R. Tatarek, Phys. Rev. A **59**, 3084 (1999).

[44] L. D. Landau and Lifshiz, in *Theoretical Physics vol.III: Quantum Mechanics (non-relativistic theory).*, 4th ed., edited by L. P. Pitaevskii (Moscow 'Nauka', 15 Leninskii ave. Moscow B-71. 117071 Russia, 1989), Vol. 3.